Taming GeV Photons & Antimatter

Formation Length-Related Bremsstrahlung Effects
& Controlling Slow Positrons

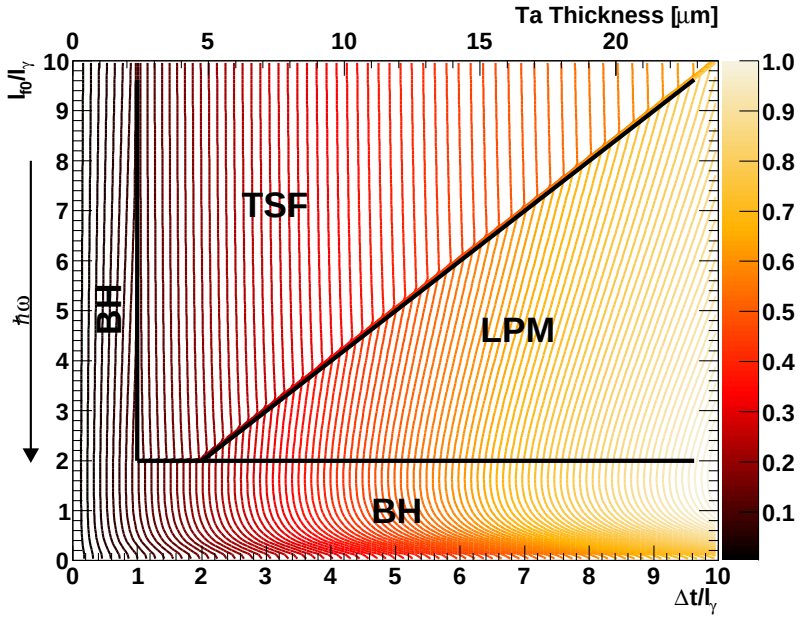

HEINE DØLRATH THOMSEN

DEPARTMENT OF PHYSICS AND ASTRONOMY
FACULTY OF SCIENCE
AARHUS UNIVERSITY, DENMARK

Dissertation for the degree of
Doctor of Philosophy
Juli 2010

Cover image: The bremsstrahlung power spectrum is plotted in the $(\Delta t, \ell_{f0}, \ell_\gamma)$ parameter space. The investigated regimes are bordered by black lines.

Department of Physics and Astronomy
Aarhus University
Ny Munkegade 120
DK-8000 Aarhus C
Email: heine@phys.au.dk
This document was compiled and typeset in LaTeX 2_ε

This thesis has been submitted to the Faculty of Science at the Aarhus University in partial fulfilment of the requirements for obtaining a PhD degree in physics. The work has been carried out under the supervision of associate professor Ulrik Ingerslev Uggerhøj at the Department of Physics and Astronomy.

CONTENTS

ABSTRACT & OUTLINE OF THE THESIS

During my PhD, I have been engaged in a small number of different fields which is also indicated by my list of publications from my time as a PhD student. I have thus actively participated in the topics of

- Measuring ionization cross sections in noble gasses with slow antiprotons as the projectile particle.
- Measuring the restricted energy loss of ultrarelativistic electrons in a thin Solid State Detector (SSD) and also of electron/positron pairs with creation vertex close to the SSD.
- Investigating bremsstrahlung phenomena from electrons/positrons of energies $E_0 \gtrsim 150$ GeV traversing amorphous foils or—to some extent—aligned crystals.
- Commissioning a state-of-the-art commercial trap for low-energy positrons ($\lesssim 1$ eV) and later performing test experiments with the high-quality positron beam.

Common to all topics is the family of interactions studied, all within the frameworks of Quantum electrodynamics (QED). Initially, the emphasis was mainly on the positron trap. However, this equipment suffered firstly from a six month delay relative to the original ETA. Secondly, it arrived somewhat damaged in Aarhus in November 2007, causing a further setback. Because of this, the repairs and commissioning were not finished until late 2008. The emphasis was thus increasingly turned towards the bremsstrahlung phenomena. As the title of my thesis suggests, the work presented here will be from the bremsstrahlung experiments and also my work with the positron trap, corresponding to Part I and II, respectively.

Part I – Formation Length Related Bremsstrahlung Phenomena

This part of the thesis deals with experimentally unexplored (or poorly explored) regions of the parameter space of the incoherent bremsstrahlung process in amorphous targets. As R. Blankenbecler states about incoherent bremsstrahlung [Bla97b]

> *. . . it is surprising that there is so much more to learn about such a well-understood process.*

Many of these regimes should also be relevant to systems where the interaction is much more complex, *e.g.* within the frameworks of Quantum chromodynamics (QCD). It is a great advantage to first study the phenomena in a QED system, where the interactions are known to extreme accuracy. After all, science is about

building on top of solid foundations. A theoretician, devising a QCD model for the phenomenon, could thus "see farther" by setting off from a model treating the QED system well. To find the latter, benchmark results are necessary. All experiments have been performed in bounds of the North Area 63 (NA63) Collaboration at Organisation Européenne pour la Recherche Nucléaire (CERN).

- Chapter 1 contains some of the basic ideas and characteristic lengths necessary to understand the suppression mechanisms of bremsstrahlung in amorphous targets. The characteristic length of the bremsstrahlung process, the formation length, is crucial in this context.

- Chapter 2 gives the reader an understanding of the experimental tools and methods applied to measure the attributes of the bremsstrahlung photon spectrum from different targets. The effects of the applied methods have been examined using toy Monte Carlo simulations unveiling—in some cases—surprisingly large systematic effects.

- Chapter 3 deals with an experiment where the targets are thin compared to the formation length. In this regime, named after Ternovskiĭ-Shul'ga-Fomin (TSF), the bremsstrahlung photon yield is not linear in thickness but logarithmic! Also, a semi-empirical logarithmic expression is presented.

- Chapter 4 gives an introduction to some of the most prominent theoretical models of bremsstrahlung from thin targets. Many of the models have been implemented and compared with our experimental results of Chapter 3. The semi-empirical logarithmic expression is justified by closely resembling Blankenbecler's theory of thin targets.

- Chapter 5 describes the experimental search for an effect which has been proclaimed by many independent theoretical models. The so-called "sandwich effect" should occur, when the formation length stretches between two amorphous foils, longitudinally separated by a small gap.

- Chapter 6 is based on two experiments—a preparation study and a recent full-scale experiment—aiming at a characterization of the Landau-Pomeranchuk-Migdal suppression, relevant in semi-infinite targets (in practice, thick relative to the formation length). This study focuses on target materials of low nuclear charge (Z). When considering electromagnetic air showers generated by cosmic rays in the atmosphere, the target material consists by nature largely of low-Z materials, and the low-Z Landau-Pomeranchuk-Migdal effect is important here.

Some of the effects treated in Chapter 3–6 have previously been studied by the SLAC E-146 experiment [A$^+$97]. However, as will be discussed, they suffered from a number of limitations, whence our study is—at least in the case of the TSF and sandwich effects—far superior. Unless else is specified, I have procured the results and figures shown in this part through either data analysis, drawing or simulation.

Part II – Positronium – Production and Decay

This part describes my work with an apparatus on the route towards creating antihydrogen ($\overline{\mathrm{H}}$), consisting of a positron (e^+) and an antiproton ($\overline{\mathrm{p}}$). This is a strong candidate for a system allowing a high-precision test of the CPT-theorem [BKR99]. To produce a bound, atom-like system, the constituents' energies must be lowered to be similar to the binding energy of the system, *i.e.* usually few eV. As is demonstrated, this is exactly what our apparatus does to energetic positrons from a ^{22}Na radioactive source. We have used the positron apparatus to create the bound system of a positron and an electron, positronium (Ps). Bound-state QED has been tested extensively by comparing theory to experiments with this purely QED system. Quite recently, a measurement of the proton charge extent in muonic hydrogen—another member of the species of exotic hydrogen-like atoms—was performed [P$^+$10]. The stirring result obtained, $\simeq 5\sigma$ deviation from hydrogen measurements and bound-state QED expectations, demonstrates that these systems are indeed still intriguing.

- Chapter 7 contains an introduction to the techniques and capabilities of a high-quality positron beam line of the type presently located at Institut for Fysik og Astronomi (IFA), Aarhus University.
- Chapter 8 describes the results of the positron source commissioning phase where the supplier's specifications were thoroughly tested.
- Chapter 9 includes the details and results of the first experiment using the positron beam line: measuring the lifetime of positronium. By performing the experiment in a strong magnetic field, a part of the lifetime changes as a result of magnetic quenching.

Finally, among the few appendices, Appendix D contains a small note on the future experiments in the NA63 collaboration, while Appendix E contains an English and Danish summary of the thesis.

ACKNOWLEDGEMENTS

Perhaps more than anything else, I would like to thank Ulrik Ingerslev Uggerhøj and Helge Knudsen for accepting me as a PhD student in their group in August 2006. Since then, Ulrik has served as my supervisor on the project. I have had the pleasure of Ulrik's company from my first day at IFA, Aarhus University in August 2002. From the start of my PhD, I have thrived under his balanced and inspiring supervision, good sense of humour, and seemingly infrangible optimism. He has often let me pursue the topics and approaches, which I found most interesting. I have highly appreciated the relaxed and informal atmosphere present in his office. Helge has always been helpful and resolute in our joint experiments. His careful recommendations are usually interlaced with comments characteristic of his cheeky sense of humour. I especially enjoyed our conversations during the visit to First Point Scientific, Inc. (FPSI).

Regarding the first part of this document, "we" will refer to the members of the NA63 collaboration at CERN. I am highly indebted to the active members of NA63 for their help in performing the experiments as well as simulations, interpretations, *etc*. Alessio Mangiarotti deserves credit for providing me a large number of LPM simulations and doing a thorough job of quality assurance. Over the years, Sergio Ballestrero's computational skills have also kept me amazed. He has been very helpful by providing almost instantaneous numerical assistance to C++, ROOT, Geant4, and bookCRY. I also acknowledge several interesting discussions with Pietro Sona regarding the modifications of the bremsstrahlung spectrum. I would like to thank all the existing and former members of NA63 for contributing to the special atmosphere present throughout the period of the experiments[1], which would usually conclude with champagne, regardless of our outcome.

I would like to thank Erik Lægsgaard for granting me the use of the Keyence LC-2430 (an ultra-high-accuracy distance meter) and showing a great interest in my progress with it. As it constitutes one of my main results, I would like to express my gratitude to Serguei P. Fomin for, among other things, directing our attention to the feasibility of measuring the thickness dependence of the TSF effect.

Regarding the experimental work with the state-of-the-art positron source, "we" especially refers to Mikkel D. Lund and myself, but also Hans-Peter E. Kristiansen and Søren Lindholt Andersen. Without Mikkel's strong hands-on mentality, the experimental work would have progressed less rapidly. I am very grateful to all employees at FPSI, especially Rod Greaves, for constructing the positron apparatus and having me as a guest at FPSI, Agoura Hills, CA, USA in September 2007. Acquiring

[1] Including the full emotional spectrum from disappointment, stress, uncertainty, anxiety to excitement, rejuvenation, and the buzz of success.

the positron source was only possible with the considerable amount of ASACUSA ¥ paying the larger part of the system's price.

Our experiments could not have been realized without the help of the local electronics, chemistry, and workshop group at IFA. Although their approaches to a problem are very different, the indispensable Per B. Christensen and Poul Aggerholm have contributed with many solutions, be they ingenious or simply something kludged together.

Over the years, I have enjoyed the good company of all the persons mentioned above. Also Jakob Esberg, Kim R. Hansen, Kristoffer K. Andersen, Christian Bruun Madsen, Thomas Kjærgaard, Lasse Arnt Straasø, the GHK Boys, and others have contributed to the good company and discussions on topics not necessarily related to physics.

I would of course also like to thank my family for supporting me during my studies and for consenting to the fact that they have had difficulties in explaining my research or job opportunities to anyone. Finally, I sincerely thank Laura for her support of my work over the years. She has on many occasions offered a sympathetic ear to my worries about the development of my project and has always managed to take my attention off the problem. Particularly, she deserves credit for patiently tolerating my physical and mental absence during the writing of this thesis.

List of Publications

Publications Directly Related to this Thesis

(**I**) **H. D. Thomsen**, J. Esberg, K. Kirsebom, H. Knudsen, E. Uggerhøj, U. I. Uggerhøj, P. Sona, A. Mangiarotti, T. J. Ketel, A. Dizdar, M. Dalton, S. Ballestrero, and S. H. Connell. On the Macroscopic Formation Length for GeV Photons. *Phys. Lett. B* **672**, 323–327 (2009). doi:10.1016/j.physletb.2009.01.053.

(**II**) **H. D. Thomsen**, J. Esberg, K. K. Andersen, M. D. Lund, H. Knudsen, U. I. Uggerhøj, P. Sona, A. Mangiarotti, T. J. Ketel, A. Dizdar, S. Ballestrero, and S. H. Connell. Distorted Coulomb field of the scattered electron. *Phys. Rev. D* **81**, 052003 (2010). doi:10.1103/PhysRevD.81.052003.

(**III**) **H. D. Thomsen** and U. I. Uggerhøj. Systematic Errors Arising From Detector Pile-Up. *In Preparation for Nucl. Instr. Meth. B* (2010).

(**IV**) The NA63 Collaboration. On the Low-Z LPM Effect. *In Preparation for Phys. Rev. D* (2010).

Additional Publications

(**V**) T. Virkus, **H. D. Thomsen**, E. Uggerhøj, U. I. Uggerhøj, S. Ballestrero, P. Sona, A. Mangiarotti, T. J. Ketel, A. Dizdar, S. Kartal, and C. Pagliarone. Direct Measurement of the Chudakov Effect. *Phys. Rev. Lett.* **100**, 164802 (2008). doi:10.1103/PhysRevLett.100.164802.

(**VI**) H. Knudsen, H.-P. E. Kristiansen, **H. D. Thomsen**, U. I. Uggerhøj, T. Ichioka, S. P. Møller, C. A. Hunniford, R. W. McCullough, M. Charlton, N. Kuroda, Y. Nagata, H. A. Torii, Y. Yamazaki, H. Imao, H. H. Andersen, and K. Tökesi. Ionization of Helium and Argon by Very Slow Antiproton Impact. *Phys. Rev. Lett.* **101**, 043201 (2008). doi:10.1103/PhysRevLett.101.043201.

(**VII**) H. Knudsen, H. P. E. Kristiansen, **H. D. Thomsen**, U. I. Uggerhøj, T. Ichioka, S. P. Møller, C. A. Hunniford, R. W. McCullough, M. Charlton, N. Kuroda, Y. Nagata, H. A. Torii, Y. Yamazaki, H. Imao, H. H. Andersen, and K. Tökesi. On the double ionization of helium by very slow antiproton impact. *Nucl. Instr. Meth. B* **267**, 244–247 (2009). doi:10.1016/j.nimb.2008.10.070.

(**VIII**) K. K. Andersen, K. R. Hansen, J. Esberg, H. Knudsen, M. D. Lund, **H. D. Thomsen**, U. I. Uggerhøj, S. P. Møller, P. Sona, A. Mangiarotti, T. J. Ketel, A. Dizdar,

and S. Ballestrero. Restricted energy loss of ultrarelativistic particles in thin targets—a search for deviations from constancy. *Nucl. Instr. Meth. B* **268**, 1412–1415 (2010). doi:10.1016/j.nimb.2010.01.026.

(**IX**) **H. D. Thomsen** and U. I. Uggerhøj. Measurements of the King-Perkins-Chudakov effect. *In Preparation for Channeling 2010 Proceedings.*

(**X**) J. Esberg, K. Kirsebom, H. Knudsen, **H. D. Thomsen**, E. Uggerhøj, U. I. Uggerhøj, P. Sona, A. Mangiarotti, T. J. Ketel, A. Dizdar, M. Dalton, S. Ballestrero, S. Connell. Experimental investigation of a Klein paradox analogue for elementary particles—strong field trident production. *In Preparation for Phys. Rev. D* (2010).

(**XI**) J. Esberg, **H. D. Thomsen** and U. I. Uggerhøj. Radiation emission as a realization of Heisenbergs microscope. *In Preparation* (2010).

(**XII**) K. K. Andersen, J. Esberg, H. Knudsen, **H. D. Thomsen**, U. I. Uggerhøj, P. Sona, T. J. Ketel, A. Dizdar, S. Ballestrero and S. Connell. Synchrotron radiation in the quantum regime. *In Preparation for Phys. Rev. D* (2010).

List of Acronyms

To ease the eye of the reader, I shall in the following document introduce a number of acronyms. Below is a list of these along with the page where they were defined, *i.e.* first used. The reader can return to this list for reference.

ADC Analog to Digital Converter . . . 21
ASACUSA Atomic Spectroscopy And Collisions Using Slow Antiprotons . . . 89
ASTRID Aarhus STorage RIng Denmark . . . 19
ATI Above Threshold Ionization . . . 141
BCPS Background Compensated Power Spectrum . . . 29
BD Blankenbecler & Drell . . . 33
BGO bismuth germanate $[(Bi_2O_3)_2(GeO_2)_3]$ . . . 19
BH Bethe-Heitler . . . 8
BK Baier & Katkov . . . 20
CAMAC Computer Automated Measurement And Control . . . 15
CCD Charge Coupled Device . . . 72
CEM Channel Electron Multiplier . . . 117
CERN Organisation Européenne pour la Recherche Nucléaire . . . vi
CFD Constant Fraction Discriminator . . . 119
CMOS Complementary Metal–Oxide–Semiconductor . . . 72
FPGA Field-Programmable Gate Array . . . 21
FPSI First Point Scientific, Inc. . . . ix
FWHM Full Width at Half Maximum . . . 23
HFS hyperfine structure . . . 112
HV High Voltage . . . 16
IFA Institut for Fysik og Astronomi [Department of Physics and Astronomy] . . . vii
LDPE low-density polyethylen . . . 83
LEPS Low-Energy Positron Source . . . 89
LG Lead Glass . . . 18
LHS left-hand-side . . . 42
LPM Landau-Pomeranchuk-Migdal . . . 12

MC Monte Carlo 20
MCP MicroChannel Plate 118
MCS multiple Coulomb scattering 10
MFC Mass Flow Controller 98
MIP Minimum Ionizing Particle 21
MPI Multi-Photon Ionization 110
MRT Multi-Ring Trap 89
NaI(Tl) sodium-iodide 19
NemBox Nuclear Electronics Miniature BOX 21
NHP No High Pulse 39
PID Proportional–Integral–Derivative 92
PMT PhotoMultiplier Tube 16
PSD Position Sensitive Device 72
PU Pattern Unit 21
PVT polyvinyl toluene 16
QCD Quantum chromodynamics v
QED Quantum electrodynamics v
RGM-1 Rare Gas Moderator-1 89
RGS Rare Gas Solid 90
RHS right-hand-side 42
RMS Root Mean Square 8
RW Rotating Wall 99
SF Shul'ga & Fomin 33
SPS Super Proton Synchrotron 3
SR Synchrotron Radiation 27
SSD Solid State Detector v
STP Standard conditions for Temperature and Pressure 64
TAC Time-to-Amplitude Converter 117
TF Thomas-Fermi 8
TFA Timing Filter Amplifier 119
TM Ter-Mikaelian 14
TOF Time-Of-Flight 142
TR Transition Radiation 38
TSF Ternovskiĭ-Shul'ga-Fomin 33

Part I

Formation Length Related Bremsstrahlung Phenomena

CHAPTER 1

BREMSSTRAHLUNG BASICS

Bremsstrahlung is the dominant mechanism of energy loss of an electron (or positron) traversing matter at electron energies $\gtrsim$ 1 GeV [Sø96, Y$^+$06], thus rendering bremsstrahlung ubiquitous in many fields of high energy physics of light leptons. This part will present experimental studies of bremsstrahlung from electrons of energies $E_0 \gtrsim 150$ GeV—energies feasible at the CERN Super Proton Synchrotron (SPS)—at which the Lorentz factor $\gamma_\mathrm{L} = E_0/mc^2 \gtrsim 3 \times 10^5$ (mc^2 is the rest mass-energy of the electron). The process has been investigated in exotic, fixed targets, the nature of which will be described later. This first chapter will introduce the reader to the elements which are crucial to understand the effects in the targets.

1.1 Accelerating a Charge

In Fig. 1.1a, the space-time coordinates to be used are visually defined. We consider an observer located at $\boldsymbol{r}$ who detects a signal (radiation) at time t. The signal was emitted from a relativistic particle of charge e at the position $\boldsymbol{r}_0$ at an earlier (retarded) time $t_0 = t - \mathcal{R}/c$, where $\boldsymbol{\mathcal{R}} = \boldsymbol{r} - \boldsymbol{r}_0$. The vector $\boldsymbol{n} = \boldsymbol{\mathcal{R}}/\mathcal{R}$ is a unit-vector pointing from the source to the observer, *i.e.* in the direction of the radiation under consideration. The particle has a velocity $\boldsymbol{v} = \boldsymbol{\beta}c$ and experiences a general acceleration $c\dot{\boldsymbol{\beta}} = c\,d\boldsymbol{\beta}/dt$. The electric field $\boldsymbol{E}$ from such a setup can be written in the form [Jac98, Eq. (14.14)]

$$\boldsymbol{E}(\boldsymbol{r},t) = \underbrace{e\left[\frac{\boldsymbol{n}-\boldsymbol{\beta}}{\gamma_\mathrm{L}^2(1-\boldsymbol{n}\cdot\boldsymbol{\beta})^3\mathcal{R}^2}\right]_\mathrm{ret}}_{\boldsymbol{E}_v} + \underbrace{\frac{e}{c}\left[\frac{\boldsymbol{n}\times\{(\boldsymbol{n}-\boldsymbol{\beta})\times\dot{\boldsymbol{\beta}}\}}{(1-\boldsymbol{n}\cdot\boldsymbol{\beta})^3\mathcal{R}}\right]_\mathrm{ret}}_{\boldsymbol{E}_a}, \tag{1.1}$$

where "ret" refers to evaluation at the retarded time $t_0 = t - \mathcal{R}/c$. Gaussian units have been used. The first term, the velocity term, is the charge's eigen field which is present even when the charge is at rest—a statement that is somewhat relaxed in Sec. 4.2. The second term, the acceleration term, exhibits a behavior characteristic

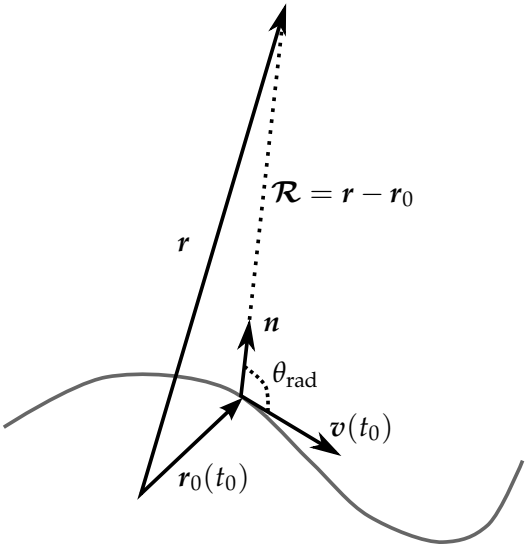

(a) Path of the particle considered.

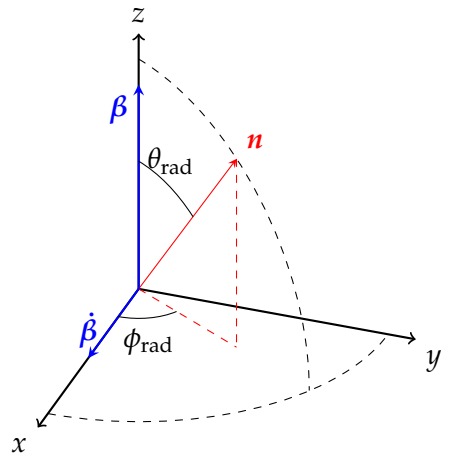

(b) Angles of radiation emission when the velocity and acceleration are perpendicular.

Figure 1.1: Visual definitions of some of the used vectors and angles.

of a radiation field—both $\boldsymbol{E}_a$ and the corresponding magnetic field component $\boldsymbol{B}_a = \left[\boldsymbol{n} \times \boldsymbol{E}_a\right]_{\text{ret}}$ are perpendicular to $\boldsymbol{\mathcal{R}}$, and $E_a \propto \dot{\beta}/\mathcal{R}$.

A non-relativistic charge experiencing an acceleration will emit radiation with an angular distribution proportional to $\sin^2(\Theta)$—Θ being the angle between the direction to the observer $\boldsymbol{n}$ and the acceleration $c\dot{\boldsymbol{\beta}}$—the well-known doughnut shape. Going through the Poynting vector $\boldsymbol{S} = \boldsymbol{E} \times \boldsymbol{B}c/4\pi$, the general, relativistic expression concerning the angular dependence of the power radiated in a unit solid angle $d\Omega$ [Jac98, Eq. (14.38)]

$$\frac{dP(t_0)}{d\Omega} = \frac{e^2}{4\pi c} \frac{\left|\boldsymbol{n} \times \{(\boldsymbol{n} - \boldsymbol{\beta}) \times \dot{\boldsymbol{\beta}}\}\right|^2}{(1 - \boldsymbol{n} \cdot \boldsymbol{\beta})^5}, \tag{1.2}$$

where Gaussian units are used and t_0 is the retarded time. The vector expression in the numerator can be rewritten using the vector identity known as Lagrange's formula $\boldsymbol{a} \times (\boldsymbol{b} \times \boldsymbol{c}) = \boldsymbol{b}(\boldsymbol{a} \cdot \boldsymbol{c}) - \boldsymbol{c}(\boldsymbol{a} \cdot \boldsymbol{b})$

$$\begin{aligned}
\left|\boldsymbol{n} \times \{(\boldsymbol{n} - \boldsymbol{\beta}) \times \dot{\boldsymbol{\beta}}\}\right|^2 &= \left|\boldsymbol{n}(\boldsymbol{n} \cdot \dot{\boldsymbol{\beta}}) - \dot{\boldsymbol{\beta}} - \boldsymbol{\beta}(\boldsymbol{n} \cdot \dot{\boldsymbol{\beta}}) + \dot{\boldsymbol{\beta}}(\boldsymbol{n} \cdot \boldsymbol{\beta})\right|^2 \\
&= \dot{\beta}^2(\boldsymbol{n} \cdot \boldsymbol{\beta})^2 - 2(\dot{\boldsymbol{\beta}} \cdot \boldsymbol{\beta})(\boldsymbol{n} \cdot \boldsymbol{\beta})(\boldsymbol{n} \cdot \dot{\boldsymbol{\beta}}) - 2\dot{\beta}^2(\boldsymbol{n} \cdot \boldsymbol{\beta}) + \beta^2(\boldsymbol{n} \cdot \dot{\boldsymbol{\beta}})^2 \\
&\quad + 2(\dot{\boldsymbol{\beta}} \cdot \boldsymbol{\beta})(\boldsymbol{n} \cdot \dot{\boldsymbol{\beta}}) + \dot{\beta}^2 - (\boldsymbol{n} \cdot \dot{\boldsymbol{\beta}})^2 \\
&= \dot{\beta}^2\left[(\boldsymbol{n} \cdot \boldsymbol{\beta})^2 - 2\boldsymbol{n} \cdot \boldsymbol{\beta} + 1\right] + \left[\beta^2 - 1\right](\boldsymbol{n} \cdot \dot{\boldsymbol{\beta}})^2 \\
&\quad + 2(\dot{\boldsymbol{\beta}} \cdot \boldsymbol{\beta})(\boldsymbol{n} \cdot \dot{\boldsymbol{\beta}})\left[1 - \boldsymbol{n} \cdot \boldsymbol{\beta}\right] \\
&= \dot{\beta}^2\left[1 - \boldsymbol{n} \cdot \boldsymbol{\beta}\right]^2 - \gamma_{\text{L}}^{-2}(\boldsymbol{n} \cdot \dot{\boldsymbol{\beta}})^2 + 2(\dot{\boldsymbol{\beta}} \cdot \boldsymbol{\beta})(\boldsymbol{n} \cdot \dot{\boldsymbol{\beta}})\left[1 - \boldsymbol{n} \cdot \boldsymbol{\beta}\right].
\end{aligned} \tag{1.3}$$

As will be made clear in the following section, only transverse accelerations ($\dot{\boldsymbol{\beta}} \perp \boldsymbol{\beta}$) are significant once $\gamma_{\text{L}} \gg 1$, hence $\dot{\boldsymbol{\beta}} \cdot \boldsymbol{\beta} = 1/2d(\boldsymbol{\beta}^2)/dt = 0$ and $\boldsymbol{\beta}^2$ is conserved.

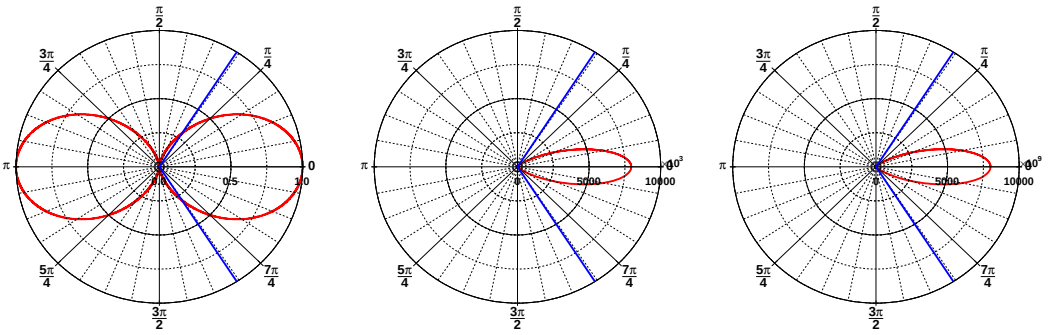

(a) $\gamma_L = 1$. **(b)** $\gamma_L = 10$. **(c)** $\gamma_L = 100$.

Figure 1.2: The angular distribution of the power emitted from a particle with Lorentz factor γ_L experiencing a purely transverse acceleration $\dot{\beta}_\perp c$. The polar scale shows $\theta_{rad}\gamma_L$, so the power is highly focused in the forward direction when increasing γ_L. Notice the very different radial scales which all bear the same arbitrary units. The blue curves mark the cone defined by $|\theta_{rad}\gamma_L| \leq 1$. In all plots $\cos^2(\phi_{rad}) = 1$.

Because of this, the last term of Eq. (1.3) vanishes and Eq. (1.2) is reduced to

$$\left.\frac{dP(t_0)}{d\Omega}\right|_{\dot{\boldsymbol{\beta}}\perp\boldsymbol{\beta}} = \frac{e^2}{4\pi c}\frac{\dot{\beta}^2\left[1-\boldsymbol{n}\cdot\boldsymbol{\beta}\right]^2 - \gamma_L^{-2}(\boldsymbol{n}\cdot\dot{\boldsymbol{\beta}})^2}{\left(1-\boldsymbol{n}\cdot\boldsymbol{\beta}\right)^5}$$
$$= \frac{e^2}{4\pi c}\frac{\dot{\beta}^2\left[\left[1-\beta\cos(\theta_{rad})\right]^2 - \gamma_L^{-2}\sin^2(\theta_{rad})\cos^2(\phi_{rad})\right]}{\left[1-\beta\cos(\theta_{rad})\right]^5}, \qquad (1.4)$$

where θ_{rad} is the azimuthal angle between the velocity $\boldsymbol{\beta}$ and $\boldsymbol{n}$, and ϕ_{rad} is the projected angle between the acceleration $c\dot{\boldsymbol{\beta}}$ and $\boldsymbol{n}$, cf. Fig. 1.1b. The power is proportional to the square of the magnitude of the acceleration and the radiation becomes highly forward directed when $\gamma_L \gg 1$, as illustrated in Fig. 1.2a–1.2c. As seen in the figures, the bremsstrahlung photon is emitted within a characteristic angle $\theta_{rad} \simeq \gamma_L^{-1}$ with respect to the original trajectory [TM72, Ugg05]. The expression above can be integrated over angles, only to find $P(t_0) \propto \dot{\beta}^2\gamma_L^4$. For comparable external forces and primary particle momenta, the integrated power is found to be proportional to m^{-6}, whence we typically consider bremsstrahlung from the lightest leptons, electrons or positrons, since—for instance—$P_{e^-}/P_{\mu^-} = (207.2)^6$ under the assumptions stated above. Also, the sign of the charge should be irrelevant with respect to this process, as only the squared charge (assumed to be the elementary charge e) occurs in the expression.

1.2 Relevant Lengths & Bethe-Heitler Yields

The Formation Length

In Fig. 1.3, two of the four lowest order Feynman diagrams describing bremsstrahlung from an electron in the nuclear field are shown. The incoming electron with energy E_0 and momentum p_0 interacts with a nucleus of charge $+Ze$ through a virtual

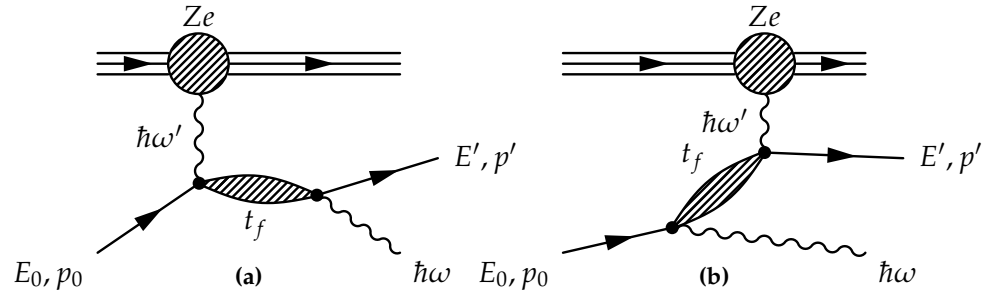

Figure 1.3: The two lowest order Feynman diagrams describing the process of bremsstrahlung in the nuclear field. Time progresses to the right. Here, only one virtual photon is exchanged, *i.e.* the Born approximation is depicted. The results of the two diagrams are indistinguishable, while the vertices occur in different order.

photon of energy $\hbar\omega'$. Finally, the electron has less energy $E' = E_0 - \hbar\omega = (1-y)E_0$ and momentum p', and the bremsstrahlung photon of energy $\hbar\omega = yE_0$ is formed. Usually, one thinks of the electron's intermediate state—shown as a grey muck—as a very short-lived condition or even a mere trick to keep the diagrams finite. However, at relativistic energies $\gamma_\mathrm{L} \gg 1$, the intermediate state is of great importance to the photon yield, as this document will show. In this regime, the photon emission angle (θ_rad) and scattering angle of the electron (θ_e) can—for simplicity—be regarded as negligible, whence the longitudinal momentum conservation simply states

$$\begin{aligned} q_\parallel &= p_0 - p' - \hbar\omega/c \\ &= \frac{E_0}{c}\sqrt{1-\left(\frac{mc^2}{E_0}\right)^2} - \frac{E_0-\hbar\omega}{c}\sqrt{1-\left(\frac{mc^2}{E_0-\hbar\omega}\right)^2} - \hbar\omega/c\,, \end{aligned} \tag{1.5}$$

where ${E_0}^2 = (pc)^2 + (mc^2)^2$ has been employed and $q_\parallel$ is the momentum-transfer to the nucleus (directions refer to projectile trajectory). By neglecting the angles, this quantity is the *minimum* momentum-transfer. In the relativistic $(E_0 \gg mc^2)$ and soft-photon regime $(E_0 \gg \hbar\omega)$, both square roots can be well approximated by the first two terms in their Taylor series, thus yielding the expression

$$q_\parallel = \frac{m^2c^3\hbar\omega}{2E_0(E_0-\hbar\omega)} = \frac{m^2c^3\hbar\omega}{2{E_0}^2(1-y)}\,. \tag{1.6}$$

The nucleus' field can be assumed spherically symmetric in the rest frame of the nucleus, the fixed target lab system $\mathcal{S}$. The field experienced by an ultra-relativistic electron will be very different in its rest frame $\mathcal{S}'$, due to a Lorentz boost of the field. The component along the particle's trajectory is heavily reduced $E'_\parallel = \gamma_\mathrm{L}^{-2}E_\parallel$ while the perpendicular component is enhanced $E'_\perp = \gamma_\mathrm{L}E_\perp$ [Jac98, Eq. (11.154)], which is sketched in Fig. 1.4a–1.4c. This justifies that at $\gamma_\mathrm{L} \simeq 10^5$, the parallel momentum transfer must be relatively small. Through Heisenberg's uncertainty principle, this corresponds to a finite distance in the longitudinal direction

$$\begin{aligned} \ell_\mathrm{f0} &= \frac{\hbar}{q_\parallel} = \frac{2{E_0}^2(1-y)}{m^2c^3\omega} = \frac{2\gamma_\mathrm{L}^2c(1-y)}{\omega} \\ &= \frac{2\gamma_\mathrm{L}^2c}{\omega^*}\,, \qquad \omega^* = \omega\frac{E_0}{E_0-\hbar\omega}\,. \end{aligned} \tag{1.7}$$

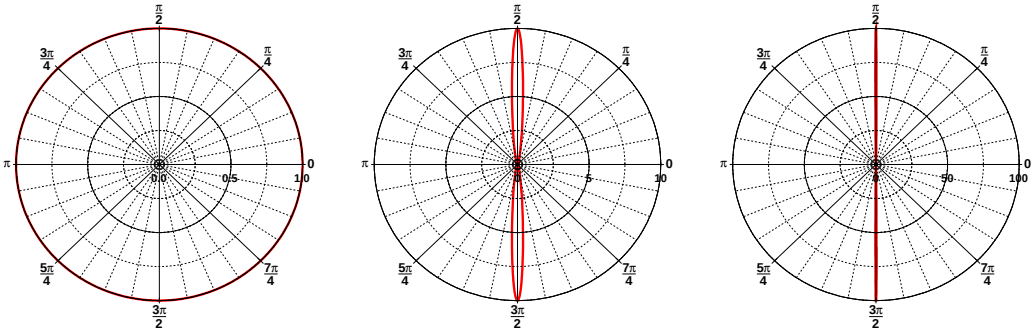

(a) $\gamma_L = 1$. **(b)** $\gamma_L = 10$. **(c)** $\gamma_L = 100$.

Figure 1.4: Nuclear field as seen in the electron's rest frame $\mathcal{S}'$. In the polar plots, the radial axis bears identical arbitrary units of electric field strength. As γ_L increases, the—at first isotropic—experienced field changes drastically and only the perpendicular component is retained (and enhanced) when $\gamma_L \gg 1$.

The characteristic longitudinal length is called the vacuum *formation* or *coherence* length [TM53] and has several physical interpretations. The photon and electron waves initially travel coherently until their different propagation speeds cause a spatial separation of one reduced photon wavelength $\lambda\!\!\!^{-} = \lambda/2\pi = c/\omega$. If the electron is ultra-relativistic with a final speed $v' \simeq c$, the separation takes a finite time ℓ_{f0}/c in which the electron travels a finite distance, the formation length. Consider the electromagnetic phase of the process

$$\Phi = \exp\left(i\underbrace{\left[\omega t - \boldsymbol{k}\cdot\boldsymbol{r}(t)\right]}_{\phi} \right), \tag{1.8}$$

where $\boldsymbol{k}$ is the photon wave vector and $\boldsymbol{r}(t)$ is the electron position at time t. The coherence is conserved while the phase ϕ is similar to unity, *i.e.* for distances $\omega t - \boldsymbol{k}\cdot\boldsymbol{r}(t) \simeq 1$. This consideration is an alternative way of finding ℓ_{f0} which will be shown in a later chapter. Of course, processes involving distances longer than ℓ_{f0} can also be relevant, although they will suffer from an inherent suppression due to the phase mismatch. The formation length ℓ_{f0} is also the reduced wavelength of the virtual photon in Fig. 1.3 [Kle99]. As accounted for in the previous section, the photon is emitted with the characteristic angle $\theta_{rad} \lesssim \gamma_L^{-1}$, whence one should in fact consider a three-dimensional zone—a cone of apex angle $\simeq 2\gamma_L^{-1}$.

Within the formation zone, the amplitudes from multiple interactions can add coherently to the total cross section [Pal68, Kle99]. The coherence can result in typical constructive and destructive interference phenomena. In the case of crystals, the radiation yield is greatly enhanced when the wavelength of the virtual photon is an integer times the atomic spacing along the incident direction [Ugg05]—an effect known as coherent bremsstrahlung in crystals. This can be understood through [Sø96, Eq. (30)] which deals with scaling of the differential bremsstrahlung cross sec-

tion when regarding a combination of N interaction sites

$$\left.\frac{d\sigma}{d\hbar\omega d^3q}\right|_N = \left.\frac{d\sigma}{d\hbar\omega d^3q}\right|_1 \times \left|\sum_{n=1}^{N} e^{i\boldsymbol{q}\cdot\boldsymbol{r}_n/\hbar}\right|^2 , \tag{1.9}$$

where the subscripts refer to the number of target atoms under consideration, $\boldsymbol{q}$ is a vector representing the momentum transferred to the nucleus, $\boldsymbol{r}_n$ is a vector giving the distance and direction to the atoms. If $\boldsymbol{q}/\hbar$ coincides with the reciprocal lattice vectors of the crystal, the interference factor can give values much larger than N—up to N^2. In this situation, the electron traverses a large number of crystal planes with an angle to them. The coherent addition of the periodic electric fields along its path gives rise to a immense augmentation of radiation at photon energies which can be tuned by varying the angle to the planes.

Diametrically opposite to a crystal of high periodicity is an amorphous medium in which the atoms are considered to be distributed completely at random. In such a material, each single interaction will introduce a random phase, and all cross terms in the factor above—leading to resonances—will on average vanish, thus reducing the coherent sum to an incoherent sum of single interactions within the formation zone. In the case of completely random phases, the scaling factor reduces to an exponential distribution with mean, Root Mean Square (RMS) and slope N. The differential bremsstrahlung photon yield from N_e particles traversing a foil of thickness Δt is then simply

$$\frac{dN_\gamma}{d\hbar\omega} = N_e \times \frac{d\sigma}{d\hbar\omega} \times n_n \times \Delta t \qquad n_n = \rho N_A/M_A , \tag{1.10}$$

where n_n is the number density of nuclei, ρ is the mass density of the material, M_A is the atomic (molar) mass and $N_A = 6.022 \times 10^{23}/\text{mol}$ is the Avogadro constant. When traversing condensed matter, the high concentration of scattering centres can introduce additional phase-shifts to either the photon or electron, hence cause the coherence to be lost quicker—reducing the effective formation length—thus affecting the radiation yield. Such phenomena will be discussed in Sec. 1.3.

The idea of a formation length is not restricted to bremsstrahlung, but is present in most electromagnetic processes (pair production, synchrotron radiation and Čerenkov radiation). Notice from Eq. (1.7) that this length only depends on E_0, $\hbar\omega$, and the identity (mass) of the primary particle.

The Bethe-Heitler Bremsstrahlung Cross Section

The Bethe-Heitler (BH) cross section [BH34, Hei54] describes the radiation emission from an electron traversing a "thin" (to be discussed in Sec. 1.3), amorphous foil. Bethe and Heitler treated bremsstrahlung relativistically and quantum mechanically using first order perturbation theory, valid when $\kappa \equiv 2Ze^2c/\hbar\beta \simeq 2Z\alpha \ll 1$, where $\alpha = 1/137.036\ldots$ is the fine-structure constant. The cross section was found by considering one isolated nuclear scattering centre, and when considering the yield from many indistinguishable atoms, one should use the incoherent sum of contributions, as discussed below Eq. (1.9). The electronic screening of the nuclear Coulomb scattering field is introduced using the Thomas-Fermi (TF) [BJ03] atomic model. In the complete screening limit ($\gamma_\text{L} \gg 1$), the formation length is large compared with

atomic dimensions, and the maximal contributing impact parameter can well be replaced by the TF atomic radius $r \simeq a_0 Z^{-1/3}$, where $a_0 = \hbar/mc\alpha = 0.529$ Å is the Bohr radius. In the complete screening limit, the differential cross section is

$$\frac{d\sigma_{\mathrm{BH}}}{d\hbar\omega} = \frac{16}{3}\alpha r_e^2 \frac{1}{\hbar\omega}\left[1 - y + \frac{3}{4}y^2\right] Z^2 \ln(183 Z^{-1/3}) \,, \tag{1.11}$$

where $y = \hbar\omega/E_0$ and $r_e = \alpha\hbar/mc = 2.82$ fm the classical electron radius. In the soft-photon regime ($y \to 0$), the BH cross section has a photon energy dependence of $d\sigma_{\mathrm{BH}}/d\hbar\omega \propto 1/\hbar\omega$, which is a result of the behaviour of ℓ_{f0}. It should be noted that the TF-model is inadequate for low Z elements ($Z \lesssim 5$) [Sø96], and here a more accurate description like [Tsa74, Eq. (3.83)] should be used

$$\begin{aligned}\frac{d\sigma}{d\hbar\omega} = \frac{16}{3}\alpha r_e^2 \frac{1}{\hbar\omega}\Bigg\{\left[1 - y + \frac{3}{4}y^2\right]\left[Z^2(L_{\mathrm{rad}} - f_{\mathrm{DBM}}[(Z\alpha)^2]) + ZL'_{\mathrm{rad}}\right] \\ + \frac{1}{9}(1-y)(Z^2+Z)\Bigg\} \,,\end{aligned} \tag{1.12}$$

$$\begin{aligned}f_{\mathrm{DBM}}(z) = z\sum_{n=1}^{\infty}\left[n(n^2+z)\right]^{-1} \simeq z(1+z)^{-1} + 0.20206z - 0.0369z^2 \\ + 0.0083z^3 - 0.002z^4 \qquad z = (Z\alpha)^2\end{aligned} \tag{1.13}$$

where $L_{\mathrm{rad}} = \ln(184.15 Z^{-1/3})$ and $L'_{\mathrm{rad}} = \ln(1194 Z^{-2/3})$ ($Z > 4$) correspond to the nuclear and electronic contribution, respectively. In [BM54], Bethe and Maximon considered bremsstrahlung and pair production without use of the Born approximation. They used modified versions of the wave functions designed by Furry—approximate solutions to the Dirac equation for an electron in the Coulomb field [Fur34]—to describe the electron initial and final state. The infinite series $f_{\mathrm{DBM}}[(Z\alpha)^2]$ [DBM54] is a correction to the Born approximation in which the interaction of the Coulomb field is treated as in perturbation theory. This function is known as the Coulomb correction, and $f_{\mathrm{DBM}} \simeq 1.20(Z\alpha)^2$ for $Z \ll \alpha^{-1}$.

As mentioned, the target electrons can also contribute to the bremsstrahlung, and this can be well incorporated Eq. (1.11) by the substitution $Z^2 \to Z(Z+k)$, where $k \approx 1$ [Hei54]. This substitution is—maybe surprisingly—simple. After all, the target electrons, contrary to the nucleus, cannot be considered static during the scattering, since large momentum and energy transfers can take place. According to Tsai [Tsa74], neglecting the last term of Eq. (1.12) introduces an error of about 1.7% (2.5%) for low (high) Z and soft photons ($y \to 0$). If this level of accuracy is acceptable and $Z^2 \to Z(Z+1)$ is introduced, Eq. (1.11) is very similar to Eq. (1.12), only without the Coulomb correction.

The Radiation Length

By using the Bethe-Heitler differential cross section of Eq. (1.11), a simple expression for the radiative stopping power can be found

$$\begin{aligned}-\frac{dE}{dx} &= n_n \int_0^{E_0} \hbar\omega \frac{d\sigma_{\mathrm{BH}}}{d\hbar\omega} d\hbar\omega \\ &= \underbrace{4 n_n \alpha r_e^2 Z^2 \ln(183 Z^{-1/3})}_{1/X_0} E_0 \,,\end{aligned} \tag{1.14}$$

where n_n is the number density of scattering nuclei. The projectile energy E_0 is thus reduced exponentially with distance x in a given foil. This exponential has a characteristic length scale known as the *radiation length* X_0. A more accurate expression for the radiation length is evidently defined by way of using the expression from Tsai, Eq. (1.12). The quantity X_0^{-1} is a measure of the probability of emitting bremsstrahlung in a certain material. Notice how this length depends solely on the choice of material, not the kinematics. Values of X_0 and f_{DBM} are tabulated in [Tsa74, Tab. III.6]. When a value of X_0 is given, it is found from this reference, unless else is specified.

Pair Production

As known for a long time, the process of bremsstrahlung and of pair production are intimately related. This is seen by the latter process' first order Feynman diagrams in Fig. 1.5. By comparison with Fig. 1.3, the crossing symmetry is evident. Also, this process is the dominant matter-interaction mechanism for photons of energies $\gtrsim 1$ MeV, like bremsstrahlung is for light leptons. The BH expression for the number of pairs $N_{\mathrm{p}} = N_\gamma n_n \sigma \Delta t$ produced by N_γ primary photons traversing a target of thickness Δt is then in the complete screening limit given by

$$\begin{aligned}\frac{1}{N_\gamma}\frac{dN_{\mathrm{p}}}{d\xi_\pm} &= \frac{\Delta t}{X_0}\left[\xi_+^2 + \xi_-^2 + \frac{2}{3}\xi_+\xi_-\right] \\ &= \frac{4\Delta t}{3X_0}\left[\xi_+^2 - \xi_+ + \frac{3}{4}\right] = \frac{4\Delta t}{3X_0}\left[\xi_-^2 - \xi_- + \frac{3}{4}\right], \end{aligned} \tag{1.15}$$

where the energy of the positron/electron is given by $E_{e^\pm} = \xi_\pm \hbar\omega$, and $\xi_+ + \xi_- = 1$, evidently. Notice that the expression is completely particle/antiparticle symmetric while being asymmetric in energy distribution. If the BH bremsstrahlung power spectrum $\hbar\omega\, dN_\gamma/d\hbar\omega$ is written from Eq. (1.11) using the simple expression for the radiation length, Eq. (1.14), and normalized to the number of primary particles N_e, a close resemblance is seen

$$\frac{\hbar\omega}{N_e}\frac{dN_\gamma}{d\hbar\omega} = \frac{1}{N_e}\frac{dN_\gamma}{d\ln\hbar\omega} = \frac{4\Delta t}{3X_0}\left[1 - y + \frac{3}{4}y^2\right]. \tag{1.16}$$

The total number of pairs per primary photon is given by

$$\frac{N_{\mathrm{p}}}{N_\gamma} = \frac{1}{N_\gamma}\int_0^1 \frac{dN_{\mathrm{p}}}{d\xi_\pm} d\xi_\pm = \frac{7\Delta t}{9X_0}, \tag{1.17}$$

whereas the corresponding integral of Eq. (1.16) yields $\Delta t/X_0$. As with the BH expression for bremsstrahlung, the review by Tsai [Tsa74] provides more accurate expressions for the pair production cross section.

The Multiple Scattering Length

While traversing the foil, the lepton can undergo repeated elastic, small-angle Coulomb scatterings off the nuclei of the matter—known as multiple Coulomb scattering (MCS). The theory of the resulting angular distribution after having traversed a distance x in the original direction is usually attributed to Molière, but has later been refined and simplified in different representations by others [Bet53, Sco63]. The

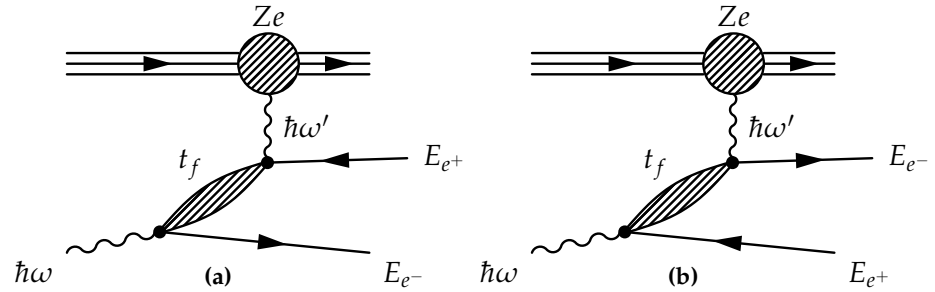

Figure 1.5: The two lowest order Feynman diagrams describing the process of pair production in the nuclear field. Time progresses to the right.

distribution of the deflection angle projected onto a plane containing the original particle direction $f(\theta_\mathrm{e})$ is in an amorphous material similar to a Gaussian distribution, only with much larger tails. The central 98% of the distribution can be well described by a Gaussian distribution with mean 0 and a RMS value $\theta_\mathrm{e}^\mathrm{RMS}$ of the form [LD91]

$$\theta_\mathrm{e}^\mathrm{RMS} = \sqrt{\langle\theta_\mathrm{e}^2\rangle} = \frac{E_s}{\beta cp} Z_1 \sqrt{x/X_0}[1 + \epsilon \ln(x/X_0)] \,, \tag{1.18}$$

where p is the projectile momentum and Z_1 is the projectile charge in units of e. The length travelled in the material along the original particle trajectory is represented by x. The non-projected angle's RMS is a factor $\sqrt{2}$ larger. By fitting to the Molière distribution, the constants $E_s = 13.6$ MeV and $\epsilon = 0.038$ are found, which gives rise to a discrepancy $\leq 11\%$ for $\beta \simeq 1$, all abundant Z_1 and $10^{-3} < x/X_0 < 100$ [Y$^+$06, Eq. (27.12)]. If we instead use the simpler definition by Rossi [Ros52, Eq. (2.16.9)] with $\epsilon = 0$

$$\begin{aligned} E_s &= \sqrt{4\pi/\alpha} mc^2 = 21.2 \text{ MeV} \\ \langle\theta_\mathrm{e}^2\rangle &= \left(\frac{E_s}{\beta cp}\right)^2 \frac{x}{X_0} = \frac{4\pi}{\alpha}\left(\frac{mc^2}{\beta cp}\right)^2 \frac{x}{X_0} \simeq \gamma_\mathrm{L}^{-2} \frac{4\pi}{\alpha X_0} x \,, \end{aligned} \tag{1.19}$$

where $\gamma_\mathrm{L} \gg 1$ has been used. Here, it is straightforward to see that a characteristic length can be defined—the multiple-scattering length

$$\ell_\gamma = \alpha X_0 / 4\pi \,, \tag{1.20}$$

which is the length x it takes for the multiple scattering distribution to reach $\theta_\mathrm{e}^\mathrm{RMS} = \gamma_\mathrm{L}^{-1}$ in a amorphous foil. In this limiting case, the electron MCS and photon bremsstrahlung RMS scattering angle are identical. As discussed in both [Kle99] and [H$^+$04], this length is not clearly defined, as in some theories $\ell_\gamma^* = 2\ell_\gamma$ is used. The length can be regarded as a measure of the projectile's mean free path in the foil, and is—like the radiation length—only dependent on the material. In tantalum $(Z = 73)$, the multiple scattering length is 2.38 μm.

1.3 Suppressing Effects

From Eq. (1.7), we see that when considering a $\simeq$ 200 GeV electron (or positron) beam emitting bremsstrahlung photons of a few GeV, having a formation length of

macroscopic dimensions (*i.e.* μm) is feasible. For instance, when $E_0 = 200$ GeV and $\hbar\omega = 100$ MeV, $\ell_{f0} = 0.60$ mm. For such soft photons, the ratio of the formation length to the photon's reduced wave length is $\ell_{f0}/\lambda\!\!\!^{-} = 2\gamma_L^2\omega/\omega^* \simeq 2\gamma_L^2$. Under the circumstances mentioned above, this factor is a whopping 3×10^{11}! Because of such long formation lengths, even "weak but cumulative factors can be important" [Kle99].

The Landau-Pomeranchuk-Migdal Effect

Once the multiple scattering length is larger or comparable to the formation length in a semi-infinite foil, $\Delta t \gtrsim \ell_{f0} \gtrsim \ell_\gamma$, the lepton can be scattered outside the formation zone, due to multiple Coulomb scattering. This causes a spatial separation of the lepton and the—not yet fully developed—bremsstrahlung photon. The separation destroys the coherence between the lepton and photon, thus reducing the radiation yield and enlarging the effective radiation length. By equating ℓ_γ and $\ell_{f0}/2$, one can estimate the photon energy threshold at which multiple scattering has a considerable influence within the formation length

$$\begin{aligned}
&\ell_\gamma \lesssim \ell_{f0}/2 \Leftrightarrow \frac{\alpha X_0}{4\pi} \lesssim \frac{\gamma_L^2 \hbar c}{\hbar\omega^*} \Leftrightarrow \\
&\hbar\omega \lesssim \frac{4\pi\gamma_L^2\hbar c}{\alpha X_0}(1-y) = \frac{4\pi\hbar {E_0}^2}{\alpha m^2 c^3 X_0}(1-y) = \frac{{E_0}^2}{E_{LPM}}(1-\hbar\omega/E_0) \\
&\hbar\omega \lesssim \hbar\omega_{LPM} \equiv \frac{{E_0}^2}{E_0 + E_{LPM}}\,, \qquad E_{LPM} = \frac{mc^2 X_0}{4\pi a_0}\,,
\end{aligned} \tag{1.21}$$

where $E_{LPM} \simeq 7.684 X_0$ TeV/cm has been introduced. This leads to a material and primary energy dependent photon energy threshold below which the bremsstrahlung process is considerably influenced by MCS. In tantalum ($Z = 73$, $X_0 = 4.094$ cm), $E_{LPM} = 3.15$ TeV and $\hbar\omega_{LPM} = 12.0$ GeV at $E_0 = 200$ GeV. The effect is attributed to Landau and Pomeranchuk's original work [LP53], which was later extended by Migdal [Mig56]. Recent systematic experimental studies [A$^+$95, H$^+$03, H$^+$04] have provided solid evidence of the effect to a high precision. The threshold shown in Eq. (1.21) includes the effect of the quantum recoil at the radiation process, relevant for hard radiation ($y \not\ll 1$). Neglecting this effect corresponds to assuming a classical formation length, *i.e.* setting $\omega^* \to \omega$ in Eq. (1.7) on page 6. This would reduce the photon threshold to $\hbar\omega_{LPM} \simeq \hbar\omega_{LPM}^c = {E_0}^2/E_{LPM} \propto \gamma_L^2/X_0$. The classical expression is valid when $E_0 \ll E_{LPM}$. In the CERN SPS experiments [H$^+$03, H$^+$04], the quantum corrections were probed to a greater extent than in the SLAC E-146 experiment [A$^+$95, A$^+$96a], simply because the primary beam energy E_0 was comparable to E_{LPM} to a different degree, $E_0 = 287$ GeV and 25 GeV, respectively.

The BH cross section is found for a single scattering off an atom, hence it must be applicable in the regime where multiple scattering is irrelevant, $\ell_\gamma \gg \Delta t$, *i.e.* in very thin foils. The BH expression is also valid for thicker foils, as long as the photon energy is large enough, $\Delta t \gtrsim \ell_\gamma \gg \ell_{f0}$. In this regime, MCS is not significant within the formation zone. Whereas the BH power spectrum is fairly flat, cf. Eq. (1.16), the Landau-Pomeranchuk-Migdal (LPM) effect changes the soft photon energy dependence to $\simeq \sqrt{\hbar\omega}$ [Kle99]. The photon yield is thus reduced relative to the BH yield by a photon energy dependent factor. The LPM bremsstrahlung cross section somewhat resembles the BH expression, Eq. (1.11), however Migdal's functions $\xi(s)$, $G(s)$

and $\phi(s)$ describe the suppression [Mig56, Kle99]

$$\frac{d\sigma_{\mathrm{LPM}}}{d\hbar\omega} = \frac{4}{3}\alpha r_e^2 \frac{\xi(s)}{\hbar\omega}\Big[y^2 G(s) + 2\big[1+(1-y)^2\big]\phi(s)\Big] Z^2 \ln\!\big(184 Z^{-1/3}\big)\ . \tag{1.22}$$

$G(s)$ and $\phi(s)$ describe the helicity changing and conserving part of the suppression, respectively. Only the latter is relevant to soft photons ($y \ll 1$). Instead of Migdal's definitions through infinite series, the functions can approximately be formulated by [S$^+$82]

$$\phi(s) \simeq 1 - \exp\!\left[-6s\big[1+(3-\pi)s\big] + \frac{s^3}{0.623+0.796s+0.658s^2}\right] \tag{1.23a}$$

$$\psi(s) = 1 - \exp\!\left[-4s - \frac{8s^2}{1+3.96s+4.97s^2-0.05s^3+7.5s^4}\right] \tag{1.23b}$$

$$G(s) \simeq 3\psi(s) - 2\phi(s)\ . \tag{1.23c}$$

The parameter s describes the degree of suppression, which is large for $s \ll 1$ and *vice versa*. In Migdal's formulation, s is defined through $\xi(s)$, whence one must resort to an iterative determination of ξ and s. Another option is to use Stanev *et al.*'s transformation, separating the two [S$^+$82, Kle99]

$$s' = \sqrt{\frac{E_{\mathrm{LPM}} \times y}{8E_0(1-y)}} \tag{1.24a}$$

$$\xi(s') = \begin{cases} 1 & s' \geq 1 \\ 1 + h - \frac{0.08(1-h)[1-(1-h)^2]}{\ln(\sqrt{2}s_1)} & 1 \gg s' > \sqrt{2}s_1 \\ 2 & \sqrt{2}s_1 > s' \end{cases} \tag{1.24b}$$

where $s_1 = \big(184 Z^{-1/3}\big)^{-2}$ and $h = \ln s' / \ln(\sqrt{2}s_1)$. The Migdal formalism reduces only to the BH level at $s \gg 1$, *i.e.* it does not include the finer parts of the bremsstrahlung cross section, such as the Coulomb correction or the electronic contribution. However, many of these corrections are normally included in a proper definition of X_0, setting the overall level of the cross section. If the relatively simple photon energy dependence of Eq. (1.22) is combined with *e.g.* Tsai's tabulated values of X_0, a good accuracy can be reached with this model. This treatment would assume that the nuclear and electronic part were equally suppressed, despite the different kinematics. However, letting the electronic part be LPM suppressed or not results only in a very small difference [H$^+$04].

The Ter-Mikaelian Effect

In the previous section, it was explained how strong small-angle scattering of the projectile can introduce a phase shift that eventually causes destructive interference. Furthermore, the material's electrons can cause a phase shift in the photon wave function by coherent forward Compton scattering, which can also break the coherence. In a medium with electronic plasma frequency $\omega_p = \sqrt{Z n_n e^2/m\epsilon_0} = c\sqrt{4\pi Z n_n r_e}$ and index of refraction $n_r = \sqrt{1-\omega_p^2/\omega^2}$ ($\omega \gg \omega_p$), the photon travels with reduced speed c/n_r. This can be introduced by substituting $\hbar\omega/c \to \hbar\omega n_r/c$

in the last term of Eq. (1.5). By using the first two terms of the Maclaurin series for $n_r \simeq 1 - \omega_p^2/2\omega^2$ and, again, assuming small angles, the expression for the minimum value of $q_\parallel$ acquires an extra term [TM72, Eq. (14.4)]

$$q_{\parallel\epsilon} = \frac{\hbar\omega^*}{2\gamma_{\mathrm{L}}^2 c} + \frac{\hbar\omega_p^2}{2\omega c}$$
$$\ell_{\mathrm{f}\epsilon} = \frac{\hbar}{q_{\parallel\epsilon}} = \left(\ell_{\mathrm{f0}}^{-1} + \ell_{\mathrm{df}}^{-1}\right)^{-1} = \frac{\ell_{\mathrm{f0}}\ell_{\mathrm{df}}}{\ell_{\mathrm{f0}} + \ell_{\mathrm{df}}}\,, \tag{1.25}$$

where $\ell_{\mathrm{df}} = 2\omega c/\omega_p^2$. The formation length ℓ_{f0} is now reduced to an effective formation length $\ell_{\mathrm{f}\epsilon}$, as, clearly, the formation lengths larger than ℓ_{df} are effectively cut away—much in analogy to the density effect concerning ionization energy loss, where impact parameters larger than $\beta c/\omega_p$ are effectively cut away [Jac98]. Because of this analogy, the effect is sometimes referred to as the longitudinal density effect, the dielectric suppression or—in respect to its deviser—the Ter-Mikaelian (TM) effect [TM72]. The effect sets in when the second term in the equation above becomes substantial, *i.e.*

$$\frac{\hbar\omega^*}{2\gamma_{\mathrm{L}}^2 c} \lesssim \frac{\hbar\omega_p^2}{2\omega c}$$
$$\hbar\omega \lesssim \hbar\omega_{\mathrm{TM}} \equiv \gamma_{\mathrm{L}}\hbar\omega_p\,. \tag{1.26}$$

By reducing the formation length, the TM effect causes a suppression at $\hbar\omega \lesssim \gamma_{\mathrm{L}}\hbar\omega_p$. In the case of tantalum, $\hbar\omega_p^{\mathrm{Ta}} = 74.7$ eV, and even at $E_0 = 200$ GeV, $\hbar\omega_{\mathrm{TM}}^{\mathrm{Ta}} = 29.2$ MeV, thus the effect is best noticeable at very low relative photon energies $\hbar\omega/E_0 = y \lesssim \hbar\omega_p/mc^2 \lesssim 2\times10^{-4}$ in very dense media. When the TM effect is dominant, the bremsstrahlung differential power spectrum falls off very rapidly since $d\sigma_{\mathrm{TM}}/d\ln\hbar\omega \propto (\hbar\omega)^2$ [TM72], very different from the other suppression mechanisms. The TM effect thus remedies the infrared divergence suggested by the BH cross section. The TM effect was observed in the SLAC E-146 experiment [A$^+$96a]. Like the LPM effect [Sø92, WGP95], the TM effect has been investigated in its QCD analogue, "bremsstrahlung" gluons from a quark traversing quark/gluon matter [KP00].

◇ ◇ ◇

It has in the previous sections been shown that the well-known BH differential cross section (or the more complex expression of Tsai) is, under special circumstances, modified due to environmental disturbances within the formation zone. The modifications can be understood using a limited number of length scales: the target thickness Δt, the vacuum formation length ℓ_{f0}, the multiple scattering length ℓ_γ and the reduced formation length ℓ_{df} of the TM effect. The identity of the dominating effect or regime will be governed by both the target material's properties and the kinematics.

Although both the LPM and TM effects were carefully examined in the SLAC E-146 experiment [A$^+$97], some regions of the parameter space $(\Delta t, \ell_{\mathrm{f0}}, \ell_\gamma)$ could not be probed due to their limited primary energy. Since the formation length scales as γ_{L}^2, increasing $E_0 = 25$ GeV (SLAC) to $E_0 \simeq 200$ GeV (SPS) makes quite a difference. Before describing our bremsstrahlung studies, the next chapter will discuss the typical experimental setup.

CHAPTER 2

THE NA63 SETUP & METHODS

During the CERN NA63 experiments at the SPS North Area (Fixed Targets), the customary experimental setup would consist of the elements shown in Fig. 2.1. The incoming particles and resulting radiation are tracked on an event-by-event basis using fast scintillator counters (cf. Sec. 2.1) and a Computer Automated Measurement And Control (CAMAC) bus system (described in Sec. 2.3). After the primary particle has traversed the target, its direction is changed horizontally ($\hat{x}$) by the 2 m purging dipole magnet labelled B16, which is of the straight pole MBPL type [CER91]. In this way, the primary particle transversely separates from the radiation while travelling in a $\simeq$ 10 m helium bag, heavily reducing the yield of additional radiation or pair production. In this way, only radiation is intercepted by the calorimeter, when B16 is run at a sufficient field. The sketch in Fig. 2.1 is not to scale, and the full longitudinal length is about 20 m.

In the following sections, further details about the setup and detectors are presented.

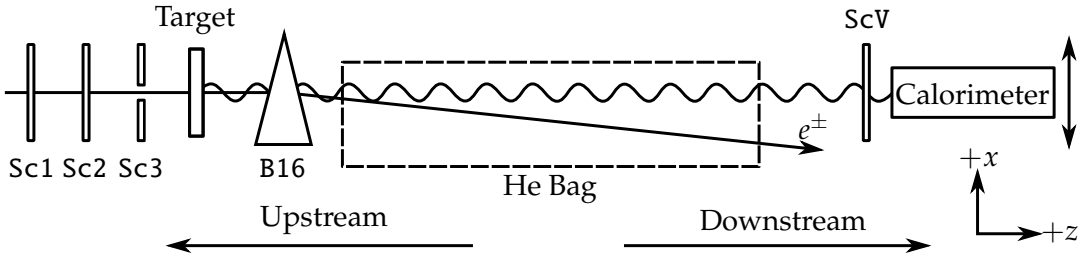

Figure 2.1: Top-view of the typical NA63 setup at the SPS. The setup consists of timing scintillators (Sc1–3, ScV), a target, a bending magnet (B16), a helium bag and an interchangeable calorimeter. Vacuum tubes (not shown in figure) were used where possible to reduce the background to a minimum. The beam is defined by $\mathtt{Sc1} \cdot \mathtt{Sc2} \cdot \overline{\mathtt{Sc3}}$.

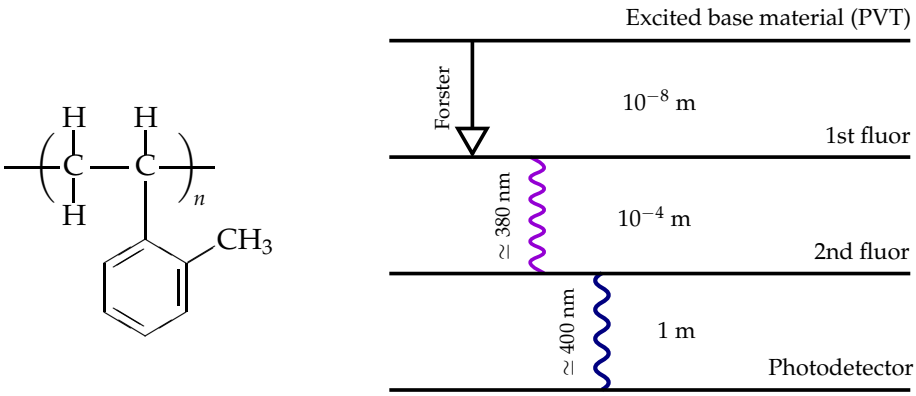

(a) The polymer polyvinyl toluene (PVT), which is the major component of scintillators used in high-energy physics. The aromatic ring in the toluene substituent is common to most scintillator materials.

(b) The excited plastic base decays and interacts with the primary fluor through the Forster mechanism. The primary fluor emits an ultra-violet photon, which is slightly redshifted by the secondary fluor. This photon is finally intercepted by a photodetector. The annotated length scales are the energy transfer distances in each sub-process. Adopted from Fig. 28.1 of [Y$^+$06].

Figure 2.2: Figures regarding high-energy scintillators.

2.1 Organic Scintillators and PhotoMultiplier Tubes

The utilized plastic scintillators are made from a solidified solution consisting primarily ($\sim$ 99%) of a polymeric base containing aromatic rings—typically polyvinyl toluene (PVT), cf. Fig. 2.2a—which is responsible for the actual scintillation process. Here, the incoming charge leaves a wake of ionization excited polymers which eventually decays and emits UV photons. Adding a small quantity of fluorescent materials (fluors) has two important effects. Firstly, the UV photon is slightly redshifted through a Stokes shift, reducing the self-absorption in the scintillator. Secondly, the fluors quench the decay of the excited base polymer by way of a resonant dipole-dipole interaction (the Forster mechanism), thus reducing the decay time by an order of magnitude to $\sim$ 2 ns [Y$^+$06, Chap. 28]. Often a primary and secondary fluor are added in decreasing amounts. This combination is sketched in Fig. 2.2b, and sometimes also a tertiary fluor is added before solidification to achieve further wavelength shift. The final photon reaches a PhotoMultiplier Tube (PMT) consisting of a photocathode, where the photon detaches an electron through the photoelectric effect, and a dynode structure. In a transmission PMT, the photocathode is a thin layer of a bi-alkali material deposited on the back of a borosilicate, lime glass or quartz window. The bi-alkali has a quantum efficiency of $\lesssim$ 25%, dependent on the photon wavelength. The dynode structure consists of $\sim$ 10–12 successive electrodes called dynodes. An increasing voltage is applied to the photocathode dynodes using a voltage divider with several steps. Typically, the photocathode will be at a High Voltage (HV) of $\simeq -2$ kV and the collecting anode will be close to ground potential. The magnitude of the final avalanche corresponds to a gain of 10^3–10^7 and it carries very little noise [Y$^+$06, Chap. 28]. The fast 12 stage Photonis XP2262 PMTs—used for the organic scintillators—are sensitive to photons in the spectral range 290–650 nm

and the anode pulse has small rise and transit times, 2.3 ns and 31 ns, respectively, at 1.9 kV [Pho10]. The rise time is defined as the time span between the anode current increasing from 10% to 90% of the maximum amplitude, assuming a light pulse with a temporal distribution resembling a delta function. The transit time is—as the name suggests—the time between a photon arriving at the photocathode and the resulting electron pulse reaching the anode. A spread in this quantity gives rise to the time resolution or *jitter* of the PMT. The PMTs are covered with mu-metal to shield the trajectory of the electron avalanche from magnetic fields. Usually, our plastic scintillators would be of the type BC-400. This has good light output and short rise and decay times of 0.9 ns and 2.4 ns, respectively. Although other plastic scintillator materials (BC-404) have slightly lower rise and decay times, these are typically $\gtrsim 4$ times more expensive. The scintillators are all wrapped in aluminized mylar foil and Tedlar tape creating a light-seal.

Depending on the scintillator density and composition, one scintillation photon is generated per $\simeq$ 100 eV of energy deposit. Scintillators based on PVT have a minimum ionizing stopping power of $dE/dx = 2.02$ MeV/cm [Y$^+$06], hence about 2×10^4 photons are generated by traversing a 1 cm scintillator. Assuming good transport efficiency and quantum efficiency of the PMT, $\lesssim 1$ cm of scintillator allows for an almost non-perturbing timing detection of a relativistic, charged particle with good timing resolution. In our setup (cf. Fig. 2.1), the scintillators `Sc1` and `Sc2` will inevitably produce some bremsstrahlung, which travels downstream along with the primary particle and eventually reaches the calorimeter, thus contributing to the bremsstrahlung background. `Sc1` and `Sc2` were usually both 0.2 cm thick, corresponding to a 0.9% X_0 radiator, $X_0^{\text{PVT}} = 42.5$ cm.

2.2 Total Absorption Calorimeters

To detect the photon/lepton energies of up to several hundreds of GeV, we have used a small variety of homogeneous calorimeters. The electromagnetic calorimeters are usually characterized by their large density and nuclear charge Z—hence short radiation length—as their common scheme is to destructively develop a shower of daughter particles through electromagnetic processes. With ultra-relativistic leptons, the shower will originate from a number of successive bremsstrahlung and pair production steps, until the particles' energy approaches the critical energy, E_c (where the ionization energy loss over one radiation length equals the particle energy, Rossi definition [Ros52]), thus ceasing further shower development. Eventually, the calorimeter has a mechanism for producing a large number of optical photons, which are detected by a PMT. The pulse height is—ideally—proportional to E_0, the energy of the primary particle[1]. The primary cause of deviation from linearity could be energy leakage occurring when the calorimeter volume is too small to contain the generated shower. The longitudinal containment is usually fulfilled for electromagnetic cascades as long as the length is $\gtrsim$ 20–30 X_0, since the range in this direction only has logarithmic dependence on E_0 [Per00]. Fig. 2.3a shows a calculation of the mean electron stopping power in units of primary energy per radiation length as a function of the calorimeter depth (x) in units of X_0. The calculation is based on a scaled gamma

[1] Actually, one should consider the particle's excess energy $E_0 - mc^2$, but usually $E_0 - mc^2 \simeq E_0$ in our experiments.

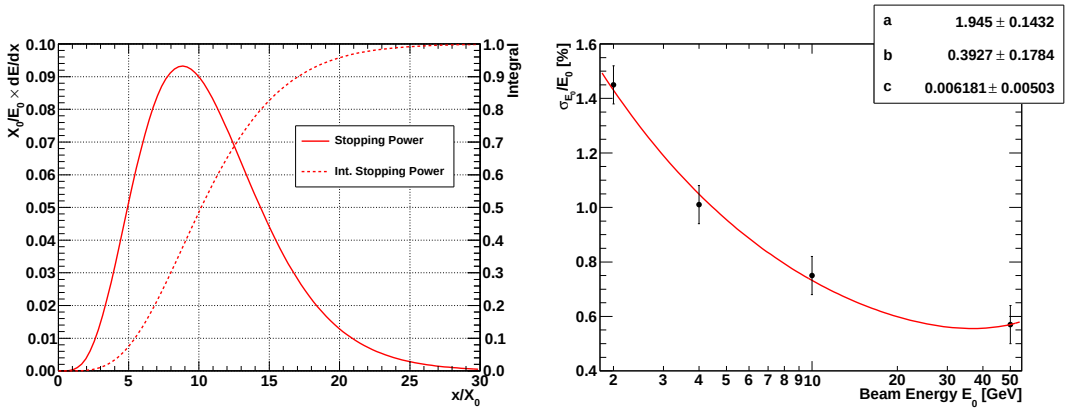

(a) Longitudinal shower development in a LG detector. The figure shows the mean scaled stopping power as a function of the depth (x) in units of radiation lengths. Also shown is the integral of the function which corresponds to the average relative energy deposited in the calorimeter.

(b) The datapoints show the relative resolution for a BGO detector as measured in [B$^+$89]. The solid line is a fit to the datapoints using the expression in Eq. (2.1).

Figure 2.3: General (measured) characteristics of a LG (BGO) calorimeter.

distribution which is a decent model, except at $x/X_0 \lesssim 2$ where the actual distribution is steeper [Y$^+$06, Sec. 27.5]. In the calculation, the calorimeter consists of Lead Glass (LG) and $E_0 = 200$ GeV. The integral of the stopping power shows the development of the relative energy deposition in the calorimeter. As is seen here, $\simeq 96\%$ of the primary energy is on average longitudinally contained within $20X_0$. A lateral propagation is introduced primarily by multiple Coulomb scattering—usually of the order of the Molière radius $R_M = E_s X_0/E_c$, where $E_s = \sqrt{4\pi/\alpha}mc^2 = 21.2$ MeV for an electron. Since the number of daughter particles in the shower is almost proportional to the primary particle energy E_0, the resolution of the calorimeter will be described partly by a statistics-related term proportional to $\sqrt{E_0}$. Typically, also a second term describing non-uniformity and radiation damage and a third term describing leakage are included. One can thus parameterize the relative resolution as

$$\frac{\sigma_{E_0}}{E_0} = \frac{a}{\sqrt{E_0/\text{GeV}}} \oplus b \oplus c \cdot E_0/\text{GeV}\,, \tag{2.1}$$

which is a modified version of the expression from [Y$^+$06, Chap. 28]. Here, $\oplus$ symbolizes addition in quadrature. The terms represent (a) statistics-related fluctuations, (b) detector non-uniformity and calibration uncertainty and (c) leakage. Since our calorimeters are primarily used to look at soft photons, where leakage is negligible, our leakage term is simply proportional to E_0.

To be able to measure photon energies over several orders of magnitude, we have used a combination of two calorimeters based on different materials.

Lead Glass

We have used F101 LG detectors of dimensions 90×90 mm^2 transverse area and 70 cm $(25X_0)$ long. The composition of F101 LG is by weight 51.2% lead tetroxide

(Pb_3O_4), 41.5% silicate (SiO_2), 7.0% potassium oxide (K_2O), and 0.2% cerium, giving rise to a radiation length $X_0^{\mathrm{LG}} = 2.78$ cm, Molière radius $R_{\mathrm{M}} = 3.28$ cm and critical energy $E_c^{\mathrm{LG}} = 17.97$ MeV [A$^+$96b]. The block of LG is like the organic scintillators wrapped in aluminized mylar foil and Tedlar. In the LG, the relativistic daughter particles produce Čerenkov radiation—due to the refractive index of $n_r = 1.65$—which is intercepted by a 3″ XP3461 PMT glued to the back of the LG block. The Čerenkov photons are subjected to absorption by the LG, and the probability of absorption must scale with the photon's distance to the PMT. The shower depth increases with primary energy, thus reducing the Čerenkov photons' distance to the PMT. This effect actually preserves linearity at larger energies, although the longitudinal leakage increases with the primary energy [A$^+$96b]. The LGs have in previous experiments [H$^+$04] been found to exhibit major leakage only at very high energies ($\gtrsim 200$ GeV), hence a linear calibration is often sufficient. A set of calibration points were in each NA63 experiment found using CERN SPS test beams of variable and well-defined energy in the range 10–250 GeV.

Typically, our LG calorimeters are sensitive down to $\simeq 2$ GeV, and the relative resolution is described by $a \simeq 15\%$, $b \simeq 10^{-3}$ and $c \simeq 10^{-4}$ [H$^+$04].

BGO

In 2008, the NA63 Collaboration bought a new total absorption calorimeter based on a $\varnothing$ 75 mm $\times$ 200 mm ($18X_0$) crystal of the inorganic material bismuth germanate [$(Bi_2O_3)_2(GeO_2)_3$] (BGO). This non-hygroscopic material is characterized by its short radiation length $X_0^{\mathrm{BGO}} = 1.12$ cm and thus low Molière radius $R_{\mathrm{M}} = 2.23$ cm. It is usually used for homogeneous calorimeters to detect particles of energies below the detection threshold of a LG and above energies detectable by a sodium-iodide (NaI(Tl)) detector of reasonable—*i.e.* affordable—size. In BGO, the signal-generating process is scintillation. Nevertheless, I shall in the following reserve the term scintillator for the plastic scintillators used for timing and refer to the BGO as a calorimeter. Our BGO is directly coupled to a 3″ XP3330 PMT which is placed in mu metal shielding. The PMT, voltage divider, and a 12 V preamplifier are all contained in an aluminum housing, neatly put together by the supplier (Scionix). An electromagnetic calorimeter array—named ECAL—consisting of 7680 BGO crystals was utilized in the L3 experiment at the CERN LEP accelerator [A$^+$90]. Prior to this, a careful calibration and investigation of the temperature dependence of the BGO crystals were performed at the CERN SPS X3 beam line [B$^+$89]. Using beams of energy 2–50 GeV, the relative resolution was found. In Fig. 2.3b, Eq. (2.1) is fitted to their datapoints. The relative resolution is well-described by the expression with $a = (1.94 \pm 0.14)\%$, $b = (0.39 \pm 0.18)\%$ and $c = (6 \pm 5) \times 10^{-5}$. Operating a BGO detector, one must beware of major temperature fluctuations, as the light yield (LY) is in fact slightly temperature dependent. The relative change in LY per degree temperature change around room temperature is in [Y$^+$06, Tab. 28.4] tabulated to be $d(\mathrm{LY})/dT = -0.9\%/\mathrm{K}$.

Since only high-energy beams are available at the CERN SPS (cf. Sec. 2.4), the BGO was calibrated using extracted electron beams from the Aarhus STorage RIng Denmark (ASTRID) (cf. Sec. 2.5 on page 23). In Aarhus, the BGO was checked for linearity with the exact same electronics and settings later utilized at CERN.

The Calorimetric Effect

Depending on the target thickness, multiple bremsstrahlung photons can be emitted from the same particle traversing the target. With the experimental scheme shown in Fig. 2.1, the calorimeter will detect only the combined energy, seemingly larger than any of the emitted photons. This multi-photon or calorimetric effect tends to "tilt" the power spectrum, such that the harder photon level is raised at the expense of the soft photon region level—a phenomenon known as pile-up. Since the radiation yield is—in most cases—proportional to $\Delta t/X_0$, the contribution from N_γ photon emission must be of the order $(\Delta t/X_0)^{N_\gamma}$. Usually, the accelerator based radiation studies use targets of only few percent radiation length to approach single photon emission, which is more attractive from a theoretician's point of view. In Monte Carlo (MC) simulations, multi-photon emission is easily implemented by using a single photon theory in a recursive manner until the lepton energy is depleted or the target is traversed. The number of emitted photons can be estimated by the probability W_0 of emitting a photon between $\hbar\omega_1$ and $\hbar\omega_2$

$$\begin{aligned} W_0 \equiv \frac{N_\gamma(\hbar\omega_1,\hbar\omega_2)}{N_e} &= \int_{\hbar\omega_1}^{\hbar\omega_2} n\Delta t \frac{d\sigma}{d\hbar\omega} d\hbar\omega \\ &= \frac{4\Delta t}{3X_0}\left[\ln\left(\frac{\hbar\omega_2}{\hbar\omega_1}\right) - \frac{\hbar\omega_2-\hbar\omega_1}{E_0} + \frac{3(\hbar\omega_2-\hbar\omega_1)^2}{8{E_0}^2}\right] \qquad (2.2) \\ W = 1-\exp\bigl(-W_0\bigr) &\simeq W_0 \quad (W_0 \ll 1)\,, \qquad (2.3) \end{aligned}$$

where the original BH expression for the differential cross section, Eq. (1.11), has been assumed for simplicity. While W_0 can reach arbitrary magnitudes (through the thickness Δt), $0 \leq W \leq 1$. The probability of observing N_γ photons in the photon energy interval $\hbar\omega_1 \to \hbar\omega_2$ can then be estimated from a Poisson distribution

$$P(N_\gamma, W) = \frac{\exp(-W)W^{N_\gamma}}{N_\gamma!}\,. \qquad (2.4)$$

This simple expression has been found to be consistent with *e.g.* full-scale MC simulations in GEANT3 [Mik97].

In the later Sec. 4.1, a theoretical approach by Baier & Katkov (BK) [BK99b] to describing multi-photon effects for soft photons ($y \ll 1$) in various target thickness regimes is discussed. Their corrective factor is for 100 μm tantalum ($Z = 73$) (2.44% X_0) about 85%–90% below the single-photon spectrum in the shown photon energy range. This level of multi-photon influence is similar to levels found through MC simulations mentioned in [Kle99, H$^+$04] concerning similar thicknesses.

The radiation spectrum will also be influenced by secondary pair production in the target. Any such pairs would not reach our calorimeters because of `B16`, leaving only the radiation. Pair production and multi-photon emission influences the radiation spectrum in similar degree due to the crossing symmetry of the two secondary processes. Using the proper LPM implementation in GEANT3 presented in [MBSU08]—only refined to apply to even lower photon energies—simulations have confirmed that the soft radiation spectrum will be additionally suppressed by subsequent pair production in the target. This second order effect is only feasibly included when resorting to MC simulations.

2.3 Electronics and Data Acquisition

The signals from the described detectors were properly delayed as to allow synchronous readout in our counting hut some 20–40 m from the setup. In the heart of the NA63 electronics setup was a CAMAC crate, allowing an event-by-event data acquisition. Here, all detectors, experimental scalers and Pattern Units (PUs) were read out, given a hardware trigger state. The experimental scalers are usually used to register the rate of occurrence of a phenomenon, whereas PUs are Boolean variables—testing a requirement of each event—that can be used in an offline analysis. In Fig. 2.4, the electronics diagram as used in the June 2009 beam time can be seen. Although this—at first glance—appears uncomplicated for a modern high-energy physics experiment, one should bear in mind that setup from scratch, delay and HV tuning, calibration and measurements would usually take place in 10–20 days, depending on the experiment's complexity. In some experiments, a number of different hardware triggers were employed simultaneously. By using a prescaler—thus selecting one in every 2^n events, $n = 0, 1, \ldots, 4$—very frequent hardware triggers could be suppressed in the recorded data in a controlled manner. This is especially important when the event rate approaches the maximum readout rate, where very few of the infrequent triggers would be registered due to system dead time, if prescaling were not used. The maximum readout rate was limited by the CAMAC and computer used to process the event, thus making the attainable readout rate dependent on the event data size, *i.e.* the number of detectors in use. With the simple setup sketched in Figure 2.1 on page 15, the readout rate was $\simeq$ 1 kS/s. An event was defined by a hardware trigger, and one of the hardware triggers was always $\mathtt{Sc1} \cdot \mathtt{Sc2} \cdot \overline{\mathtt{Sc3}}$, identifying the particles that cause Sc1 and Sc2 but not Sc3 to fire, ideally all the beam particles going parallel through the $\varnothing$ 9 mm hole in Sc3. These events were considered event candidates. If the subsequent event were to occur within 6 µs after, the two events would be considered double event candidates and be discarded. All triggers were properly gated by the SPS Start-Of-Burst and End-Of-Burst signals. Many of these logical operations and coincidence checks were recently gathered in the Wiener Nuclear Electronics Miniature BOX (NemBox) [Wie10]—basically a Field-Programmable Gate Array (FPGA)—thus heavily simplifying the use of external gating modules.

The scintillators were connected to discriminators and—in some cases—also a charge sensitive Analog to Digital Converter (ADC) (*i.e.* an integrating ADC). With the latter option, one can distinguish the number of Minimum Ionizing Particles (MIPs) in the offline analysis. The LG calorimeter PMT was directly connected to a charge sensitive ADC, whereas the signal from the BGO preamplifier is passed through an $\times 10$ attenuator, and then an Ortec 452 amplifier. The resulting signal was digitized by a peak sensitive ADC.

When considering the radiation generated from traversing very thin targets (few percent X_0), it is possible that no or only very low energy bremsstrahlung is emitted, although a hardware trigger causes a readout of the calorimeter. Under these circumstances, the ADC value would be the integral/level of the offset value read from the LG PMT/BGO amplifier. This signal is referred to as the low energy pedestal, the fluctuation of which resembles the noise of the electronics. The pedestals could be probed by introducing fake/random triggers when the beam was not present. The pedestals are used in the calibration as a zero-energy calibration point, which can be

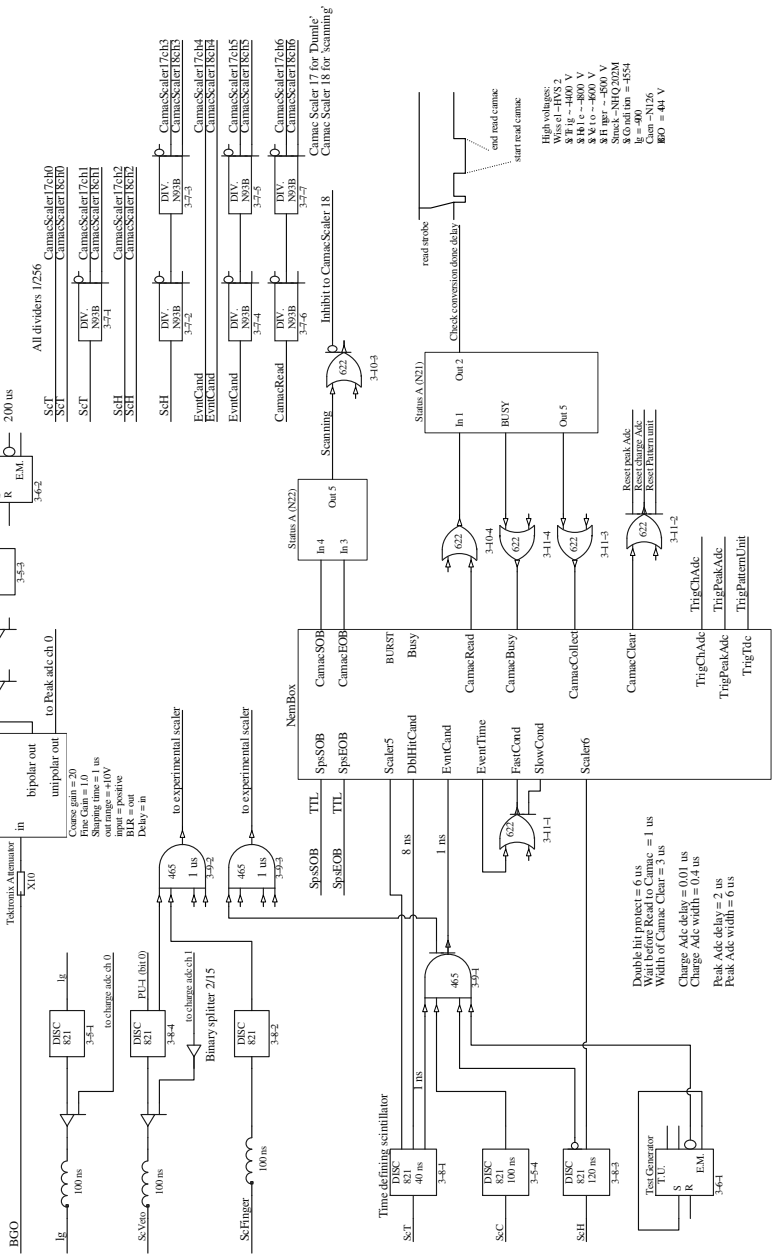

Figure 2.4: Electronics diagram for the NA63 setup during the beamtime of June 2009. The diagram is read down-to-up. Courtesy of P.B. Christensen. Here, `Sc1`, `Sc2` and `Sc3` are labeled `ScT`, `ScC` and `ScH`, respectively.

important when looking towards low photon energies.

2.4 Beam Conditions

All experiments were performed in the H4 beam line of the CERN SPS in a tertiary beam of electrons or positrons with variable momentum in the range 10–300 GeV/c, but with low intensities at very low or very high energies. The leptons are a product

of a SPS burst of $\simeq 4 \times 10^{12}$ protons hitting a beryllium target (T2) and creating pions. The following photons are converted to e^+e^- pairs. The particle momentum relative to charge is selected through a magnetic rigidity acceptance using a combination of several magnetic fields, while many other particles are discarded in a dump target (TAX). The magnetic lattice is operated on the basis of the filter mode optics—an unspecific but versatile lattice producing a horizontally and vertically parallel beam—on the cost of transverse size. In October 2009, the horizontal parallelism of a beam with this optics was measured with drift chambers to $\simeq 250$ µrad Full Width at Half Maximum (FWHM). In this way, the resulting photon beam size at the calorimeter front surface would be $\simeq \varnothing$ 4 mm FWHM, neglecting MCS in the target.

The lepton bursts reaching our experimental area consisted of $\simeq 10^4$ particles giving rise to the norm trigger $(\mathtt{Sc1} \cdot \mathtt{Sc2} \cdot \overline{\mathtt{Sc3}})$ during the $\simeq 10$ s burst at the beam energy $E_0 = 149$ GeV. This of course depends on collimator settings, and thus momentum spread. The beam intensity is reduced by $\simeq 2$ when increasing the beam energy by 30 GeV. The utilized beam energies were usually chosen as a trade-off between having macroscopic formation lengths during emission of photons with energies of up to a few GeV and retaining acceptable beam intensities. The burst repetition rate was about 2–3/min, depending on the CERN Proton Synchrotron super cycle, consisting of a number of 1.2 s cycles.

2.5 Calorimeter Calibration

BGO

As mentioned in Sec. 2.2 on page 19, test beams of energies $\lesssim 10$ GeV are not available at the SPS, whence the BGO was calibrated at a different facility—the ASTRID at Aarhus IFA. The PMT HV was kept at 405 V, despite Scionix' recommendations of 700–1100 V. Even at 540 V, the BGO PMT exhibited saturation effects during test at the SPS. Here, the BGO signal contained a distinct artifact consisting of a peak in high end of the photon spectrum. The erroneous signal was explained by the fact that the BGO—capable of detecting up to few GeV photons—was also subjected to photons of $\gtrsim 100$ GeV, dependent on the primary beam energy E_0. Such hard radiation is believed to generate a shower of such magnitude that the XP3330 PMT completely saturates, giving rise to about the same signal from the peak sensitive ADC. The artifact disappeared when lowering the HV to 405 V. Here, the BGO could detect photons of energies up to $\gtrsim 3$ GeV. With many different, well-defined electron beam energies, the BGO was found to exhibit linearity despite the fact that it was operated well below the recommended HV, cf. Fig. 2.5a.

At ASTRID, the extracted electron beam's position was poorly transversely localized, thus leading to a broadening of the photopeaks due to inadequate containment of showers originating from electrons hitting the BGO non-centrally. Using a scintillator oriented with its thinnest side facing upstream, the 580 MeV beam's vertical and horizontal profile was measured to be about 4 and 7 cm wide, respectively. Please take notice that this leakage is less energy dependent than the effect described above Eq. (2.1)—it is purely due to very non-central particles.

Using Geant4 [Gea03], simulations of electrons' energy deposit in the BGO have been performed. The simulations include all relevant electromagnetic processes, BGO crystal geometry and resolution, electron beam size, but not PMT resolution

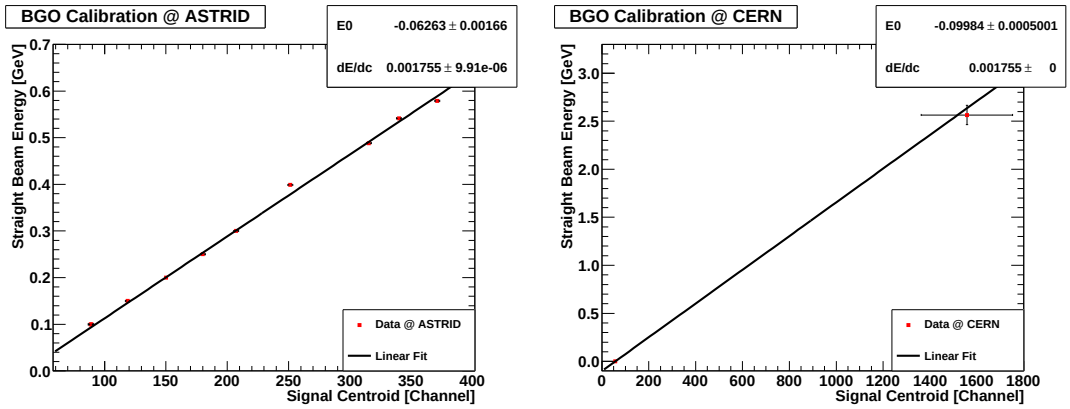

(a) BGO calibration at ASTRID. Datapoints are shown with error bars representing statistical errors only.

(b) BGO calibration at CERN. The energy error bars of the datapoint obtained through a tagged electron beam is relatively large due to a momentum spread of the accepted beam. Nevertheless, the ASTRID calibration is well verified only with a slight energy shift.

Figure 2.5: BGO Calibrations.

nor amplification[2]. In Fig. 2.6, the simulations are compared with the calibration data at six of the energies. As expected, the photopeaks all have a low-energy tail due to leakage. It should be noted that the simulation showing the electrons' energy deposit have been calibrated in order to have the maximum at the beam's energy. Not only is the BGO very linear despite the low HV, but the ASTRID calibration data is also in good accordance with Geant4 simulations at all calibration energies. The low energy peak seen in the data but not the simulations are due to the experimental triggering system—a scintillator with a transverse area larger than the BGO's area.

The detector resolution is extracted in two ways. Firstly, the peaks have been fitted with skewed Gaussian distributions of the type proposed in [OL76, Wik10]. The energy resolution is taken to be the root of the estimator's energy variance. Secondly, the peaks have been fitted with pure Gaussian distributions from slightly below the centroid to the upper endpoint energy. The relative energy resolution as found by the methods can be seen in Figure 2.7a and 2.7b, respectively. In both cases, Eq. (2.1) has been fitted to the relative resolution. The skewed fits generally suggest a larger resolution which is mainly caused by a heavy leakage (the parameter c). With the second type of fit—which should be less affected by the unfocused beam—the relative resolution is found to be described by $a = (2.49 \pm 0.02)\%$, $b = (0.86 \pm 0.12)\%$ and $c \simeq 0\%$. The values are all in good accordance with the result found from [B$^+$89], cf. Fig. 2.3b on page 18.

Using the same equipment and settings later at CERN, we trust the slope of the calibration to persist, but the baseline offset of the BGO signals could have been slightly different. To check this, we performed a calibration verification using a deflected electron beam having passed through a Cu radiator. The optimal radiator

[2]I am very grateful to Sergio Ballestrero who implemented the BGO materials and a simple geometry.

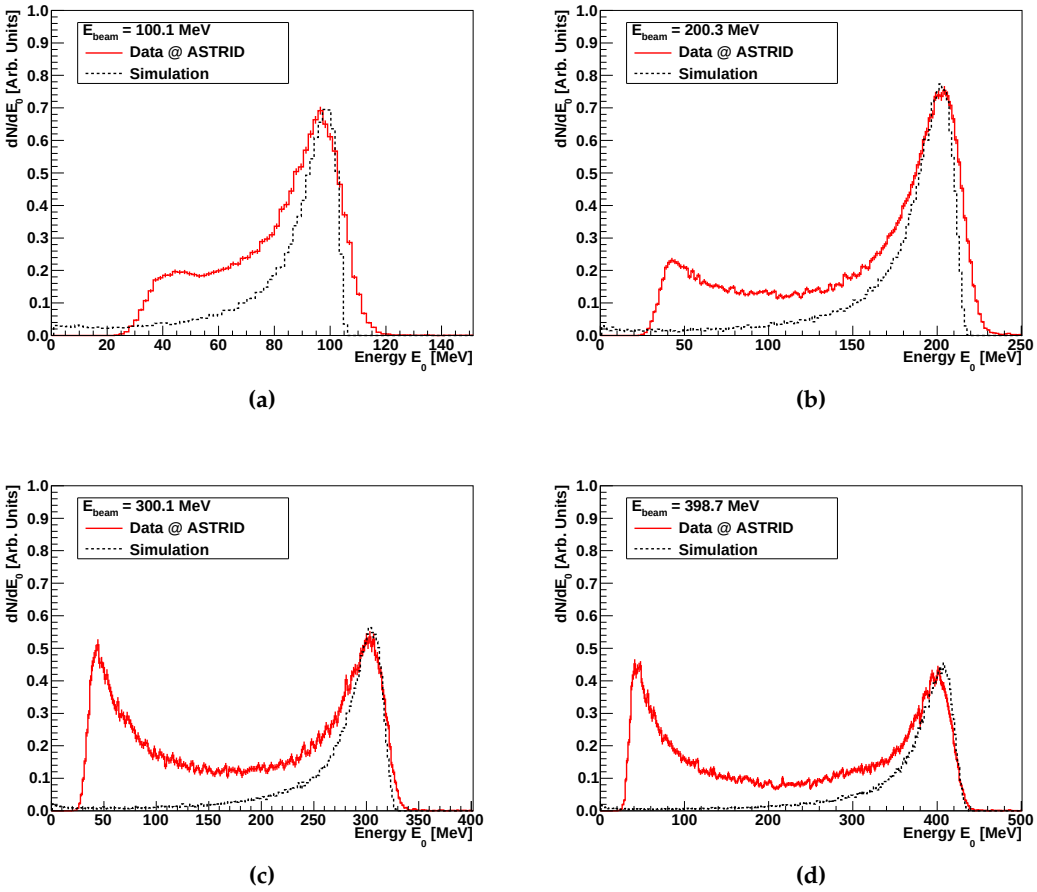

Figure 2.6: Continues on page 26.

thickness $\Delta t/X_0 \simeq 10\%$ was found through a MC simulation as a trade-off between obtaining a high intensity of the secondary electron beam and low MCS in the foil (which increases the momentum acceptance of the calorimeter). The geometry and well-known integrated field of B16 dictated an accepted energy of 2.57 GeV. A linear fit to these points can be found in Fig. 2.5b. The slope of the fit is fixed to the value obtained from the Aarhus data, cf. Fig. 2.5a. Notice that the CERN calibration is shifted $\simeq -37(2)$ MeV relative to the ASTRID one. The CERN calibration is used for the data analysis, unless else is specified.

2.6 Background Compensation

Typically, the photon energy data would be projected onto a logarithmically binned histogram with left edge of the ith bin following 10 MeV $\times\, 10^{(i-1)/25}$, *i.e.* 25 bins/decade. This binning is used throughout the thesis unless else specified. By having the logarithmic binning, the histogram mimics the photon power spectrum entirely

$$\frac{dN_\gamma}{d\ln\hbar\omega} = \hbar\omega\frac{dN_\gamma}{d\hbar\omega}\,. \tag{2.5}$$

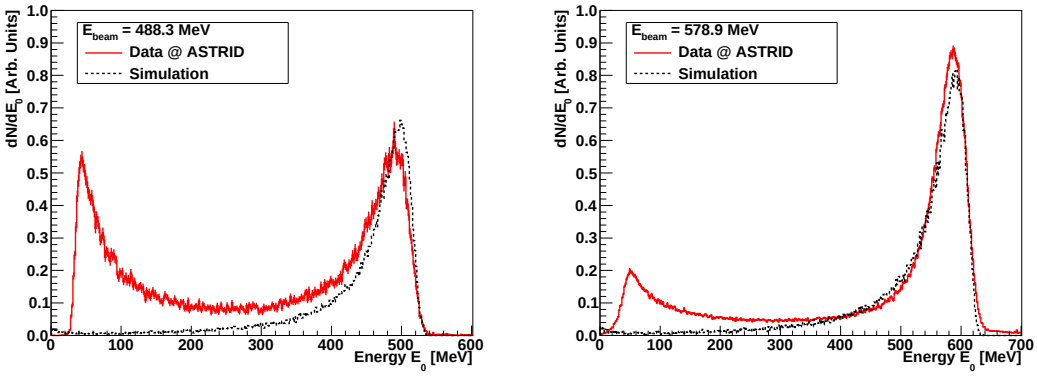

(e) **(f)**

Continued Figure 2.6: Comparison between e^- BGO calibration data obtained at ASTRID (full, red) and Geant4 simulation (dotted, black).

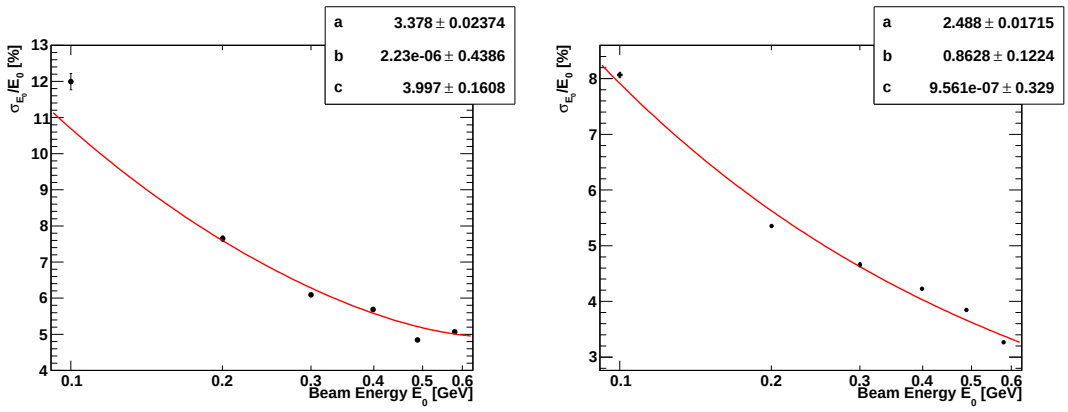

(a) BGO relative resolution. The photopeaks are fitted with asymmetric Gaussians.

(b) BGO relative resolution. Upper half of the photopeaks are fitted with symmetric Gaussians.

Figure 2.7: BGO Resolutions.

Unless else is specified, all spectra have also been normalised to the logarithmic bin width $\ln(10)/N_b \simeq 2.30/N_b$ where N_b is the number of bins per energy decade. In this way, the histogram level is unaffected by the chosen bin size—only the size of statistical error bars depends on the choice of N_b—which allows for easy comparison with theoretical curves. Of course, the binning should not be chosen coarser than the structures of the power spectrum. The BH power spectrum is fairly flat, hence deviations from this behaviour is evident in a power spectrum.

When using foils of only a few percent radiation length as targets in the H4 experiment area, one has to perform a thorough background examination and compensation, as the background can easily be comparable to an equivalent radiator of similar thickness. In this document, I will apply the following nomenclature: a *raw* spectrum refers to the result of a measurement on a target in an environment with a radiator *background*. Where applicable, considerable beam time would be dedicated

to a background measurement—normally with an empty target holder—to bring down the statistical errors of this spectrum. If one could experimentally eliminate the background, one would measure the *pure* spectrum of the target. A naïve guess would be that the pure spectrum is exactly obtained as a difference between the raw and background spectrum, with some proper normalizations. However, the difference can contain some considerable deviations from the pure spectrum as described in [III] and below.

Influence of Synchrotron Radiation

The low energy photon spectrum will be affected by the distribution of Synchrotron Radiation (SR), inevitably introduced by the purging magnet B16, cf. Figure 2.1. The SR contribution is characterised by the critical energy [Jac98, Eq. (14.81)]

$$\hbar\omega_c = \frac{3}{2}\frac{\gamma_{\mathrm{L}}^3\hbar c}{\rho} = \frac{3}{2}\frac{\gamma_{\mathrm{L}}^3\hbar ceB}{p}\,, \tag{2.6}$$

where ρ is the radius of the particle's circular path in the magnetic field of strength B. The magnetic rigidity $Be = p/\rho$ has been used above. The maximum field in the magnet is $B_{\max} \simeq 2\mathrm{T}$ at which $\hbar\omega_c = 30$ MeV (57 MeV) for 149 GeV (207 GeV) electrons. Beyond this energy, the power spectrum per electron $(d\epsilon/d\hbar\omega)$ falls off roughly exponentially [Jac98, Eq. (14.91)]

$$\frac{d\epsilon}{d\hbar\omega} \equiv \frac{1}{N_e}\frac{dN_\gamma}{d\ln\hbar\omega} = \frac{\sqrt{3}e^2\gamma_{\mathrm{L}}}{c}\frac{\omega}{\omega_c}\int_{\omega/\omega_c}^{\infty} K_{5/3}(x)\,x\,dx \tag{2.7}$$

$$\simeq \sqrt{\frac{3\pi}{2}}\frac{e^2\gamma_{\mathrm{L}}}{c}\left(\frac{\omega}{\omega_c}\right)^{0.5}\exp(-\omega/\omega_c) \qquad \omega \gg \omega_c\,, \tag{2.8}$$

where K_ν is the modified Bessel functions of the second kind and order ν [AS64, Sec. 9.6]. Much like the traditional pile-up phenomenon discussed on page 20, the calorimeter will register only the combined energy $\hbar\omega$ of a number N_γ^{B} of bremsstrahlung photons and a number N_γ^{SR} of SR photons

$$\hbar\omega = \underbrace{\sum_{i=0}^{N_\gamma^{\mathrm{B}}}\hbar\omega_i}_{\text{Target}} + \underbrace{\sum_{j=0}^{N_\gamma^{\mathrm{SR}}}\hbar\omega_j}_{\text{SR}}\,, \tag{2.9}$$

where $\hbar\omega_0 = 0$, obviously. Fortunately, the SR distribution has limited range ($\hbar\omega \lesssim 10\hbar\omega_c$) which makes the latter term almost irrelevant at larger photon energies. The mean number of SR photons $\langle N_\gamma^{\mathrm{SR}}\rangle \propto E'$ (where E' is the final electron energy) and depends also on the detector solid angle. The mean SR photon energy is proportional to ω_c, which can be considered constant in the soft photon regime, since $E' = E_0 - \hbar\omega \simeq E_0$, cf. Eq. (2.6). In the BH (and LPM) regime, $\langle N_\gamma^{\mathrm{B}}\rangle \propto \Delta t$, cf. Eq. (2.3), and because of this, $\langle N_\gamma^{\mathrm{B}}\rangle/\langle N_\gamma^{\mathrm{SR}}\rangle$ must be a linear function of the target thickness, *i.e.* the relative SR contamination decreases with increasing target thickness. Even if one could establish the thickness dependence, the numbers N_γ^{B}, N_γ^{SR} and each individual photon energy $(\hbar\omega_{i/j})$ are all stochastic variables, *i.e.* both the number and

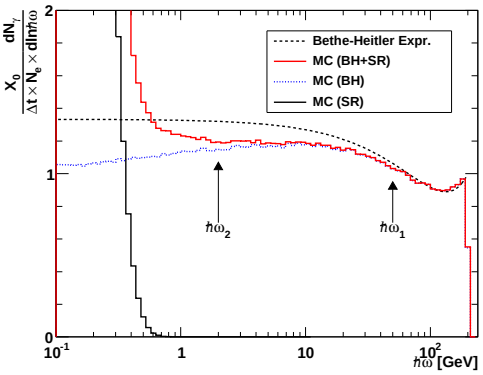

(a) Pure power spectra for $\Delta t/X_0 = 2.5\%$. Multi-photon emission (blue line) and SR clearly alters the soft-photon single-emission spectrum (black, dotted line).

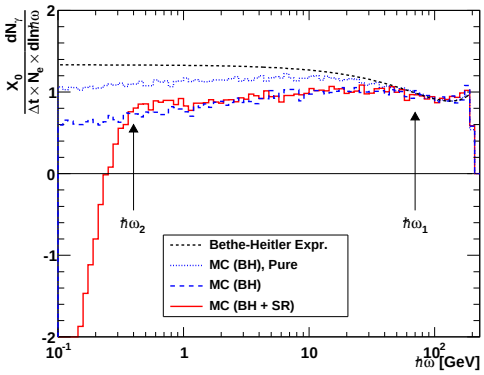

(b) Difference between two simulated spectra corresponding to $\Delta t/X_0 = 5.0\%$ and $\Delta t/X_0 = 2.5\%$, each normalized to their respective number of events (here the same). The red curve corresponds to BH + SR, while the blue dashed curve corresponds to multi-photon BH exclusively. For comparison, the blue dotted curve is the pure multi-photon $\Delta t/X_0 = 2.5\%$ simulation of (a). All spectra but the latter have been manipulated by the method employed to compensate for background.

Figure 2.8: Bremsstrahlung and synchrotron radiation MC simulations based on $N_e = 1 \times 10^7$ electrons of energy $E_0 = 200$ GeV traversing a target and a magnetic field $B = 2$ T (maximum field of B16).

individual energy of the detected photons are *random* for each event. Despite the SR distribution being well-determined, it is thus very difficult to cleanse the spectra for the SR contamination, hence we chose to steer clear of the SR infected region. The SR contamination could be investigated and remedied through a thorough MC study of the problem sketched above, but this has not been done here.

In Figure 2.8a, a number of MC simulations based on $N_e = 1 \times 10^7$ particles of energy $E_0 = 200$ GeV traversing a $\Delta t/X_0$ foil are shown to mimic this effect. All curves are normalized to bin width, target thickness and N_e. The bremsstrahlung energy is sampled from Eq. (1.15) on page 10, shown with a dashed black line, while the number of photons is sampled from the Poisson distribution of Eq. (2.4) on page 20. In this way, the bremsstrahlung spectrum including multi-photon emission (blue line) is found. Below a photon energy $\hbar\omega_1 \simeq 70$ GeV, this spectrum is seen to deviate significantly from the single-photon BH expression. The normalized SR distribution is simulated using Eq. (2.8), and it is shown as the black, steeply rising spectrum at low photon energies. Finally, when the SR distribution and bremsstrahlung are combined as outlined in Eq. (2.9), the result is the red spectrum, which below $\hbar\omega_2 \simeq 2$ GeV deviates significantly from the multi-photon spectrum (blue). Unless else is stated, $\hbar\omega$ will refer to the combined energy of the radiated photons seen by our calorimeters.

In the offline analysis, the *modus operandi* of compensating for the background was to normalize the target and background spectra to their respective number of triggering events N_e, and the background would be subtracted from the target spec-

trum, bin by bin. Mathematically, this results in a histogram of zero integral. The background was typically of the order of $\lesssim 2\%\ X_0$, while the raw spectrum would intrinsically correspond to a target thicker by $\Delta t/X_0$. Because the background is thinner, a zero-energy readout (combined with *e.g.* SR) to the pedestal is more prone to occur, hence the pedestal region is more predominant in the background than in the target spectrum. This gives rise to a negative pedestal when subtracting background from target spectra. An example of this is simulated in Figure 2.8b, where a background of $\Delta t/X_0 = 2.5\%$ and a raw spectrum of $\Delta t/X_0 = 5.0\%$ are simulated with the same parameters as in Figure 2.8a. The resulting difference is normalized by the net radiator thickness of $\Delta t/X_0 = 2.5\%$. Below $\hbar\omega_2 \simeq 0.4$ GeV, the difference in SR contamination makes the spectrum dive considerably. The spectrum is of course unreliable below this kink. By comparing the BH + SR simulation to the one based purely on multi-photon BH, it can be seen that a SR contamination does not heavily influence the Background Compensated Power Spectrum (BCPS) besides in the region below the kink at $\hbar\omega_2$.

To reduce multi-photon effects—which is desirable from a theoretician's point of view—an experimental study is limited to thin targets, *i.e.* $\Delta t/X_0 \lesssim 2\%$. To have a decent signal-to-background ratio, one must do a thorough reduction of the background material—for instance, 3 m of air alone amounts to 1% X_0. Ironically, reducing the background only increases the relative SR contamination in the background spectrum, thus accentuating the effect seen in Figure 2.8b, when the described method of background compensation is applied. With typical magnetic field strengths, it is of course an artifact which is only present at the very lowest photon energies, *i.e.* only of seemingly large extent on a logarithmic scale. The energy range of the SR contamination could be reduced by using an experimental setup with greater distance from purging magnet to calorimeter, thus facilitating a lower magnetic field.

The Statistical Errors

For simplicity, we shall consider the statistical errors of only one bin with R and B counts in the raw and background spectra, respectively. Also, the number of primary particles N_e are assumed identical in both spectra. The statistical error of the spectrum level after background subtraction and normalization to N_e is

$$\begin{aligned}\sigma\left(\frac{R-B}{N_e}\right) &= \frac{\sqrt{R+B}}{N_e} \\ &= \frac{\sqrt{S+2B}}{N_e} \geq \frac{\sqrt{S}}{N_e}\,,\end{aligned} \tag{2.10}$$

assuming Poisson statistics. In the final step, $S = R - B$ is introduced. In our analysis, we assume that the number of counts S correspond to the photons originating from the target in absence of background. As will be discussed in the following section, this is only the case under idealized circumstances. Be that as it may, the expression above shows that the radiator background will considerably augment the statistical errors of the BCPS when $S \gg 2B$.

The Exaggerated Pile-up

Another interesting effect of the background compensation arises from the non-linearity of multi-photon emission. We here assume that the thickness dependence of the power spectrum per triggering event $d\epsilon/d\hbar\omega = 1/N_e \times dN_\gamma/d\ln\hbar\omega$ from a $\Delta t/X_0$ radiator is described by the simple expression

$$\frac{d\epsilon}{d\hbar\omega} = \frac{4}{3}\frac{\Delta t}{X_0}\left(1-\eta\frac{\Delta t}{X_0}\right), \qquad \eta \geq 0\,, \tag{2.11}$$

where the latter term describes pile-up due to secondary photon emission. The quantity η contains all the photon energy dependence. For simplicity, we first consider a fixed photon energy and comment on the dependence later. The simple pile-up expression is compliant with the BH expression in the soft-photon limit ($y \ll 1$) and $\eta \to 0$. We now consider a measurement on a target of thickness $s\Delta t/X_0$ in a background environment of thickness $b\Delta t/X_0$, where s and b are the signal (target) and background fraction, respectively, of their combined thickness $\Delta t/X_0$, *i.e.* $s+b=1$. The BCPS is thus found to be

$$\begin{aligned}
\left.\frac{d\epsilon}{d\hbar\omega}\right|_{s+b} - \left.\frac{d\epsilon}{d\hbar\omega}\right|_{b} &= \frac{4}{3}\frac{\Delta t}{X_0}\left(1-\eta\frac{\Delta t}{X_0}\right) - \frac{4}{3}\frac{b\Delta t}{X_0}\left(1-\eta\frac{b\Delta t}{X_0}\right) \\
&= \frac{4}{3}\frac{s\Delta t}{X_0} - \frac{4}{3}\eta\left(1-b^2\right)\left(\frac{\Delta t}{X_0}\right)^2, \qquad 1 = s^2+b^2+2sb \\
&= \frac{4}{3}\frac{s\Delta t}{X_0}\left(1-\eta\left(s+2b\right)\frac{\Delta t}{X_0}\right) \leq \left.\frac{d\epsilon}{d\hbar\omega}\right|_{s}, \qquad b \geq 0 \qquad (2.12)\\
\left.\frac{d\epsilon}{d\hbar\omega}\right|_{s} &= \frac{4}{3}\frac{s\Delta t}{X_0}\left(1-\eta\frac{s\Delta t}{X_0}\right). \qquad (2.13)
\end{aligned}$$

The first term of Eq. (2.12) corresponds to the single-photon BH level of a target of thickness $s\Delta t/X_0$, while the latter term corresponds to pile-up in a target of thickness $\sqrt{s^2+2sb}\Delta t/X_0$. As seen by comparing the last two equations above, the BCPS complies with the pure signal multi-photon spectrum (Eq. (2.13)) only in the limit $s \gg 2b$ ($1 \gg 3b$). Unless this is the case, the BCPS will possess a shape dependent on both the signal and background spectrum, due to pile-up. The observed pile-up will, generally, seem more severe than that of a pure spectrum.

The exaggerated pile-up effect is clearly seen by comparing the two blue lines of Figure 2.8b, both representing MC simulations of multi-photon BH. The dotted blue line corresponds to the pure $\Delta t/X_0 = 2.5\%$ simulation (also seen in Figure 2.8a), while the dashed blue line is a result of the difference between a raw spectrum of $\Delta t/X_0 = 5.0\%$ and a background of $\Delta t/X_0 = 2.5\%$, *i.e.* $s = b = 0.5$, not uncommon in our measurements. While the former has an absolute value of $\simeq 1.05$ at the lowest photon energy, the latter is here reduced to $\simeq 0.6$, clearly a considerable methodical effect, which is—as introduced by multi-photon emission—experimentally almost impossible to avoid. To measure the absolute soft-photon power spectrum level from thin targets with reasonably low systematic errors is thus complicated by the effect. One could, however, find a correction by comparing the BCPS from a trusted reference target to the simulation of the pure target spectrum. The correction

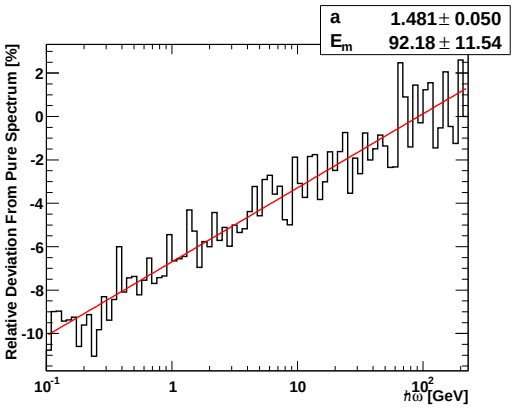

(a) Target of $\Delta t/X_0 = 2.5\%$ with a background of $\Delta t/X_0 = 0.5\%$

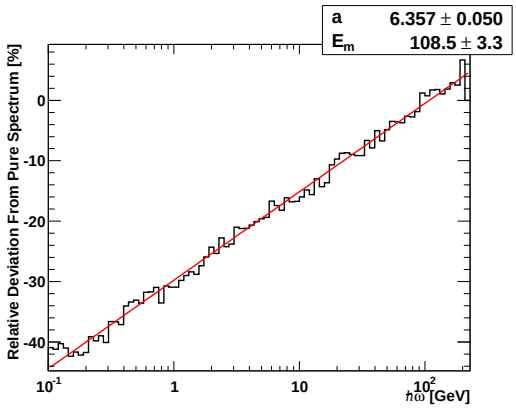

(b) Target of $\Delta t/X_0 = 2.5\%$ with a background of $\Delta t/X_0 = 2.5\%$

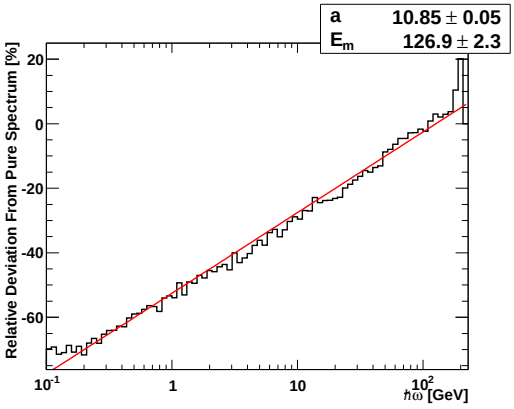

(c) Target of $\Delta t/X_0 = 2.5\%$ with a background of $\Delta t/X_0 = 5.0\%$

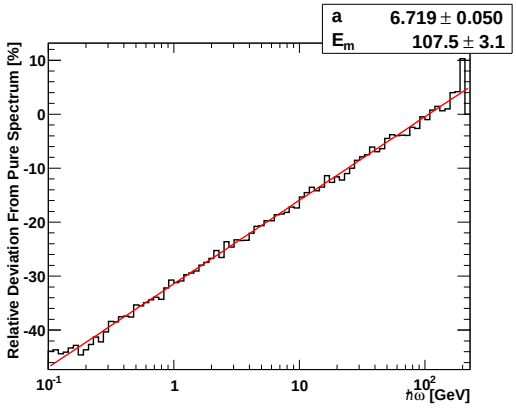

(d) Target of $\Delta t/X_0 = 5.0\%$ with a background of $\Delta t/X_0 = 2.5\%$

Figure 2.9: MC simulations of the relative difference between a background compensated and a pure power spectrum. Each simulation is a result of $N_e = 10^7$.

should be applicable to the spectra of other targets of same thickness[3], giving rise to—effectively—relative power spectra.

By using the simple assumption of Eq. (2.11) with the result of Eq. (2.12) and (2.13), the relative deviation of a BCPS from its corresponding pure spectrum can be estimated

$$r \equiv \frac{\left(\left.\frac{d\epsilon}{d\hbar\omega}\right|_{s+b} - \left.\frac{d\epsilon}{d\hbar\omega}\right|_{b}\right) - \left.\frac{d\epsilon}{d\hbar\omega}\right|_{s}}{\left.\frac{d\epsilon}{d\hbar\omega}\right|_{s}} = -\frac{2\eta\frac{b\Delta t}{X_0}}{1-\eta\frac{s\Delta t}{X_0}}. \tag{2.14}$$

The relative deviation from the pure spectrum is thus approximately linear in the background equivalent radiator thickness in units of radiation lengths, while it is

[3]The correction must depend on the values of target and background equivalent radiator thickness, where the latter should be kept constant during a consistent experiment.

less dependent on the target thickness, since $\eta s \Delta t / X_0 \ll 1$ for pile-up in thin targets, cf. Eq. (2.13). In Figure 2.9, examples of the relative deviations r have been found through simulations of the multi-photon BH as seen in Figure 2.8. The SR is neglected here for simplicity. In all cases, the simulated deviations have a convincing logarithmic photon energy dependence. A close to logarithmic multi-photon correction is also found in [BK99b] in the BH regime. In all figures, a fit has been made with the expression

$$r(\hbar\omega) = a \ln\left[\hbar\omega / E_m\right] , \qquad r(E_m) = 0 , \tag{2.15}$$

where a is a dimension-less scaling, and E_m is a characteristic energy. In all fits, $E_m \simeq E_0/2$ and the value of r is roughly linear in $b\Delta t / X_0$, comparing Figure 2.9a–c, and almost independent on $s\Delta t / X_0$, comparing Figure 2.9b with 2.9d.

It is important to mention that although the phenomenon should be present where a considerable background is present, the magnitude and photon energy dependence depend on the differential bremsstrahlung cross section, *i.e.* it will generally be slightly different in the *e.g.* LPM and TM suppression regimes. Above, only the simple BH regime and secondary photon emission was considered.

Our method of background compensation was also employed in the SLAC E-146 LPM and TM experiments. However, their backgrounds were dominated by SR, not bremsstrahlung. Judging from [A$^+$97, Fig. 4], their background radiator level at $E_0 = 8$ GeV corresponded to $\Delta t / X_0 \lesssim 0.02\%$. Their background compensated data was thus not influenced by the exaggerated pile-up effect but did possess the SR kink. To reduce edge effects, the spectrum of a thin target was subtracted from the spectrum of a bulkier target, giving rise to "edge-effect subtracted data". In the case of carbon, the difference between a 6% X_0 and 2% X_0 spectrum was computed. This operation will give rise to a significantly exaggerated pile-up, which Anthony *et al.* also discretely state. They circumvented the problem by comparing the edge-effect subtracted data to MC simulated curves having undergone the same manipulation.

◇ ◇ ◇

As seen above, compensating for a non-zero background can have greater implications on the resulting spectrum than simply to increase the resulting statistical errors. The outlined method of background compensation is widely used, and probably the best available. Nevertheless, it is important to be aware of its shortcomings as the effects can be severe.

CHAPTER 3

THE TSF EFFECT

3.1 Introduction

In Sec. 1.3, the LPM effect was discussed. If MCS is strong in the target ($\Delta t \gtrsim \ell_\gamma$), a suppression will occur when $\ell_{f0} \gtrsim \ell_\gamma$. Landau-Pomeranchuk-Migdal considered only semi-infinite targets, but for particle energies of $E_0 = 200$ GeV, the formation length of a 100 MeV photon becomes more than 600 μm long, as stated previously. In this case, *e.g.* a 30 micron thick target can clearly not be considered semi-infinite. By equating the target thickness Δt and ℓ_{f0}, a photon energy threshold, below which the formation length will stretch beyond the thin target, can be estimated

$$\hbar\omega \lesssim \hbar\omega_{\mathrm{TSF}} \equiv \frac{E_0}{1 + \dfrac{\Delta t}{2\gamma_{\mathrm{L}}\lambda\!\!\!^{-}_{\mathrm{c}}}}\,, \tag{3.1}$$

where $\lambda\!\!\!^{-}_{\mathrm{c}} = \hbar/mc = 386$ fm is the reduced Compton wavelength. This regime was first considered by Ternovskiĭ [Ter61] and later a classical theory for thin targets was developed by Shul'ga & Fomin (SF) [SF78, FS86, SF98b] giving name to the Ternovskiĭ-Shul'ga-Fomin (TSF) effect. For a fixed target thickness, the TSF photon energy dependence is very similar to that of the BH regime, *i.e.* it leads to an almost flat power spectrum, but the power spectrum averaged over electron scattering angles is reduced in magnitude by approximately [SF98b, Ugg06]

$$\kappa \equiv \frac{\langle dN_\gamma/d\ln\hbar\omega\rangle_{\mathrm{TSF}}}{\langle dN_\gamma/d\ln\hbar\omega\rangle_{\mathrm{BH}}} \simeq \frac{6\ell_\gamma}{\Delta t}\left[\ln\left(\frac{\Delta t}{\ell_\gamma}\right) - 1\right] < 1\,. \tag{3.2}$$

In a later paper [SF98a], SF included the corrections due to quantum recoil. Meanwhile, Baier & Katkov (BK) developed a full quantum theory of the LPM effect with Coulomb corrections, including emission in a thin foil [BK98]. Moreover, Blankenbecler & Drell (BD) [BD96] supplemented by a calculation based on their eikonal approximation to beamstrahlung phenomena. These three approaches will be presented and discussed in the following chapter, whence they will only be commented

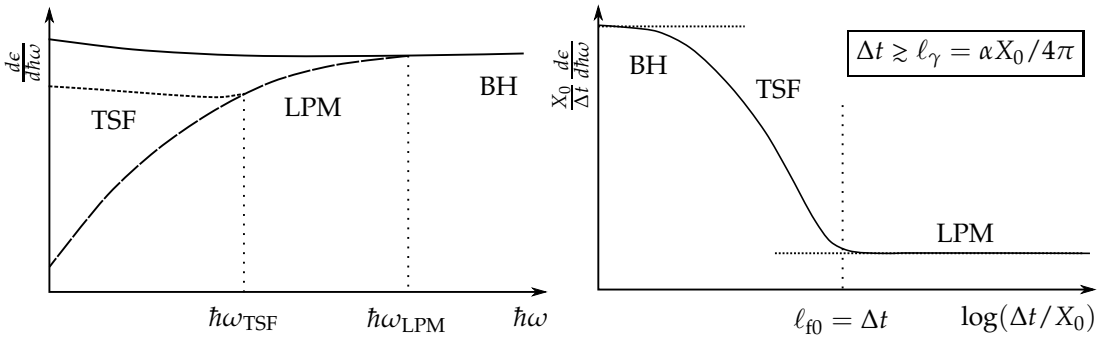

(a) Photon energy dependence of the bremsstrahlung power spectrum. The three regimes BH, LPM and TSF are shown.

(b) Thickness dependence of the bremsstrahlung power spectrum shown on a logarithmic abscissa. The TSF regime is seen to be a thickness transition from the BH to LPM regime. The ordinate is normalized by $\Delta t/X_0$.

Figure 3.1: Sketches of the single photon power spectrum level's dependence on $\hbar\omega$ and Δt. The TSF and LPM regimes are only reached if MCS is significant in the target, $\Delta t \gtrsim \ell_{\mathrm{f0}}$.

briefly here. They give almost identical results concerning radiation emission from thin foils, and common to them all is that the radiated intensity in the intermediate regime between BH and LPM becomes—for a fixed photon energy—a *logarithmic* function of the thickness, *i.e.* a major component of the power spectrum level is well-described by an expression of the type $\ln\left[\mathcal{L}(\Delta t')\right]$, where $\Delta t'$ is a scaled target thickness variable and $\mathcal{L}$ is a linear transformation performing scaling and/or translation. In Fig. 3.1a, the photon power spectrum is sketched in the three regimes BH, LPM and TSF. The ordinate axis displays the power spectrum level per number of primary particles $d\epsilon/d\hbar\omega = N_e^{-1} dN_\gamma/d\ln\hbar\omega = \Delta t \times n_n \times d\sigma/d\ln\hbar\omega$.

The alleviation of the LPM effect in the TSF regime has been observed in connection with experimental investigations of the LPM effect at SLAC by Anthony *et al.* [A$^+$97] where it turned out that these target boundary effects were important, see also [I]. Anthony *et al.* were limited by their maximum primary energy of 25 GeV, thus being able to see the effect only in their second-thinnest target (in units of X_0), a 0.7% X_0 gold foil[1]. Consequently, they could not establish the thickness dependence directly, but showed good agreement as a function of photon energy with the mentioned theories supporting logarithmic thickness dependence. In Fig. 3.1b, the power spectrum level normalized by $\Delta t/X_0$ is sketched as a function of thickness for a fixed photon energy. The TSF regime is here seen to be a transition between the two other where $d\epsilon/d\hbar\omega \propto \Delta t/X_0$. Because of the thickness normalization of the ordinate, the logarithmic, dominant component of the transition has the shape of $\ln\left[\mathcal{L}(\Delta t')\right]/\Delta t'$ in this figure.

Near the edge of the hypothetical strange quark stars, a layer of electrons reside, the electrosphere. The thickness of this layer is very small—of order $c/\omega_p \simeq 1$ pm due to the large plasma frequency of the quark matter. So far only the standard LPM theory has been applied to calculations of the bremsstrahlung radiation cooling of

[1] With the thinnest target, 0.1% X_0 gold, the ratio $\Delta t/\ell_\gamma$ was a mere 1.7, and MCS was thus not strong.

the star [J$^+$04, HC05], a problem where thin target corrections could be necessary. Regarding quarks, the TSF mechanism has also been considered in its QCD analogue, a gluon traversing a finite nucleus [KST99] during a heavy-ion collision. Here, a similar suppression phenomena was found, but it was discovered to be accompanied by an enhancing effect at larger gluon energies, probably due to the non-Abelian component of QCD.

This chapter will present a systematic study of the shape of the thickness dependence using 149 GeV electrons impinged on 16 targets with thicknesses in the range 0.03%–5% X_0. Within this range of thicknesses, for photon energies 0.2–3 GeV, the dependence of radiation intensity on thickness is shown to be a simple logarithmic dependence in the scattering region between the BH and LPM regimes.

3.2 The Target Assemblies

As discussed in Sec. 2.2, multi-photon and other calorimetric effects will influence the spectrum shape considerably even when using targets of only few percent radiation length. The thickness dependence of the power spectrum in the TSF regime—which can stretch several orders of magnitude, depending on E_0—should thus be adjusted by a complicated function describing multi-photon effects in the thickness range. The previously mentioned multiplicative shape modification function $f(\Delta t, \hbar\omega)$ describing multi-photon emission by BK [BK99b] is not directly applicable as it must be derived from the single photon spectrum, which itself changes with Δt. To avoid differences due to calorimetric effects with our targets, we considered in our experiment structured targets consisting of N_f foils, each of thickness δt. The total thickness was then given by $\Delta t = \sum \delta t = N_\mathrm{f} \times \langle \delta t \rangle$. When keeping the combined thickness in units of X_0 very similar in all target assemblies, the calorimetric correction would be the same.

Only targets with $\delta t \lesssim 5\%\ X_0$ have been considered here, since entering the TSF regime in the case of thicker targets would require extremely large values of E_0 or low values of $\hbar\omega$. Already at 5% X_0, $\ell_{\mathrm{f}0} \gtrsim \delta t$ requires $\hbar\omega \lesssim 164$ MeV at $E_0 = 149$ GeV $\left(y = 1.10 \times 10^{-3}\right)$, cf. Eq. (3.1), in the case of tantalum. Hence, with thicker targets the LPM regime will be predominant at typical accelerator and photon energies. Nevertheless, when turning to cosmic rays, the immense energies—beyond the reach of any terrestrial accelerator—could make the TSF effect relevant to much thicker targets.

The Target Foils

All targets consisted of a number of layers of disc-shaped foils of $\varnothing$ 25 mm and varying thickness δt and material. The number of layers in a target (N_f) was set such that the total target thickness Δt would correspond as closely as possible to 100 μm of tantalum $(2.44\%\ X_0)$. This choice of total thickness was a trade-off between obtaining an acceptable signal-to-background ratio and keeping multi-photon events at a minimum. The influence of the latter is already substantial $(\sim 20\%)$ at this thickness [Kle99, H$^+$04], as discussed in Sec. 2.2. Interference between adjacent foils was avoided by placing 1 mm precision steel ring spacers between neighbouring foils. Each spacer had a $\varnothing$ 18 mm concentric hole, hence the spacers in the assembly did not contribute to the target material in the beam accepted by $\mathtt{Sc1} \cdot \mathtt{Sc2} \cdot \overline{\mathtt{Sc3}}$,

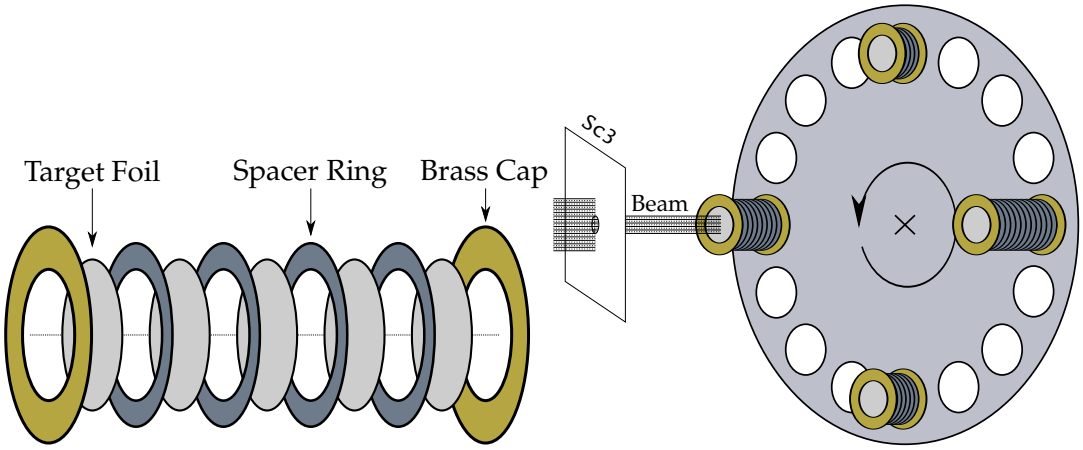

(a) Exploded view of a $N_f = 5$ target. The dotted line illustrates beam z-axis.

(b) Sketch of the target wheel. For simplicity, only four targets are shown mounted. The figure is generally not to scale, except for the beam width (selected by $\overline{\text{Sc3}}$) relative to the free target area in a target assembly.

Figure 3.2: Target assembly & target wheel.

cf. Fig. 2.1. The target assemblies were each held together by two brass end cap rings, which would be screwed tightly together. A drawing, showing an exploded view of the elements of a target assembly with $N_f = 5$ layers, is shown in Figure 3.2a. Having adjacent foils effectively separated by a gap $\delta g = 1$ mm of air, formation length related interference phenomena were excluded as long as $\ell_{f0} \lesssim \delta g$, corresponding to $\hbar\omega \gtrsim 34$ MeV using the 149 GeV beam, cf. Eq. (3.1). Under these circumstances, the radiation from the assembly will be the incoherent sum of the contribution from the N_f foils. The shape of the experimental power spectrum is thus that of a foil with thickness δt (and the power spectrum level is a factor N_f larger).

The target assemblies are in the following labelled by the nomenclature $N_f \times$ Aδt[μm]Bδg[μm], where A and B refer to the foil and gap material, respectively. An example could thus be $2 \times$ Ta50Air1000, corresponding to two Ta foils, each 50 μm thick, separated by 1 mm air.

The thicknesses of the many foils were carefully determined. With the thinner ones, this was done by measuring their weight and transverse dimensions, whereas the thicker ones could be measured directly with acceptable accuracy using a micrometer gauge. In this way, $\langle \delta t \rangle$ could be determined to $\simeq 1\%$, cf. Table 3.1. As seen here, all targets but one were assembled from tantalum, a relatively cheap, high Z material ($Z = 73$, $X_0^{\text{Ta}} = 4.094$ mm, $\ell_\gamma = 2.38$ μm). To have foils of very small thicknesses, $\delta t / X_0 \simeq 10^{-4}$, one would have to use extremely thin Ta foils ($\delta t \simeq 0.5$ μm) or choose a different material with a larger radiation length. We built a large aluminum ($Z = 13$, $X_0^{\text{Al}} = 88.97$ mm, $\ell_\gamma = 51.7$ μm) target $80 \times$ Al25Air1000 for this purpose. Since for each individual Al foil $\delta t \lesssim \ell_\gamma$, this target should belong to the BH regime and be a simple, good spectrum reference. The aluminum and tantalum foils were of 99.999% and 99.9% purity, respectively, according to the supplier (Goodfellow). There were some targets that differed considerably from the intent of having same total thickness—viz. $4 \times$ Ta30Air1000, $2 \times$ Ta75Air1000, $1 \times$ Ta125, $1 \times$ Ta150

Element	N_f	δt_{Nom} [μm]	$\langle \delta t \rangle_{Meas}$ [μm]	$N_f \times \langle \delta t \rangle_{Meas} / X_0$ [%]
Al	80	25.0±3.8	25.56±0.03	2.30±0.00
Ta	20	5.0±1.3	4.41±0.02	2.15±0.01
	17	6.0±1.5	5.94±0.08	2.47±0.03
	14	7.5±1.9	8.43±0.07	2.88±0.02
	11	9.0±2.3	8.03±0.11	2.16±0.03
	10	10.0±1.5	9.74±0.11	2.38±0.03
	8	12.5±1.9	11.7±0.2	2.30±0.03
	7	15.0±2.3	13.7±0.2	2.33±0.04
	4	25.0±3.8	26.3±0.3	2.57±0.03
	4	30.0±4.5	31.4±0.3	†3.07±0.03
	2	50.0±5.0	52.0±0.5	2.54±0.03
	2	75.0±7.5	74.1±0.7	†3.62±0.03
	1	100±10	107.8±1.5	2.63±0.04
	1	125±13	132.7±1.3	†3.24±0.03
	1	150±15	152.3±0.2	†3.72±0.01
	1	200±20	210.2±0.4	†5.14±0.01

Table 3.1: Nominal and measured foil thicknesses. The measured values are all within suppliers tolerances, which are listed as uncertainties on δt_{Nom}. The targets with thickness not consistent with 100 μm Ta are marked with a †.

and 1 × Ta200. There were also some smaller discrepancies in $N_f \times \langle \delta t \rangle / X_0$ due to supplier's tolerances, cf. Table 3.1.

The many targets were mounted at 16 positions forming a concentric circle of 100 mm radius on a target wheel, which allowed a remote-controlled target change by an azimuthal turn of the wheel, cf. Figure 3.2b. The angular position could be set and read back with a precision of a thousandth of a degree corresponding to 1.7 μm arc length, far beyond our need of azimuthal alignment. The target-wheel was placed about 10 cm from $\overline{\texttt{Sc3}}$.

3.3 Analysis

The BGO Background

At the experiment, considerable beam time was dedicated to empty target measurements on a target holder with a few spacer rings but no foils. This was done at the two primary energies $E_0 = 149.053\ (149)$ GeV and 207.519 (207) GeV. In the following, the shortened values will be used as reference to the beam energies. The experimental background power spectra per triggering event $d\epsilon/d\hbar\omega$ can be seen in Figure 3.3. The backgrounds clearly contain a structure which grows close to exponentially when going to lower photon energies. The onset of the structure scales roughly with the characteristic frequencies of SR $\omega_c^{207}/\omega_c^{149} = 1.94$. Compare also the background spectrum's shape with Figure 2.8a on page 28. The lower photon energy detection limit is chosen as this onset of SR, $\simeq$ 200 MeV ($\simeq$ 300 MeV) at

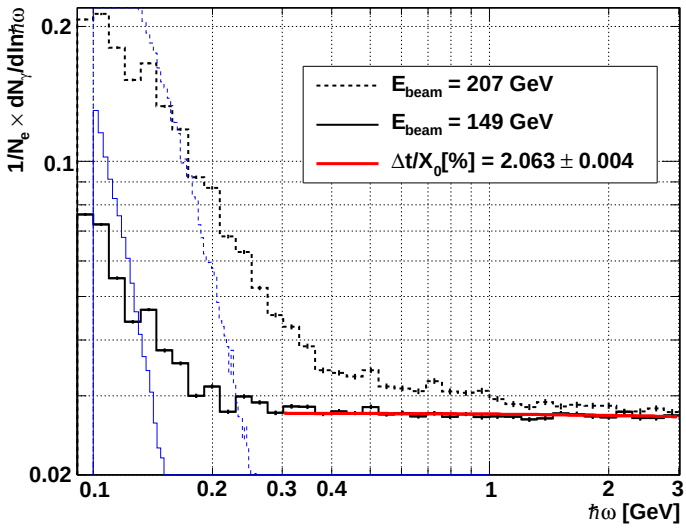

Figure 3.3: BGO Backgrounds. Black lines are experimental data measured on empty target holders, and blue lines are Geant4 simulations of synchrotron radiation generated in `B16` at the two beam energies.

$E_0 = 149$ GeV (207 GeV). The backgrounds per electron reach the same level at higher photon energies in accordance with BH, Eq. (1.16)—a reassuring feature.

The low energy region is besides SR also best avoided by reason of two relatively low-energy effects—the Ter-Mikaelian (TM) effect and Transition Radiation (TR). The TM effect will set in from $\hbar\omega \lesssim \hbar\omega_{\mathrm{TM}} = 21.5\ (30.0)$ MeV at $E_0 = 149$ GeV (207 GeV) and cause a heavy suppression. Although the TR yield is augmented by using structured targets, this effect shares the upper threshold of $\gamma\hbar\omega_p$ with the TM effect and is thus also negligible at $\hbar\omega \gtrsim 200$ MeV.

The Bethe-Heitler expression, Eq. (1.16), is fitted to the 149 GeV background in the energy interval 0.3–3 GeV, where SR should be negligible. In this manner, the background is found to correspond to the radiation from a 2.06% X_0 radiator. The fit is shown with a red, solid line in Figure 3.3. With such low energy bremsstrahlung photons from a high energy beam, the LPM-suppression and pile-up effects could have set in, subsequently rendering expression (1.16) somewhat inappropriate in this region. Nevertheless, this level is in good accordance with backgrounds found in previous experiments with a similar setup [H$^+$04]. An inevitable part of this is due to the scintillators `Sc1` and `Sc2` before `B16` (cf. Figure 2.1 on page 15) which contribute to the photon background. Their combined thickness corresponds to $\Delta t \simeq 0.9\%\ X_0$.

The BGO Efficiency

The BGO was vital in our experiment to detect photons of energies down to 200 MeV, ($y \simeq 10^{-3}$). During the preliminary tests of the BGO, cf. the ASTRID calibration discussed in Sec. 2.5, it was found to be well suited for this task. Nevertheless, we have found on several occasions that running this relatively low-energy calorimeter in the high energy experiment area at CERN is not an easy task. Firstly, at the low relative

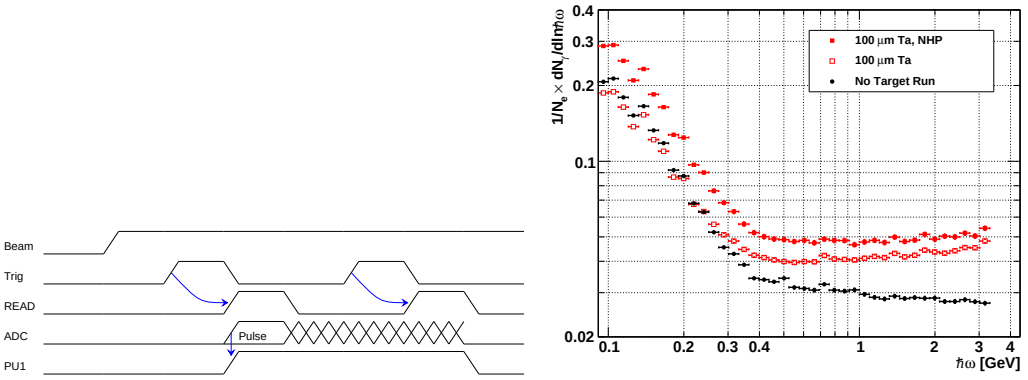

(a) NHP logics sketched. The first event (Trig) is a large pulse, which causes the analog PMT signal to enter an undefined state. PU1 tags the possible, subsequent events, that are considered flawed.

(b) NHP Analysis. By comparing the square datapoints, rejecting events following large pulses is seen to clearly change the level of the raw power spectra.

Figure 3.4: Results of applying the NHP condition.

photon energies, both SR contamination and the accentuation of pile-up, discussed in Sec. 2.6, can change the measured spectrum a great deal. Secondly, the hard radiation of energies up to the electron beam's energy $\hbar\omega \sim E_0 = 149$ GeV should at least cause a deviation from linearity by heavy leakage. In addition, the large calorimeter photon shower generated by a very high-energy photon could completely drain the PMT, subsequently leaving the detector inefficient for some time. We saw indications of the BGO running with an overall reduced efficiency due to PMT overloads, although the High Voltage (HV) of the BGO was lowered as described in Sec. 2.5.

An examination of the latter effect was attempted by setting up a Pattern Unit (PU) in the CAMAC data acquisition system which would mark the events following ≤ 200 μs after a very high pulse from the PMT—the logics are sketched in Figure 3.4a. In this way, a No High Pulse (NHP) condition could be set in the off-line analysis. Figure 3.4b shows raw power spectra that are normalized to the number of particle triggers in the respective spectra. Of special interest in this figure is a comparison of the red, open (no pattern condition) and filled squares (NHP condition). Applying the condition clearly has an effect on the level of the power spectrum. In this case, the raw spectrum level is raised by $\lesssim 25\%$ by applying the condition.

A refined version of the proper GEANT3 implementation of bremsstrahlung described in [MBSU08] (including BH with electronic contribution and Coulomb correction [Tsa74, Eq. (3.83)] and Migdal's LPM formulation [Mig56]) was used to perform MC simulations of the experiment including solid angle of the detector, pair production in air and foil, multi-photon emission and other relevant, physical processes, but not the SR[2]. The BGO efficiency $\mathcal{E}(\hbar\omega)$ was analytically examined by comparing such a simulation with the BCPS of the Al reference target, cf. Table 3.1. In Figure 3.5, such BCPS normalized to target thickness $(\Delta t / X_0)$ are shown as points with error bars illustrating statistical errors only. The uncorrected power spectrum

[2]I am very grateful to Alessio Mangiarotti (Universidade de Coimbra, Portugal) for maintaining the code and performing the simulations on request.

(red squares) is seen to be some $\simeq$ 20–40% below the GEANT3 simulation. In previous experiments, good agreement between the simulations and experiment has been found [H$^+$04, MBSU08], whence the discrepancy is believed to originate mainly from three sources. Firstly, the background compensation will exaggerate the multi-photon effect to a degree primarily depending on the constant background radiator level. Secondly, hard radiation from the more energetic photons are believed to have drained the PMT, thus leaving it incapable of delivering power for the pulse from the subsequent particle. Thirdly, as described in more detail in [II], it was found in the offline analysis that the primary electron beam was only of $\gtrsim$ 90% purity while the $\lesssim$ 10% other particles exhibited Lead Glass energy deposits typical of μ^- and π^-, ionization energy loss and nuclear showers, respectively. The purity of the beam is usually better at the SPS, and we suspect an imperfect setting of the beam filter mode optics to be the cause of this. The spectra should ideally be normalized by the actual number of radiating particles (e^-), and when normalizing by the number of triggering particles (e^-, μ^- and π^-), the overall norm of the power spectrum is erroneously lowered by the purity of the beam. We believe the beam purity was constant during the beam time, since the beam settings were left untouched after data accumulation began.

Although the mentioned sources, which all generally lower the BGO power spectra, are of very different origin, I will refer to the overall problem and correction as the BGO efficiency. Since the sources of the inefficiency should remain constant throughout the steady beam and background conditions, a time-independent correction should be attainable. The BGO efficiency and beam purity is presumed to be well-described by a quadratic polynomial of photon energy above the SR kink

$$\mathcal{E}(\hbar\omega) = a + b \times \hbar\omega/\mathrm{GeV} + c \times \left(\hbar\omega/\mathrm{GeV}\right)^2 . \tag{3.3}$$

The BCPS divided by such a model are matched to the GEANT3 simulation within the photon energy region marked in Figure 3.5 by minimizing a χ^2-statistic. Notice how the spectrum dives towards zero when $\hbar\omega \lesssim 200$ MeV, indicating an increasing SR contamination below this point. The obtained model parameters a–c along with a plot of the fitted efficiency and the 95% confidence interval from the fit can also be seen in this figure, where the data and $\mathcal{E}$ share ordinate. The efficiency should be applicable to spectra of targets of almost equal thickness. The BGO temperature was monitored during the experiment and only very small deviations were found ($\lesssim 1$ K), and thus not corrected for.

3.4 Results

The Power Spectra

The BCPS are efficiency-corrected and normalized to the measured values of $\Delta t/X_0$. The spectra can be seen in Fig. 3.6a–3.6d on page 42. The spectra tend to mutually converge at large photon energies, giving good trust in the quality of the respective normalizations of the spectra. At lower photon energies, where the formation length ℓ_{f0} grows, the power spectra tend toward levels seemingly dependent on the foil thickness δt. They clearly have different shapes, although the targets all have approximately the same total thickness in units of radiation lengths $\Delta t/X_0 \simeq 2.44\% \sim$

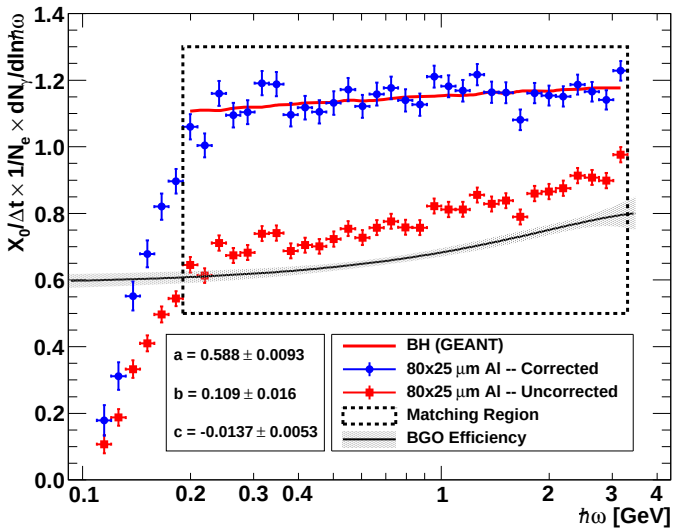

Figure 3.5: BGO efficiency correction. A relatively flat polynomial can bring the datapoints in good agreement with simulations above 0.2 GeV.

$1 \times$ Ta100. For each target geometry, a theoretical curve—based on the Blankenbecler & Drell (BD) formalism [BD96]—is shown. As discussed in Sec. 2.2, any single-photon emission based theory (such as the BD formalism) should be corrected to take multi-photon and pair production into account, even for the thin targets used. Such a shape-correcting function could have been estimated by MC studies. Instead, the theoretical curves have been scaled by a factor 0.85. The quality of this correction will be discussed later.

The power spectra almost all tend to have a kink around $\hbar\omega \simeq 0.3$ GeV, below which the datapoints seem to be systematically lower than the theory curves. This could be caused by a still present contamination of SR, which would be more predominant in the background spectrum, hence cause an overestimation of the background. The lower detection threshold is thus taken to be $\hbar\omega \simeq 0.3$ GeV.

The power spectrum level's outlined dependence on δt is in the following examined by plotting the level as a function of $\delta t / X_0$, photon bin by bin. To quantify the data's logarithmic resemblance in the TSF regime, the data is compared with a simple logarithmic expression of the form $\ln\left[\mathcal{L}(\Delta t')\right]$. The next section is devoted to give a short discussion of construction and behaviour of such an expression.

The Semi-Empirical Logarithmic Expression

Before setting about with a logarithmic thickness dependence, the reader is reminded that the BH power spectrum per electron for a foil of thickness δt has the following appearance in the soft photon limit $(y \ll 1)$

$$\frac{1}{N_e}\frac{dN_\gamma}{d\ln\hbar\omega} \simeq \frac{4}{3}\frac{\delta t}{X_0} \qquad y \ll 1\,, \tag{3.4}$$

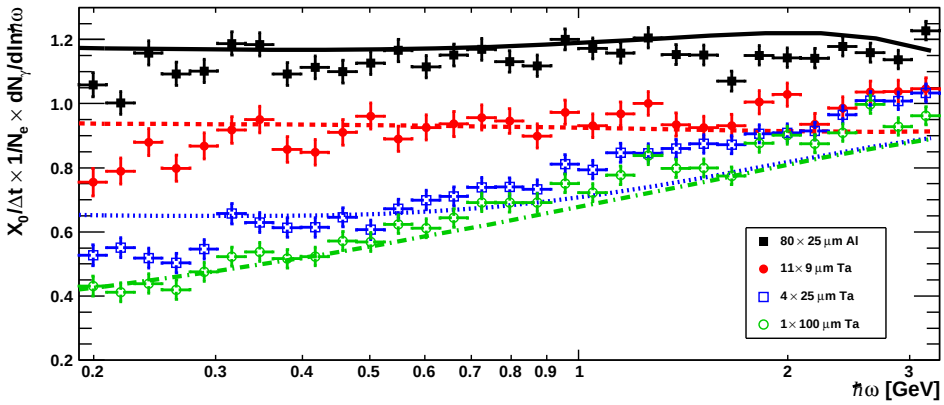

(a)

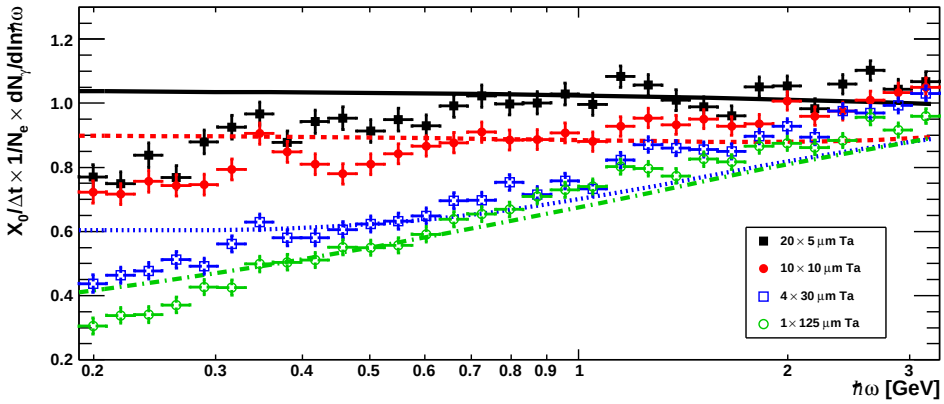

(b)

Figure 3.6

i.e. linearly dependent on the foil thickness, cf. Eq. (1.16). One can devise a simple logarithmic power spectrum description which converges properly to the BH limit

$$\frac{1}{N_e}\frac{dN_\gamma}{d\ln\hbar\omega}\bigg|_1 = a\frac{\delta t}{X_0} \times \frac{\ln(b\times\delta t+1)}{b\times\delta t}\,, \tag{3.5}$$

where the subscript indicates the number of independent foils being considered. The right-hand-side (RHS) will converge towards $a \times \delta t/X_0$ as $\delta t \to 0$. By comparing with the left-hand-side (LHS), the factor a is thus seen to represent the unitless value of the BH power spectrum normalized to thickness $(\delta t/X_0)$ and number of particles (N_e). This factor is of order unity—4/3 in the BH case—and slightly dependent on $\hbar\omega$. The constant b describes the rate at which the thickness normalized power spectrum level decreases with thickness—*i.e.* at $\delta t = 1/b$ the power spectrum is reduced by a factor $\ln(2)$ compared to the BH value a. Both sides of the equation above are unitless, while b has dimension of inverse length. When considering an assembly of N_f foils, the contributions from each foil add incoherently (if interference

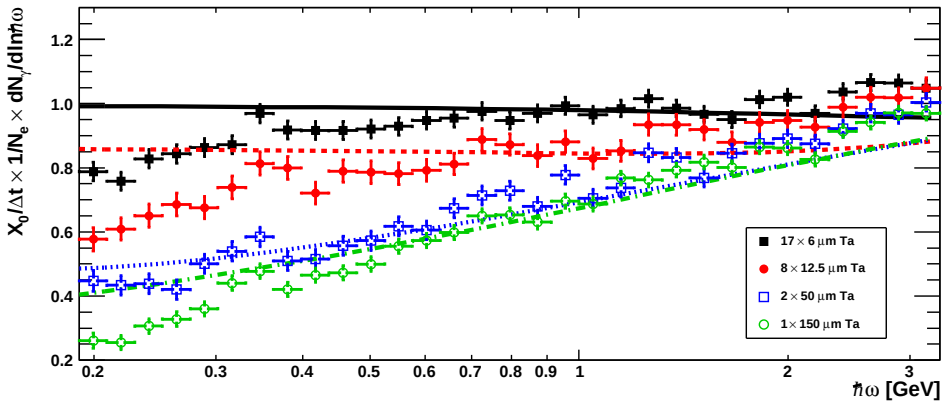

(c)

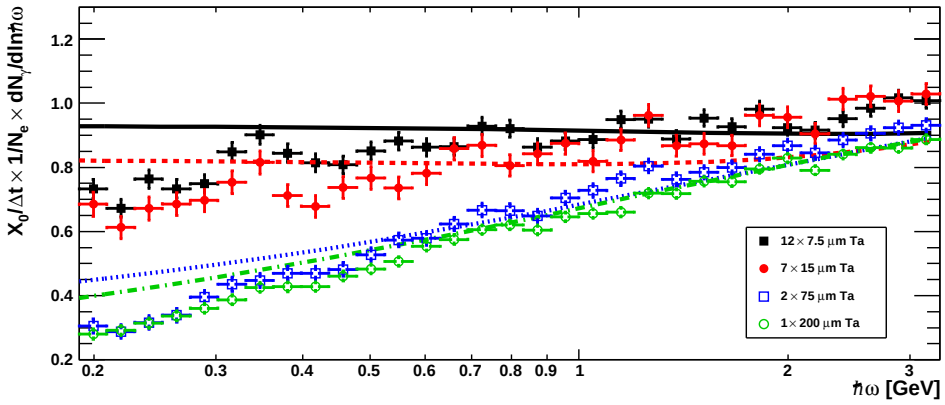

(d)

Continued Figure 3.6: The datapoints show the number of photons emitted N_γ in a logarithmically binned interval of photon energies (25 bins/decade) for various targets of the type $N_\mathrm{f} \times \mathrm{A}\delta t\mathrm{Air1000}$. The resulting power spectrum compensated by background, corrected with the BGO efficiency and normalized to both the number of events N_e and the combined target thickness in units of the material's radiation length $\Delta t / X_0$. The lines show calculations of the power spectrum of each target using the Blankenbecler-Drell formalism [BD96].

effects are negligible), and the thickness is replaced with average thickness $\delta t \to \langle \delta t \rangle$

$$\frac{1}{N_e}\frac{dN_\gamma}{d\ln\hbar\omega}\bigg|_{N_\mathrm{f}} = N_\mathrm{f} \times \frac{1}{N_e}\frac{dN_\gamma}{d\ln\hbar\omega}\bigg|_{1}$$

Dividing by the total target thickness in units of X_0, and employing $\Delta t = \sum \delta t = N_\mathrm{f}\langle\delta t\rangle$

$$\begin{aligned}\frac{X_0}{\Delta t}\frac{1}{N_e}\frac{dN_\gamma}{d\ln\hbar\omega}\bigg|_{N_\mathrm{f}} &= a \times \frac{N_\mathrm{f}\langle\delta t\rangle}{\Delta t} \times \frac{\ln(b\times\langle\delta t\rangle + 1)}{b\times\langle\delta t\rangle} \\ &= a \times \frac{\ln(b\times\langle\delta t\rangle + 1)}{b\times\langle\delta t\rangle}\,. \end{aligned} \tag{3.6}$$

The quality of this semi-empirical logarithmic expression is discussed more thoroughly in Sec. 4.4, where it is also shown to be the major component of the theory for thin foils in [Bla97b], from which an expression for the value of b is found

$$b_{\mathrm{B}} = \frac{2\pi}{3\alpha X_0} = \left(6\ell_\gamma\right)^{-1} \simeq 287/X_0 \,. \tag{3.7}$$

This characteristic length scale $6\ell_\gamma$ is also present in the asymptotic expression of Eq. (3.2), also describing the thickness dependence relative to the BH value. The simple expression also closely approximates (accuracy $\lesssim 3\%$) the much more complex theoretical expression [SF98b, Eq. (4.9)], and $b_{\mathrm{SF}} = 319/X_0$ is found by fitting Eq. (3.6) to their data curve.

The Thickness Dependence

In Fig. 3.7a–3.7e, the power spectrum level is plotted as a function of foil thickness in units of X_0 for a selected range of photon bin centers. All of the numerous figures showing the thickness dependence of the power spectrum for fixed photon energy can be inspected in [II] but have also been compiled into an animation which can be found online[3]. Notice the resemblance between Figure 3.7 and the sketch of the anticipated thickness dependence shown in Figure 3.1b on page 34.

The data is compared with the GEANT3 simulation of the BH and LPM level (shown as horizontal lines) for $1 \times$ Ta100 at the corresponding value of $\hbar\omega$. The data is also compared with numerous theoretical models, all of which are presented and discussed in Chapter 4 and are here only mentioned for reference. The numerically implemented models include Baier & Katkov (BK) Eq. (5.15) with (5.12) of [BK98] (red, full line), Shul'ga & Fomin (SF) Eq. (4.9) [SF98b] (red, dashed line)[4] and Blankenbecler & Drell (BD) [BD96] (green, dotted line). All models are capable of calculating the modification of the BH spectrum at many different target thicknesses, although the original work by SF supplies an expression only valid in the TSF regime, whence it is only displayed above the LPM level, in accordance with SF's approach [SF98b]. Also, the implemented, asymptotic BK expression is only valid for targets of "intermediate" thickness, whence the curve is only shown for $\delta t/X_0 \gtrsim 10^{-3}$. As the photon energy increases, the formation length decreases, and more target thicknesses enter the LPM regime, as $\delta t \gtrsim \ell_{\mathrm{f0}} \gg \ell_\gamma$.

The hitherto listed theories only consider single-photon emission, but multi-photon emission has a considerable effect on the photon spectrum, even at the thin foils we have considered experimentally, rendering the theories somewhat inappropriate. In consequence, the level of all the theoretical curves have been scaled with an overall factor of 0.85 to account for the calorimetric effect. The quality of this theoretical correction is discussed in Sec. 4.1. I stress again that pile-up (multi-photon) effects will to first order depend on the *total* target thickness $(\Delta t/X_0)$—not $\langle \delta t \rangle / X_0$, which is shown on the abscissa. The diamond shaped datapoints in Figure 3.7 mark the Ta targets with a thickness deviating noticably from $1 \times$ Ta100 $(\Delta t/X_0 \gtrsim 1.2 \times 2.44\%)$. These are seen to lie significantly lower than both the LPM simulations and the neighboring datapoints. This deviation is partly explained by multi-photons, which

[3] `http://www.phys.au.dk/~ulrik/tsf_animation.gif`

[4] This curve was calculated using a Mathcad implementation by U.I. Uggerhøj. I am very grateful for his work with implementing and debugging the code (with the help of S.P. Fomin).

give a reduction of 13–15% at 200 μm thickness compared to 100 μm Ta for which the simulations have been performed.

The simple, logarithmic model in Eq. (3.6) has been utilized to quantify the data's logarithmic resemblance. In each of the thirty photon energy bins from 0.2–3 GeV, a least-squares fit with the model has been performed. In each fit, the parameter a is fixed to the GEANT3 simulated value of the BH level. Since the model does not include the LPM effect, the fit is only performed to the datapoints with δt below the crossing point of the LPM curve and the theoretical curve of SF [SF98b], close to the condition $\delta t = \ell_{f0}$. The values of b extracted from the fit, shown in Figure 3.8, are in fair agreement with the expected theoretical value, and therefore almost the entire data set of 30 logarithmic bins in photon energy is well described by the same simple logarithmic function.

At the very lowest photon energies above the detection threshold, the datapoints in Figure 3.7a are seen to be systematically lower than the theory curves, as previously noted in the power spectra, Fig. 3.6a–3.6d. At $\hbar\omega \lesssim 0.3$ GeV, this effect results in a systematically larger value of b, since a is fixed to the simulated BH level. At $\hbar\omega \gtrsim 2.2$ GeV only one or two datapoints contribute to the fit making its credibility questionable. The discrepancy with theory at high photon energies may also be due to the total uncertainty in the detection efficiency, which we estimate to be about 5% in the interval 0.3–2.2 GeV (filled squares), *i.e.* there is a systematic uncertainty of about the same size as the statistical. Outside this range, the BGO calibration has a systematic uncertainty at least about twice as large (open squares). The systematic errors should be estimated better through studies of toy MC data that have undergone the manipulations of our analysis, as demonstrated in Sec. 2.6. This has not been performed here, and only statistical errors are shown in the plots.

◇ ◇ ◇

With the methods and results presented above, the general trends of the theoretical models are verified. The magnitude of experimental uncertainties (systematic and statistical) compared to the modest mutual discrepancies of the different theoretical models renders it difficult to discern the quality of the theories. It was shown that a very simple semi-empirical logarithmic expression containing only one parameter can explain the power spectrum's thickness dependence relative to the corresponding BH level at $\delta t \to 0$ with proper convergence in this limit. The shape-determining parameter b is found—within the statistical and systematic errors—moderately constant over almost an order of magnitude in photon energy and also in good accordance with corresponding values extracted from [SF98b] and [Bla97b].

In the following chapter, a more thorough discussion of the mentioned theoretical models and the semi-empirical logarithmic expression is given.

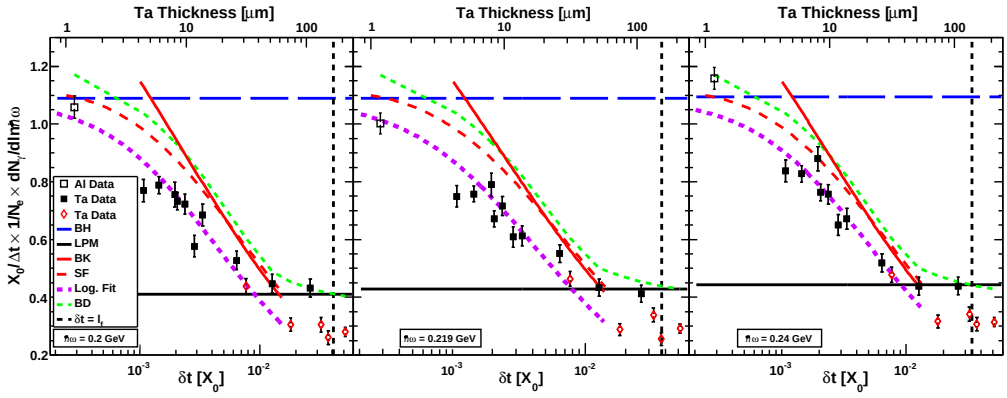

(a)

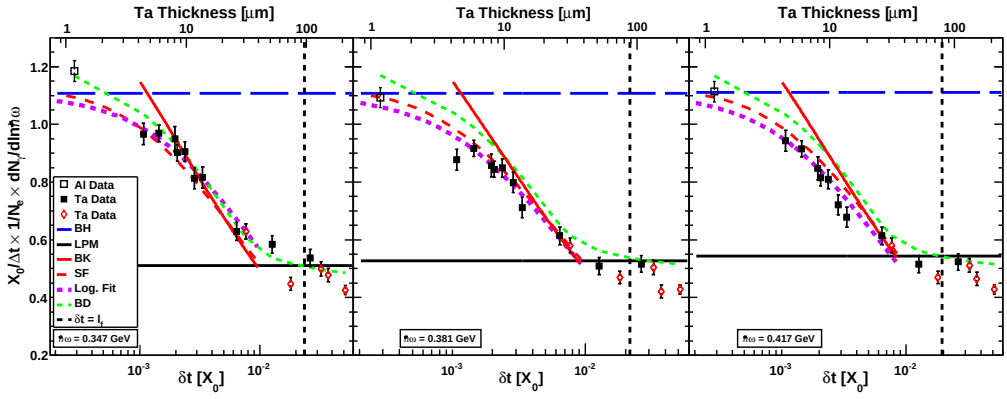

(b)

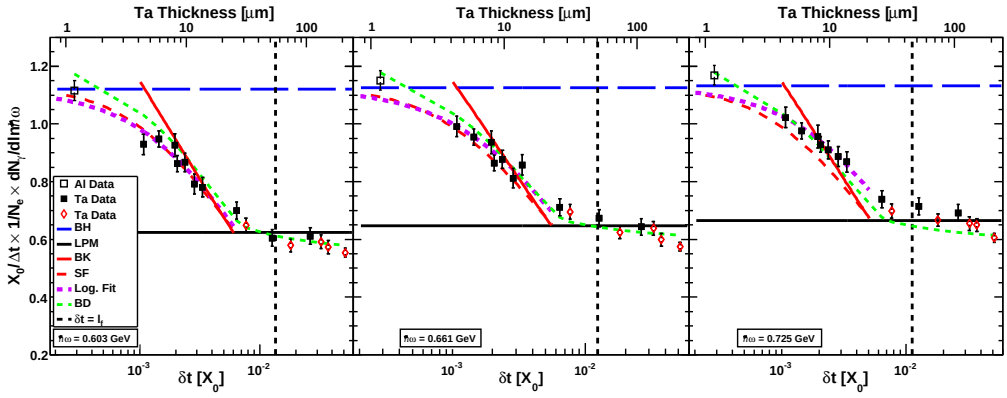

(c)

Figure 3.7

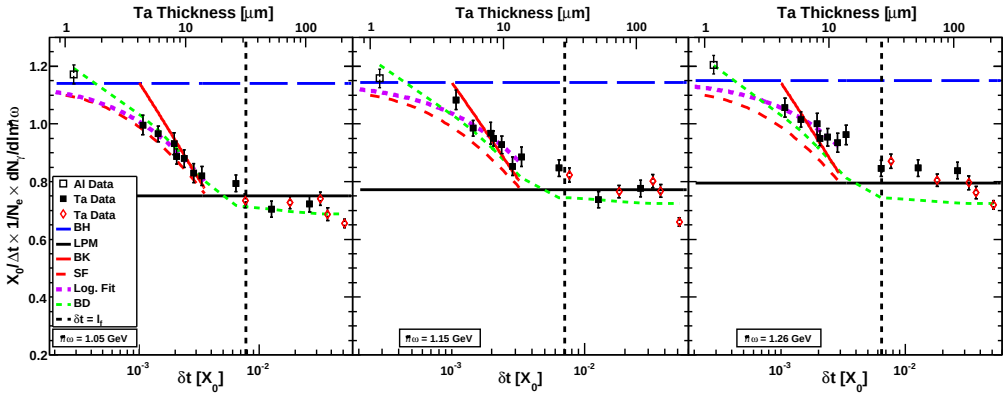

(d)

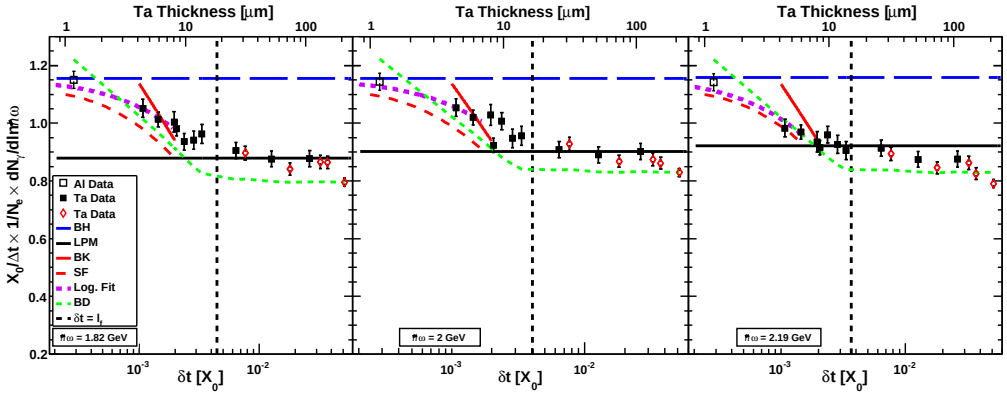

(e)

Continued Figure 3.7: The normalized power spectrum level as a function of the independent foil thickness ($\langle \delta t \rangle$ in units of X_0 on lower scale, equivalent tantalum foil thickness on upper scale) in the different photon energy bins with the centroid value given. With squares and diamonds are shown the measured values with error bars denoting the statistical uncertainty only. The open, square datapoint at $\delta t = 3 \cdot 10^{-4}$ is for the 80×25 μm Al target, while the open, diamond datapoints are for the targets with $\Delta t / X_0 \gtrsim 1.2 \times 2.44\%$—*i.e.* not quite comparable to 100 μm Ta. The horizontal lines are the GEANT3 simulated values for 100 μm Ta according to BH (long-dashed line) and LPM theory (full line) [MBSU08]. The descending curves are calculations of the logarithmic dependence of intensity on thickness (which decreases when divided by the thickness) following [SF98b] (long-dashed), [BK98] (full), [BD96] (dashed) and the function in Eq. (3.6) (dotted). The vertical dashed line shows the thickness corresponding to the formation length, *i.e.* the critical thickness for the given photon energy.

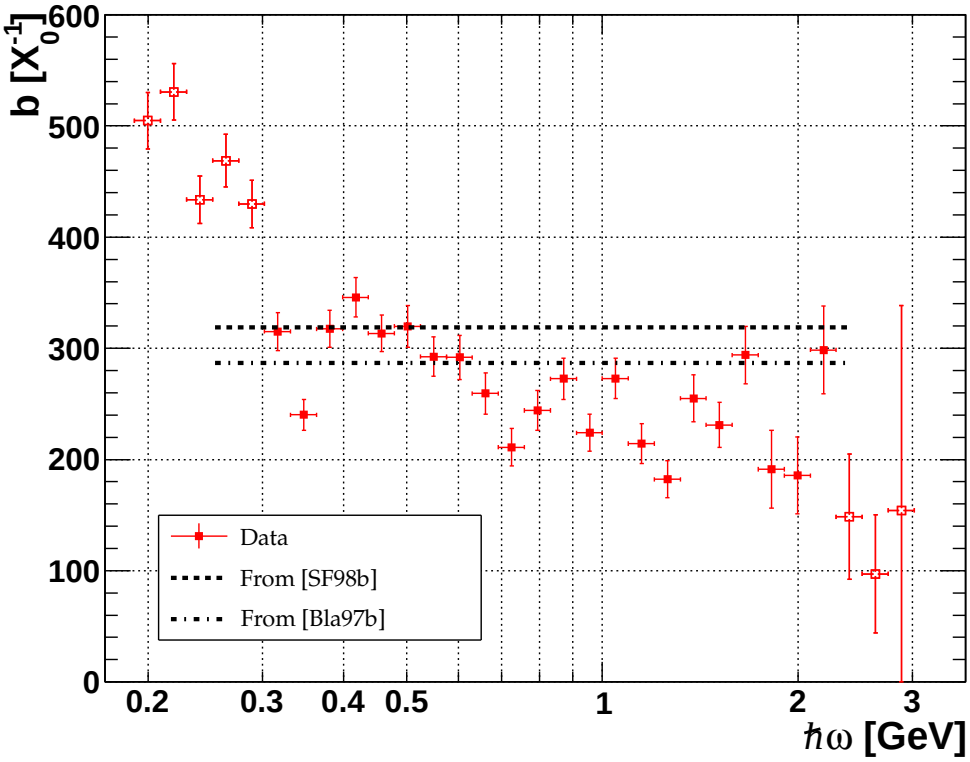

Figure 3.8: The b parameter extracted from least-squares fits with the logarithmic function $a\ln(b \times \langle \delta t \rangle + 1)/(b \times \langle \delta t \rangle)$, as a function of photon energy. The horizontal lines show the value of b estimated from [SF98b] and the leading order value found from [Bla97b, Eq. (30)], shown in Eq. (3.7), page 44. Systematic uncertainties are estimated to be $\simeq 5\%$ (filled points) and $\simeq 10\%$ (open points).

CHAPTER 4

THEORETICAL APPROACHES TO BREMSSTRAHLUNG FROM THIN TARGETS

In the wake of the experimental LPM study of Anthony *et al.* [A$^+$95, A$^+$96a, A$^+$97], many theoretical models [Zak96, BD96, BK98] were developed to explain the data to adequate accuracy. Most of the models are also able to calculate the radiation yield from a general target geometry, *i.e.* also thin foils or a structured target. The next sections will present the ideas and results of the methods in no prioritized order.

In this chapter, I will for simplicity refer to a single foil of thickness Δt, not the structured target presented in Chapter 3, unless explicit details regarding the latter are discussed.

4.1 Baier & Katkov

In [BK98], Baier & Katkov (BK) set off to treat LPM suppression due to multiple scattering to a precision within a few percent. To reach this goal, they include polarization of the medium (the TM effect), a nuclear form factor relevant for impact parameters smaller than the nuclear size, $R_A \simeq 1.2 \text{ fm} \times A^{1/3}$ [Dun04] and a modified screening distance including Coulomb corrections

$$a_2 = \underbrace{0.81 a_0 Z^{-1/3}}_{\simeq a_{\text{TF}}} \exp\left[0.5 - f_{\text{DBM}}\left([Z\alpha]^2\right)\right], \tag{4.1}$$

where $f_{\text{DBM}}(z)$ is the Coulomb correction from [Tsa74], cf. Eq. (1.13), a_{TF} is the Thomas-Fermi radius [BJ03] and $a_0 = \lambda\!\!\!^{-}_{\text{c}}/\alpha = 0.529$ Å is the Bohr radius. The electron state propagator is initially found for a screened Coulomb potential in the Born approximation and then expanded perturbatively [Kle99]. Going through a number of variable changes, they consider various thickness regimes with favorable outcome. Regarding thin targets ($\ell_{\text{f0}} \gtrsim \Delta t$), they find convergence to the Bethe-Heitler result, if MCS is not relevant ($\ell_\gamma \gg \ell_{\text{f0}}$). On the other hand, if MCS *is* relevant, the power

spectrum normalized to the number of electrons can be written as

$$\frac{1}{N_e}\frac{dN_\gamma}{d\ln\hbar\omega} = \frac{\alpha}{\pi}\left(r_1 + r_2 \times J\right) \tag{4.2a}$$

$$r_1 = \left(\frac{\hbar\omega}{E_0}\right)^2 \qquad r_2 = 1 + \left(\frac{E_0 - \hbar\omega}{E_0}\right)^2 . \tag{4.2b}$$

where

$$J = 2\int_0^\infty \varrho d\varrho K_1^2(\varrho)\left\{1 - \exp\left[-k\varrho^2\left(1 - \frac{1}{L_t}\ln\frac{\varrho^2}{\varrho_t^2}\right)\right]\right\} \tag{4.3a}$$

$$L_t = 2\ln\frac{2a_2}{\lambda\!\!\!^{-}_c\varrho_t} - C \tag{4.3b}$$

where K_ν is the modified Bessel function of the second kind and order ν, $\varrho_t = 1$ is the minimum impact parameter in units of the Compton wavelength, and $C = 0.577\ldots$ is the Euler-Mascheroni constant. The function J is approximated by [BK98, Eq. (5.12)]

$$J = J_1 + J_2$$

$$J_1 = \frac{1}{k}\int_0^\infty \left[K_0\left(\sqrt{\frac{z}{k}}\right)K_2\left(\sqrt{\frac{z}{k}}\right) - K_1^2\left(\sqrt{\frac{z}{k}}\right)\right]\exp(-z)z\,dz \tag{4.4a}$$

$$J_2 = -\frac{1}{kL_t}\int_0^\infty K_1^2\left(\sqrt{\frac{z}{k}}\right)\exp(-z)\ln(z)z\,dz\,. \tag{4.4b}$$

Here, $k = \pi n_n (Z\alpha\hbar c/mc^2)^2 L_t \Delta t$ and n_n is the target's density of atoms. They further approximate the expressions to [BK98, Eq. (5.13)]

$$J_1 + J_2 = \left(1 + \frac{1}{2k}\right)[\ln(4k) - C] + \frac{1}{2k} - 1 + \frac{C}{L_t}\,. \tag{4.5}$$

The two expressions have been implemented, and their numerical evaluation as a function of the target thickness Δt in units of the radiation length X_0 can be seen in Fig. 4.1. Firstly, their Eq. (5.13) is seen to have a limited applicability within the shown range of thicknesses. Secondly, their more accurate Eq. (5.12) is seen to overshoot the Bethe-Heitler level at very small values of Δt.

Spencer Klein later reminded BK that multi-photon emission is indeed relevant even at the thin targets considered. This calorithmic effect changes the single-photon spectrum shape. This weakness of [BK98] was later remedied in [BK99b]. Here, BK describes multi-photon effects for soft photons ($y \ll 1$) in various foil thickness regimes [BK99b]. The correction is in each case described by a multiplicative function $f(\Delta t, \hbar\omega)$, which is calculated from the single-photon emission probability. The magnitude and dependence on photon energy will thus generally change with target thickness. Implementation of BK's multi-photon correction is only feasible using asymptotic expressions in the various thickness regimes in which the correction factors are slightly different, rendering a calculation over our range of thicknesses somewhat troublesome.

In Fig. 4.2a, the multi-photon correction in the LPM regime is plotted [BK99b, Eq. (2.27)]. As can be seen here, the correction to their single-photon expression

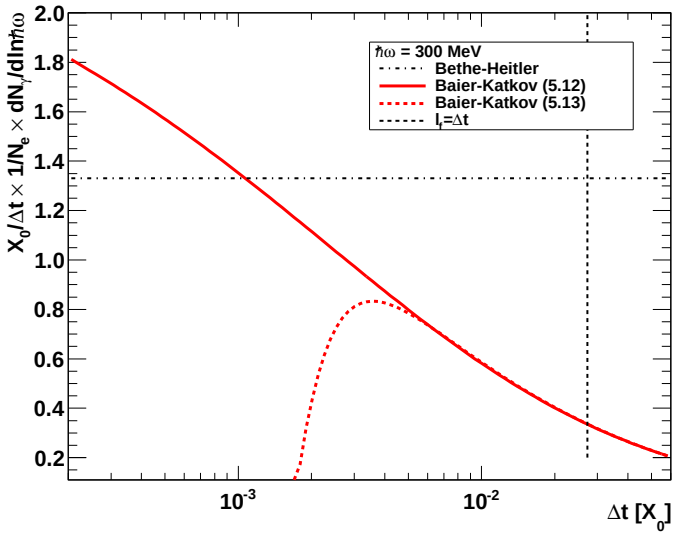

Figure 4.1: Calculations of the thickness dependence of the power spectrum level in the limit $\ell_{f0} \gg \Delta t$. The full line is based on [BK98, Eq. (5.12)], while the dashed line is an approximation [BK98, Eq. (5.13)]. The exact expression is seen to overshoot the simple BH level (horizontal dash-dotted line). The vertical dashed line marks the condition $\ell_{f0} = \Delta t$ for $E_0 = 149$ GeV.

depends very much on the total target thickness. The correction is by nature also photon energy dependent. The correction for 100 μm tantalum $(2.44\%\ X_0)$ is seen to be some 85%–90% of the single-photon spectrum level in the shown photon energy range. As discussed in Sec. 2.2, one should treat secondary bremsstrahlung photon emission and pair production of the initial photon on an almost equal footing, whence the BK multi-photon correction is probably too conservative to describe the full calorimetric correction. Because of this issue, the single-photon theoretical curves presented in Figure 3.7 on page 47 were *not* corrected by the BK's function function $f(\Delta t, \hbar\omega)$ but simply by multiplying their level by a smaller constant of 85%—hence ignoring the dependence on $\hbar\omega$. The magnitude of the constant was chosen by demanding the corrected theories in best accordance with the BH GEANT3 simulations at $\delta t \to 0$. Utilizing such a simple correction is not uncommon, cf. for instance [Zak96] in which Zakharov found good agreement between the 0.7% X_0 Au target data of [A$^+$95] and his calculations, when multiplying the latter by an arbitrary factor of 0.93, probably also due to calorimetric effects. As seen in Figure 4.2a, a small, relative difference $\simeq$ 8% has been neglected with the simple correction applied. The simple correction adds to the systematic uncertainty of the theoretical curves shown in Figure 3.7.

The BGO efficiency correction applied to the experimental data was found by comparing the BH 80 × Al25Air1000 spectrum to simulations. It was assumed to be applicable to other spectra from targets of equal thickness in units of X_0 measured under the same background conditions. The differently shaped power spectra (BH, LPM or TSF) will, however, slightly change the multi-photon effect. The quality of the BGO correction could be further examined from MC simulations taking this into

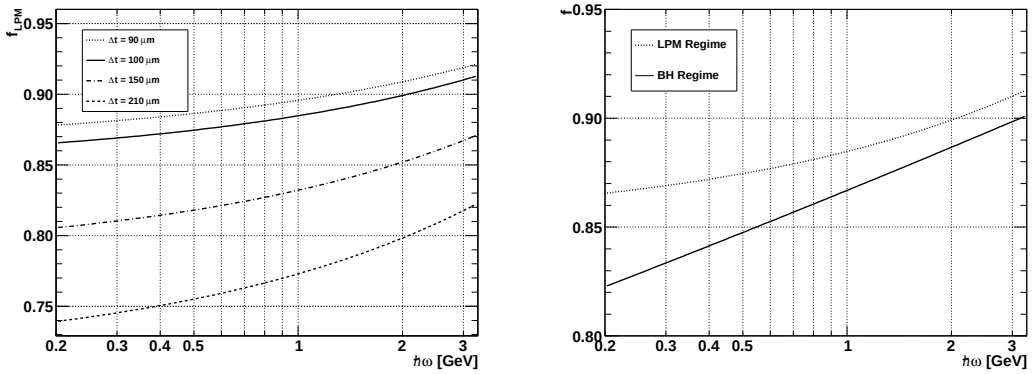

(a) Multi-photon correction factor for Ta foils of various total thickness Δt. These calculations presuppose a single-photon spectrum based on the LPM effect.

(b) Comparison of the BK multi-photon correction factor in the LPM and BH regime for $\Delta t = 100$ μm tantalum. In the TSF regime, the factor is expected to lie in between the two curves.

Figure 4.2: Baier-Katkov multi-photon calculations.

account. In Figure 4.2b, the BK multi-photon function for 100 μm Ta is calculated in the BH and LPM regime. As seen here, the difference is relatively small, but will, however, contribute to the systematic errors of the power spectra of Figure 3.6 and 3.7 with a few percent.

4.2 Shul'ga & Fomin

In [FS86], Shul'ga & Fomin consider the retarded solution of the Maxwell equations for the vector potential $\boldsymbol{A}'(\boldsymbol{r}, t)$ describing the eigen-field of an electron having traversed a thin layer of amorphous material at times $t > 0$. Similar results are found for the electric scalar potential. Appendix A contains a small note on solving the wave equations for the magnetic vector and electric scalar potential using the method of Green's functions and writing the solutions in terms of a Fourier integral representation. When considering a thin foil, where the transit time $\Delta\tau_{\text{tr}} \simeq \Delta t/v$ is short—v (v') is the initial (final) speed of the primary particle—they find an approximate expression for the final state vector potential $\boldsymbol{A}'$ under the assumption $\omega \cdot \Delta\tau_{\text{tr}} - \boldsymbol{k} \cdot \boldsymbol{r}(\Delta\tau_{\text{tr}}) \ll 1$, where $\boldsymbol{k}$ is the photon wave vector of magnitude $k = \omega/c$

$$\boldsymbol{A}'(t > \Delta\tau_{\text{tr}}) \simeq \frac{e}{2\pi^2 c} \operatorname{Re} \int \frac{d^3k}{k} \exp\left[i\left(\boldsymbol{k}\cdot\boldsymbol{r} - \omega\cdot t\right)\right] \times \left[\underbrace{\frac{\boldsymbol{v}}{k - \boldsymbol{k}\cdot\boldsymbol{\beta}}}_{A_k} + \underbrace{\frac{\boldsymbol{v}'}{k - \boldsymbol{k}\cdot\boldsymbol{\beta}'}\left\{\exp\left[i(\overbrace{k\cdot c - \boldsymbol{k}\cdot\boldsymbol{v}'}^{\phi})t\right] - 1\right\}}_{A'_k}\right], \tag{4.6}$$

where $\boldsymbol{\beta} = \boldsymbol{v}/c$. The expression contains two terms recognizable as Lienard-Wiechert potentials in Fourier representation (cf. Appendix A). The first term, labeled A_k, describes the Fourier components of the electron eigen-field with wave vector $\boldsymbol{k}$ along the electron's *initial* trajectory $\boldsymbol{\beta}$ while the latter term, labeled A'_k, describes the same

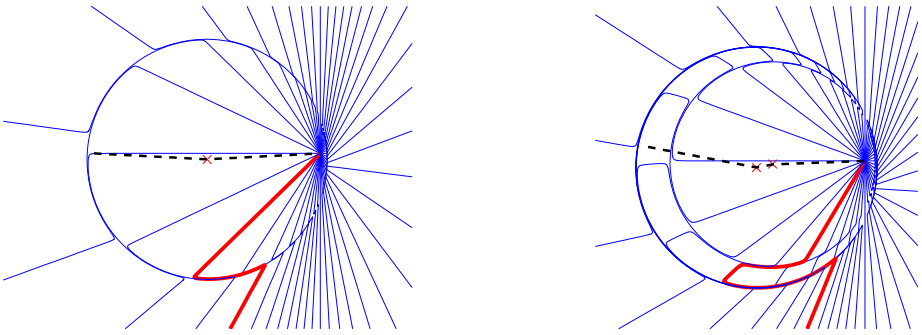

(a) Single Scattering. **(b)** Double Scattering.

Figure 4.3: The electric field lines shortly after the electron has scattered once (a) and twice (b), respectively. For illustration purposes, the velocity of the particle has been set to $\beta = 0.9$ along a horizontal line towards the right. The tangential component of the field lines can be interpreted as the radiation field, propagating outwards at the speed of light [Tsi72, Oha80]. As seen from one of the field lines (indicated by the thick red line), the rapid succession of scattering events may lead to closely spaced tangential component field lines pointing in opposite directions. To the observer, these field lines partially cancel each other for low frequencies. Courtesy of K.K. Andersen.

quantity along the *final* trajectory $\boldsymbol{\beta}'$. Notice that it takes a time $\Delta\tau_{\mathrm{SB}} \lesssim 1/\phi$ before the the second term of Eq. (4.6) is non-zero, *i.e.* it takes a time for the eigen-field to appear along the final electron direction, $\boldsymbol{v}'$. In this way, the electron can be regarded as traveling along the final velocity, while a part of its eigen-field—which later evolves into the radiation field caused by the initial scattering—continues along the direction of $\boldsymbol{v}$. The time interval $\Delta\tau_{\mathrm{SB}}$, in which the primary particle lingers in such a semi-bare final state, can be approximated by expanding the phase around small angles [FS86]

$$\begin{aligned}\phi = k\cdot c - \boldsymbol{k}\cdot\boldsymbol{v}' = \omega\left[1-\boldsymbol{n}\cdot\boldsymbol{\beta}'\right] &\simeq \omega\left[1-\beta\cos(\theta_{\mathrm{rad}})\right] \simeq \omega\left[1-\beta\left(1-\theta_{\mathrm{rad}}^2/2\right)\right] \\ &= \omega\left[\frac{(1-\beta)(1+\beta)}{(1+\beta)} + \frac{\beta\theta_{\mathrm{rad}}^2}{2}\right] \\ &\simeq \omega\left[\frac{1}{2\gamma_{\mathrm{L}}^2} + \frac{\theta_{\mathrm{rad}}^2}{2}\right] = \frac{\omega}{2\gamma_{\mathrm{L}}^2}\left[1+\gamma_{\mathrm{L}}^2\theta_{\mathrm{rad}}^2\right]\,, \qquad (4.7)\end{aligned}$$

where $\theta_{\mathrm{rad}} \simeq 1/\gamma_{\mathrm{L}} \ll 1$ and $\boldsymbol{n} = \boldsymbol{k}/k$ were defined in Figure 1.1a. Soft photon limit and $\beta' \simeq \beta \simeq 1$ has been assumed above. The time $\Delta\tau_{\mathrm{SB}}$ is hereby estimated to $\gamma_{\mathrm{L}}^2/\omega$ which is half the formation time $\tau_{\mathrm{f}} \simeq \ell_{\mathrm{f0}}/c = 2\gamma_{\mathrm{L}}^2/\omega$ for $\beta \simeq 1$ and soft photons $(y \ll 1)$. The effect is thus noticeable for low photon energies from primary particles of high energies.

The concept of a semi-bare electron, introduced by Feinberg [Fei66], is questionable [BS97], although at first appealing. Charges cannot be stripped of their electric eigen-field without violating the Gauss theorem $\oint_{\mathcal{S}} \boldsymbol{E}\cdot d\boldsymbol{\mathcal{A}} = Q_{\mathrm{encl}}/\epsilon_0$, where Q_{encl} is the net charge enclosed within a volume with surface $\mathcal{S}$. Despite the imperfect

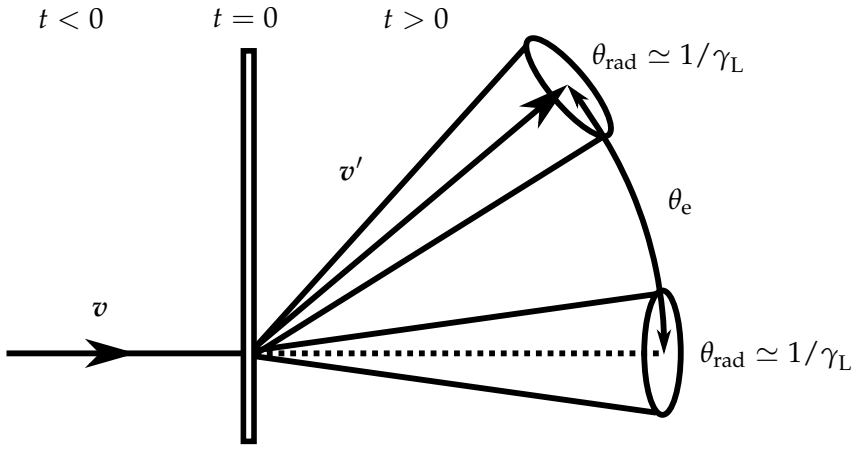

Figure 4.4: An electron with initial velocity v traverses a thin foil at time $t = 0$. Radiation from the first scattering is detected within the narrow cone around v, and the electron is in a semi-bare state during the remaining scatterings, leading to a reduced yield of radiation within the cone around the final velocity v'. Adapted from [AS96].

interpretation, the main conclusions remain valid: a) it takes time for the eigen-field to reorganize following a scattering, and b) during this time, the electron will in the subsequent collisions carry a distorted Coulomb field, hence cause a changed radiation yield compared to a particle carrying a non-distorted field. If $\Delta\tau_{\rm SB} \gtrsim \Delta\tau_{\rm tr}$ (or expressed in another way, $\ell_{\rm f0} \gtrsim \Delta t$), the particle engages in all collisions—except the first—with a distorted Coulomb field.

In Fig. 4.3a–b, the distorted Coulomb field of a relativistic point charge as a result of a single or double transverse scattering events, respectively, is shown. The electric field lines are drawn using the versatile time parametrization of the field described in [Tsi72]. This classical formalism is well capable of producing field line pictures visualizing many high-energy radiation phenomena along a single plane of motion[1]. A similar field line interpretation is also applicable for the magnetic field [Oha80]. In the figures, the scattering centres are marked by a red cross and the path of the electron is marked by a dashed curve. In both cases, the initial disturbance is seen to introduce a tangential component to the field lines, which can be interpreted as the radiation field. In [BS97], the characteristics of the transverse field connecting the two fields on either side of the event horizon were found to truly correspond to a radiation field. This event horizon travels outwards with the finite speed of light, and beyond this the field is still unchanged.

After the first scattering event, the Coulomb field of the electron is clearly distorted due to the finite propagation speed of the event horizon. If a subsequent scattering centre resides in the vicinity of the first, the Coulomb field is not fully reestablished before the second collision. Because of this, closely spaced tangential component field lines pointing in opposite directions can occur, cf. Figure 4.3b. An observer will see a limited radiation yield due to mutual cancellation of such oppos-

[1]The model of [Tsi72] was implemented by Kristoffer K. Andersen, and I am indebted to him for the pictures of Figure 4.3.

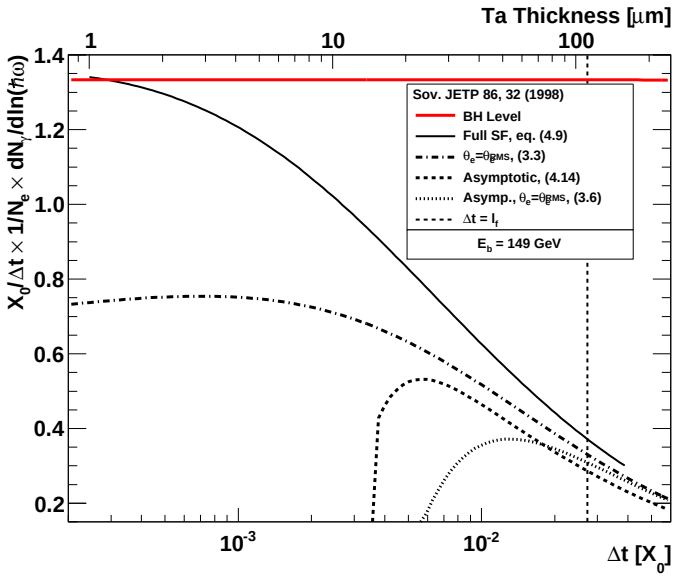

Figure 4.5: Calculations based on [SF98b] of thickness dependence of power spectrum normalized by $\Delta t/X_0$ and number of particles (N_e) for $E_0 = 149$ GeV. The vertical dashed line marks the condition $\ell_{\mathrm{f0}} = \Delta t$ for emitting a 300 MeV photon.

ing field vectors, if he cannot temporally—or rather spatially, through c—resolve the individual field components. The latter problem is—according to the similarity theorem of Fourier decomposition—relevant at the low frequency components of the radiation, the ones with the longest separation in time. The radiation intensity per scattering event is here less than the double of a single scattering. In this way, the field-line picture not only gives information on the direction and intensity but also on the spectral composition, albeit in a qualitative manner only. As the field line picture does not include a quantity corresponding to the formation length, is fails to describe the central conditions of the TSF: $a)$ that MCS is strong in the foil $(\ell_{\mathrm{f0}} \gg \ell_\gamma)$ and $b)$ the foil is thin $(\ell_{\mathrm{f0}} \gg \Delta t)$.

Regarding thickness, the TSF regime governing thin targets $(\ell_{\mathrm{f0}} \gtrsim \Delta t > \ell_\gamma)$ lies in between the Bethe-Heitler limit of very thin targets $(\ell_\gamma > \Delta t)$ and the LPM regime with thicker targets $(\Delta t \gtrsim \ell_{\mathrm{f0}} \gtrsim \ell_\gamma)$. As opposed to these two regimes, the power spectrum level is in the TSF regime nonlinear in the number of scattering events, *i.e.* thickness, cf. Figure 3.1. Although the radiation emission angle θ_{rad} is typically $\sim 1/\gamma_{\mathrm{L}}$, the electron scattering angle $\theta_{\mathrm{e}} = |\boldsymbol{v}' - \boldsymbol{v}|/v$ has a distribution $f(\theta_{\mathrm{e}})$ determined by the nature of the target (*e.g.* nonuniform external fields, crystals or amorphous materials). In [SF98b, SF98a], a nice discussion of how to treat the electron scattering angle in the latter case—relevant to our experiments—is given. SF find an expression [SF98b, Eq. (3.3)] which is independent of material type, as it has not yet been averaged with the distribution of electron scattering angles

$$\frac{1}{N_e}\frac{dN_\gamma}{d\ln\hbar\omega} = \frac{2\alpha}{\pi}\left[\frac{2\zeta^2+1}{\zeta\sqrt{\zeta^2+1}}\ln\left(\zeta+\sqrt{\zeta^2+1}\right)-1\right], \tag{4.8}$$

where $\zeta = \gamma_L \theta_e / 2$. The asymptotic values when $\zeta \ll 1$ or $\zeta \gg 1$ are [SF98b, Eq. (3.4)]

$$\frac{1}{N_e}\frac{dN_\gamma}{d\ln\hbar\omega} = \frac{2\alpha}{3\pi}\begin{cases} \gamma_L^2\theta_e^2 & \gamma_L^2\theta_e^2 \ll 1\,, \\ 3\big[\ln\big(\gamma_L^2\theta_e^2\big)-1\big]+\mathcal{O}\big[(\gamma_L\theta_e)^{-2}\big] & \gamma_L^2\theta_e^2 \gg 1\,. \end{cases} \tag{4.9}$$

which again has to be averaged with the distribution $f(\theta_e)$. In the case of an amorphous target, $\langle\theta_e^2\rangle \propto \Delta t / X_0$ (to logarithmic accuracy, cf. Eq. (1.18) and (1.19)). If multiple scattering is relevant ($\gamma_L^2\theta_e^2 \gg 1$), the power spectrum thus has a logarithmic thickness dependence. This limit is illustrated in Figure 4.4. SF show in [FS86] convergence to the BH result in the other asymptotic limit where multiple scattering is insignificant ($\gamma_L^2\theta_e^2 \ll 1$).

In Figure 4.5, some of the expressions of [SF98b] have been used to calculate the thickness dependence of the power spectrum level normalized to target thickness $\Delta t / X_0$ for photon energies $\hbar\omega \lesssim \hbar\omega_{TSF}$, *i.e.* in the TSF regime. The lower horizontal scale shows Δt in units of X_0, while the upper scale displays the equivalent tantalum target thickness in microns. The red line shows the simple BH level of Eq. (1.11). Since the vertical scale is normalized by thickness, this level is a horizontal line. Shul'ga & Fomin's main result [SF98b, Eq. (4.9)] is relatively complex, as it contains functions defined by integrals that require heavy numerical solving. Nevertheless, numerical implementation is viable and the result is shown with a black, solid line in Figure 4.5. This is also the curve labelled "SF" in Figure 3.7, but in Figure 4.5 shown uncorrected for the calorimetric effect. Notice the convergence to the BH limit at very small Δt. Their theory does not contain the transition to the LPM regime—or rather, they replace their theory with the LPM theory beyond the applicable range, giving rise to a discontinuous derivative at the transition. SF also provide some asymptotic expressions for the thickness dependence which have also been plotted in Fig. 4.5. The dash-dotted line is Eq. (4.8) naïvely averaged with a primitive distribution $f(\theta_e) = \delta\big(\theta_e - \theta_e^{RMS}\big)$, where $\theta_e^{RMS} = \sqrt{\langle\theta_e^2\rangle}$ is the RMS value of the MCS angle in a amorphous target. The dashed curve is an asymptotic expression derived from their Eq. (4.9) for $\gamma_L^2\langle\theta_e^2\rangle \gg 1$, *i.e.* an asymptote to a properly averaged expression, supposedly valid in the region of substantial multiple scattering. The dotted curve is the asymptotic expression valid for $\gamma_L^2\theta_e^2 \gg 1$ averaged with $f(\theta_e) = \delta\big(\theta_e - \theta_e^{RMS}\big)$, corresponding to [SF98b, Eq. (3.6)].

The curves are all clearly distinct besides convergence at larger thicknesses. The naïve expressions evidently fall short of the full expression of their Eq. (4.9) at very thin thicknesses ($\Delta t \lesssim 1\% X_0$). The utilized $\gamma_L^2\theta_e^2 \gg 1$ and $\theta_e = \theta_e^{RMS}$ will become bad assumptions as the thickness becomes very small. Here, the scattering angle will be small and the distribution will eventually not be well-represented by a Gaussian. Because of this, the approximate curves do not have convergence to the BH expression. The approximate expression of Eq. (3.2) on page 33 is found to be valid for a limited region of thicknesses $\Delta t / X_0 \gtrsim 0.5\%$—similar to the dashed line in Figure 4.5.

I here present an interpretation based on distortion of the primary particle's eigen-field, inspired by the interpretation given in [SF78]. I consider the thickness dependence under a fixed photon energy, where $\ell_{f0} \gg \ell_\gamma$. The ordinate scale of the TSF power spectra (Figure 3.7) can be interpreted as the probability of radiation emission per target atom encounter (thickness). With very thin targets ($\ell_\gamma \gg \delta t$), the MCS is somewhat insignificant. A scattering event is unlikely to be affected by the distortion of the Coulomb field of the electron resulting from a previous event, and

the BH value is obtained. Then, as the thickness increases, the emission probability per encounter drops drastically (a factor 3 for $\hbar\omega \simeq 0.3$ GeV) in the TSF regime. Here, the distortion of the electron Coulomb field is beginning to influence the radiation emission in the consecutive scattering events. Finally, a level determined by the LPM mechanism is reached, where multiple scattering dominates the process and essentially all events are influenced by the reduction.

4.3 Blankenbecler & Drell

The method by BD [BD96]—which is presented in Appendix B—is very versatile, as one can define general longitudinal target geometries with varying radiation length along the original projectile trajectory. Although calculating the resulting power spectrum often involves heavy numerical integration, the formalism is applicable in many regimes of beam and radiation energies. The formalism is in [BD96] shown to treat both the BH, LPM and TSF regime properly, *i.e.* it is able to calculate modifications of the power spectrum over many orders of magnitude in thickness with the same code. One of the limitations of their approach is their neglect of the polarization of the medium (*i.e.* the TM effect). Secondly, their result does not include secondary processes such as multi-photon emission and pair production from the bremsstrahlung photon.

In [BD96], the shape function $F(\hbar\omega, \Delta t, E_0)$ is introduced. This quantity describes the ratio of the calculated power spectrum to the Bethe-Heitler result

$$\frac{d\sigma_{\text{tot}}}{d\hbar\omega} = F(\hbar\omega, \Delta t, E_0) \times \frac{d\sigma_{\text{BH}}}{d\hbar\omega} ,$$

where

$$F(\hbar\omega, \Delta t, E_0) = \int_{-\infty}^{\infty} db \int_{-\infty}^{\infty} db_2 F(b_2, b, b_t) , \tag{4.10}$$

and the function $F(b_2, b, b_t)$ can be examined in Eq. (B.10) of Appendix B.

In the early stages of my PhD, I began a MATLAB implementation of the BD formalism. Although I quickly found good accordance with BD's results for a thin, single foil, the calculations were quite time-consuming, thus rendering a thorough debugging process very cumbersome. Also, we intended to use the code for the much larger and complicated target geometries presented in Chapter 5, only further prolonging the necessary computation time.

Meanwhile, a FORTRAN 77 implementation was written primarily by Pietro Sona with the help of Sergio Ballestrero, members of NA63. Fortunately, this implementation led to computation times more similar to those reported by Blankenbecler [Bla06], and Sona did a tremendous job of successfully testing the code in many ways. All BD curves in this document have been calculated using their FORTRAN 77 implementation for which I am very grateful.

4.4 The Logarithmic Thickness Dependence

Although many papers refer to a *logarithmic* thickness dependence in the regime $\ell_{\text{f0}} \gtrsim \Delta t > \ell_\gamma$ [BK98, SF98b, SF98a], none of them have produced a simple but accurate logarithmic term which describes the power spectrum within this thickness

regime with proper convergence to the BH limit, $\Delta t \to 0$. This section will present a simple semi-empirical expression which describes both data and theory well. Blankenbecler's expression F, describing the modification to the Bethe-Heitler value, can in the limit $\ell_{\mathrm{f0}} \gg \Delta t$ and for soft photons be approximated by [Bla97b, Eq. (30)]

$$F(\ell_{\mathrm{f0}} \gg \Delta t, T_{\mathrm{B}}, y \ll 1) \simeq \frac{1}{2T_{\mathrm{B}}} \int_0^1 \left(\frac{3T_{\mathrm{B}} + 1}{1 + 6T_{\mathrm{B}} w(1-w)} - 1 \right) dw \,, \tag{4.11}$$

where T_{B} is a scaled variable of the thickness in units of radiation lengths, $T_{\mathrm{B}} = \pi \Delta t / 3\alpha X_0 = \Delta t / 12 \ell_\gamma$. Solving the RHS integration analytically yields

$$\mathrm{RHS} = \frac{1}{2T_{\mathrm{B}}} \left(\frac{\operatorname{arccosh}(a)}{\sqrt{1 - a^{-2}}} - 1 \right) \,, \tag{4.12}$$

where $a = 3T_{\mathrm{B}} + 1$. In our TSF experiment, the target size variables had the ranges $T_{\mathrm{B}} \in \left[4.3 \times 10^{-2}; 7.2\right]$ and $a \in \left[1.1; 23\right]$. The size of the ranges renders it difficult to find a series expansion in either a or T_{B} that approximates the full expression above acceptably within the first few terms. Instead, the logarithmic variable $u = \ln(2T_{\mathrm{B}} + 1) = \ln(2/3a + 1/3)$, $u \in \left[8.3 \times 10^{-2}; 2.7\right]$ is introduced. The expression can now be re-written

$$F(\ell_{\mathrm{f0}} \gg \Delta t, T_{\mathrm{B}}, y \ll 1) \simeq \frac{1}{2T_{\mathrm{B}}} \underbrace{\left(\frac{\operatorname{arccosh}\left(\frac{3e^u}{2} - \frac{1}{2} \right)}{\sqrt{1 - \left(\frac{3e^u}{2} - \frac{1}{2} \right)^{-2}}} - 1 \right)}_{G(u)} = \frac{G(u)}{2T_{\mathrm{B}}} \,. \tag{4.13}$$

If the function $G(u)$ is written in a Maclaurin series, the terms are

$$G(u) = \sum_{n=0}^{\infty} \frac{G^{(n)}(0)}{n!} u^n = u + \frac{u^2}{20} - \frac{11u^3}{420} + \frac{u^4}{240} + \\ + \frac{19u^5}{18480} - \frac{3859u^6}{7207200} + \cdots \tag{4.14}$$

In Fig. 4.6a, the contribution from the first six non-vanishing terms of the series expansion is shown and compared with Eq. (4.12). As can be seen here, substituting $G(u)$ in Eq. (4.13) with the first term of the series expansion, leading to $F = u/2T_{\mathrm{B}} = \ln(2T_{\mathrm{B}} + 1)/2T_{\mathrm{B}}$, is a very good approximation to the expression for the factor F in the limit $\ell_{\mathrm{f0}} \gg \Delta t$. We define $G_n(u)$ to be the truncated Maclaurin series neglecting terms of order u^{n+1} and beyond, thus $G(u) \simeq G_n(u) + \mathcal{O}(u^{n+1})$. In Fig. 4.6b, the relative deviation between [Bla97b, Eq. (30)] and $G_n(u)$ is shown. Within the selected thickness range, $G_1(u) = u$ deviates only 3% from $G(u)$, only surpassed by truncated Maclaurin series with $n \geq 4$. Within the experimental range of thicknesses, the soft power spectrum level with $\ell_{\mathrm{f0}} \gg \Delta t$ should thus—from a theoretical point of view—be well described by

$$\frac{X_0}{\Delta t} \frac{1}{N_e} \frac{dN_\gamma}{d \ln \hbar\omega} = \overbrace{\left. \frac{X_0}{\Delta t} \frac{1}{N_e} \frac{dN_\gamma}{d \ln \hbar\omega} \right|_{BH}}^{a} \times F \\ \simeq a \times \frac{u}{2T_{\mathrm{B}}} = a \times \frac{\ln(b_{\mathrm{B}} \times \Delta t + 1)}{b_{\mathrm{B}} \times \Delta t} \,, \tag{4.15}$$

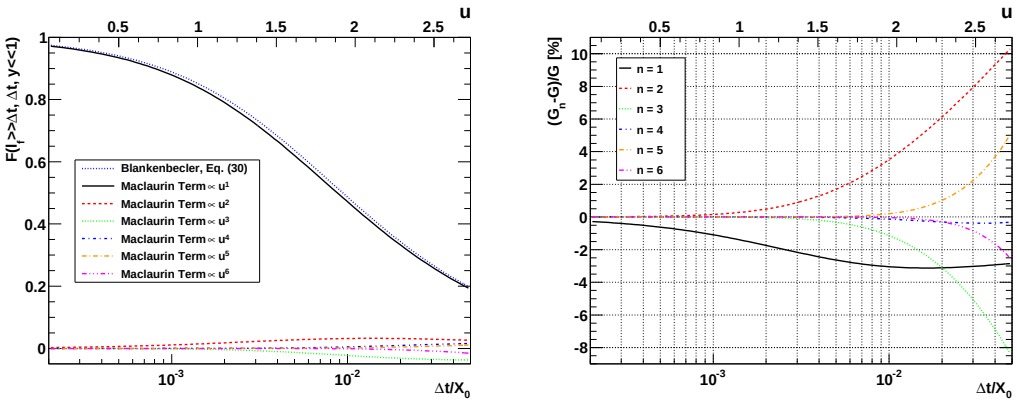

(a) Terms of the Maclaurin series.

(b) Relative deviation between the truncated Maclaurin series and Eq. (4.12).

Figure 4.6: Characteristics of the logarithmic expression.

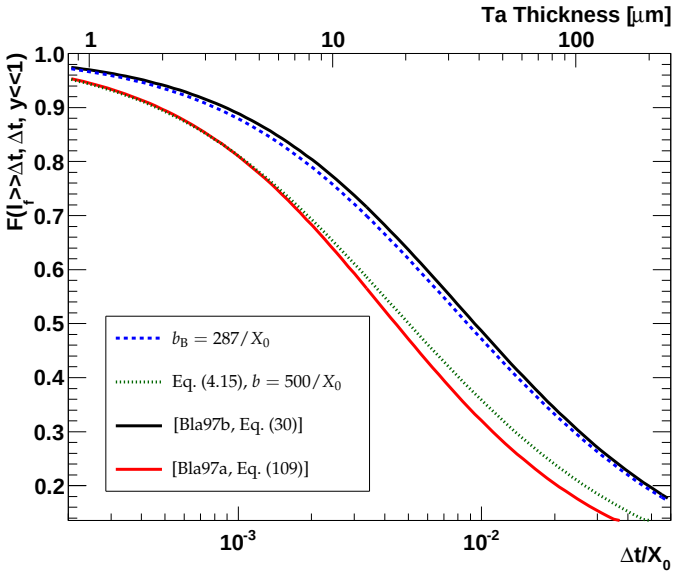

Figure 4.7: Characteristics of the logarithmic expressions. The dotted and dashed line are plots of Eq. (4.15) with different values of the parameter b. The full lines are plots of Blankenbecler's asymptotic expressions of the thickness dependence.

where a is close to unity and slightly dependent on $\hbar\omega$, and $b_B = 2\pi/3\alpha X_0 = \left(6\ell_\gamma\right)^{-1} \simeq 287/X_0$. The semi-empirical expression contains the mentioned logarithmic thickness dependence and proper convergence to the BH limit. The comparison between Eq. (4.15) and [Bla97b] was also presented in [II].

In a later paper [Bla97a], Blankenbecler included a correlation between phase and amplitude in the eikonal wave function. It was shown that such a correlation reduces the soft-photon level of the spectrum by typically 5%–15% [Kle99] and the shape is also slightly different. In Figure 4.7, a comparison is made between Blankenbecler's TSF expressions of [Bla97b, Bla97a]. Like the other results of [Bla97a], this

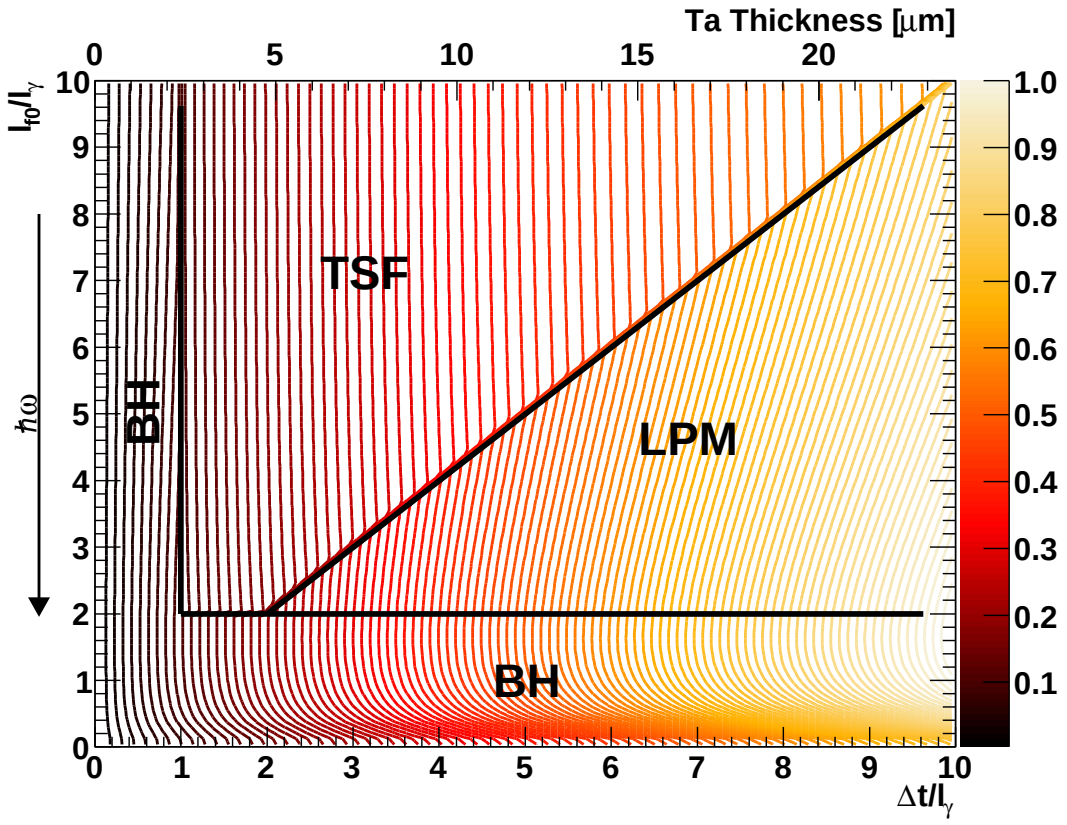

Figure 4.8: The bremsstrahlung power spectrum level (in arbitrary units) in a small part of the $(\Delta t, \ell_{f0}, \ell_\gamma)$ parameter space. The contours trace lines of equal bremsstrahlung yield. Upper horizontal axis shows the equivalent tantalum thickness. For the calculation, $E_0 = 200$ GeV and tantalum have been assumed.

theoretical curve is seen to be up to 30% below the corresponding curve of [Bla97b], as is also clear in [Bla97a, Fig. 2][2]. Notice that whereas Eq. (4.15) describes the theory of [Bla97b] well with $b_B = 287/X_0$, one must use at least $b \simeq 500/X_0$ to describe the thickness dependence of [Bla97a]. This heavy thickness dependence is not supported by the results presented in Figure 3.8 on page 48, casting doubt upon the quality of [Bla97a] compared to [Bla97b].

To summarize, the single-photon bremsstrahlung power spectrum level has in Figure 4.8 been computed in the $(\Delta t, \ell_{f0}, \ell_\gamma)$ parameter space for a fixed primary energy. The discussed bremsstrahlung regimes are in the plot bordered by black lines. The abscissa shows the foil thickness in units of the multiple scattering length, while the ordinate shows the formation length, also in units of ℓ_γ. Following the definition of considerable multiple Coulomb scattering within the formation length leading to Eq. (1.21), only the BH regime is located below $\ell_{f0}/\ell_\gamma \lesssim 2$. This regime is also present for very thin foils, $\Delta t/\ell_\gamma \lesssim 1$. The diagonal line illustrates $\Delta t = \ell_{f0}$, the characteristic threshold between the TSF and LPM regimes.

The power spectrum level has been computed from Eq. (1.22) and Eq. (4.15) with $b_B = 1/6\ell_\gamma$. The latter is only applied in the TSF region. Generally, the matching

[2]The ordinate label in [Bla97a] must be wrong—it should say $F/2$, not F.

between the TSF and LPM regimes is not complete, as this transition is not described by any analytical expression.

Moving along a horizontal line in the figure corresponds to the thickness dependence for a fixed value of $\hbar\omega$, while a vertical line gives the photon energy dependence for a fixed thickness. The direction of growing $\hbar\omega$ is indicated by the vertical arrow, $\ell_{\mathrm{f0}} \propto 1/\hbar\omega^*$. The special LPM photon energy dependence is distinct. Also, the logarithmic thickness dependence in the TSF regime is very different from the linear one in the case of BH and LPM. At $\Delta t/\ell_\gamma = 6$, $\Delta t = 1/b_{\mathrm{B}}$, *i.e.* the TSF level is reduced by a factor $\ln(2)$ relative to the corresponding BH level.

The plot is for illustration purposes only and encapsulates the tendencies shown in Figure 3.1a and Figure 3.1b.

◇ ◇ ◇

A number of highly sophisticated models describing bremsstrahlung have been implemented and discussed above. I would like to point out that although the theory of B.G. Zakharov [Zak96] has only been mentioned briefly and not implemented, his model is also very versatile and includes the sandwich effect (the topic of the following chapter), the LPM and TSF effect. He refers to the latter as the "frozen-size" regime, since the transverse coordinate of the primary particle here can be regarded as almost constant, leading to an eikonal approximation. Like BD, he does not consider the TM effect nor multi-photon emission.

In the search for a simple expression describing the thickness dependence of the TSF effect of good quality and complexity suitable for back-of-the-envelope calculations, I tried combining simplistic electron scattering angle distributions with Eq. (4.8) and (4.9). However, none of the attempts led to results of a quality comparable with that of SF's full calculation [SF98b, Eq. (4.9)]. Eventually, a simple single-parameter logarithmic expression was deduced following an expression from [Bla97b]. This expression possess the proper convergence to the BH regime and matches the SF and BD theory within $\lesssim 5\%$ over a large range of thicknesses.

CHAPTER 5

THE SANDWICH EFFECT

In Chapter 3, I considered a structured target composed of N_f targets of thickness $\langle \delta t \rangle$ mechanically separated by a gap of width $\langle \delta g \rangle$ ensuring that the foils could be considered independent. To complicate things, the following question could be posed: how is the spectrum perturbed as the gap width is diminished, such that the formation length eventually stretches from one foil to the neighbouring ($\ell_{f0} \gtrsim \delta g$, $\delta t \gtrsim \ell_\gamma$)? In this chapter, I will present the theoretical predictions of the modifications to the bremsstrahlung power spectrum and a number of experimental measurements on systems seemingly fulfilling this condition.

5.1 Theoretical Foundations

In [Bla97b], Blankenbecler uses the BD formalism [BD96] to consider a structured target consisting of N_f identical foils of radiation length X_0^t separated by $N_f - 1$ gaps of vacuum, $X_0^g \to \infty$. He finds that for calculations of $N_f \geq 2$ Au targets

> *The photon spectrum is clearly developing a peak where the formation length is approximately equal to the distance between the centers of the plates.*

The peak is located in what would have been the TSF photon energy regime of a single foil of thickness $\delta t = \Delta t / N_f$, and the maximum value of the peak exceeds this level. At lower photon energies, the power spectrum approaches the TSF level of a target of the combined target thickness Δt. The interference over the distance between the backside of one foil and the frontside of the adjacent foil must lead to the onset of the peak. Therefore, Eq. (1.7) can be inverted setting the formation length ℓ_{f0} equal to the target spacing δg, leading to an onset of resonance at a photon energy

$$\hbar\omega < \hbar\omega_r \equiv \frac{E_0}{1 + \dfrac{\delta g}{2\gamma_L \lambda\!\!\!^{-}_c}} \simeq \frac{2\gamma_L^2 \hbar c}{\delta g} \,, \tag{5.1}$$

where the approximate expression is valid for soft photons ($y \ll 1$). In this regime, the expression coincides with Ter-Mikaelian's "resonance condition" in a stratified medium [TM72, Eq. (28.10')]. Notice the similarity between this threshold and the TSF one, Eq. (3.1) on page 33.

In Figure 5.1a, some calculations of the BD F-function describing the modulation of the BH power spectrum [BD96] are shown. In each case, the target consists of $N_\mathrm{f} \times \delta t = 100$ μm of tantalum. Curves are shown for $N_\mathrm{f} = 1, 5, 10$ and 20. Where $N_\mathrm{f} > 1$, the gaps consist of 100 μm air at Standard conditions for Temperature and Pressure (STP), $X_0^{\mathrm{Air}} = 303.9$ m [Y$^+$06]. In this way, $T \equiv N_\mathrm{f} \times \delta t / X_0^\mathrm{t} = 2.44\%$ but $G \equiv (N_\mathrm{f} - 1) \times \delta g / X_0^\mathrm{g} < 6.25 \times 10^{-6} \ll T$, *i.e.* close to Blankenbecler's idea. From Eq. (5.1), $\hbar\omega_r = 0.646$ GeV at the primary energy of the calculations, $E_0 = 206$ GeV. Clearly, the higher the degree of segmentation, the larger values of F are obtained near $\simeq$ 0.8 GeV. The reached values are up to about double the corresponding value for the $1 \times$ Ta100 target but more modest ($\simeq 15\%$) with respect to the corresponding value for infinite spacing, $N_\mathrm{f} \times \mathrm{Ta}\delta t\mathrm{Air}\infty$ (the TSF level)[1]. It is also interesting to see that some destructive interference is introduced at larger photon energies corresponding to distances shorter than the gap width δg. This phenomenon is not surprising, as $\ell_{\mathrm{f}0}$ is not a limiting but characteristic length, cf. discussion below Eq. (1.8) on page 7. In Figure 5.1b, a corresponding set of calculations are shown for the same target geometry, $10 \times$ Ta10Air100, but varying primary energy from 120–206 GeV (feasible energies at the CERN SPS). As expected, the curve shapes are seen to be shifted (on a logarithmic scale) by an amount in photon energy approximately proportional to γ_L^2 in accordance with Eq. (5.1).

The small augmentation of the radiation yield around $\hbar\omega_r$ can be explained by the fact that the formation zone, originating from scattering processes in one foil, reaches the neighboring foil by which further scattering centres are introduced in the formation zone, all contributing incoherently to the radiation yield. This increases the bremsstrahlung photon yield with respect to the TSF effect, relevant to infinite spacing for a fixed δt. Judging from Figure 5.1a, the increase is expected to be of modest relative magnitude, also due to the fact that it is a second order process with respect to the TSF effect.

The peak never exceeds $F = 1$, corresponding to the BH level, which would be reached in the limit of extreme segmentation ($N_\mathrm{f} \to \infty$) for a fixed value of δg, where all scattering centres contribute incoherently and all suppression is alleviated. Although the target bears similarities to a transition radiator—a stack of alternating materials with different indexes of refraction—TR has the characteristic energy scale $\gamma_\mathrm{L}\hbar\omega_p \simeq 30$ MeV at the conditions listed above. The target geometry (a gap) dictates a range of photon energies, where the bremsstrahlung suppression mechanisms otherwise present are somewhat reduced. The sandwich effect is also found theoretically by others using different approaches [Zak96, BK99a]. Although the later paper by Blankenbecler [Bla97a] tends to predict smaller sandwich structures at lower energies than what he found in [Bla97b], the latter theory was found in much better accordance with our data in the TSF regime. Because of this, we tend to lend more credence to [Bla97b], the basis of our BD calculations.

[1] Here, the ∞ symbol simply represents a gap spacing that excludes interference between adjacent foils at all photon energies considered, *i.e.* it depends on the lower photon energy threshold of the detector. Truly infinite air gaps would of course cause $G \to \infty$ due to the finite radiation length of STP air. These BD calculations are simply performed with the geometry $1 \times \mathrm{Ta}\delta t\mathrm{Air}100$.

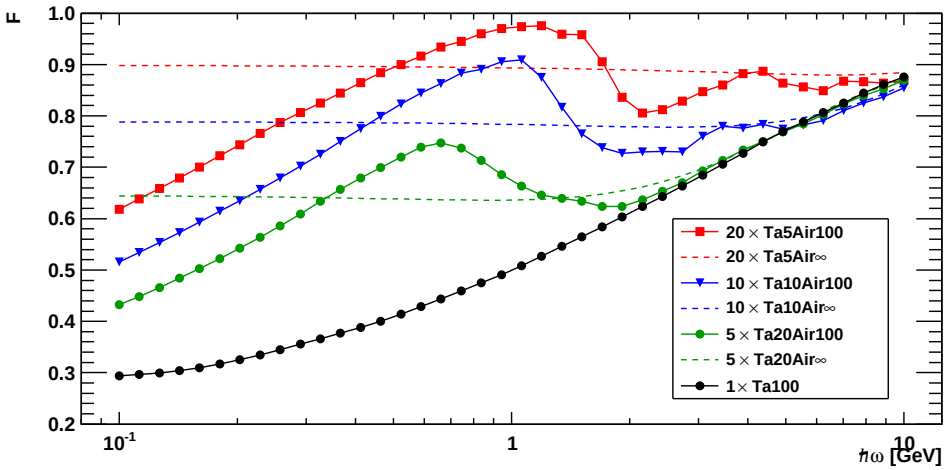

(a) Segmenting a foil of 100 μm Ta. For each value of δt, the TSF level is shown with dashed lines (also calculated with the BD program, for consistency). The gaps consist of STP air. Beam energy is 206 GeV.

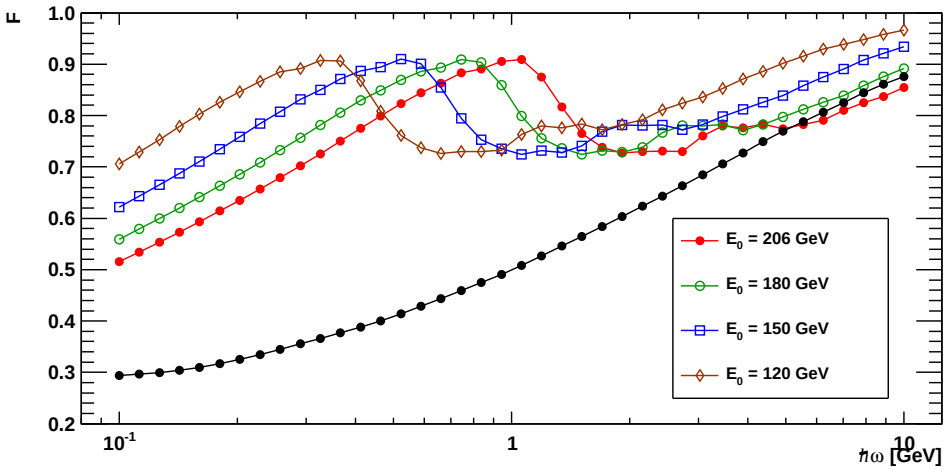

(b) Variation of the primary energy E_0 for the same target geometry, 10 × Ta10Air100. The curves are seen to shift along the abscissa approximately as γ_L^2, in accordance with the formation length (cf. Eq. (1.7) or (5.1)). The 1 × Ta100 curve at $E_0 = 206$ GeV from Fig. (a) is shown again for comparison.

Figure 5.1: Calculations of the BD F function on sandwich target geometries.

There are some similarities between the idea of the sandwich effect and that of coherent bremsstrahlung. In the latter case, large augmentations of the bremsstrahlung yield are obtained when the electron traverses the periodic planes of a crystal and the formation covers a number of crystal planes, *i.e.* free-free transitions above the crystal plane potential barriers. But whereas coherent bremsstrahlung can give large resonances at photon energies tunable by changing the primary energy or the angle between the particle trajectory and crystal planes, the sandwich effect is not expected to exceed the BH yield. Nevertheless, Blankenbecler has high hopes for the effect [Bla97b]

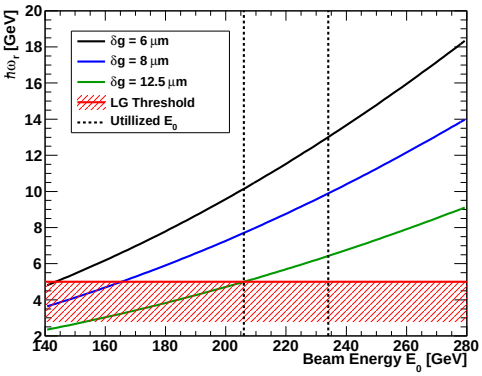

(a) A plot of Eq. (5.1) as a function of E_0 for three values of δg. Typical primary energies are shown with dashed vertical lines, whereas the region close to the LG threshold is bordered by the horizontal line.

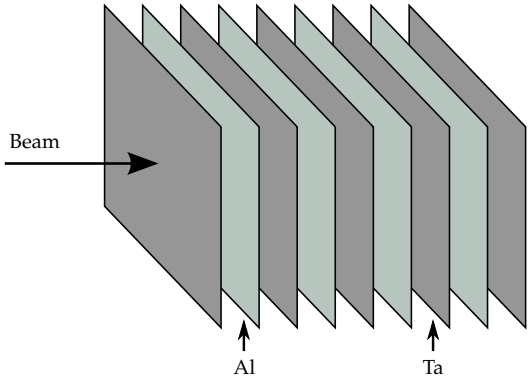

(b) Exploded view of a simple sandwich target with $N_\mathrm{f} = 5$ Ta foils separated by $N_\mathrm{f} - 1$ Al foils.

Figure 5.2: Devising the sandwich targets for the early study.

It may be possible to design structured targets to yield bremsstrahlung spectra with desirable and interesting characteristics such as suppressing the soft photon part of the spectrum or enhancing the photon yield in a chosen energy regime.

Although using sandwich targets as sources of resonant radiation seems doubtful because of the limited yield, observing the sandwich effect would be an indirect way of measuring the macroscopic formation length.

One can also interpret the effect using the field line picture of which examples are shown in Fig. 4.3 on page 53. As stated there, it is found from the field line picture that the radiation intensity per unit length for scattering events in close succession is suppressed at low frequencies. Furthermore, the frequency interval which is suppressed, depends on the distance between the scattering centers—the longer this distance, the lower the suppressed frequency. If one considers the gap of a sandwich target, this can be considered as a zone with elimination of the scattering centres present in a homogeneous radiator of equivalent thickness. The relocation of the scattering centers results in an "alleviation" of the suppression. For example, by segmenting a foil and keeping a distance $\delta g \gg \ell_{\mathrm{f}0}$ the LPM is alleviated, and the TSF level is reached. In this way, the sandwich peak can be understood as a result of suppression $\rightarrow$ alleviation $\rightarrow$ stronger suppression, when going from higher to lower photon energies, or *vice versa* with respect to formation lengths.

We have in the NA63 Collaboration made a number of attempts to realize Blankenbecler's idea. The different ways of constructing sandwich targets are presented in the following chapter. In each of the attempts, about 24 h of beam time were allocated to the experiment.

Label	δt [μm]	δg [μm]	T	G	$T+G$	$\hbar\omega_r$ [GeV]
$1 \times$ Ta100	100	0	2.44%	0	2.44%	—
$20 \times$ Ta5Al6	5	6	2.44%	0.13%	2.57%	10.2 (13.0)
$20 \times$ Ta5Al8	5	8	2.44%	0.17%	2.61%	7.7 (9.9)
$10 \times$ Ta10Al12.5	10	12.5	2.44%	0.13%	2.57%	5.0 (6.4)

Table 5.1: Target assemblies used in the initial sandwich experiment. The sandwich structure is expected at $\hbar\omega_r$ when $E_0 = 206\ (234)$ GeV. Only nominal distances are listed.

5.2 The Sandwich Targets

Early Attempts

Before spring 2008, the NA63 only had LG calorimeters. A lower energy threshold of $\simeq 2$ GeV the available beam energies at the CERN SPS put some constraints on the gap size. In Figure 5.2a, the condition of Eq. (5.1) has been plotted as a function of the primary energy E_0 for three gap widths 6–12.5 μm. Anything below $\simeq 5$ GeV will surely not be detectable due to the LG threshold, hence targets with $\delta g \lesssim 10$ μm must be considered. Our method of accomplishing this was to use thin foils (of a material with a relatively large radiation length) as spacers. In our case, the sandwich targets were assembled from alternately a Ta ($X_0^{\text{Ta}} = 4.094$ mm) and a Al ($X_0^{\text{Al}} = 88.97$ mm) foil, as sketched in Figure 5.2b. Since $X_0^{\text{Al}}/X_0^{\text{Ta}} \simeq 22$, $T = N_{\text{f}} \times \delta t / X_0^{\text{Ta}}$ is much larger than $G = (N_{\text{f}} - 1) \times \delta g / X_0^{\text{Al}}$, *i.e.* essentially no bremsstrahlung will originate from an Al spacer foil relative to a Ta foil of similar thickness. We used spacings of 6, 8 and 12.5 μm Al foils (with mechanical tolerances of ±25%), which should give detectable resonanses at both $E_0 = 206$ GeV and 234 GeV, cf. Table 5.1.

Moving to lower photon energies

The targets described in the previous section were designed taking the LG threshold into account. The small gaps necessitated strong demands on the mechanical tolerances of the spacers. If the spacer foils had bumps increasing the effective gap width by a mere 10 μm, the structure would shift below the detector threshold.

To remedy this, the group purchased the BGO. With this "low-energy" calorimeter, the SR from the purging magnet `B16` constituted the effective lower threshold, *i.e.* a order of magnitude lower, depending on the primary energy and field in `B16`. Under these circumstances, using thicker gap foils becomes possible—even $\delta g \gtrsim 100$ μm, which corresponds to $\hbar\omega_r \lesssim 0.646$ GeV at $E_0 = 207$ GeV, the beam energy used in this experiment. Gap foils of such dimensions can be provided with better tolerances, and the relative influence of foil bumps is smaller. With the more resilient spacer foils, it was possible to mechanically remove a central hole of ⌀ 18 mm, and the spacers were used in a target assembly similar to the one sketched in Figure 3.2a on page 36. The structured target comes in this central region very close to Blankenbecler's original idea, since $X_0^{\text{Air}} = 303.9$ m [Y$^+$06]. Because the electrons selected by the trigger condition $\texttt{Sc1} \cdot \texttt{Sc2} \cdot \overline{\texttt{Sc3}}$ would not pass through the spacer material, the choice of material was not restricted to ones with long radiation lengths. According

to the local workshop, surface polished foils of phosphor-bronze came closest to the mechanical properties we sought, and would—hopefully—provide equidistant Ta foils.

By using a micrometer gauge, 9 spacers' mean width was measured to $\langle \delta g \rangle_s = 88.1 \pm 0.7$ μm corresponding to $\hbar\omega_r = 0.736$ GeV. Using these spacers, a sandwich target $10 \times$ Ta10Air90 and a reference target $10 \times$ Ta10Air1000 (TSF) were prepared. By measuring the sandwich target assembly's full thickness with a micrometer gauge and subtracting the known amount of material besides the spacer foils, we have estimated the total mean spacing to $\langle \delta g \rangle_t = 91.2 \pm 0.7$ μm, not far from the expected 88.1 μm. The $\langle \delta g \rangle_a = 3.1$ μm extra material most likely stems from air between non–close-fitting foils.

Although the measured mean spacing in the target seems right, a large variation of the individual distances could blur the peak to a degree where it would not be detectable within our uncertainties. We consider three normalized Gaussian distributions P_s, P_a and P_t representing the spacer width, extra air gap, and the total, measured gap. The three Gaussians have RMS values $\sigma_s = 0.7$ μm, σ_a and $\sigma_t = 0.7$ μm, respectively. If the spread of extra air (σ_a) is large, the effect could should occur at a distribution of photon energies, *i.e.* not so distinctly. The combination of spacers of random width with random widths of air is expressed through a convolution—leading to a new Gaussian distribution with a mean $\langle \delta g \rangle_c = \langle \delta g \rangle_s + \langle \delta g \rangle_a = 91.2$ μm and RMS

$$\sigma_c = \sqrt{\sigma_s^2 + \sigma_a^2} \tag{5.2}$$

By integrating the product of the convolution and P_t, the probability of actually having extra air with a spread σ_a is found. The product of two Gaussians is yet another Gaussian with RMS σ and area P

$$\sigma = \frac{\sigma_c \sigma_t}{\sqrt{\sigma_c^2 + \sigma_t^2}} \tag{5.3a}$$

$$P = \frac{\sqrt{2\pi}\sigma}{2\pi\sigma_c\sigma_t} = \frac{1}{\sqrt{2\pi(\sigma_s^2 + \sigma_a^2 + \sigma_t^2)}} \,. \tag{5.3b}$$

With our parameters and $\sigma_a = 10$ μm, P is a mere 4%. Thus, the spacing of foils is likely to be 91.2 μm with a variation of $\lesssim 5\%$. To measure the individual, actual spacings in the assembly without disassembling the target, and thus affecting the result, is very difficult and has not been attempted.

We considered measuring the spread of the spacings by setting up a standing sound wave across the target. Using a frequency generator, a sound wave of frequency f_s could be produced. With our distance between the center of the foils $\delta t + \delta g \simeq 100$ μm, a resonance in the transmitted sound wave would occur when the nodal points would coincide with the target foils, leading to the condition

$$\begin{aligned} \delta t + \delta g &= n\lambda_s/2 \\ f_s = \frac{c_s}{\lambda_s} &= n\frac{c_s}{2(\delta t + \delta g)} = nf_1 \,, \end{aligned} \tag{5.4}$$

where n is a positive integer and $c_s = 343$ m/s is the propagation speed of sound. When measuring the amplitude of the transmitted sound wave with a transducer

	Fit, 206 GeV		Fit, 234 GeV		Measured
Label	$T+G$	χ^2/DOF	$T+G$	χ^2/DOF	$T+G$
$1\times$ Ta100	2.09(5)%	0.97	2.02(7)%	1.00	2.58(1)%
$20\times$ Ta5Al6	2.00(5)%	1.01	1.94(6)%	1.01	2.29(1)%
$20\times$ Ta5Al8	2.05(4)%	0.96	—	—	2.33(1)%
$10\times$ Ta10Al12.5	2.54(5)%	0.97	—	—	3.01(1)%

Table 5.2: Thickness of targets found by fitting and measuring. For each fit, the minimized χ^2 per degree-of-freedom (DOF) is shown.

while scanning f_s, the width of the resonance near nf_1 should resemble the spread of $\delta t + \delta g$. With our conditions, $f_1 = 1.72$ MHz and we thought of using piezoelectric elements as actuator and transducer. However, it turned out that typical piezoceramics would have resonances—due to their geometry—in our frequency domain. After these considerations, the method was abandoned.

In the following section, I present the results of measurements on the sandwich target types mentioned above. To summarize, the main objective is to be able to distinguish the TSF effect of each foil and the anticipated sandwich effect, when the formation zone extends across a gap between two foils in our experiment.

5.3 Analysis & Results

With the sandwich targets built by Ta foils kept apart by 6, 8 and 12.5 μm Al foils, measurements were performed at 206 GeV and—in the case of $1\times$ Ta100 and $20\times$ Ta5Al6–also at 234 GeV. The data was projected onto histograms with linear binning which were background compensated and normalized to N_e, but not the thickness. Instead, the BH expression of Eq. (1.16) was fitted to each power spectrum in the region 22–45 GeV, where suppression effects should not have set in. While fitting, data was properly weighted by the statistical error and E_0 was kept fixed, leaving the total thickness in units of X_0 $(T+G)$ as the only free parameter. The thicknesses found from fitting can be seen in Table 5.2. The fitted values of $T+G$ are systematically smaller than the nominal ones (cf. Table 5.1), so I measured the area density of the Ta foils using a precise weight and a vernier caliper to measure the area of a foil. The equivalent target thicknesses are also listed in Table 5.2 and are in better agreement with the nominal values from foil supplier. Since some differences between the BH spectrum and data are anticipated due to the exaggerated pile-up effect originating from the background compensation, the experimental thicknesses are expected to appear a bit smaller than the nominal ones.

To avoid some systematic errors, the data was in [I] presented in the form of a power spectrum enhancement—here defined by the sandwich power spectrum relative to that corresponding to $1\times$ Ta100. As seen in Figure 5.3a, the ratio of the spectra is consistent with 1 at $\hbar\omega \gtrsim 10$ GeV. At lower photon energies a $\simeq 50\%$ enhancement is seen. The equivalent plots for the other targets show the same tendency and can be inspected in [I]. The shown error bars represent only the statistical errors, and, unfortunately, the magnitude of these alone makes it difficult to determine the number

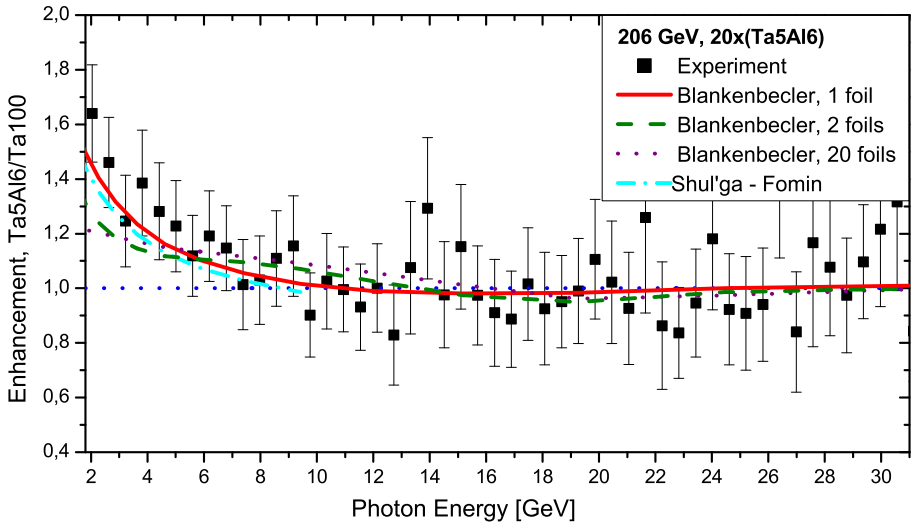

(a) Linear scale.

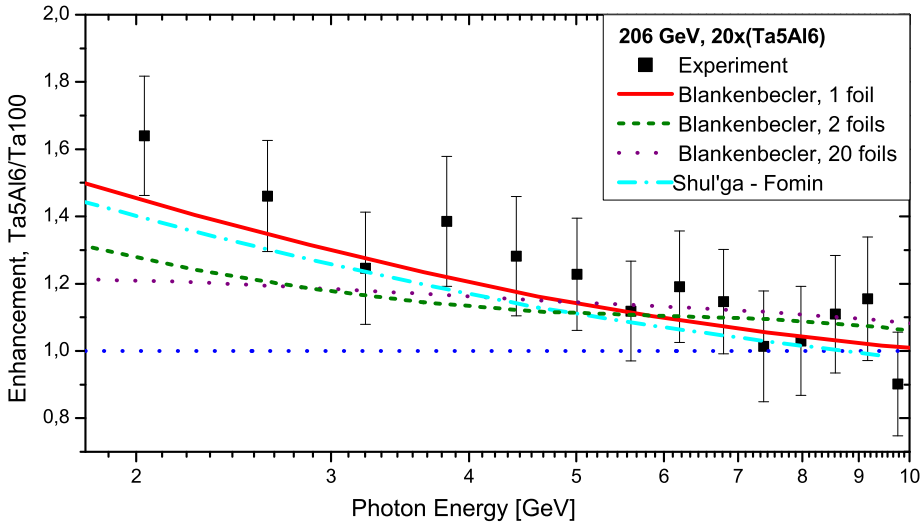

(b) Lower energy part of the enhancement spectrum shown on a logarithmic scale.

Figure 5.3: The enhancement of the 20 × Ta5Al6 relative to 1 × Ta100 as a function of photon energy at $E_0 = 206$ GeV. The enhancement is compared to the corresponding theoretical values as calculated using the BD [BD96] and SF formalism [SF98b]. Only statistical errors are shown.

of foils contributing to the effect, *i.e.* to distinguish between the TSF and sandwich effect.

At the later experiment involving the BGO and the $\delta g \simeq 90$ µm phosphor-bronze spacers, the relative statistical errors were brought down considerably. In Figure 5.4a, the BCPS of the sandwich target (10 × Ta10Air90) and the reference target (10 × Ta10Air1000) are shown. For comparison, the measured spectrum of a 1 × Ta100 is also shown. All spectra have here been corrected by the BGO efficiency discussed in Sec. 3.3—a method that generates a small contribution to the systematic

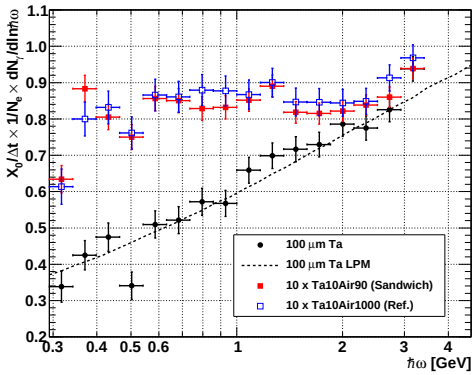

(a) Normalized power spectra for the different foil types. A background spectrum has been subtracted, and all spectra have been corrected by the BGO efficiency shown in Fig. 3.5 on page 41. Data for a $1 \times$ Ta100 target is shown for reference. The latter spectrum is compared to LPM simulations based on [MBSU08] and good accordance is evident.

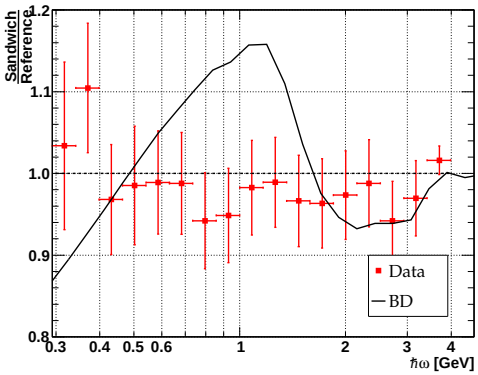

(b) Ratio of measured power spectra, $(10 \times$ Ta10Air90$)/(10 \times$ Ta10Air1000), and corresponding ratio of BD calculations [BD96].

Figure 5.4: Absolute and relative sandwich spectre measured at $E_0 = 207$ GeV. The reference and sandwich target spectra are close to identical.

errors of the spectra. To avoid this, the ratio of the power spectra is computed, cf. Figure 5.4b, by which the multiplicative BGO efficiency is eliminated. Also found in the plot is the ratio of theoretical BD calculations [BD96, Bla97b] of the spectra based on the target geometries. As seen, an effect of the expected magnitude—which is $\simeq 15\%$ on this scale—is clearly not supported by our data. The distinct peak at $\simeq 1$ GeV in the calculations is absent in the data, and it seems that the best description of the data is that there is no effect originating from bringing the foils closer together. These results were also presented in [II].

5.4 Improving the Setup

Quite recently, a vastly improved sandwich experiment setup was designed with the target holder equipment shown in Fig. 5.5. Using a high-precision remote-controlled z translation table, the distance between only $N_\mathrm{f} = 2$ foils can be varied from $\simeq$ 10 μm to $\simeq$ 200 μm with an accuracy of ± 3 μm. To lower the value of N_f was suggested by the late Vladimir N. Baier during his visit in Aarhus, as a larger number of target foils in the assembly could "destroy the effect" [BK10].

Controlling Foil Surfaces and δg

The improved setup is inspired by the so-called plunger device presented in [BDSS77]. Here, the similar device was used to study nuclear life times using the recoil distance method. Two circular $\varnothing$ 25.0(5) mm Ta foils of nominal thickness $\Delta t = (20 \pm 3)$ μm were stretched across the target holders, like a drum hide. After the mounting pro-

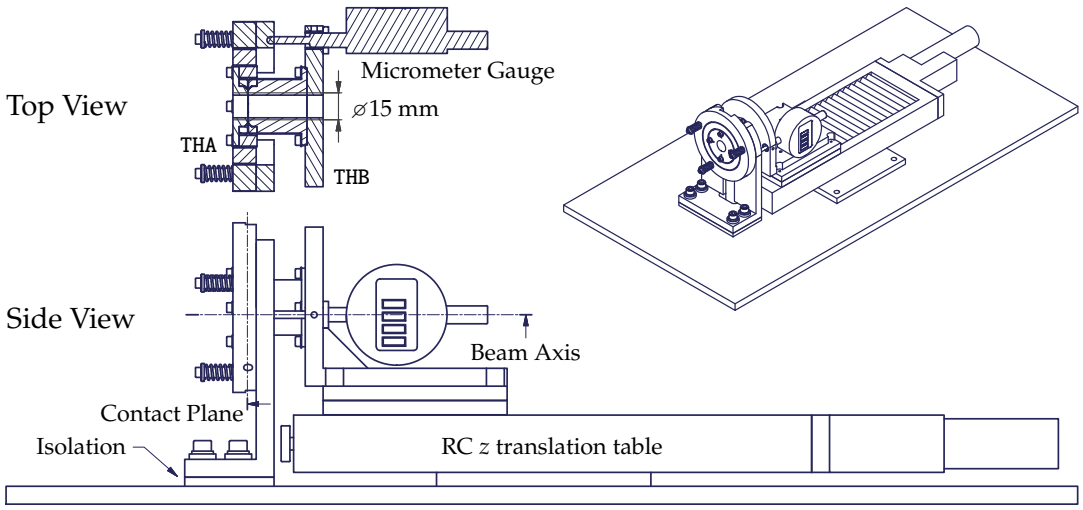

Figure 5.5: *Top View*: The two target holders (THA and THB) can slide together allowing the foils to obtain contact. THA is mounted on a gyro such that it aligns angularly with THB when $\delta g \to 0$. The detector holders have central holes of ⌀15 mm, intended for the ⌀9 mm electron beam. *Side View:* δg is remote-controlled (RC) by moving THB with a z translation table of very high precision. THA is electrically isolated from the remaining setup. In this way, the distance δg can be probed both by reading a micrometer gauge and measuring the electrical resistance/capacitance between the target holders. Courtesy of IFA's workshop.

cess, it is imperative that the foils are still flat on the scale of few microns. Because the supplied Ta foils are reflective, their surfaces could be examined using a laser-based, ultra-high-accuracy distance meter—in our case, the Keyence LC-2430. A laser diode projects a small spot onto a reflective surface at an angle. The reflected laser beam hits a Position Sensitive Device (PSD), and the distance is determined by triangulation, cf. Figure 5.6. The PSD could be a Charge Coupled Device (CCD) or a Complementary Metal–Oxide–Semiconductor (CMOS) sensor. The Keyence LC-2430 sensor can measure distance with a resolution of 0.02 μm within an operating distance of 30.0 ± 0.5 mm. The minimum laser spot size is as little as 30×20 μm^2, depending on the operating distance. Any curvature or angle of the surface will cause the laser beam angles ϕ and ϕ' (with respect to a normal to the apparatus) to be unequal. When the laser spot probes an angled surface, the apparent distance will be different from the actual distance, and any curvature will thus be slightly exaggerated. A negatively sloped surface $(dz/dx < 0)$ on Figure 5.6 will give rise to $\phi < \phi'$, and the apparent distance will be larger than the actual and *vice versa*.

When measuring the distance to the target surface to the mentioned level of precision, the slightest angle of the target plane relative to the plane in which the distance meter is moved influences the measured value of z. Even angles $\simeq 10$ mrad are detectable and will appear as linear correlations between z and the transverse coordinate of a 1D scan—x or y. We are not particularly interested in this angle since THA is mounted on a gyro allowing the target holders to align, *i.e.* compensate for such average mounting/measuring angles. Because of this, a linear fit $f_1(x)$ is made to the $z(x)$ data, and $z_{\text{corr}}(x)$ is the distance between $z(x)$ and $f_1(x)$. As a test of

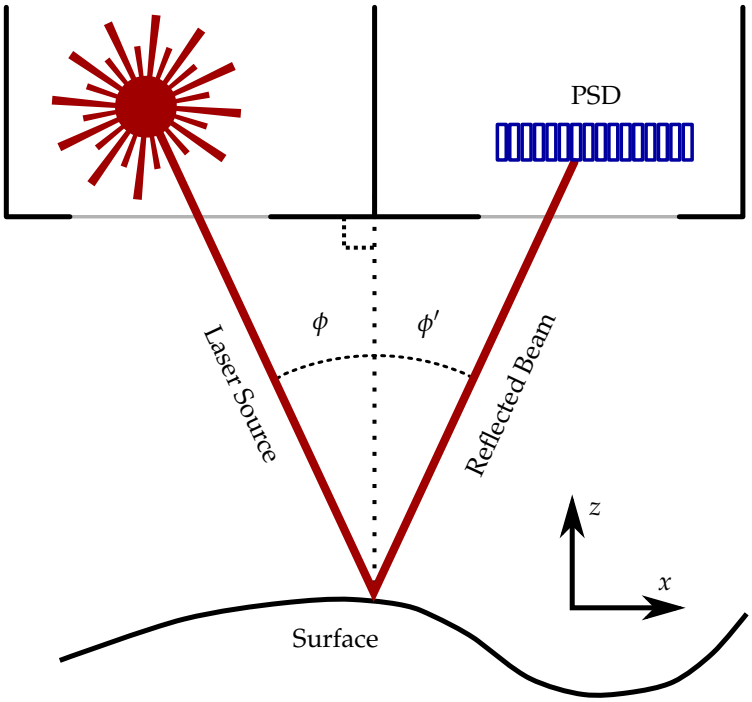

Figure 5.6: Measuring surface uniformity using triangulation on a reflected laser spot. The reflected beam's position in the PSD is a linear function of the distance z.

the accuracy of the distance meter setup, I scanned a hard disk drive platter, still mounted in its spindle. In a hard disk drive, the small separation between the spinning platter and the read/write head hovering over the platter (tens of nm in newer drives) necessitates an extreme degree of flatness of the platter. By spinning the platter a random angle and measuring, an RMS of z_{corr} was found to be (1.2 ± 0.2) µm, primarily resembling the accuracy of our setup in Figure 5.6.

A number of ways of mounting a set of Ta foils on the target holders have been attempted—including clamping them on with concentric metal rings, using araldite glue, or thin double-sided tape. In each case, the surface uniformity was examined after mounting. The mounting technique, which was found to give rise to the highest degree of target surface uniformity, was to mount the foils on thin glass plates and then install the glass plates on the respective target holders, in both cases using thin double-sided tape. Each piece of glass was 150 µm thick, corresponding to 0.14% X_0 of background.

In Figure 5.7, examples of the target examinations are shown. In all cases, the mounted target is a Ta target with nominal thickness of 20 µm. The RMS of z_{corr} is seen to be less than 3µm, thus facilitating $\delta g \gtrsim 30$ µm with good relative accuracy. With the value of $\delta t = 20$ µm, the origin of the formation length (somewhere in the first foil) is relatively well-defined relative to a gap width of *e.g.* $\delta g = 3\delta t = 120$ µm. Also, the combined thickness of $2 \times$ Ta20Airδg is 0.98% X_0 ($\delta g \lesssim 1$ cm), so using thinner foils would be unfeasible, considering the typical radiator background level.

The gap can be measured by reading back the z-translation table and a precision micrometer gauge. An indirect determination of δg is possible by measuring the capacitance between the foils, as `THA` is electrically isolated from the remaining setup.

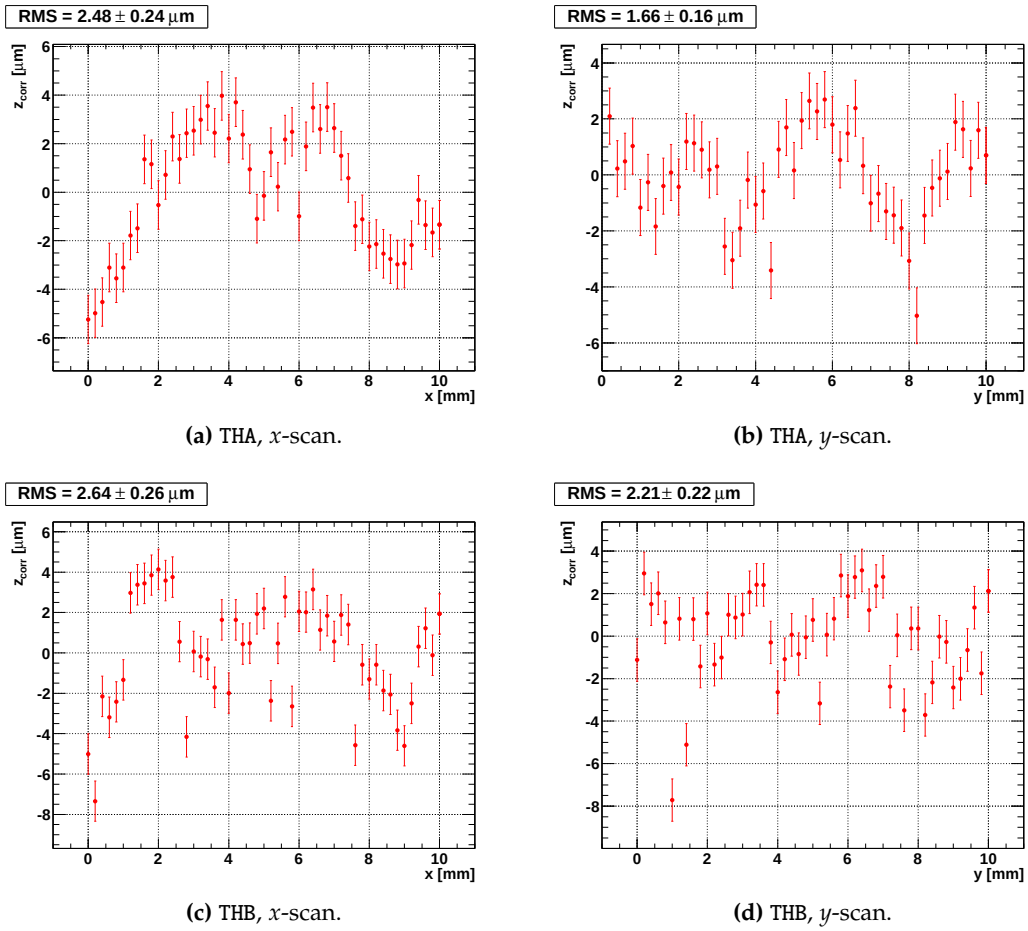

(a) THA, x-scan. **(b)** THA, y-scan.

(c) THB, x-scan. **(d)** THB, y-scan.

Figure 5.7: Preliminary checks of quality of mounting techniques. The corrected surface distance z_{corr} is shown as a function of the transverse coordinate (x/y). The RMS value of z_{corr} is in each case shown as a quality measure of the surface uniformity.

The sandwich effect supposedly occurs at photon energies near $\hbar\omega_r$, cf. Eq. (5.1). The inherent dependence on δg could be examined by comparing spectra from two different δg settings. It is especially interesting to find the difference between a spectrum corresponding to a low gap and one corresponding to a very large gap, $\delta g \gg \ell_{\text{f0}}$ for the photon energies accessible with the BGO. Because the foils of the two configurations are identical, many systematic errors, *e.g.* those originating from the background compensation and target foil differences, will cancel in the subtraction.

Theoretical Expectations

In [BK99a], Baier & Katkov (BK) treat the radiation emission from a stack of thin foils, including the LPM effect, TM polarization effects, and emission from the target boundaries (TR). For the general case of N_{f} foils, however, they only give an explicit formula for the strong scattering, large spacing case where $b_{\text{BK}} = \alpha X_0^{\text{t}}/2\pi\delta t \ll 1$ (the scattering variable) and $T_{\text{BK}} = (\delta t + \delta g)/\ell_{\text{f0}} \gg 1$ [BK99a, Eq. (2.49))]. In the

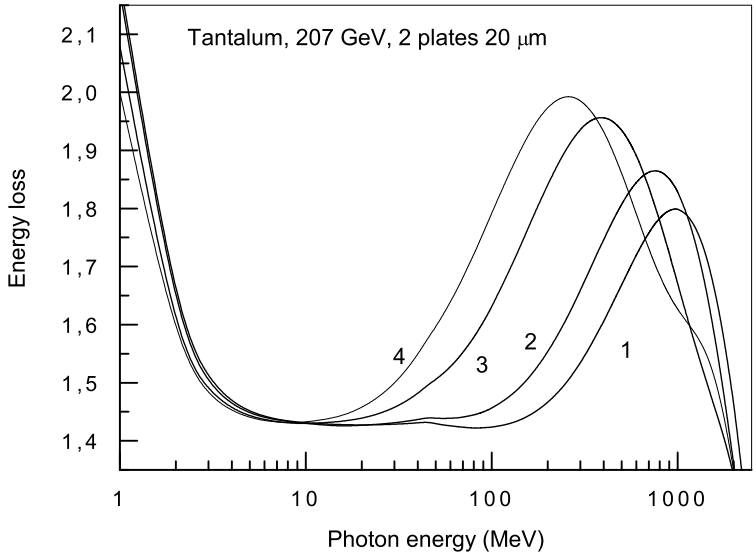

Figure 5.8: Baier's calculation of $2 \times$ Ta20Airδg [BK10]. The curves labelled 1–4 correspond to $\delta g = 1, 2, 6$ and 10 multiples of $\delta t = 20$ μm. Ordinate scale is in units of $2\alpha/\pi$, in which the BH level of 40 μm Ta is $4\Delta t/3X_0^{\mathrm{Ta}} \simeq 2.80 \times 2\alpha/\pi$. Courtesy of V.N. Baier [BK10].

case of the $10 \times$ Ta10Air90 targets, $b_{\mathrm{BK}} = 0.48$ does not fulfill the requirement, and the length variable $T_{\mathrm{BK}} \not\gg 1$ for photon energies in the interesting region, for instance $T_{\mathrm{BK}} = 1.08$ for $\hbar\omega = 0.700$ GeV at $E_0 = 207$ GeV. The theory of BK is thus not directly applicable for $b_{\mathrm{BK}} \simeq 1$ and large values of N_{f}, as BK also notes in [BK99a] during a comparison with the $N_{\mathrm{f}} = 4$ results of [Bla97b]. Hence, BK perform only qualitative analysis during this comparison.

BK's theory presented in [BK99a] is—like [BK98]—close to complete with respect to the effects and corrections considered, but alas, at the cost of transparency. Nevertheless, they were so helpful as to supply us with results based on [BK99a] of the expected power spectrum from targets of the type $2 \times$ Ta20Airδg where $\delta g/\delta t = 1, 2, 6, 10$ [BK10]. For example, with the target $2 \times$ Ta20Air40, $b_{\mathrm{BK}} = 0.24$ and $T_{\mathrm{BK}} = 1.40$ for $\hbar\omega = 1.50$ GeV at $E_0 = 207$ GeV. Their result is shown in Figure 5.8. In Figure 5.9, the BK curves are scaled to the BH level of 40 μm Ta, *i.e.* the curves now correspond to the BD F function. At the larger foil spacings, BD and BK more or less agree on the peak position and absolute magnitude of the effect, though BD's TSF level lies lower than BK's. At the two smallest spacings—and larger photon energies, generally—the mismatch between the set of calculations is larger. Conceptually, the F function should approach unity at larger photon energies. The reason why the solid lines (BK) seem to plunge at the largest photon energies is unknown, but it could be due to the onset of some destructive interference.

Optimal Foil Thickness

The difference between the spectrum of a $N_{\mathrm{f}} = 2$ sandwich target ($2 \times$ TaδtAir120) and its corresponding TSF spectrum ($2 \times$ TaδtAir∞) is considered. To be more specific, we estimate the relative statistical error arising from a subtraction of the two.

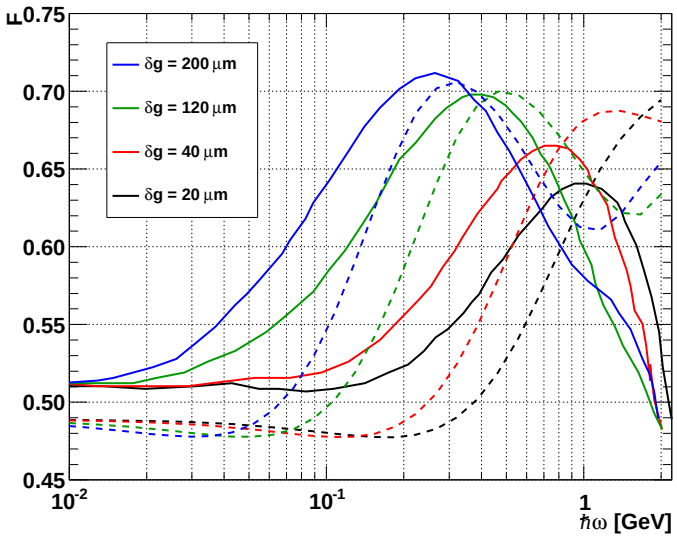

Figure 5.9: The solid lines are BK's from Figure 5.8 only with the ordinate scaled by the BH level of 2×20 μm Ta. Each solid curve is accompanied by a dashed curve calculated with the BD code for the same energy ($E_0 = 207$ GeV) and geometry parameters.

The number of photons in a photon energy interval can be found by combining Eq. (2.2) with the BD F-function

$$N_\gamma(\hbar\omega_1, \hbar\omega_2) = N_e W_0 F = N_e w_0 \Delta t F \,, \tag{5.5}$$

where $w_0 \equiv W_0/\Delta t$. Considering a logarithmically binned spectrum, $\hbar\omega_1$ and $\hbar\omega_2$ are taken to be the upper and lower edge of a single bin. The photon counts in this bin are labelled $S+B$ and $R+B$ in the raw sandwich and raw reference spectrum, respectively. Neglecting multi-photon effects, S and R represent the pure spectrum counts, while B represents the number of background counts. Assuming Poisson-statistics, the difference in bin content and the variance can be computed

$$D = (S+B) - (R+B) = S - R \tag{5.6a}$$

$$\sigma_D^2 = (S+B) + (R+B) = S + R + 2B \,. \tag{5.6b}$$

We can use Eq. (5.5) to express the number of photons from each source, *i.e.* $X = N_e w_0 \Delta t_X F_X$, where X is S, R or B. The relative statistical error of D can then be expressed as

$$\begin{aligned} \frac{\sigma_D}{D} &= \frac{\sqrt{N_e w_0 [2\delta t (F_S + F_R) + 2\Delta t_B F_B]}}{N_e w_0 2\delta t (F_S - F_R)} \\ &= \frac{\sqrt{\delta t (F_S + F_R) + \Delta t_B F_B}}{\sqrt{2 N_e w_0} \delta t (F_S - F_R)} \,, \end{aligned} \tag{5.7}$$

where $\Delta t_S = \Delta t_R = 2\delta t$ has been used. The BD functions F_S and F_R depend on the target geometry $(\delta t, \delta g)$, E_0 and $\hbar\omega$, while $F_B = 1$ can be assumed. For many

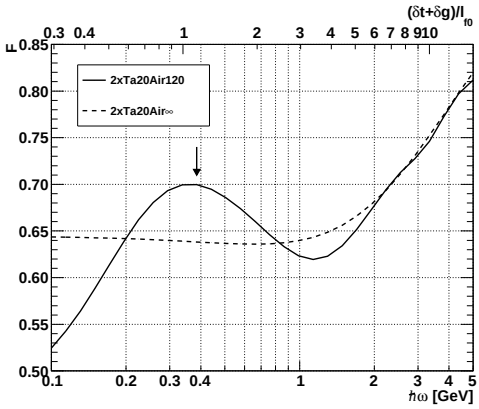

(a) Example of the Blankenbecler curves under consideration. A sandwich target is compared to its corresponding TSF calculation. The arrow marks the photon energy where the difference is largest.

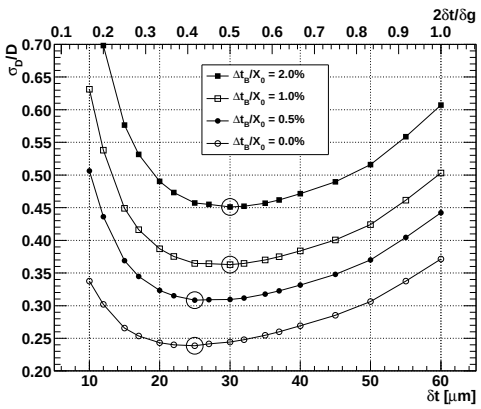

(b) The relative error is found at point of maximum effect. By assuming different background levels, the thickness δt, which causes minimum relative error, is seen to shift slightly. At each value of δt, a set of Blankenbecler curves—as seen in (a)—has been calculated.

Figure 5.10: Finding the optimal thickness of the $N_\mathrm{f} = 2$ foils when considering a background. In all calculations, $N_e = 2 \times 10^6$ and $E_0 = 178$ GeV.

different values of δt, F_S and F_R have been calculated for $\delta g = 120$ μm with the BD formalism. An example of the results can be seen in Figure 5.10a. In each case, the maximum value of $F_S - F_R$ is located and found near $(\delta t + \delta g)/\ell_{\mathrm{f}0} = 1$. At this point, marked by an arrow in the figure, F_S and F_R are extracted.

Assuming $N_e = 2 \times 10^6$ primary particles, $\hbar\omega_1 = 0.33$ GeV, and $\hbar\omega_2 = 0.42$ GeV (10 bins per decade), $F = 1$ leads to a bin content of $N_\gamma = 1.5 \times 10^4$ in the case of 100 μm tantalum. As a function of δt and Δt_B, σ_D/D can be computed using Eq. (5.7), and the result is shown in Figure 5.10b. Since the sandwich effect is of limited magnitude, *i.e.* $F_S \lesssim 1$, the effect will disappear $(F_R \to F_S)$ when the reference spectrum approaches the BH level at very thin targets. This makes the relative uncertainty increase rapidly at low values of δt. At very large foil thicknesses, the effect is smeared once the gap becomes less pronounced in the geometry, *i.e.* $2\delta t/\delta g \simeq 1$. In between these regimes, a value of δt minimizing the relative error given a background radiator level can be found. For each curve, the minimum point is marked with a ◯. A non-zero background is seen to have two effects. Firstly, the relative errors are generally increased—especially where $2\delta t/X_0 \ll \Delta t_B/X_0$ causes a poor signal-to-background ratio. Secondly, since the background makes thin targets unfavorable, the optimal value of δt is slightly increased by the background. The optimal thicknesses are not far from the tested $\Delta t = (20 \pm 3)$ μm foils.

It is clear from Figure 5.10b that even the typical backgrounds can threaten significant detection of the sandwich effect. Although the background is eliminated by the subtraction, the statistical errors can be greatly increased. Even in the absence of backgrounds, the statistical errors are considerable, and the chosen number of primary events per spectrum is definitely a minimum and corresponds to $\simeq 5$ h of beam per spectrum, if the optimal beam intensity at $E_0 = 178$ GeV experienced in May 2010 can be reproduced. If so, even $N_e = 2 \times 5 \times 10^6$ would be attainable within

$\simeq$ 24 h of beam, thus reducing the statistical errors. Increasing the bin width slightly has the same effect, but the chosen binning ($\hbar\omega_1 = 0.33$ GeV and $\hbar\omega_2 = 0.42$ GeV) seems appropriate to resolve the sandwich structure, cf. Figure 5.10a.

◇ ◇ ◇

The results from a number of different attempts at realizing the sandwich targets have been presented. Although several independent theoretical models predict a structure where the formation length stretches across a gap of relatively long radiation length $\ell_{f0} \gtrsim \delta g$, no experimental confirmation of the effect is seen using targets of $N_f \geq 10$ foils. The theoretical approaches agree, to some extent, on the magnitude of the effect, which should be within our experimental errors.

The absence of the effect could be explained by a considerably larger mean or deviation of the individual gap spacing δg. The prior is ruled out in the case of the spacers of nominal width $\delta g = 90$ μm, but the latter could compose a relevant problem, although shown to be unlikely. With the improved setup based on only $N_f = 2$ foils but with well-controlled, variable gap, it is shown that the surface of the mounted foils are smooth even to $\lesssim 5$ μm scale. If the effect is of the predicted magnitude, it should be detectable by comparing a spectrum measured at, for example, $\delta g = 120$ μm to one measured at $\delta g = 5$ mm, cf. Figure 5.9. With the improved setup, the sandwich target parameters can be controlled and the target distance δg can be varied *in situ*, thus eliminating the systematic errors due to target differences. In an attempt to find the optimal choice of δt in the $N_f = 2$ target, the effect of the background and statistical errors were studied.

The improved setup has yet only been tested under few hours of erratic beam conditions yielding no credible results.

CHAPTER 6

THE LOW Z-LPM EFFECT

In 2009, using the same setup as during the TSF experiment, cf. Chapter 3, we performed a pilot study of the possibility to measure the low-Z LPM carbon and aluminum. The results were presented in [II] where they were met with great interest from the referees. A more thorough study of the effect in low-Z materials is motivated by experimental hints of deviation from acknowledged theories.

6.1 Motivation

As mentioned in Sec. 1.3 on page 12, the LPM effect is by now experimentally well-studied in the classical and—to some extent—also the quantum regime, primarily for high-Z targets. The careful SLAC experiments included 8 and 25 GeV electrons impinged on 2% or 6% X_0 carbon ($Z = 6$) foils [A$^+$97]. The exhibited power spectrum shapes were compared with MC simulations including TR, the LPM and TM effect. They used the original Migdal formulation [Mig56] as their LPM model. Good accordance was found in almost all cases except for the targets of iron and carbon, cf. Figure 6.1 for data of the latter element. As seen in the figure, the full simulation (solid line) fit the low-Z data to an impressing degree at $E_0 = 8$ GeV, whereas at the larger primary energy [A$^+$97]

> *...the suppression appears to turn on at higher [photon] energies and more gradually than predicted by the MC simulation...*

Explanations for this discrepancy cover target density inhomogeneities (*i.e.* leading to inhomogeneous degrees of suppression throughout the target), need of a 20% calorimeter signal diminution (at only these elements), implausibly large levels of target contamination by elements of larger Z. In the case of carbon—their target of lowest Z—Spencer Klein also poses the idea that Migdal's LPM model could be deficient with respect to low-Z targets [Kle99]. Indeed, many of the theoretical models are optimized for high-Z materials, in which the LPM effect is also best tested in accelerator based experiments due to the limited primary energy. For example, BK's

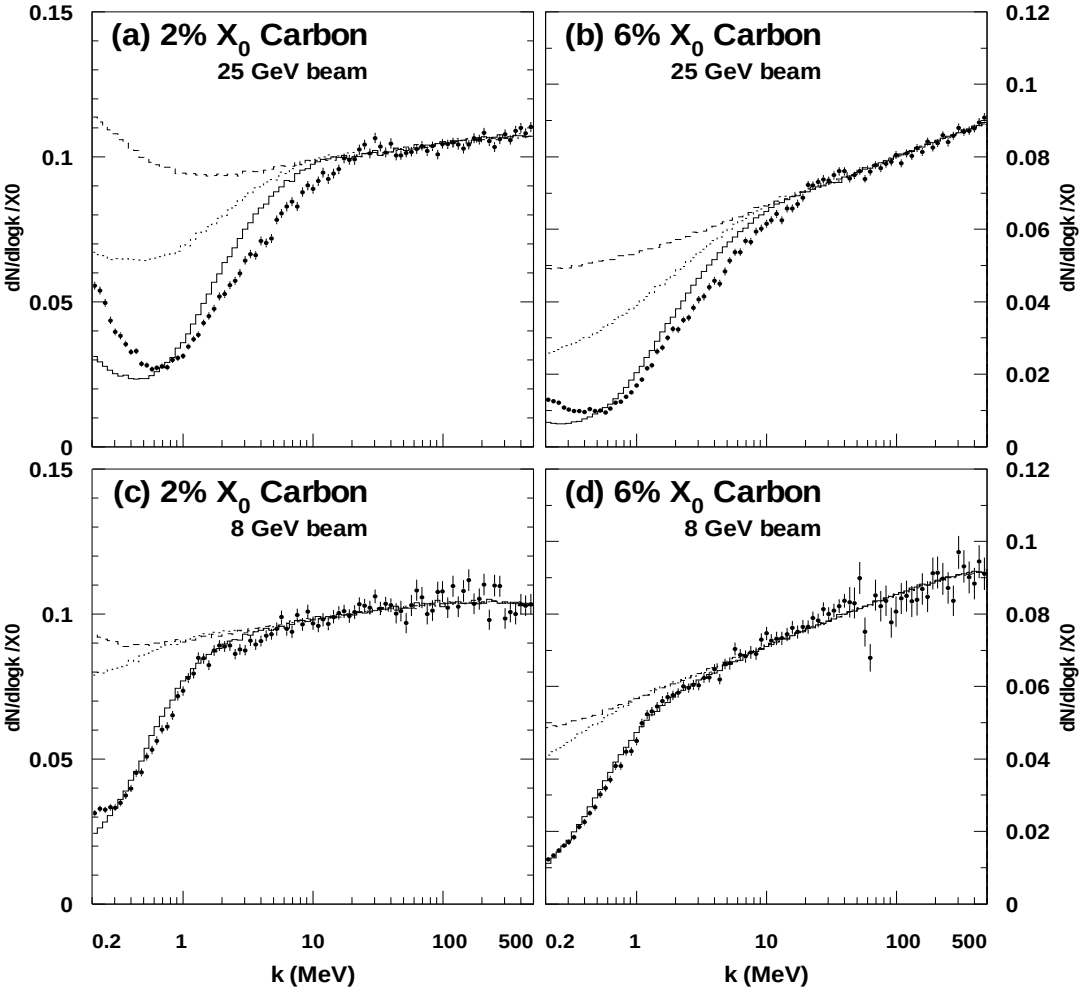

Figure 6.1: The carbon data from the SLAC E-146 experiment. The lines correspond to MC simulations including LPM + TM + TR (solid line), LPM + TR (dotted line) or BH + TR (dashed line). The 8 GeV data (lower panels) is clearly seen to fit better with simulations than the 25 GeV data (upper panels). Adapted from [A$^+$97].

sophisticated screening distance including Coulomb corrections [BK98]—Eq. (4.1) on page 49—is based on the Thomas-Fermi (TF) radius $0.81a_0Z^{-1/3}$, which is known to poses caveats in low-Z materials. As carbon is on the verge of the typical range of applicability of the TF model, $Z \geq 5$ [Tsa74], the electron screening in carbon must be described to a lower level of precision. The lower precision will propagate to the accuracy of the LPM formalisms not treating the low-Z screening properly.

As it is, the Migdal formalism is known to have at least one small flaw leading to a discontinuous first derivative of the resulting power spectrum. The Migdal formalism is the basis of the LPM bremsstrahlung implementation described in [MBSU08], and results, obtained using an improved version of this, are shown in Figure 6.2a. The full curves are based on the Migdal theory and possess the problem described. The problem stems from Migdal's $\zeta(s)$ function, and the dashed curves are a result of adding a small term to the function, thus trying to remedy the problem without affecting the rest of the spectrum. One would have to measure the power spectra to

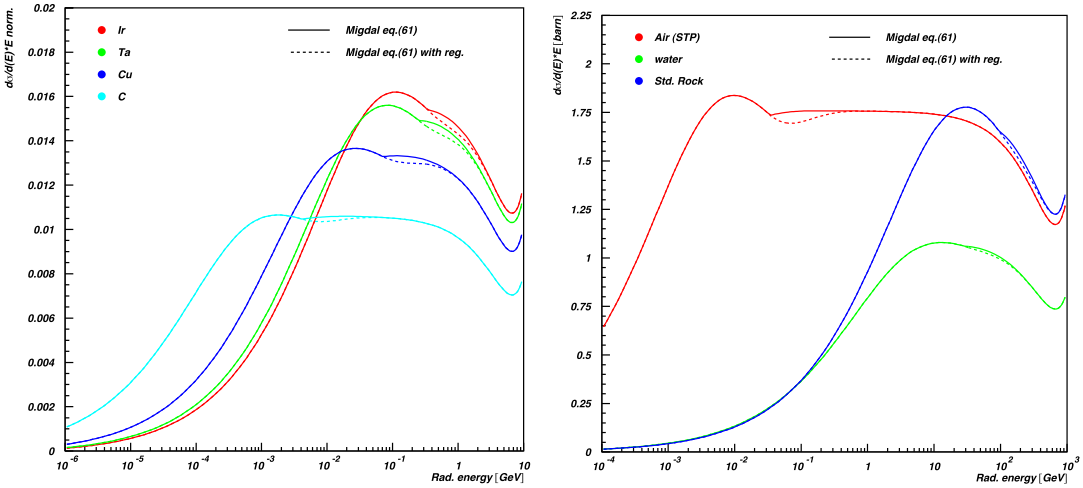

(a) $E_0 = 10$ GeV electrons traversing foils of iridium, tantalum, copper and carbon. Full lines show the results of the regular Migdal formulation, while the dashed lines are with the regularization attempting to rectify the spectrum only where its first derivative is discontinuous.

(b) $E_0 = 1$ TeV electrons traversing STP air, water and rock. The definition of standard rock ($Z = 11$, $A = 22$ $\rho = 2.65$ g/cm^3, $X_0 = 10.0$ cm) is adapted from [Kle99]).

Figure 6.2: Photon power spectra found from GEANT3 MC studies using the improved version of [MBSU08]. Courtesy of Alessio Mangiarotti.

a level of precision far beyond the scope of NA63 to determine whether the small correction is right.

To verify the LPM theory for materials of low-Z becomes crucial when treating cosmic ray generated air showers of immense energies—up to the Greizen-Zatsepin-Kuz'min cutoff $\simeq 5 \times 10^{19}$ eV—since the atmosphere consists predominantly of low-Z materials (N_2, O_2, Ar, CO_2). At the larger primary energies, almost the entire power spectrum is influenced by the LPM effect, cf. Eq. (1.21) and Figure 6.2b. As with many other aspects of the LPM effect, Klein gives a nice review of this in [Kle99].

6.2 The Pilot Study

As mentioned previously, the pilot study was performed with the same setup as the TSF experiment, cf. Chapter 3. The results of the pilot study were also presented in [II]. One difference was the larger primary energy of $E_0 = 207$ GeV, which was chosen as a trade-off between increasing the value of the LPM upper thresholds $\hbar\omega_{\mathrm{LPM}} \propto {E_0}^2$ ($E_0 \ll E_{\mathrm{LPM}}$), cf. Eq. (1.21), while retaining proper beam intensities.

In Tab. 6.1 on the following page, the thickness and $\hbar\omega_{\mathrm{LPM}}$ are shown for the three targets composed of carbon (rigid graphite), aluminum and tantalum. As seen in the table, at least aluminum (and tantalum) should be within the LPM regime using a $E_0 = 207$ GeV beam. As also seen here, the targets are of comparable thickness in units of X_0. Although their shapes are not mutually compared, the thickness $\Delta t / X_0$ determines the relative influence of Synchrotron Radiation (SR) in the background compensated power spectra, as described in Sec. 2.2. In the experiment, the LPM

	X_0 [mm]	E_{LPM} [TeV]	Δt [$\%X_0$]	$\hbar\omega_{\mathrm{LPM}}^{149}$ [GeV]	$\hbar\omega_{\mathrm{LPM}}^{207}$ [GeV]
C	245.4	189	1.97(1)	0.118	0.228
Al	88.97	68.4	2.27(2)	0.324	0.628
Ta	4.094	3.15	2.63(4)	6.74	12.8

Table 6.1: Radiation lengths [Tsa74], E_{LPM}, target thicknesses and LPM photon energy thresholds for the three materials and beam energies used.

targets were mounted on the target wheel (cf. Fig. 3.2b on page 36), and $N_e \simeq 1 \times 10^6$ events were registered for each of the three targets and the background.

Analysis & Results

The resulting normalized power spectra with 15 bins/decade—with background subtracted properly—were corrected by the BGO efficiency (cf. Fig. 3.5 on page 41) found at $E_0 = 149$ GeV. As seen in Figure 6.3a, the tantalum data is in excellent agreement with a LPM simulation, giving confidence to the method applied, *i.e.* the BGO efficiency is applicable also at $E_0 = 207$ GeV. With the method justified, the Al and C data is shown in Figure 6.3b and 6.3c, respectively, along with MC simulations of the corresponding BH and LPM curves found using [MBSU08]. Because of the larger primary energy, the SR contamination influences larger photon energies, thus increasing the lower limit of the BGO energy threshold as seen in Fig. 3.3 on page 38. From the low-Z LPM data, it is evident that the power spectra are heavily influenced by SR from $\hbar\omega \lesssim 0.34$ GeV, corresponding to the lowest energy bin shown. The same bin of the Ta data seems unaffected which can be explained by the fact that the Al and C targets are 13.7% and 25.1% thinner than the Ta target, respectively (cf. Tab. 6.1). In this way, the SR has a larger relative influence on the Al and C data.

The efficiency-corrected data is—at least in the cases of aluminum and tantalum—in remarkable agreement with the LPM simulations. As for carbon, the LPM threshold lies below the lower detection limit and the statistics are too low to see a consistent tendency. There are nevertheless no indications of discrepancies except at the lowest photon energy. The data of the pilot study was first presented in [II], where the referees showed great interest in the results, although the number of targets were limited. A more systematic low-Z LPM study was approved as an addendum to the NA63 experimental program, and this is discussed in the following section.

6.3 The Full Study

Judging from the pilot study, performing a systematic LPM study down to at least $Z = 13$ should be feasible at the CERN SPS. In Fig. 6.4 on page 84, GEANT3 MC simulations of the LPM power spectrum from $N_e = 2 \times 10^8$ primary particles impinged on $\Delta t/X_0 = 2.50\%$ targets consisting of materials spanning a wide range of Z-values from $Z = 6$ (C) to $Z = 77$ (Ir). Again, the GEANT3 simulations are based on an improved version of the LPM implementation described in [MBSU08]. As

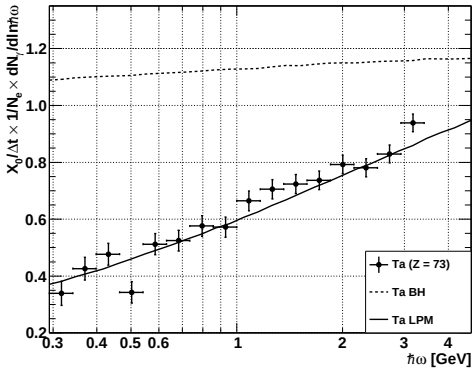

(a) Tantalum.

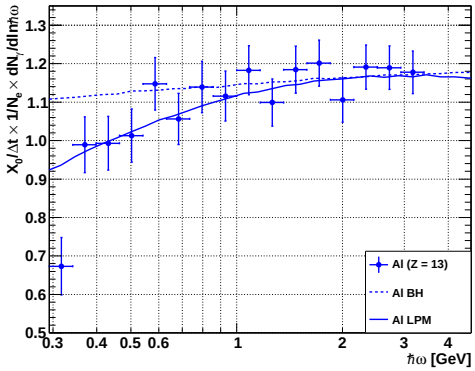

(b) Aluminum.

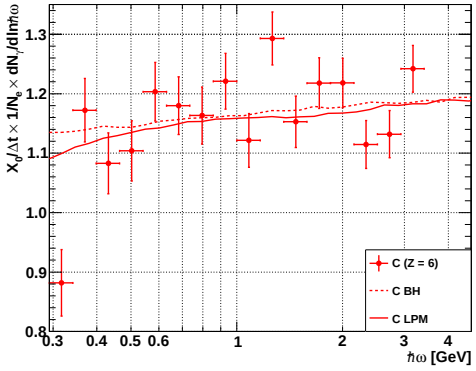

(c) Carbon.

Figure 6.3: The power spectra for Ta, Al and C targets in the LPM regime are measured at $E_0 = 207$ GeV. Fig. (a) makes us trust the applied method of efficiency correcting the BGO. The Al data in Fig. (b) tends to follow the LPM curve, although one should note the relatively large statistical error bars shown. Fig. (c) shows the carbon data. In this material, the LPM curve separates only little from the BH curve within the accessible photon energy range.

seen in the figure, the LPM effect could be measured for the low-Z elements under the circumstances mentioned—even when taking the BGO lower limit into account.

In June 2010, a dedicated low-Z LPM experiment was performed by the NA63 collaboration. Here, measurements on foils of the materials and thicknesses listed in Table 6.2 with $E_0 = 178$ GeV electrons were performed. The nine materials ranged from low-density polyethylen (LDPE), $(CH_2)_n$, to Ta. The $80 \times$ Al25Air1000 reference target used during the TSF study (cf. Table 3.1 on page 37) was used again. Also, the LPM threshold of the LDPE target is below our detection limit with the BGO and thus served as a secondary reference target.

With the experience from the TSF experiment, a reduction of the SR pile-up phenomenon was attempted by running the `B16` at a minimum current to lower the threshold of the SR ($\omega_c \propto B$). The experimental radiator background was reduced by using fragile scintillators only 0.5 mm thick for `Sc1` and `Sc2`, thus reducing their

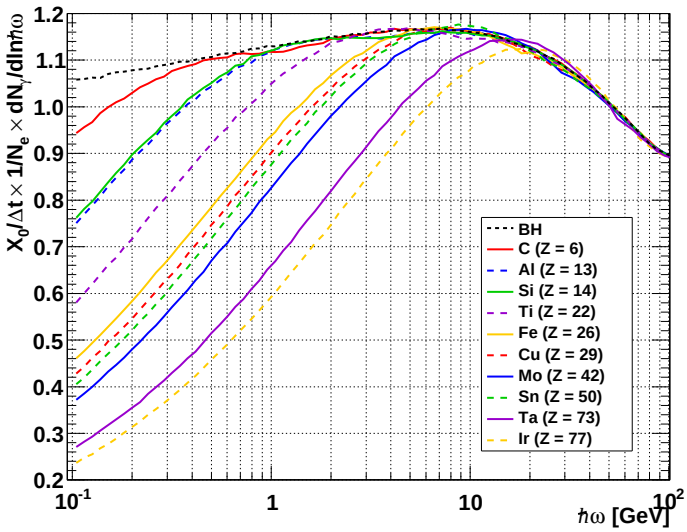

Figure 6.4: LPM simulations based on the method of [MBSU08] for elements with Z in the range 6–77 performed at $E_0 = 178$ GeV. The simulations take the detector solid angle into account. All targets are 2.50% X_0 thick, and $N_e = 2 \times 10^8$ electrons are simulated. Maybe at first surprising, the Sn $(Z = 50)$ curve lies above the Mo $(Z = 42)$ curve. This is explained by the low density of Sn relative to its nuclear charge.

Material	X_0 [mm]	$\hbar\omega_{\mathrm{LPM}}$ [GeV]	Δt [mm]	$\Delta t / X_0$ [%]
LDPE	503.1	0.08	13.16(4)	2.62(1)
C	245.4	0.17	4.84(2)	1.97(1)
Al	88.97	0.46	2.27(1)	2.55(2)
Ti	35.9	1.14	0.94(1)	2.61(2)
Fe	17.6	2.31	0.478(3)	2.72(2)
Cu	14.4	2.81	0.349(2)	2.42(2)
Mo	9.59	4.19	0.243(2)	2.53(2)
Sn	12.1	3.34	0.316(2)	2.61(2)
Ta	4.094	9.52	0.108(1)	2.63(4)

Table 6.2: Specifications of the targets used for the LPM study 2010. The LPM energy threshold is calculated at $E_0 = 178$ GeV, cf. Eq. (1.21).

background contribution from $\Delta t \simeq 0.9\%\ X_0$ to $\simeq 0.24\%\ X_0$. However, by reducing the background, the SR pile-up phenomenon described in Sec. 2.6 on page 25 is more pronounced in the background spectrum, thus moving the kink seen in Figure 2.8b to slightly larger photon energies, $\simeq 0.5$ GeV. It is evident that a method of correcting for the SR contamination has to be devised to reach the very lowest photon energies ($\simeq 100$ MeV). Following the procedure outlined near Figure 3.5 on page 41, a second order polynomial was fitted to the ratio of the power spectra of the aluminum reference target and its corresponding GEANT3 simulation. The simple

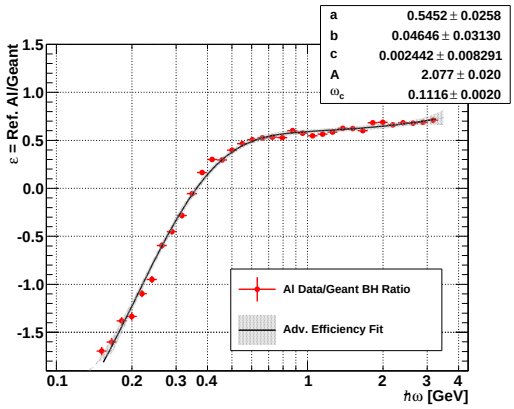

(a) The ratio of the Al reference target's power spectrum and the corresponding GEANT3 simulation. A fit is performed with Eq. (6.1) to the ratio. The 95% confidence interval from the fitting procedure is also shown.

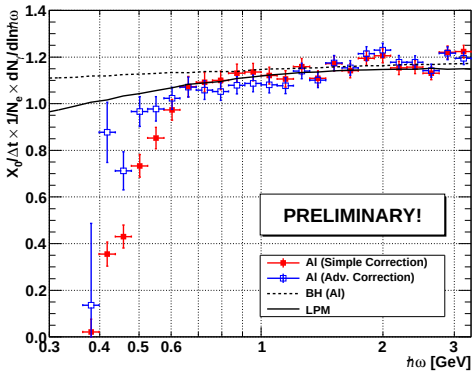

(b) The Al power spectrum as an example of the state of the analysis of the full experimental LPM study performed in June 2010. The red and blue datapoints have been corrected by a simple quadratic efficiency and the more advanced one of Eq. (6.1), respectively.

quadratic efficiency is only fitted at photon energies above the SR kink, whence the found efficiency is applicable in an unsatisfactorily limited photon energy range. In an attempt to extend the applicability below the kink, the following expression was devised

$$\mathcal{E}_A(\hbar\omega) = \mathcal{E}(\hbar\omega) - \exp\big(A - \omega/\omega_c\big)\left(\frac{\omega}{\omega_c}\right)^{0.5}, \tag{6.1}$$

where $\mathcal{E}(\hbar\omega)$ is the regular quadratic efficiency of Eq. (3.3), and the latter term represents a SR contamination, cf. Eq. (2.8). Since the background was checked regularly and found to be constant throughout the experiment and the targets are of almost identical thicknesses, the SR contamination is assumed to be very similar in the power spectra of the materials, *i.e.* the parameters A and ω_c should be alike for all data.

In Figure 6.5a, the expression above is fitted to the ratio of the reference spectrum and its corresponding GEANT3 simulation down to $\hbar\omega \simeq 0.150$ GeV. The function is seen to describe the ratio very well. In Figure 6.5b, both a simple quadratic efficiency (found above the kink) and the advanced efficiency shown in Figure 6.5a has been applied to the non-reference Al data. First of all, both expressions seem to bring the data in good accordance with simulations at $\hbar\omega \gtrsim 0.7$ GeV. Also, the statistical errors have been heavily reduced relative to those of the pilot study, cf. Figure 6.3. However, at $\hbar\omega \lesssim 0.6$ GeV the simple quadratic expression clearly falls short of correcting the data. The advanced expression extends the credible spectrum only a few bins before $\mathcal{E}_A \simeq 0$ at $\hbar\omega \simeq 0.35$ GeV makes the statistical errors increase vastly upon division with the efficiency. This problem could be avoided by considering an alternative correction consisting of first adding an expression resembling SR, cf. Eq. (2.8), to a BCPS and then dividing the result with a quadratic efficiency. The parameters of this operation could be found by matching the result to the GEANT3 simulation. With this solution, division by a correction $\simeq 0$ would not occur. Of course, the qual-

ity of such a correction should be carefully studied by applying it to toy MC data, where the pure spectra are well-known.

◇ ◇ ◇

In the pilot low-Z experiment, good accordance between data and simulations for the LPM effect has been found at $E_0 = 149$ GeV in aluminum. Because the LPM threshold for carbon is lower, the difference between the carbon BH and LPM simulations is smaller within our detection range. The carbon data suffers from too large statistical errors to discern the better model of the two.

At the time of writing, analysis of the full LPM study is still in progress. More explicitly, a method of correcting for the heavy SR contamination at the lowest photon energies is searched for. Before this problem is solved, the BGO spectrum is not credible at $\hbar\omega \lesssim 0.5$ GeV, corresponding to about half of the desired spectrum range on a log scale.

Part II

Positronium
Production and Decay

CHAPTER 7

THE ASACUSA POSITRON BEAM LINE

As a part of the CERN based collaboration Atomic Spectroscopy And Collisions Using Slow Antiprotons (ASACUSA), our group in Aarhus took the responsibility of testing a commercial low-energy ($\simeq$ 1 eV) positron source based on a ^{22}Na β^+ radioactive source. Since low-energy positrons are somewhat evasive, as they annihilate (predominantly to two photons of energy mc^2) when encountering electrons, they must be guided from the source in a vacuum chamber utilizing many ingenious techniques, which will be described in the following.

The positron source arrived in Aarhus in November 2007 and is now fully assembled and operational. The "turn-key" system is designed and manufactured by the Californian company FPSI [GM03]. It consists of two individual systems in succession: the Rare Gas Moderator-1 (RGM-1) for the first positron energy moderation, and the two-stage Multi-Ring Trap (MRT) for short-term storage and beam quality improvements. The RGM-1 will be further described in Sec. 7.1 as the MRT will be in Sec. 7.3. For lack of a better name, the combined system will be referred to as the Low-Energy Positron Source (LEPS), which can be seen in Figure 7.1. The results of our thorough examination of the combined system are presented in Chapter 8.

7.1 The RGM-1

A more detailed sketch of the RGM-1 can be seen in Figure 7.3a. The positrons come from a ^{22}Na β^+ radioactive source, in our case with an activity 10.64 mCi (as of September 26, 2007). The allowed decays of ^{22}Na are shown in Table 7.1. This isotope has a half-life of 2.60 y and decays almost exclusively (99.9%) to an excited state of ^{22}Ne due to the selection rules of the β and electron capture decays. The excited nucleus later decays to the ground state by emitting a 1.275 MeV photon. With a large branching ratio (BR) of 0.903, the decay of the sodium nucleus will produce a positron (e^+) with a continuous distribution of kinetic energies up to $Q = 0.546$ MeV, *i.e.* comparable to the rest mass energy of the positron. If one aims for antihydrogen ($\overline{\mathrm{H}}$) production, it is necessary to diminish the positron energies to the scale

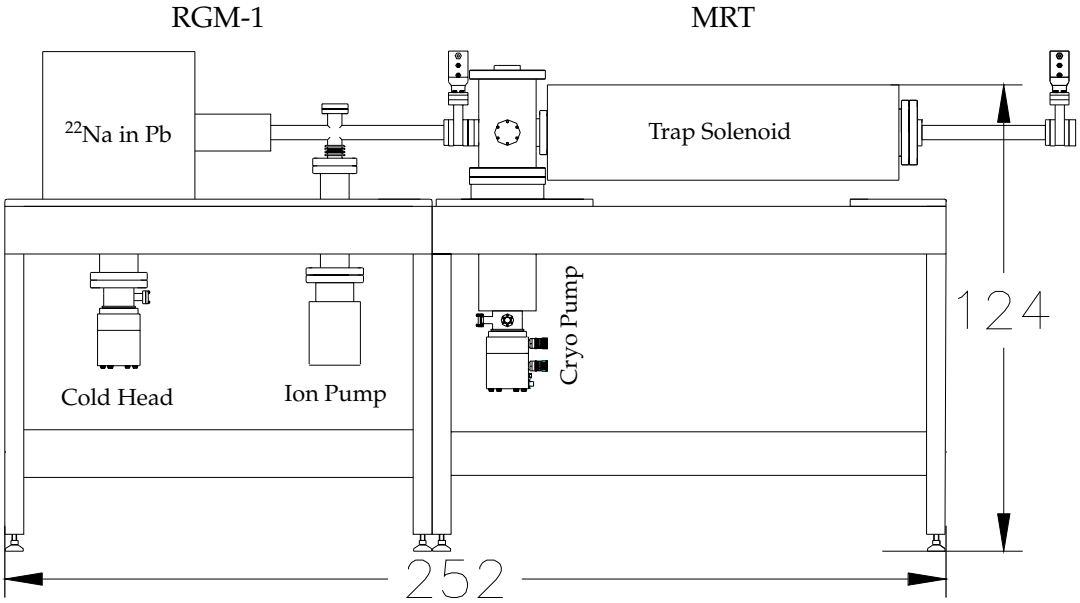

Figure 7.1: The LEPS comprises two subsystems, the RGM-1 and the MRT. The ion and cryo pumps are supported by a set of turbomolecular/diaphragm pumping stations, cf. Figure 7.2. Courtesy of FPSI.

BR [%]	Q [keV]			
90.3	546	^{22}Na	$\rightarrow$	^{22}Ne$^{*}(1.275\ \text{MeV}) + \nu_e + e^+$
9.6	1568	$e^- + {}^{22}$Na	$\rightarrow$	^{22}Ne$^{*}(1.275\ \text{MeV}) + \nu_e$

Table 7.1: The allowed weak decay channels of ^{22}Na with branching ratios (BR) and energy produced by the reactions (Q) [Gal].

of atomic binding energies, *i.e.* almost two orders of magnitude to $E_+ \simeq$ eV. This energy moderation is usually carried out by a large number of inelastic processes in a condensed matter, the moderator. Of course, the moderator also introduces a heavy particle loss through the annihilation channel. In the following section, I will describe the state-of-the-art moderator system of the RGM-1.

The Ne (s) Moderator

The members of the family of solidified (*i.e.* frozen) rare gasses have turned out to posses satisfying moderator attributes. This was first pointed out in [GMJ86], where Ar, Kr and Xe were examined. The Rare Gas Solids (RGSs) all classify as insulators and have positive positron work functions $(\phi_+ > 0)$, *i.e.* positrons with energy below ϕ_+ are trapped in the material. When traversing the solid, the positron initially loses energy by engaging in inelastic, electronic excitations of the material. However, this mechanism ceases once the positron energy is less than the threshold of creating a free electron-hole pair in the insulator, the band gap of $E_g \simeq$ 10–20 eV. Requiring slightly less energy, the positron can also excite the material by creating an exciton, in which the electron-hole pair travels together and thus transports no

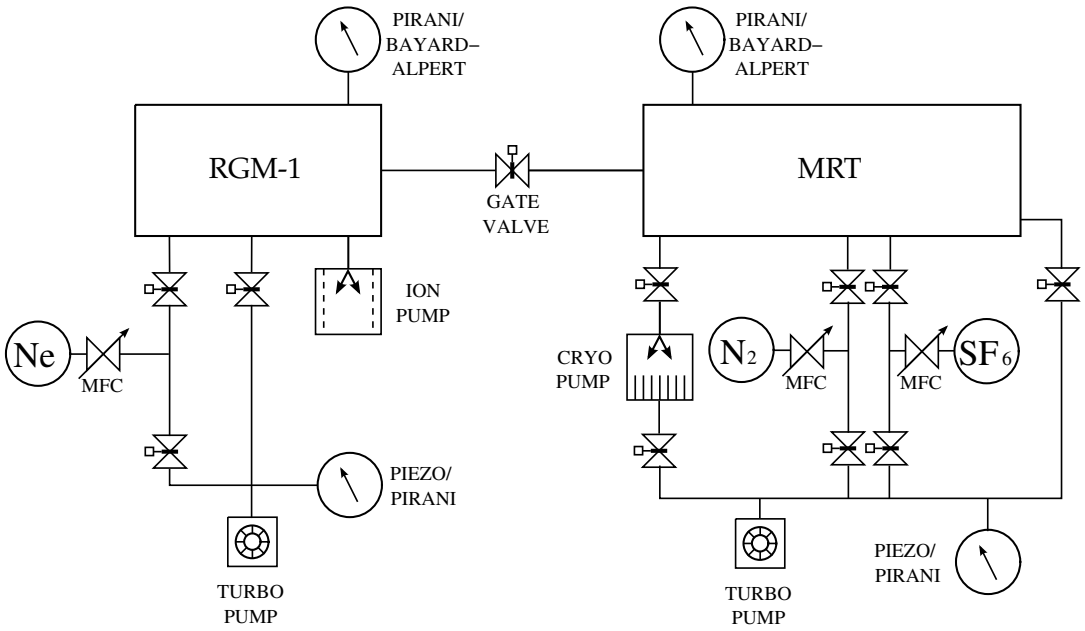

Figure 7.2: The vacuum diagram of the LEPS. Almost all valves and pumps are remote-controlled through LabVIEW software. From [Lun09], courtesy of M.D. Lund.

net-charge. Also, the positron can lose energy by creating the meta-stable atom-like state of an electron and a positron, positronium (Ps), which is the topic of Chapter 9. This process has the energy threshold $E_{\mathrm{Ps}} = E_g - B_{\mathrm{Ps}} - \phi_+$, where $B_{\mathrm{Ps}} = 6.8$ eV is the binding energy of positronium. Below these thresholds, the main mechanism of further positron energy loss is phonon excitation with energies typically on the scale of few meV, giving rise to long positron diffusion lengths [GMJ86]. Our RGS moderator material is frozen neon, Ne (s), which was first studied in [MJG86]. Here, it was found to exhibit the best moderation efficiency ϵ_m—*i.e.* number of moderated positrons relative to the full number from the radioactive source—of all RGSs. Generally, the deeper the positrons were deposited in the RGS, the lower transverse energy widths of the re-emitted positrons were achieved, which can be understood by the larger number of phonon excitations before reaching the RGS surface. Since Mills Jr. and Gullikson's pioneering work in 1986, cryogenic equipment have become more conventional and inexpensive. The RGM-1 includes a cold head—a cryogenic device basically consisting of an expansion chamber with a piston and two valves. In the chamber, a pressurized ($\simeq$ 17 bar) He gas is supplied through the high-pressure valve from a He compressor and allowed to expand, thus cooling the surrounding walls. After expansion, the piston empties the chamber through the low-pressure valve, leading the gas back to the He compressor. The cooling cycle thus consists of intake–expansion–exhaust–compression. The efficiency of the device is greatly improved by introducing a regenerator, essentially a heat reservoir where the high-pressure (low-pressure) gas can deposit (gain) thermal energy. Also, successive stages of refrigeration are introduced, such that one stage refrigerates the following, leading to temperatures $\simeq$ 5 K at the final stage. Previously, this was attained using three stage cold heads, but with today's improved efficiencies, reaching

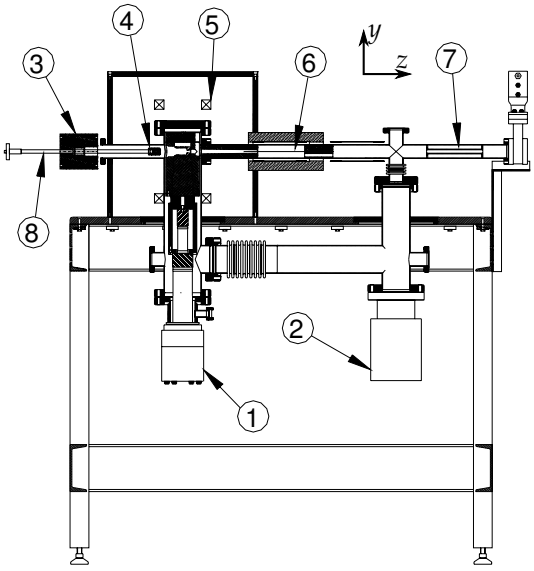

(a) The elements of the RGM-1: (1) the cold head with radiation shielding in vacuum chamber; (2) the ion pump; (5) the major Helmholtz coils; (6) the beam tube solenoid, with a magnetic chicane consisting of two consecutive saddle coils; (7) a pumping restriction to minimize contamination of the moderator by the buffer gas from the trap. The transfer of the radioactive source (4) from its shipping cask (3) to the thermally isolated copper holder on top of the cold head is depicted here, cf. Figure 7.3b. Courtesy of FPSI.

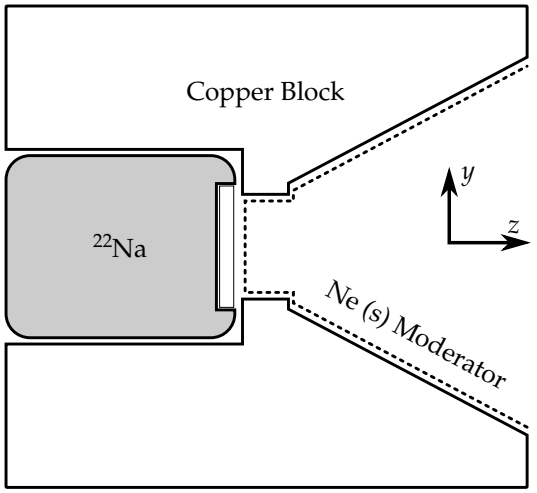

(b) A sketch of the moderator area. The copper block houses the ^{22}Na source and rests on the top of the cold head. When neon is deposited, both the conical hole of the Cu block and the window of the source will be covered with a layer of Ne (s). The layer must be traversed by the positrons travelling in the $+z$ direction.

Figure 7.3: The RGM-1 and the moderator region.

this temperature with a two-stage cold head is feasible.

In our case, the ^{22}Na source is housed in a gold-plated copper block which rests at the top of a two-stage cryogenic cold head, cf. Figure 7.3a and 7.3b. The second stage of our cold head and the copper block nests in a radiation shield of Elkonite to give good thermal isolation. The cold head includes a 5 W heater, which is used to Proportional–Integral–Derivative (PID) regulate the temperature of the block. The Cu block thus routinely reaches a steady temperature of 6.8 K, while Ne freezes at 24.56 K [Y$^+$06][1]. When admitting Ne, a frozen layer of neon will cover both the ^{22}Na source and the conical hole in the Cu block. Hereby, a combined transmission and backscattering RGS moderator is created, *i.e.* the positrons travelling in the beam direction $(+z)$ must traverse the Ne (s) near the source surface and are then likely to hit and backscatter from Ne frozen at the cone, cf. Figure 7.3b. A similar setup was studied in [MJG86], where a record-breaking moderation efficiency of $\epsilon_m = 0.70(2)\%$ was achieved. The positron energy was of order $E_+ \simeq 1$ eV with an energy width of 0.58 eV FWHM. Using the novel technique, the efficiency was more than twice the value obtained with the standard moderator material at that time, metallic foils, typically tungsten.

[1]The referenced value is given at atmospheric pressure. At the much lower pressure in our vacuum chamber, the melting point is somewhat lower, $\simeq 15$ K.

The purity of the moderator is determined by the purity of the admitted Ne gas and the pressure in the vacuum chamber. The pressure will reach $\simeq 2 \times 10^{-9}$ mbar when the ion pump is on (cf. Figure 7.3a) and the cold head is at $\simeq 7$ K. The latter lowers the pressure by one order of magnitude, as it stops the heavy outgassing of the Elkonite radiation shield, and generally freezes out much of the background gas. The moderator slowly deteriorates, which will also be discussed in the following chapter, but a new moderator is grown through a software-controlled recipe lasting less than an hour—by far easier than replacing an old-fashioned metallic moderator.

Guidance in RGM-1

By applying a number of magnetic fields, cf. (5)–(7) in Figure 7.3a, the moderated positrons are guided from the source to the gate valve, shown at the end of the beam tube. Essentially, a homogeneous field parallel to the beam axis ensures radial confinement through the Lorentz force

$$\boldsymbol{F} = e\left[\boldsymbol{E} + \boldsymbol{v} \times \boldsymbol{B}\right] . \tag{7.1}$$

If no electrical fields are present, this introduces a centripetal acceleration which balances the azimuthal speed, *i.e.* cyclotron motion in the plane orthogonal to the beam tube axis. A particle with a transverse speed $v_\perp \ll c$ relative to the beam axis will perform a helical motion of radius

$$r = \frac{m v_\perp}{eB} , \tag{7.2}$$

along the magnetic field of strength B. Inside the shielding barrel—containing huge quantities of lead shots[2]—a set of Helmholtz coils are located, (5) in Figure 7.3a. These supply a homogeneous field of $\simeq 120$ G guiding the positrons to the beam tube of RGM-1. A solenoid is wound around the beam tube with which a $\simeq 250$ G field is applied. The first of two sets of saddle coils is located in a slab of Elkonite wrapping the first part of the beam tube outside the shielding barrel. The first saddle coil adds a magnetic perturbation ($\simeq 21$ G) in the $-\hat{\boldsymbol{y}}$ direction to the much larger field in the $\hat{\boldsymbol{z}}$ direction. The second set of saddle coils restores the magnetic field by adding a magnetic field perturbation in the $+\hat{\boldsymbol{y}}$ direction. This has the overall effect of shifting the beam slightly in the $-\hat{\boldsymbol{y}}$ direction. A magnetic chicane is thus defined by the saddle coils and a cylinder with a non-concentric aperture placed in the beam tube, cf. (6) in Figure 7.3a. For a fixed saddle coil current, the transferred positron energy and energy resolution are determined by the aperture's distance from the beam center axis and the aperture size, respectively. In this way, unmoderated positrons, the 0.511 MeV annihilation photons and the 1.275 MeV photons following γ-decay of the $^{22}\mathrm{Ne}^*$ nucleus (cf. Table 7.1), does not escape the shielding barrel.

At the end of the beam tube, a gate valve is located. This valve separates the RGM-1 from the MRT in the LEPS. Before describing our complex MRT (a modified Penning trap) in Sec. 7.3, the general idea of the behaviour of a charged particle in a much simpler trap is presented in the following section.

[2] According to FPSI, the shielding should be adequate even for a 150 mCi ^{22}Na source!

7.2 Behaviour in a Penning Trap

The following derivations follow the one presented in the renowned paper [BG86]. I will use a cylindrical coordinate system $(\hat{\boldsymbol{\rho}}, \hat{\boldsymbol{\phi}}, \hat{\boldsymbol{z}})$, since most traps aim for a high degree of azimuthal $(\hat{\boldsymbol{\phi}})$ symmetry. The idealized Penning trap consists firstly of a uniform magnetic field along the trap axis $\boldsymbol{B} = \pm B\hat{\boldsymbol{z}}$, which gives radial confinement through the Lorentz force, cf. Eq. (7.1). In absence of electrical fields, this gives rise to azimuthal cyclotron motion with the characteristic frequency $\omega_c = eB/m$. The second element of the Penning trap is to superimpose an electrostatic quadrupole field, *i.e.* introduce a saddle-point shaped potential of azimuthal symmetry

$$V(\rho, \phi, z) = V_0 \frac{z^2 - \rho^2/2}{2d^2} \,, \tag{7.3a}$$

$$\boldsymbol{E}(\rho, \phi, z) = -\nabla V = \frac{V_0}{d^2}\left(\frac{\rho}{2}, 0, -z\right) \,, \tag{7.3b}$$

where d is a characteristic length scale based on the trap dimensions, as we shall see shortly. The quadrupole field can be realized using only tree hyperbolically shaped ring electrodes with azimuthal symmetry

$$z_e^2 = z_0^2 + \rho^2/2 \tag{7.4a}$$

$$z_c^2 = \frac{1}{2}(\rho^2 - \rho_0^2) \,, \tag{7.4b}$$

where the subscripts stand for end cap (e) and central (c) electrode. Such a geometry is illustrated in Figure 7.4a for the parameters $z_0 = 1$ and $\rho_0 = 2$ (in arbitrary units). These parameters are seen, from the equations above and the figure, to be the minimum distance from the trap center to the respective electrodes. With the choice of $2d^2 = z_0^2 + \rho_0^2/2$, V_0 is simply the constant electric potential difference between the central ring and the end cap ones.

An Isolated Charge

For simplicity, I will consider only a single classical, non-relativistic particle of mass m and charge $+e$. The equations of motion follow from Eq. (7.1) with the trap electric field of Eq. (7.3b)

$$\ddot{z} + \omega_z^2 z = 0 \,, \qquad \omega_z^2 = \frac{eV_0}{md^2} \tag{7.5a}$$

$$\ddot{\boldsymbol{\rho}} - \frac{e}{m}\left[\boldsymbol{E}_\rho + \dot{\boldsymbol{\rho}} \times \boldsymbol{B}\right] = \ddot{\boldsymbol{\rho}} - \omega_c \hat{\boldsymbol{z}} \times \dot{\boldsymbol{\rho}} - \frac{\omega_z^2}{2}\boldsymbol{\rho} = 0 \,, \tag{7.5b}$$

where $e\hat{\boldsymbol{z}} \cdot \boldsymbol{B} = -eB$ has been chosen. The first equation describes a simple harmonic axial motion with characteristic bounce frequency ω_z, independent of the superimposed magnetic field. The radial differential equation is in [BG86] solved by defining

$$\omega_\pm = \frac{1}{2}\left[\omega_c \pm \sqrt{\omega_c^2 - 2\omega_z^2}\right] \tag{7.6a}$$

$$\boldsymbol{V}^{(\pm)} = \dot{\boldsymbol{\rho}} - \omega_\mp \hat{\boldsymbol{z}} \times \boldsymbol{\rho} \,. \tag{7.6b}$$

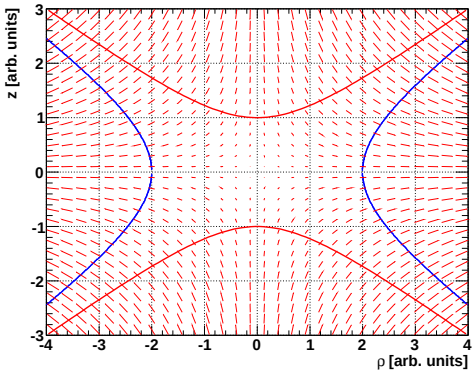

(a) The end cap (central) electrode geometry is shown with red (blue) curves. A constant potential difference between the electrodes gives rise to the electrical quadrupole field sketched with small arrows. The minimum distance from $(0,0)$ to the end cap and central electrode is $z_0 = 1$ and $\rho_0 = 2$, respectively.

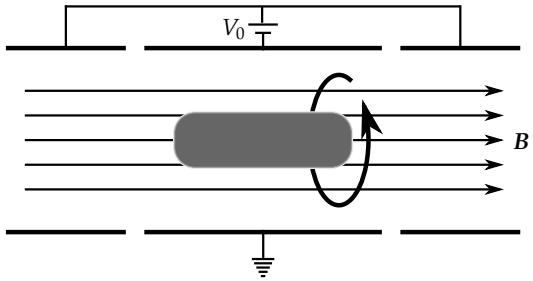

(b) The often used Malmberg-Penning trap of simpler geometry (essentially a segmented cylinder).

Figure 7.4: Variations of Penning traps.

With these definitions, Eq. (7.5b) can be restated in a simple way

$$\dot{\boldsymbol{V}}^{(\pm)} = \omega_{\pm} \hat{\boldsymbol{z}} \times \boldsymbol{V}^{(\pm)} \,, \tag{7.7}$$

which is the standard expression for defining rotating reference frames, *e.g.* the vector $\boldsymbol{V}^{(+)}$ rotates with frequency ω_+ relative to the original reference. Perhaps one can already now perceive that the radial motion is simply a combination of two decoupled circular motions with same direction of rotation. The modified frequencies $\omega_\pm$ fulfill

$$\omega_+ + \omega_- = \omega_c \tag{7.8a}$$

$$\omega_+^2 + \omega_-^2 + \omega_z^2 = \omega_c^2 \,, \tag{7.8b}$$

where the latter equation is the Brown-Gabrielse invariance theorem [BG82], which is crucial in high-precision experiments in non-idealized Penning traps. The motion with frequency $\omega_+ \equiv \omega_c'$ is called the cyclotron motion since for typical parameters, the modified cyclotron frequency almost matches the pure frequency, $\omega_c' \simeq \omega_c$. The other rotation with frequency $\omega_- \equiv \omega_m = \omega_z^2/2\omega_c'$ is called the magnetron motion. In contrast to the two other stable motions (axial and cyclotron), this is only metastable, since the magnetron motion is "an orbit about the top of a radial potential hill" [BG86]. Nevertheless, the lifetimes of the magnetron modes are of the order of years. In experimental setups, the effect of the imposed magnetic field is much stronger than the quadrupole field, and the three characteristic frequencies are of very different magnitudes

$$\omega_c' \gg \omega_z \gg \omega_m = \omega_z^2/2\omega_c' \,. \tag{7.9}$$

Since $\omega_c/B \simeq \omega_c'/B$ is the particle's charge-to-mass ratio, the hierarchy of frequencies becomes most pronounced for the lightest leptons $(e^\pm)$ in strong magnetic fields,

where $\omega_c'/\omega_z \gtrsim 10^3$ is feasible. Because of this, the combination of the fast cyclotron motion and the slow magnetron motion gives rise to an epicyclic pattern.

The derivation above is of course only valid for an idealized trap where the perfect electrode geometry admits one to solve the equations of motion without using approximations. In a real-life trap, many factors can be the source of imperfections, *e.g.* misaligned or inhomogeneous magnetic field, imperfect trap electrode geometries and relative placement, which all break the trap symmetry and cause particle loss. The experimental electrodes are of course also always truncated, since semi-infinite electrodes are generally not feasibly manufactured! Nevertheless, the equations above give a good understanding of the general behaviour of a charged particle in a Penning-based trap.

The Malmberg-Penning trap is based on the same confinement ideas, albeit with simpler design as it is essentially a cylinder segmented axially in at least 3 electrodes, cf. Fig. 7.4b on the preceding page. By choosing proper dimension of the ring electrodes, the axial potential can come very close to being harmonic [BG86]. It is generally easier to load and extract particles from this trap type, and complex potentials can be realized using a larger number of electrodes. This is exploited by the ALPHA and ATRAP collaborations at the CERN Antiproton-Decelerator facility, when mixing antiprotons with positrons in nested Malmberg-Penning traps to produce antihydrogen, $\overline{\mathrm{H}}$. Figure 7.4b shows not only a single particle but a trapped cloud of charged particles, which is the topic of the following section.

Adding Particles

I will here briefly consider how the found behaviours are modified when adding a number of particles (N_{e^+})—a cloud of particles—to the trap. As this number grows, the motion of a particle will be influenced by the electrical field generated by its neighboring particles, giving rise to the space-charge potential, ϕ_p, which approaches zero near the trap walls.

If the particle density n_e becomes large relative to their mean energy, the cloud is referred to as a nonneutral plasma, since the group of charges will start to exhibit collective behaviours, much like in a neutral plasma, where the mobility of the electrons is typically much larger than the ions'. The plasma state occurs if the trap potential is effectively screened out by Debye shielding, which takes place over the characteristic Debye length λ_D

$$\lambda_\mathrm{D} = \sqrt{\frac{\epsilon_0 k T_e}{n_e e^2}} = \sqrt{\frac{k T_e}{m\omega_p^2}}\,, \tag{7.10a}$$

$$\omega_p = \sqrt{n_e e^2/m\epsilon_0} \tag{7.10b}$$

where k is the Boltzmann constant, T_e is the temperature of the charges and ω_p is the particle plasma frequency. A plasma state is thus reached when λ_D is smaller than the extent of the particle cloud, *i.e.* with high densities and low temperatures. Finding the particle distribution is a self-consistent problem, *i.e.* one must solve the Poisson equation for the sum of the trap (ϕ_t) and space-charge potential

$$\nabla^2(\phi_t + \phi_p) = -\frac{e n_e}{\epsilon_0}\,, \tag{7.11}$$

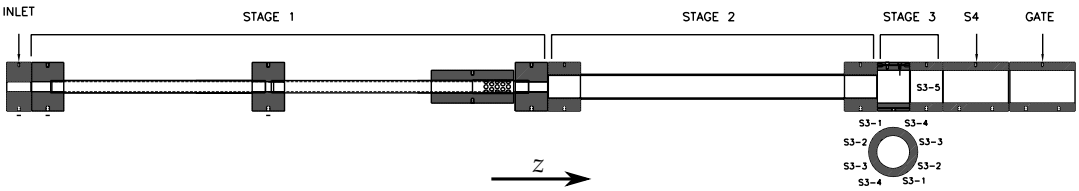

(a) Structure of the two-stage MRT comprising six electrodes and a pumping restriction.

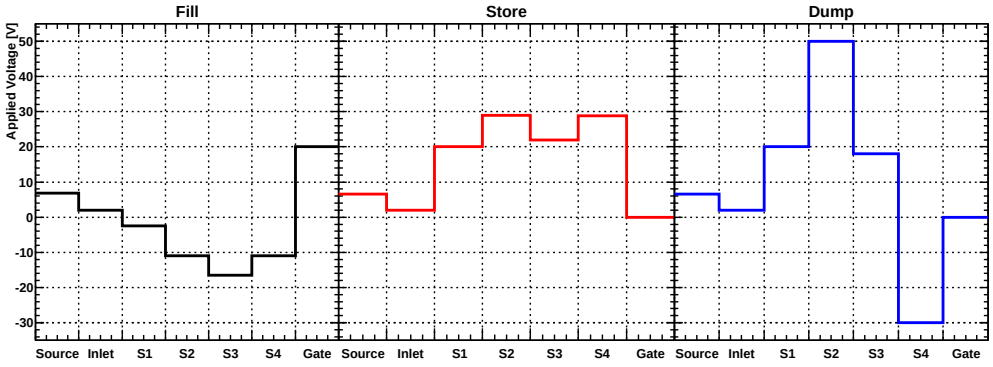

(b) Plots of the voltages applied to the trap electrode structure in the fill, store dump phase, respectively. The positrons are stored and cooled near S3, which is kept at a local minimum voltage in the fill and store phases.

Figure 7.5: The MRT blueprints and voltages.

but it is evident that the local charge density also influences the space-charge here. Hence, the solutions must be found through a self-consistent, iterative process. The thermal equilibrium states of a nonneutral plasma have been investigated extensively [Dav90, DO99]. The thermal equilibrium plasma rotates as a rigid rotor with a frequency ω about the magnetic field in the trap center. Whereas the shape of the plasma depends on the trap geometry, the bulk density is almost uniform and the density at the surface drops to zero in few Debye lengths.

7.3 The Multi-Ring Trap

The trap part of LEPS includes a modified Penning trap, some gas handling systems, and a cryo pump, cf. Figure 7.1 and 7.2. The latter is similar to the cold head in operation, but in the cryo pump, the geometry is optimized for providing a large surface on which the background gas condense or solidify, thus lowering the vapor pressure of the gas considerably. With the cryo pump, the trap pressure can go as low as $\simeq 4 \times 10^{-9}$ mbar.

The electrode structure of our two-stage MRT is shown in Figure 7.5a. The MRT comprises six ring electrodes of varying length—especially stage 1 and 2 are particularly long. The trap is based on the original tree-stage design by by Surko *et al.* [SLP89]. Here, positrons were captured in the trap potential minimum by inelastic collisions with a N_2 buffer gas. This gas has a relatively low cross section towards annihilation but a high one towards a $^1\Pi$ electronic excitation of $\simeq 9$ eV [GS02]. In

the first panel of Figure 7.5b, our trap potentials during filling of the trap is shown. The trap potential steps are tuned to match the N_2 resonance, and as the positrons collide with N_2, they will eventually by trapped near the global potential minimum (S3). The trap design exploits differential pumping, *i.e.* regionally different pumping speeds determined by the aperture sizes. Since the apertures of the ring electrodes increase in $+\hat{z}$ direction, the pressure is relatively large near the gas inlet in S1 (ensuring a high initial trapping probability), lower in S2 (reducing the risk of annihilation), and lowest ($\simeq 10^{-5}$ mbar) beyond this to give large positron lifetimes ($\tau_{\text{trap}} \simeq 1$ s) near S3.

Unfortunately, N_2 is not very efficient for further cooling with a characteristic cooling time of $\tau_c(N_2) = 115$ s. A better choice is SF_6 or CF_4 with cooling times of $\tau_c(SF_6) = 0.36$ s and $\tau_c(CF_4) = 1.2$ s [GS00]. These cooling buffer gasses both have vibrational resonances around $\lesssim 0.1$ eV. On the other hand, these are very inefficient for trapping, and the solution is a mixture of the two [SLP89, GS02], which enables cooling of the positrons to electrode temperature. While a N_2 partial pressure of $\gtrsim 10^{-6}$ mbar gives reasonable trapping efficiencies, only very little amounts (partial pressures of $\simeq 10^{-8}$ mbar) of the cooling gas are necessary. In the MRT bunch mode, two Mass Flow Controllers (MFCs) admit 0.30 and 0.10 cm^3/min of STP N_2 and SF_6, respectively, to the trap inlet electrode. This gives rise to a steady pressure of $\gtrsim 10^{-5}$ mbar.

In the two other panels of Figure 7.5b, the voltages of the store and dump phases are shown. The DC beam from the ^{22}Na source is thus accumulated and stored for cooling near S3 before extraction. During the dump phase, the electrodes S3, S4 and Gate are seen to accelerate the particles in a controllable manner by adding $eV_{\text{S3}}^{\text{dump}}$ to the particles' energy in the trap. The electrodes also have an overall spatially focusing effect on the extracted beam, similar to an einzel lens. The bunch shot repetition frequency $1/t_{\text{cycle}}$ depends on the duration of the respective phases

$$t_{\text{cycle}} = t_{\text{fill}} + t_{\text{store}} + t_{\text{dump}} \,, \tag{7.12}$$

and under normal operations, $t_{\text{cycle}} \simeq 0.11$ s, cf. Table 7.2, corresponding to a bunch extraction rate of $\simeq 9$ Hz. The ^{22}Na source is in each of the phases biased such that the $E_+ \simeq 1$ eV positrons can overcome the neon positron work function $E_+ + eV_{\text{Source}} > \phi_+$, where $\phi_+ \simeq 5.5$ eV for neon [MJG86].

In the so-called Direct Current (DC) mode, the trap electrode potentials would be set in a descending staircase pattern, allowing a single passage through the trap, which would not contain any buffer gas. In this way, the positrons could be detected almost one by one. This mode is used as reference in several of the diagnostic techniques, cf. Chapter 8. In the bunching mode, the changing electrode voltages define a timing reference of the bunch, *i.e.* when the voltage of S4 drops below -15 V (cf. Table 7.2), the bunch is extracted. The timing resolution of the extraction is found to be $\lesssim 5$ ns. In the DC mode, we have no timing reference of the particles from the trap.

The Rotating Wall

Because the trap possess azimuthal symmetry, the time-invariant Hamiltonian of a single particle in an idealized trap and the z-component of the canonical angular momentum commute $[H, L_z] = 0$, *i.e.* L_z is a conserved quantity. The radial confinement of a cloud of particles is true for all processes that conserve the canonical

Name	t [ms]	f_{RW} [MHz]	V_{Source}	V_{Inlet}	V_{S1}	V_{S2}	V_{S3}	V_{S4}	V_{Gate}
Fill	100	4.6	6.8	2	-2.5	-11	-16.5	-11	20
Store	10	5.1	6.5	2	20	29	22	28.75	0
Dump	1	5.1	6.5	2	20	50	18	-30	0

Table 7.2: The duration t, RW frequency and trap electrode potentials (in V) during the phases of the bunching cycle.

angular momentum (*e.g.* internal particle collisions and plasma turbulence). The z component of the angular momentum can be written as

$$\begin{aligned} L_z &= \sum_j m v_{\phi_j} r_j + (e/c) A_\phi(r_j) r_j \\ &= \sum_j m v_{\phi_j} r_j + \frac{eB}{2c} r_j^2 \simeq \frac{eB}{2c} \sum_j r_j^2 \,, \end{aligned} \tag{7.13}$$

where the gauge $\boldsymbol{A} = \boldsymbol{B} \times \boldsymbol{\rho}/2$ is used. The final step is valid only when considering a nonneutral plasma consisting of particles of same charge (here e). Nevertheless, any experimental trap will contain imperfections. As seen in the rotating reference frame of the plasma, these imperfections are now rotating and introduce a torque on the plasma, *i.e.* lead to a non-conservation of L_z. Radiation emission from the plasma and scattering with the buffer gas will have the same effect. The quality of the radial confinement would thus benefit from introducing an external torque neutralizing—or even surpassing—the ambient trap torques.

Half of the S3 electrode is azimuthally segmented into eight, allowing for application of a so-called Rotating Wall (RW) of electric fields, cf. Figure 7.6a. In this well-known plasma manipulation technique [AHD98, DO99], an rf sinusoidal voltage

$$V_{jw}(t) = A_w \cos\left(m_\phi \phi_j - 2\pi f_{\mathrm{RW}} t\right) \,, \tag{7.14}$$

is applied with a phase $m_\phi \phi_j$ to the jth segment at azimuthal angle $\phi_j = 2\pi j/8$. In our case, it is a rotating quadrupole ($m_\phi = 2$), the amplitude A_w is ~ 1 V, and the frequency of the signal generator f_{RW} is 4.6–5.1 MHz, cf. Table 7.2. Experimentally, the four different phases of the rf field are generated by a single electronics module. The resulting electric field applies a torque to the plasma, thus allowing to drive the plasma rotation frequency ω [AHD98]. By accelerating the plasma's azimuthal speed in the trap's magnetic field, the Lorentz force will either compress or expand the plasma radially (depending on the applied phases in the RW), thus enabling true radial confinement. The efficiency of the rotating wall has in the plasma regime been correlated with excitation of so-called rotating Trivelpiece-Gould plasma states [GS00]. The efficiency of the RW has also been studied in the single-particle regime (*i.e.* non-plasma) [GM08]. Here, the efficient RW frequency values were found to lie in a band of frequencies below the axial bounce frequency (ω_z). The technique can give positron density enhancement factors of $\simeq 15$ in $\lesssim 2$ seconds of application [GS00]. We have varied the trap potentials and frequencies during the phases of the bunching cycle to optimize the positron content of the bunches.

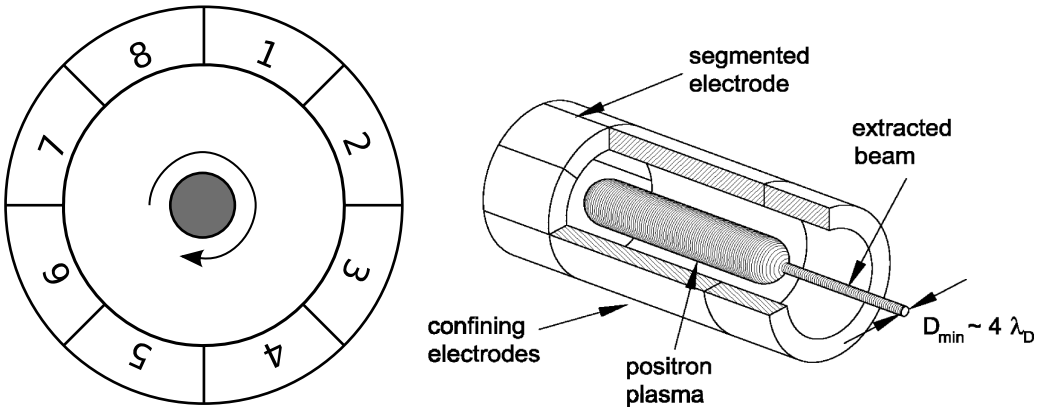

(a) Segmented electrode (view along beam axis) with rotating plasma.

(b) The RW reduces the beam diameter during slow extraction. From [GM03, SG04].

Figure 7.6: Introducing a RW of electric fields.

The RW does a work on the plasma which must be counteracted by a cooling mechanism, in our case the cooling buffer gas, the efficiency of which is believed to be the limiting factor in obtainable plasma densities [GS02]. If the gate electrode potential is slowly lowered to be comparable to the plasma space charge potential, the most energetic positrons in the plasma will escape where the confining potential is lowest—on the trap center axis. By this technique—which is illustrated in Figure 7.6b—one can obtain beam diameters as low as $D_{\min} \sim 4\lambda_D$ [DSSS03].

◇ ◇ ◇

The advanced, commercial FPSI systems have already contributed to state-of-the-art positron physics, for instance in the recent indications of the simplest leptonic "molecule", Ps_2 [CDG$^+$05, CMJ07]. The following chapter will discuss the found capabilities and specifications of our system, while Chapter 9 describes our first experiment.

CHAPTER 8

COMMISSIONING OF LEPS

The task of commissioning the ASACUSA LEPS was appointed to the Danish part of the ASACUSA collaboration, located at IFA, Aarhus. Unfortunately, the apparatus bore marks of having had a far from boring journey from FPSI, Agoura Hills (CA) to Aarhus University: several bellows were torn apart and a part of the buffer gas handling system lay in the bottom of the shipping crates. Also, a flange had sustained blows of a magnitude almost breaking its welding entirely! This meant that the apparatus had to be disassembled and carefully examined. Although the repairs caused a setback in the commissioning phase, the disassembly meant that we quickly became acquainted with some of the finer points of the apparatus. As presented in the following, the LEPS was fortunately found to meet—and in some cases even exceed—the supplier's specifications.

8.1 The Tools

The standard methods for characterising a positron source are based on either detecting the 0.511 MeV annihilation quanta or the particles directly. For the latter, a phosphor screen was installed after the gate electrode inside the trap. The screen was typically put at -6 kV. In front of the screen was a fine conducting mesh held at ground voltage, hence the particle acceleration took place in the gap between these.

We ordered a CCD to measure the accumulated light from the phosphor screen during dumping, but the camera was heavily delayed. Eventually, as a consolation, we received the state-of-the-art Apogee Alta U4000 CCD camera[1] at a very favorable price. The camera features a 2048×2048 pixel (each of 7.6×7.6 μm^2) KAI-4021M monochrome CCD, far beyond our needs. Unless else is stated, the CCD signal was corrected by a background measurement, and the CCD well charge content—ideally proportional to N_{e^+}—was normalized to the exposure time.

The efficiency (including the solid angle) of a $\varnothing$ 3″ $\times$ 3″ NaI(Tl) crystal with PMT was found as a function of distance using a calibrated ^{137}Cs source, which decays

[1] http://www.ccd.com/alta_u4000.html.

to an excited state of barium, $^{137}Ba^*$, successively emitting a $E_\gamma = 0.662$ MeV photon, similar to the positron annihilation photon. The found detector efficiency[2] was well-described by a power expression $\epsilon_{\mathrm{NaI(Tl)}} = a \times (x/\mathrm{cm})^{-b}$ with $a = 0.760$ and $b = 1.80$. By placing the detector in a distance to a fairly localized annihilation site, the count rate of the $E_\gamma \simeq 0.511$ MeV peak can be converted to a measure of the absolute number of positrons annihilating per time unit, if where pile-up effects are negligible. With the outlined method, the number of positrons annihilating on the RGM-1 gate valve per time unit was found to be $\simeq 2 \times 10^6/\mathrm{s}$, in accordance with FPSI's specifications scaled to our ^{22}Na source strength. On the other hand, if the detector is brought close to the annihilation site, *i.e.* covers a considerable solid angle, pile-up will occur if the positron annihilations are frequent. The measured pulse will be proportional to N_{e^+} (neglecting saturation and non-linear effects). The detector is then run in proportional mode as opposed to the single-particle mode mentioned above.

The NaI(Tl) has an energy resolution of $\simeq 8\%$ in the energy region of interest, but suffers from a poor timing resolution due to its slow exponential decay rate of 230 ns [Y$^+$06, Tab. 28.4]. When in need of a better timing resolution, we used a 5 cm thick fast plastic scintillator with a PMT, having an overall timing resolution of $\gtrsim 5$ ns, albeit with a much lower photon detection efficiency.

With these few tools, many of the parameters of the RGM-1 and MRT could be determined, as described in the following section.

8.2 Key Parameters

The Moderator

As mentioned earlier, the process of growing a Ne (s) moderator is software controlled and has four main phases: initialization, gas admission, moderator annealing and a finalizing phase. The parameters of the process have conveniently been set by FPSI, and we have only made diminutive modifications. In Figure 8.1a and 8.1b, the pressure in the RGM-1 and the NaI(Tl) counts at all particle energies as measured 48 cm from the closed RGM-1 gate valve, respectively, are shown during the process of growing a moderator.

Initialization: Any old moderator is evaporated by setting the moderator temperature PID setpoint to 23 K. The evaporation causes a heavy pressure increase from the typical $\simeq 2 \times 10^{-9}$ mbar, thus excluding usage of the ion pump. Afterwards, the temperature is taken down to 8.3 K and consecutively stabilized at 9.2 K, while the ion pump purges the vacuum again.

Gas Admission: A third MFC admits 2.00 cm^3/min of STP Ne (g) for 9 min. The Ne nozzle points to the $\simeq 40$ K radiation shielding of the second stage of the cold head, and most gas impurities will thus freeze out before reaching the 9.2 K copper cone, cf. Figure 7.3b. During this phase, the NaI(Tl) count rate, *i.e.* the number of positrons reaching the gate valve per time unit, increases an order

[2] It was Helge Knudsen, who performed the calibration of our initial NaI(Tl) detector. When this accidentally broke, I reproduced his result for a similar detector.

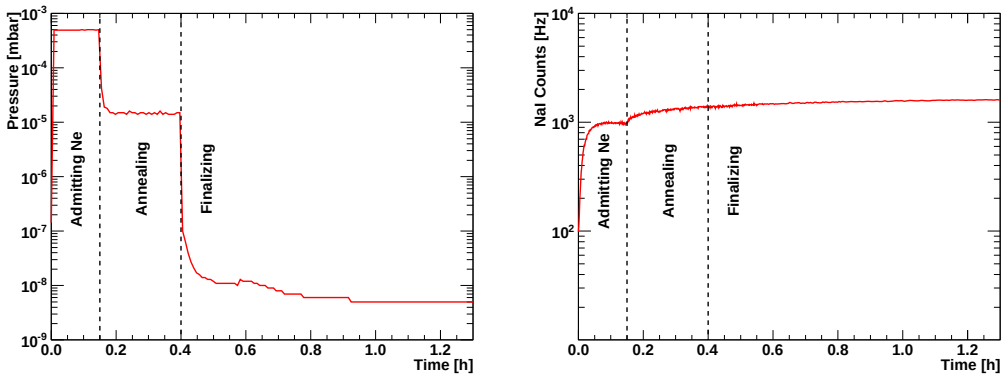

(a) Pressure.

(b) Annihilation events on the gate valve, as measured with our 3″ NaI(Tl).

Figure 8.1: The main stages of growing a solid neon moderator.

of magnitude from the background rate ($\simeq 10^2$ Hz). In this phase, no pumping is performed on the chamber, causing the pressure to reach $\simeq 5 \times 10^{-4}$ mbar.

Annealing: The neon MFC is now closed, causing a pressure drop to $\simeq 10^{-5}$ mbar. The lower base pressure and the annealing of the grown Ne (s) crystal at the 9.2 K cause a slow increase of the moderated positrons reaching the gate valve during this 15 min phase.

Finalizing: The ion pumping is restarted and the PID temperature setpoint is reduced to the typical 6.8 K. In $\simeq$ 15 min, the pressure goes below 10^{-9} mbar.

As seen in Figure 8.1b, the moderator efficiency increases slightly in the finalizing phase. At a different occasion, the moderator development was monitored for almost six days after growing, cf. Figure 8.2. The moderator efficiency would always increase $\simeq$ 25% for the first few days. After this, the moderator would exhibit an exponential deterioration. The moderator efficiency is primarily degraded by contaminants from the background gas in the vacuum chamber. When the gate valve between the RGM-1 and MRT was closed, base pressures as low as 1–3 $\times 10^{-9}$ mbar were reached as a result of the ion pump and cold head. The data of Figure 8.2 was measured under these circumstances, and the decay rate was found to be $\lambda_{\text{Mod}} = (1.26 \pm 0.01)\%/\text{d}$ through an exponential fit. Despite the large pumping speed of the cryo pump and the RGM-1 pumping restriction, (7) in Figure 7.3a, the RGM-1 base pressure would rise to $\simeq 10^{-8}$ mbar, due to the introduction of buffer gasses when including the MRT in bunching mode. This is expected to increase the moderator decay rate to $\lambda_{\text{Mod}} \simeq 4\%/\text{d}$ [Gre07] (depending on the choice of cooling buffer gas), but has not been measured in our setup.

Bunch Reproducibility

Many of the standard methods used for characterizing a positron source are based on destructive diagnostics, which—of course—relies on a high degree of shot-to-shot reproducibility. This was studied by measuring N_{e^+} per bunch with a set of

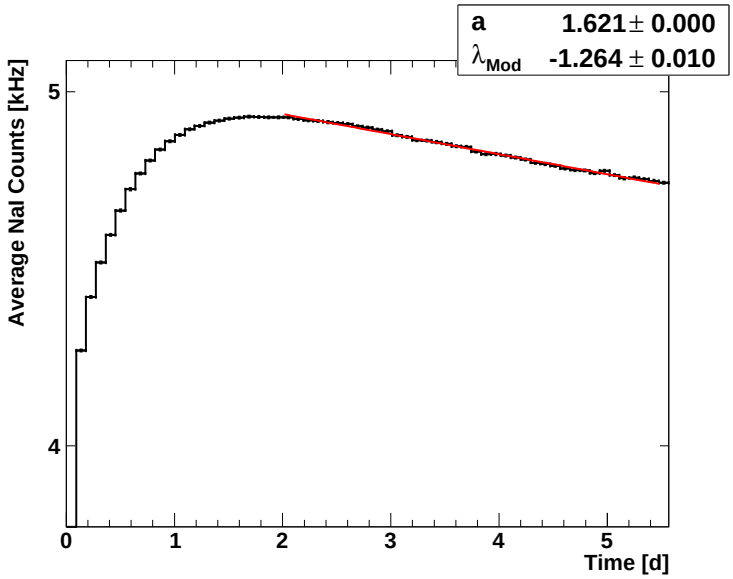

Figure 8.2: Moderator lifetime. The datapoints with statistical errors only are NaI(Tl) counts, while the red line is an exponential fit of the type $f(t) = \exp(a + 100\% \times \lambda_{\mathrm{Mod}} t)$. Although difficult to tell, the ordinate scale is logarithmic.

detectors. The positrons were in all cases dumped on the phosphor screen after the Gate electrode. The accumulated light yield was measured with the CCD, and the peak-to-peak signal of the annihilation burst was measured with the NaI(Tl) or the 5 cm plastic scintillator, both run in proportional mode.

In Fig. 8.3 on the next page, the measurements over a 2 h period (260 averaged measurements) with the three detectors are shown. For all detectors, the signal has been scaled to the mean signal over the period. Using the CCD, the relative RMS is found to be a mere $2.6(1)\%$. For the two other detectors, the distributions are about twice as wide, $5.7(3)\%$ and $5.2(3)\%$. The difference among the detectors could be the result of a convolution by the different detector resolutions.

Bunch Temporal Width

With the fast scintillator placed near the trap during a positron spill on the phosphor screen, we attempted to measure the bunch temporal width. As an average of a large number of bunches, the temporal width of the annihilation pulse was found to $\simeq (35 \pm 5)$ ns FWHM. This quantity should be related to the positrons' axial bounce frequency through the similarity theorem of Fourier decomposition. For our trap's parameters, $V_0 = V_{\mathrm{S4}} - V_{\mathrm{S3}} = 6.75$ V (during store phase), $4\rho_0 \simeq z_0 \simeq 5.0$ cm, the period of the axial motion in an idealized Penning trap is found

$$T_z^s \equiv \frac{2\pi}{\omega_z} = 2\pi \sqrt{\frac{mc^2}{2eV_0} \frac{(z_0^2 + \rho_0^2/2)}{c^2}} = 207 \text{ ns} . \tag{8.1}$$

In the dump phase, a relatively large voltage is applied to the S2 electrode, $V_0 = V_{\mathrm{S2}} - V_{\mathrm{S3}} = 32$ V, cf. Figure 7.5b. Although the trap is axially open in the $\hat{\mathbf{z}}$ direction, the greater potential curvature will have a temporally focusing effect. If one could

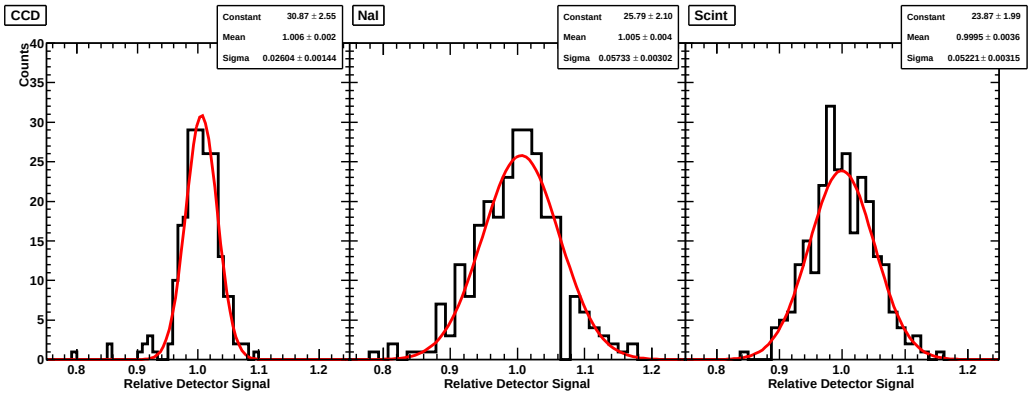

Figure 8.3: Shot-to-shot reproducibility of the trap as measured over 2 h (260 shots) with three detectors: a) The CCD measuring the light from the phosphor screen. b) The NaI(Tl) peak-to-peak signal and c) the scintillator signal, also peak-to-peak. In all figures, the signal has been scaled to the mean signal and a Gaussian distribution has been fitted to the data.

again assume a symmetric harmonic axial potential, the found period of the axial motion would be $T_z^d = 95.1$ ns, in better accordance with the measured value.

This temporal bunch width is thus—to some extent—tunable by setting the depth of the harmonic trap, V_0. The temporal bunch width specification is $\gtrsim 20$ ns. During a visit at FPSI, the width was measured to be $\lesssim 27$ ns with a fast BaF_2 detector.

Trap Lifetime

We now consider operating the trap with varying fill time and constant store time, while measuring the NaI(Tl) signal when the positrons are dumped on the phosphor screen. One can construct a differential equation consisting of two terms—the exponential decay of positrons due to the buffer gas and the constant addition of fresh positrons (during the fill phase)

$$\frac{dN_{e^+}}{dt_{\text{fill}}} = -\frac{N_{e^+}}{\tau_{\text{trap}}} + k$$

The differential equation is solved, and the particular solution fulfilling the constraint $N_{e^+}(0) = 0$ is chosen

$$N_{e^+}(t_{\text{fill}}) = k\tau_{\text{trap}}\left[1 - \exp(-t_{\text{fill}}/\tau_{\text{trap}})\right], \tag{8.2}$$

At some fill time, the rates of the two opposing processes will balance each other and a steady-state is reached, as is also seen from the expression. In Fig. 8.4a, the result of the proposed experiment is seen. The expression of Eq. (8.2) is fitted to the datapoints with the free parameters k (Norm) and τ_{trap}. In this way, $\tau_{\text{trap}} = (0.60 \pm 0.03)$ s is found. The NaI(Tl) signals measured in Figure 8.4a are, however, very large when $t_{\text{fill}} \gtrsim 2$ s. Saturation of the NaI(Tl) could thus influence the extracted lifetime. One could also find the trap lifetime by monitoring the NaI(Tl) signal while varying the

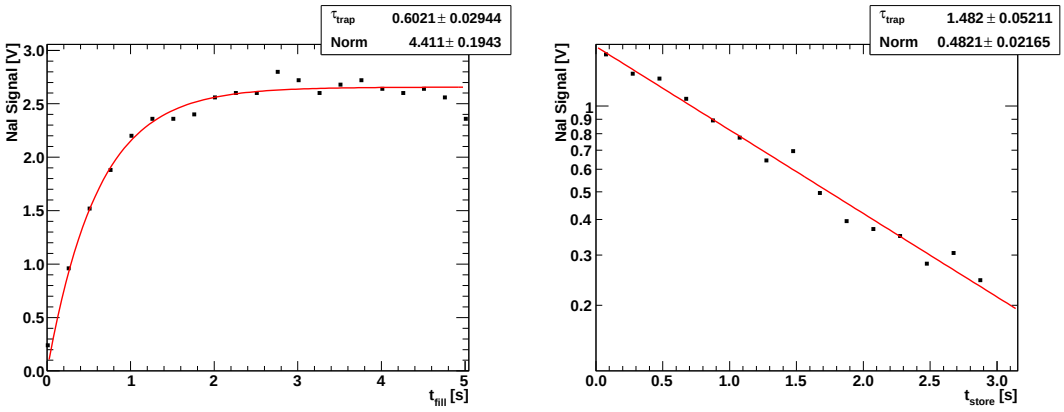

(a) Determining the lifetime of the trap by varying the fill time and measuring the resulting annihilation signal with a 3″ NaI(Tl) run in proportional mode. The fitted expression is defined in Eq. (8.2).

(b) Determining the lifetime of the trap by varying the store time. A simple exponential fit describes the data well.

Figure 8.4: A study of the positron lifetime in trap containing buffer gas.

store phase duration t_{store}. The latter approach is probably more reliable as the rate equation determining the number of particles left at time of extraction is also less complicated

$$\frac{dN_{e^+}}{dt_{\text{store}}} = -\frac{N_{e^+}}{\tau_{\text{trap}}} \,. \tag{8.3}$$

With this approach, the lifetime is found to be larger, $\tau_{\text{trap}} = (1.48 \pm 0.05)$ s, cf. Figure 8.4b. FPSI's specifies a lifetime of $\tau_{\text{trap}} \simeq 1.80$ s.

Positron Energy Spread

Because of the background cooling gas (SF_6), the energy spread of the positrons will diminish until it is on the scale of the vibrational and later rotational transitions, *i.e.* eventually reaching ambient thermal energies. The magnetic field could also cool the positrons through cyclotron radiation with a rate of approximately [SG04]

$$\lambda_c \simeq \left(\frac{B/\text{G}}{2 \times 10^4}\right)^2 \text{Hz} \,. \tag{8.4}$$

However, this mechanism is only relevant in traps with $B \gtrsim 1$ T $= 10^4$ G. In our trap, the magnetic field is a mere $B_{\text{trap}} = 500$ G, leading to $\lambda_c^{-1} \simeq 26$ min. Due to the finite buffer gas cooling rate and the lifetime of the positrons in the trap, there is a trade-off in t_{store} between the number of positrons per bunch and the energy spread.

We measured the energy spread in two similar but different ways. By setting the potential of the Gate electrode such that $V_{\text{Gate}} > V_{\text{S3}}$ during the dump phase, only the component of the positrons with energy $E_+ > e(V_{\text{Gate}} - V_{\text{S3}})$ is extracted, leading to annihilation on the phosphor screen. The retained positrons slowly annihilate due to the buffer gas (giving rise to an annihilation background) and are dumped after each measurement. In this way, the last few electrodes of our MRT can be used as a

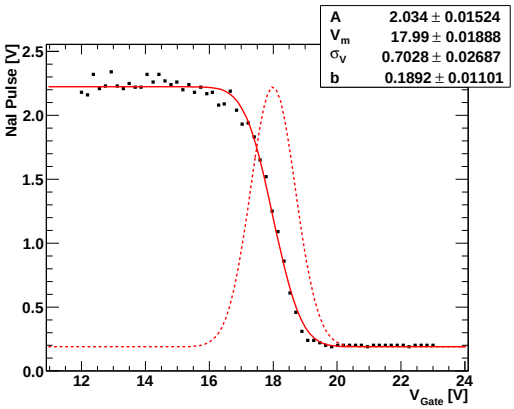

(a) The energy spread of the trapped positrons is measured by varying the retarding potential V_{Gate}, *i.e.* 'closing' the trap increasingly from bunch to bunch. The full line shows a fit with Eq. (8.7), while the dashed line is the corresponding Gaussian distribution.

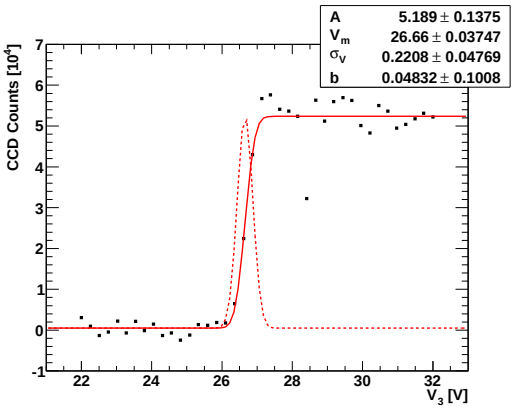

(b) Estimation of the parallel energy distribution in a way similar to Figure 8.5a, only here measuring with the CCD and increasingly 'emptying' the trap by raising V_3.

Figure 8.5: Determination of the parallel energy distribution of the positrons.

retarding potential analyzer. If the energy distribution of the positrons in the trap is assumed to be a Gaussian with a mean energy eV_m and width $e\sigma_V$

$$\frac{dN_{e^+}}{dV'} = \frac{N_{e^+}}{\sqrt{\pi}} \exp(-\chi^2) \frac{d\chi}{dV'} , \qquad \chi = \frac{V' - V_m}{\sqrt{2}\sigma_V} , \tag{8.5}$$

the number of positrons with an energy above eV_{Gate} can be stated through the complementary error function, $\text{Erfc}(x)$

$$N_{e^+}(V' > V_{\text{Gate}}) = \frac{N_{e^+}}{2} \underbrace{\frac{2}{\sqrt{\pi}} \int_{\chi_{\text{G}}}^{\infty} d\chi \exp(-\chi^2)}_{\text{Erfc}(\chi_{\text{G}})} , \qquad \chi_{\text{G}} = \frac{V_{\text{Gate}} - V_m}{\sqrt{2}\sigma_V} . \tag{8.6}$$

When varying the gate potential, the resulting proportional mode NaI(Tl) signal should thus be described by

$$S_{\text{NaI}} = \frac{A}{2} \times \text{Erfc}\left(\frac{V_{\text{Gate}} - V_m}{\sqrt{2}\sigma_V} \right) + b , \tag{8.7}$$

where A is proportional to the full number of particles in the trap, N_{e^+}, and b is a background. In Figure 8.5a, the result of the retarding potential analysis is shown. By comparing the signal from a number of bunches extracted with different values of V_{Gate}, the positron energy width was found from a fit with Eq. (8.7) to be $e\sigma_V = (0.70 \pm 0.02)$ eV. The mean energy of the positrons is also found to be $eV_m = (17.99 \pm 0.02)$ eV, consistent with eV_{S3} during the dump phase, cf. Table 7.2 on page 99.

The energy distribution was explored in greater detail by M.D. Lund [Lun09]. In the analysis shown above, the retarding potential $V_{\text{Gate}} - V_{S3}$ was varied while keeping V_{S3} fixed. Off course, one could also have held V_{S4} at a large, constant value, in our case 28.75 V, while raising the bottom of the trap, V_{S3}, from bunch to bunch.

Here, the number of exiting particles should be governed by the potential difference $V_{S4} - V_{S3}$, so the expression of Eq. (8.7) is still applicable after the replacement $(V_{\text{Gate}} - V_m) \rightarrow -(V_3 - V_m)$. The data measured as a function of V_{S3} all contained small artifacts, cf. Figure 8.5b. Firstly, the mean energy needed to escape the trap is found to be $V_m \simeq 26.7$ V, *i.e.* less than $V_{S4} = 28.75$ V. Secondly, the signal contains a reoccurring dip near V_{S4}. Although not fully understood, both effects could maybe follow from the fact that the axial potential profile is not applied instantaneously when changing trap phase. On the contrary, the electrode voltages are set one after another with some computational processing and communication in between. Also, the RW quadrupole introduces time dependent perturbations, of ± 1 V amplitude at the electrode surfaces, to the axial potential V_{S3}. Nevertheless, the effect of the quadrupole is zero on the center axis. If these are indeed the sources of the artifacts, it is hard to comprehend why they have not influenced any of our other ways of operating the trap. Be that as it may, any methodical effects causing the measured energy width to be smaller than the actual are hard to conceive. The main result thus seems reliable and the lower value of $e\sigma_V = (0.22 \pm 0.05)$ eV complies better with FPSI's specifications $(\lesssim 0.2$ eV$)$.

Bunch Transverse Size

The transverse size of the bunched beam was studied by observing the accumulated light from the phosphor screen when a number of bunches were dumped on it. The CCD was run in accumulation mode, where successive images—each of short duration—are summed. This is to avoid having overflows of the CCD potential wells (called blooming). By relating to the phosphor screen diameter, the CCD images were calibrated to physical distance. This calibration was under normal circumstances $\simeq 0.25$ mm per CCD pixel.

Being able to measure the beam spot on the phosphor screen, we found it interesting to vary the amplitude of the RW and observe its effect on N_{e^+} per bunch and the bunches' transverse extent. In Figure 8.6a, an image of the beam spot with 100% RW amplitude (typical operating conditions) is seen. The measured beam is very distinct and localized (radial RMS $\simeq 2.5$ mm) on top of a nearly uniform 2D plateau (a background image has been subtracted). In contrast to this, a similar image only with 10% RW amplitude is seen in Figure 8.6b. Although the beam spot is still distinguishable from the background, the beam spot is clearly broadened and the intensity is lower, *n.b.* the different intensity scales in the two pictures.

For a range of RW amplitudes, CCD images were taken and analysed by fitting a 2D Gaussian with a uniform background to the peaks. In this way, the volume of the Gaussian represents the number of positrons hitting the phosphor screen and the horizontal (x) and vertical (y) radial RMS values can be extracted from each fit. The results are presented in Figure 8.7. At the larger amplitudes 60–100%, the radius is almost constant at RMS $\simeq 2.5$ mm, while the number of positrons increases slowly. There is thus a slight tendency to saturation of the RW's effect. At lower amplitudes, the beam radius increases to about twice the size, but what is more important, the beam intensity drops almost to the background level. The latter is likely to be caused by annihilation at the trap electrode apertures during the fill and store phases.

It is shown that the beam radius can be brought down to (2.30 ± 0.05) mm RMS at the maximum RW amplitude. One should bear in mind, though, that this is mea-

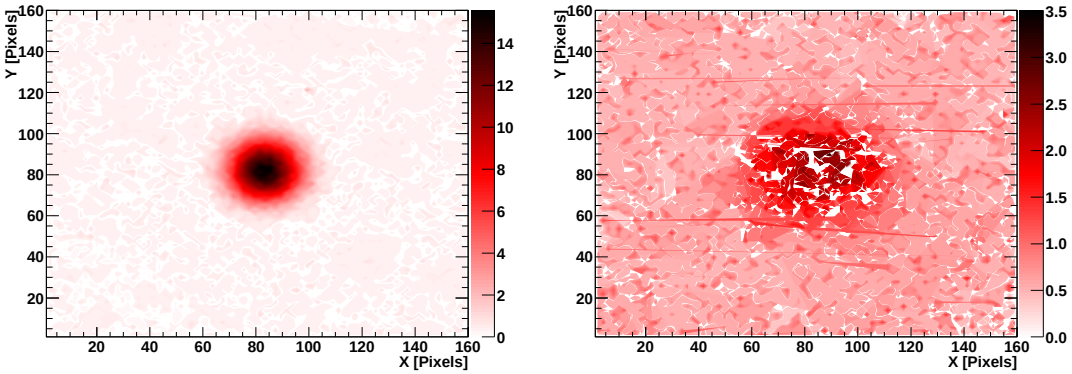

(a) Rotating Wall amplitude at 100%

(b) Rotating Wall amplitude at 10%.

Figure 8.6: Rotating wall at different amplitudes.

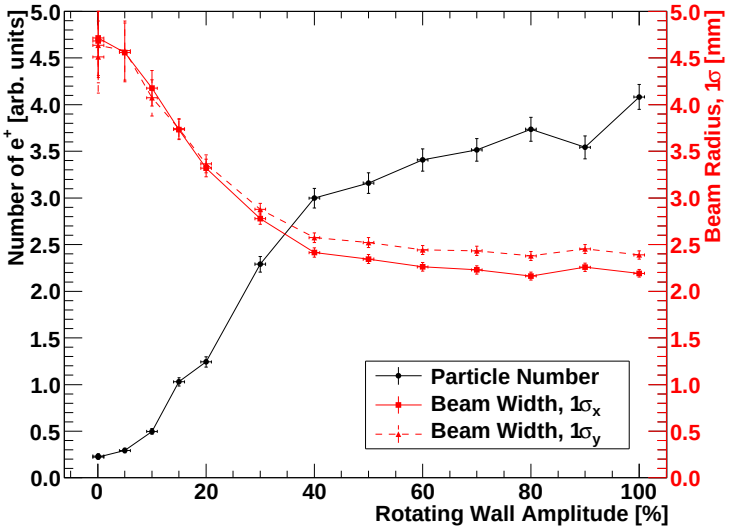

Figure 8.7: Effect of the rotating wall on bunch radius and N_{e^+}. Varying the RW amplitude clearly has an effect on the number of positrons per bunch and the radius of the beam.

sured in the $B_{\text{trap}} = 500\,\text{G}$, and during extraction (in a slowly varying magnetic field) to a different field B', an adiabatic expansion will change the beam RMS radius to r' [Jac98, Sec. 12.5]

$$r' = r_{\text{trap}} \times \sqrt{\frac{B_{\text{trap}}}{B'}} \simeq \frac{(51.4 \pm 1.1)\text{mm}}{\sqrt{B'\,[\text{G}]}}\,, \tag{8.8}$$

or put in another way: the number of magnetic field lines enclosed by the particle's cyclotron motion is an invariant. One should beware of this effect when considering apertures in a setup utilizing the extracted beam.

Trapping Efficiency

Due to imperfect transport of positrons from RGM-1 to and in the MRT, annihilation in the buffer gas, and the fill phase duty cycle of the bunching mode, not all positrons will be available in the bunched beam. The trapping efficiency is defined as the number of positrons in a bunch $(N_{e^+}^b)$ to the number positrons in the DC mode $(N_{e^+}^{\mathrm{DC}})$ in the duration of a bunch cycle.

$$\epsilon_{\mathrm{trap}} = \frac{N_{e^+}^b}{N_{e^+}^{\mathrm{DC}}} = \frac{V_{\mathrm{CCD}}^b}{V_{\mathrm{CCD}}^{\mathrm{DC}}} \,, \tag{8.9}$$

where V_{CCD}^m is the volume of the CCD 2D Gaussian $(\propto N_{e^+}^m)$ relative to the CCD exposure time in the mode m (bunch/DC). In both modes, the volume was extracted from an average of four CCD images, each of 10 s exposure. A careful analysis showed a trapping efficiency of $\epsilon_{\mathrm{trap}} = 25.9\%$. This trapping efficiency exceeds the manufacturer's specification of 17%. By comparing the CCD signal of the DC beam $(V_{\mathrm{CCD}}^{\mathrm{DC}})$ to $N_{e^+}^{\mathrm{DC}}/\mathrm{s}$ as measured with the NaI(Tl) of well-determined efficiency, the actual number of positrons per bunch could be established

$$\begin{aligned} \frac{N_{e^+}^b}{\mathrm{bunch}} &= \epsilon_{\mathrm{trap}} \times \frac{N_{e^+}^{\mathrm{DC}}}{\mathrm{s}} \times \left(\frac{\mathrm{bunch}}{\mathrm{s}}\right)^{-1} \\ &= 0.259 \times 5.89 \times 10^5 \ \mathrm{Hz} \times (2 \ \mathrm{Hz})^{-1} \\ &= 7.6 \times 10^4/\mathrm{bunch} \,, \end{aligned} \tag{8.10}$$

where the bunch rate is determined as t_{cycle}^{-1}, cf. Eq. (7.12), which was 2 Hz during these measurements.

With the bunch specifications found previously, we can estimate the positron bunch density (assuming spherical uniformity) to be $n_e \simeq 1.16 \times 10^6/\mathrm{cm}^3$, using $r = 2.30$ mm and $kT = 0.2$ eV. Here, the Debye screening radius $\lambda_{\mathrm{D}} = 2.72$ mm, cf. Eq. (7.10a). Since the Debye screening length is only slightly larger than the particle transverse extent, our particles should be considered not quite in the plasma regime. As is under consideration, the particle density could, however, be increased by purchasing a more intense ^{22}Na source, *e.g.* 50 mCi, thus also lowering the Debye screening length.

◇ ◇ ◇

Despite the rough and unfortunate beginning of our work with LEPS, it has proven to be a truly wonderful apparatus. After some revision by us, the central, LabVIEW-based controls allows for automatising complex maintenance and measuring schemes with ease. With the present ASACUSA plans, the LEPS is likely to stay in Aarhus for at least several years, whence a number of experiments utilizing the apparatus have been planned—most of which are described in [B$^+$04]. Many of the plans involve positronium (Ps) and charged positronium (Ps^-). One of the more long-standing experiments involves Multi-Photon Ionization (MPI) of positronium using an intense Nd:YAG laser [B$^+$04, ML99, Mad04]. Appendix C presents a feasibility study of the MPI experiment. The following chapter presents the results of our first experiment involving LEPS: measuring the Ps lifetimes.

CHAPTER 9

THE LIFETIME OF ORTHO-POSITRONIUM

With the high-quality positron beam of LEPS at our disposal, a test experiment involving positronium was devised. Positronium (Ps) is a bound atom-like, metastable state consisting of an electron and its antiparticle, the positron. There are thus some similarities between Ps and QCD quarkonium systems (charmonium $c\overline{c}$ and bottomonium $b\overline{b}$) [Per00]. Ps is entirely unaffected by hadronic effects, whence this non-relativistic bound system seems tailor-made for tests of QED, known for its extreme accuracy. The system can be used in searches for physics beyond the Standard Model, as discussed in [Rub04]. Extensive theoretical and experimental results have driven each other to ever greater precision—Karshenboim gives a nice discussion of the development [Kar03]. Also, since the positron and the electron are believed to be of identical masses[1], some of the corrections of hydrogen—scaling as the ratio of the electron and proton mass $m/m_p \simeq 1/1836$—are greatly enhanced in Ps, as we shall see. Our test experiment comprises a measurement of the decay rates of Ps—a field where discrepancies between theory and experiments have existed until recently. As will be discussed, our experiment aims—for now—for proof-of-principle.

9.1 Positronium Characteristics

Positronium is similar to the simple hydrogen atom, which has been well-investigated during the previous century, theoretically as well as experimentally. But whereas the reduced mass μ_r of the two-body system of hydrogen is close to the electron mass, $\mu_r = 0.9995m$, the reduced mass of the Ps system is exactly $m/2$. Many characteristics of Ps can thus simply be found by scaling the hydrogen results

$$B_{\mathrm{Ps},n} = \frac{\alpha^2 \mu_r c^2}{2n^2}\,, \qquad B_{\mathrm{Ps},1} = 6.80\ \mathrm{eV} \tag{9.1a}$$

$$r_{\mathrm{Ps},n} = n^2 a_0 \frac{m}{\mu_r}\,, \qquad r_{\mathrm{Ps},1} = 2a_0 = 1.06\ \text{Å}\,, \tag{9.1b}$$

[1] The relative mass difference is found to be less than 8 ppb at a 90% confidence level [Y$^+$06]. In this document, $m = 0.510998910(13)\mathrm{MeV}/c^2$ is used both for the electron and positron mass.

where $B_{\mathrm{Ps},n}$ is the Ps binding energy of the state n (neglecting any fine structure), and r_n is the nth Bohr orbit. The binding energy of Ps is half of that in H, while the extent of the Ps system is twice the size of the H-system.

Both the leptons are spin-$\frac{1}{2}$ fermions, $s = \frac{1}{2}$, $m_s = \pm\frac{1}{2}$, where s and m_s are the characteristic quantum numbers of an angular momentum operator. The combined spin states in Ps can be found by the formal theory of combining angular momenta. We will consider the two sets of basis states labelled $|S, M\rangle$ (S and M now describes the combined system) and $|m_s^-, m_s^+\rangle$, respectively, where m_s^c refers to the projected spin quantum number of the particle with charge c. The two basis sets are related through the Clesch-Gordan coefficients

$$|S = 1, M = +1\rangle = |+,+\rangle \tag{9.2a}$$

$$|S = 1, M = -1\rangle = |-,-\rangle \tag{9.2b}$$

$$|S = 1, M = 0\rangle = \frac{1}{\sqrt{2}}\big[|+,-\rangle + |-,+\rangle\big] \tag{9.2c}$$

$$|S = 0, M = 0\rangle = \frac{1}{\sqrt{2}}\big[|+,-\rangle - |-,+\rangle\big]\,. \tag{9.2d}$$

The spin triplet states, ortho-Ps ($S = 1$), are seen to be symmetric under particle interchange, in contrast to the singlet state, para-Ps ($S = 0$). The particle spatial states are characterized by the quantum numbers n and $l < n$. In hydrogen, the levels are split primarily by fine structure (FS) at an energy scale $E_{\mathrm{FS}} \propto \alpha^3 mc^2$ (caused by a relativistic correction, electron spin-orbit coupling and the Darwin term) and secondly by hyperfine structure (HFS) (caused by the nuclear spin-orbit coupling and spin-spin interaction) at an energy scale $E_{\mathrm{HFS}} \propto \alpha^5 mc^2$. The HFS is thus smaller than the FS by a factor of $\simeq \alpha^2$ in regular atoms.

In Ps, both particles have magnetic moments of one Bohr magneton $\mu_{\mathrm{B}} = e\hbar/2m$, the inter-particle distance is doubled and higher-order QED processes (*e.g.* virtual annihilation) land the Ps splitting somewhat in between the ordinary FS and HFS, and the combined splitting will be referred to as HFS. The Ps states are labelled after the nomenclature $n^{2S+1}L_J$, where $L = S, P, D, F$ for $l = 1, 2, 3, 4$, and J is the quantum number for the sum of the orbital and spin angular momenta. The ground state HFS, *i.e.* energy difference between *o*–Ps and *p*–Ps, is approximately [Ric81]

$$\Delta_1 \equiv E(1^3S_1) - E(1^1S_0) \simeq \frac{7}{12}\alpha^4 mc^2 = 0.846 \text{ meV}\,, \tag{9.3}$$

quite close to the best theoretical value of $\Delta_1 = 0.841$ meV given in [Ric81], where the lowest order virtual annihilation channel of *o*–Ps contributes by an impressive $\alpha^4 mc^4/4 \simeq \Delta_1/2$. The $n = 1$ Ps is typically formed through mechanisms involving energies much larger than Δ_1, and Ps is thus statistically divided in the triplet (*o*–Ps) and the singlet states (*p*–Ps) in the ratio 3:1.

Annihilation Lifetimes

The Ps states are eigenstates of the charge and space parities, $\hat{C}$ and $\hat{P}$, respectively. As discussed below Eq. (9.2), the spin states have the symmetry

$$\hat{P}|S, M\rangle = (-1)^{S+1}|S, M\rangle\,,$$

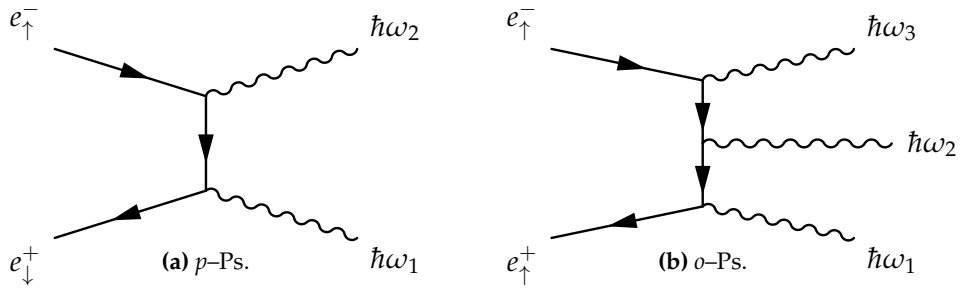

Figure 9.1: Lowest order Feynman diagrams displaying the decay of the two ground states of Ps. There are $(2!-1)$ and $(3!-1)$ other, indistinguishable diagrams of same leading order in α, respectively. The small arrows symbolize the projected spin quantum number.

under particle interchange, while the spatial functions have the symmetry $(-1)^{L+1}$. The latter stems from the symmetry of the spherical harmonics, $\hat{P}Y_L^M = (-1)^L Y_L^M$, times the product of the intrinsic parities of the electron and positron. The charge interchange operation $\hat{C}$ must comprise a spatial and spin interchange, having the overall eigenvalue $(-1)^{L+S+2} = (-1)^{l+S}$ [Ric81, Per00]. The eigenvalue of $\hat{C}$ applied to a system consisting of n photons is $(-1)^n$, and from this, we can understand that Ps states with quantum numbers L and S will predominantly decay to $n_{\min}$ photons, where $n_{\min}$ is the minimum integer $n \geq 2$ fulfilling $(-1)^{n-(L+S)} = +1$, *i.e.* conserving the charge quantum number and momentum in the Ps rest frame. By this reasoning, o–Ps (1^3S_1) is expected to decay to $n = 3$ photons, while p–Ps (1^1S_0) decays directly to $n = 2$ photons. In Figure 9.1, the lowest order Feynman diagrams describing the annihilation of p–Ps and o–Ps are shown. In the p–Ps rest frame, the photons, each with an energy mc^2, are emitted back-to-back. Following [Per00, p. 104], the decay rate of p–Ps (λ_S) can be estimated to leading order through simple, dimensional arguments. Judging from the number of electromagnetic vertices, the leading order in α contributing to the rate should be α^2. Also, the rate of decay must be determined by the chance of spatial encounter of the leptons, *i.e.* by the quantum mechanical probability density function of the Ps ground state, $|\Psi_{1S}(0)|^2 = (\pi a_{\mathrm{Ps},0}^3)^{-1}$, where $a_{\mathrm{Ps},0} = 2a_0 = 2\lambda\!\!\!^{-}_{\mathrm{c}}/\alpha$. The dimension of the product is changed to time through the fundamental constants of the problem $(\hbar, m, c)$

$$\begin{aligned}\lambda_S &= \alpha^2 \times \frac{1}{\pi a_{\mathrm{Ps},0}^3} \times c\left(\frac{\hbar}{mc^2}\right)^2 \\ &= \alpha^2 \times \frac{\alpha^3}{8\pi\lambda\!\!\!^{-3}_{\mathrm{c}}} \times c\lambda\!\!\!^{-2}_{\mathrm{c}} = \frac{\alpha^5 mc^2}{8\pi\hbar}\,. \end{aligned} \tag{9.4}$$

By applying the Feynman rules to the first order diagrams, a similar rate is found, $\lambda_{S0} = \alpha^5 mc^2/2\hbar$. This rate corresponds to an exponential lifetime of $\tau_{S0} = 124.49$ ps $(1/\lambda_{S0})$, close to the best theoretical calculation of $125.1624(6)$ ps [Kar03].

Regarding the decay of o–Ps, cf. Figure 9.1b, the process can be thought of as a combination of a spin-flip, leading to the emission of one photon, and a two-photon decay, like p–Ps. Because of the extra electromagnetic vertex, $\lambda_T/\lambda_S \sim \alpha$ is expected.

By analyzing the possible diagrams to lowest order in α

$$\lambda_T = \underbrace{\frac{2(\pi^2-9)}{9\pi\hbar}\alpha^6 mc^2}_{\lambda_{T0}} + \mathcal{O}(\alpha^7)\,, \tag{9.5}$$

is found [Ric81], where the leading order term corresponds to a lifetime of $\tau_{T0} = 138.67$ ns $(1/\lambda_{T0})$. Whereas the decay of p–Ps and unbound positrons in contact with electrons are almost indistinguishable (as they both annihilate to two monoenergetic photons on a very short timescale), the slower annihilation rate and distributed single-photon energies of o–Ps can be used as a confirmation of Ps formation [MJ83].

Adkins *et al.* have managed to include the corrections up to $\mathcal{O}(\alpha^8)$, leading to the theoretical lifetime $\tau_T = (142.0468 \pm 0.0002)$ ns [AFS00, AFS02]. As stated in [AFS02], the most precise experimental value of that time [NGRZ90] (found in vacuum) deviated 5.1 experimental standard deviations from this theoretical value, thus defining the o–Ps Lifetime Puzzle. The latter is believed to be resolved by the vacuum experiments by Vallery *et al.* finding $\tau_T = (142.037 \pm 0.020)$ ns [VZG03]. Shortly after their experimental convergence with theoretical calculations, the Tokyo group (Asai *et al.*) measured the lifetime of o–Ps formed in SiO_2 powders with improved accuracy and found good accordance [AJK04]. Their accuracy was here at the $\simeq$ 200 ppm level, like Vallery *et al.*'s result. Recently, the Tokyo group has pushed the accuracy even further to the $\simeq$ 150 ppm level [KAK09], or 100 ppm when combining their results. At this level of precision, their study is the first to have successfully tested the QED corrections of order α^2 [AFS00, AFS02]. As A. Rubbia implies in [Rub04], both studies contain minor dubious elements, and an independent study is justified even though the o–Ps lifetime puzzle seems resolved by both vacuum and SiO_2 powder studies.

Recently, Kniehl *et al.* expressed a part of the radiative corrections of Adkins *et al.* in a closed analytical form, allowing for a computation of these to an arbitrary precision [KKV08], thus slightly lowering the uncertainty and changing the value to (142.0459 ± 0.0002) ns.

Applying a Magnetic Field

If one applies a space- and time-invariant magnetic field $\boldsymbol{B} = B\hat{\boldsymbol{z}}$, the magnetic contribution to the Ps Hamiltonian is [Hal54]

$$\hat{H}_m \simeq \frac{g'}{2}\mu_B B\left[\sigma_z(e^-) - \sigma_z(e^+)\right]\,, \tag{9.6}$$

where $g'/2 \simeq 1.00116$ [HFG08] is the anomalous electron g-factor and $\sigma_z(e^c)$ is the Pauli spin matrix, diagonal in the subspace $|s^c, m_s^c\rangle$ of $|m_s^-, m_s^+\rangle = |s^-, m_s^-\rangle \otimes |s^+, m_s^+\rangle$ with eigenvalues $2m_s^c$. This perturbation gives rise to non-diagonal elements of the energy matrix as expressed in the spin basis introduced in Eq. (9.2)

$$\begin{aligned}\langle 1,0|\hat{H}_m|0,0\rangle &= \frac{g'}{2}\mu_B B\langle 1,0|\left[\sigma_z(e^-) - \sigma_z(e^+)\right]\frac{1}{\sqrt{2}}\left[|+,-\rangle - |-,+\rangle\right] \\ &= g'\mu_B B\langle 1,0|\underbrace{\frac{1}{\sqrt{2}}\left[|+,-\rangle + |-,+\rangle\right]}_{|1,0\rangle} = g'\mu_B B\,,\end{aligned} \tag{9.7}$$

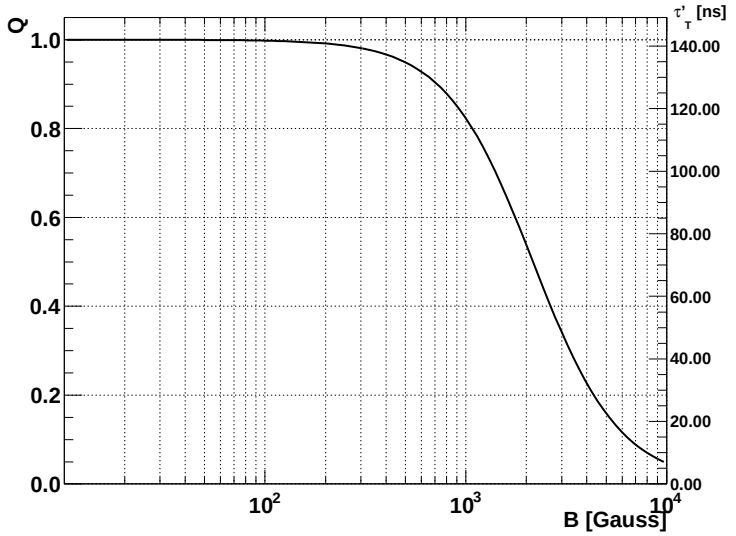

Figure 9.2: The relative quenched lifetime of the *o*–Ps state $|1,0\rangle$. The right scale shows the absolute lifetime in ns. Near $B = 10^3$ G, the quenching is a 20% effect.

leading to $\langle S', M'|\hat{H}_m|S, M\rangle = g'\mu_B B\delta_{M',M}$. After a re-diagonalization, the energy eigenstates have the following eigenvalues of the combined Hamiltonian operator

$$E'\big(|1,\pm1\rangle\big) = E(1^3S_1) \tag{9.8a}$$

$$E'\big(|1/2\pm1/2,0\rangle\big) = \frac{1}{2}\big[\underbrace{E(1^3S_1)+E(1^1S_0)}_{\Sigma_1}\big] \pm \frac{1}{2}\big[\underbrace{E(1^3S_1)-E(1^1S_0)}_{\Delta_1}\big]\times[1+x^2]^{1/2}\,, \tag{9.8b}$$

where $x = 2g'\mu_B B/\Delta_1 \approx B/36288.3$ G [Ric81]. This leaves only $|1,\pm1\rangle$ degenerate, while mixing the $|1,0\rangle$ and $|0,0\rangle$ states. The mixing has radical effects on the decay rates of the affected states, especially $|1,0\rangle$, since a component of the state will now be allowed to decay through the $n = 2$ photon channel, essentially a factor $\simeq \alpha^{-1}$ faster, giving rise the magnetic quenching of Ps. The decay rates of the mixed states due to magnetic quenching are given by [BP80]

$$\begin{bmatrix} \lambda'_T \\ \lambda'_S \end{bmatrix} = \frac{1}{1+y^2}\begin{bmatrix} 1 & y^2 \\ y^2 & 1 \end{bmatrix}\begin{bmatrix} \lambda_T \\ \lambda_S \end{bmatrix}\,, \qquad y = \frac{x}{1+\sqrt{1+x^2}}\,. \tag{9.9}$$

In a $B = 1$ kG field, the quenched lifetimes are $\tau'_T = 116.9$ ns and $\tau'_S = 0.1252$ ns. A coefficient describing the degree of quenching of the $|1,0\rangle$ state can be defined

$$Q(B) \equiv \frac{\lambda_T}{\lambda'_T} = \frac{\tau'_T}{\tau_T} = \frac{1+y^2}{1+y^2(\tau_T/\tau_S)}\,, \tag{9.10}$$

which depends on B through the parameters y and x. The theoretical curve of the coefficient is plotted in Figure 9.2. Due to the quenching, the rate of delayed $n = 3$

photon decays of the $|1,0\rangle$ state is reduced from λ_T to $\lambda'_T(3\gamma) = \lambda_T/(1+y^2)$, while the number of delayed $n = 2$ photon decays increases from $\lambda_T(2\gamma) = 0$ to $\lambda'_T(2\gamma) = y^2\lambda_S/(1+y^2)$, such that the relative 3γ yield is [Ric81][2]

$$\begin{aligned} F_{3\gamma} &= \frac{1}{3}\left[2\frac{\lambda_T(3\gamma)}{\lambda_T(3\gamma)+\lambda_T(2\gamma)} + \frac{\lambda'_T(3\gamma)}{\lambda'_T(3\gamma)+\lambda'_T(2\gamma)}\right] \\ &= \frac{1}{3}\left[2 + \frac{1}{1+y^2\lambda_S/\lambda_T}\right], \end{aligned} \tag{9.11}$$

where the terms correspond to the $|1,\pm1\rangle$ and $|1,0\rangle$ states, respectively. With a setup sensitive to $F_{3\gamma}$, *e.g.* having a segmented detector covering a large solid angle, versus B, Δ_1 can be found if λ_S/λ_T is known, or *vice versa*. In this way, Deutsch and Dulit first measured Δ_1 to 15% precision [DD51]. Later, Deutsch vastly improved the precision by adding a rf magnetic field $\boldsymbol{B}(t) = B\hat{\boldsymbol{z}} + B_y\cos(\omega t)\hat{\boldsymbol{y}}$, which drives the transition $|1,\pm1\rangle \leftrightarrow |1,0\rangle$, eventually giving rise to a Lorentzian resonance, when varying B [DB52, Hal54].

Returning to the uniform magnetic field $\boldsymbol{B}(t) = B\hat{\boldsymbol{z}}$, it is important to stress that a population of Ps will possess three lifetime components in a magnetic field, since the $|1,\pm1\rangle$ states are unaffected.

$$\begin{aligned} N(t) &= N_0\left\{(1-\beta)\exp(-\lambda'_S t) + \frac{\beta}{3}\left[2\exp(-\lambda_T t) + \exp(-\lambda'_T t)\right]\right\} \\ &= N_0\left\{(1-\beta)\exp(-\lambda'_S t) + \frac{\beta\exp(-\lambda_T t)}{3}\left[2 + \exp[-(\lambda'_T - \lambda_T)t]\right]\right\}, \end{aligned} \tag{9.12}$$

where $\beta \simeq 0.75$ as mentioned. At typical fields, τ'_S is still very short, *i.e.* hard to measure directly, due to experimental limitations. Nevertheless, with a setup sensitive to the change in decay rate $\lambda'_T - \lambda_T$ in a magnetic field, λ_S can be extracted, if the quenching transformation of Eq. (9.9) (including Δ_1) is well-known. Our experiment is an attempt at determining λ_s in this indirect manner. The lower limit of the precision is set by the precision of the quench transformation, *e.g.* the value of the Ps HFS splitting Δ_1. To measure the lifetime of Ps is not a new business, but so far, the vacuum p–Ps lifetime has only been found through magnetic quenching in experiments where a background gas served as the production target of Ps [ARG94]. Although the found lifetime is extrapolated to zero partial pressure, it would be a purer experiment to measure the lifetimes in a vacuum, as we have attempted.

9.2 Experimental Setup

Production of Positronium

When positrons enter the bulk of a foil with positron (electron) work function ϕ_+ (ϕ_-), they will lose energy through various inelastic processes (such as phonon excitation) by which some end up being thermalized, i.e. having kinetic energies E_+

[2]Here, it has been assumed (for simplicity) that o–Ps decays exclusively to $n = 3$ photons when no magnetic field is present. Higher-order decays are of course also possible, although suppressed at least by a factor α^2. In a strong magnetic field, the magnetic quenching is stronger than the higher-order corrections.

of order kT_{foil}. The thermalization typically takes places on a timescale $\simeq 10^{-12}$ s [SL88]. The fate of a thermalized positron inside a foil with $\phi_+ > E_+$ is either annihilation with bulk electrons or formation of positronium. In the latter process, one distinguishes between two mechanisms—that of capture in flight (prompt Ps) and thermal activation. In prompt emission, the positron picks up an electron just before reentering vacuum. This is energetically favorable when the formation potential $\epsilon_{\text{Ps}} = \phi_+ + \phi_- - B_{\text{Ps}}$ is negative. In the case of thermally activated Ps, the positron diffuses to the surface of the material and becomes bound in the image potential wells of the surface with an energy $E(e^+, \text{image})$. Ps can be formed here by thermally desorbing a positron along with a bulk electron—a process which has the activation energy [CMJM81, PCC$^+$91]

$$\Delta E = -E(e^+, \text{image}) + \phi_- - B_{\text{Ps}} \,.$$

The process rate can be enhanced greatly by heating the foil [CMJB74]. The velocity distribution typically resembles a Maxwell-Boltzmann distribution with a high-energy tail. We define the distance ℓ_τ traversed in one *o*–Ps lifetime by Ps with a kinetic energy E_{Ps}

$$\ell_\tau \equiv \tau_T v_{\text{Ps}} = \tau_T c \sqrt{\frac{E_{\text{Ps}}}{mc^2}} \,, \tag{9.13}$$

where scattering off a background gas or surfaces has been neglected. From this quantity, 1 eV *o*–Ps is found to travel 6.0 cm in one lifetime. If one is interested in measuring the *o*–Ps lifetime, it is evident that thermalization of the *o*–Ps in the production target bulk is important, since *o*–Ps with $E_{\text{Ps}} \gtrsim 1$ eV will be able to stray to regions of lower annihilation detection efficiency, thus lowering the measured decay spectrum at longer times. The thermalization thus provides some spatial confinement of the Ps. *o*–Ps not reaching the surface again will annihilate with a $\simeq$ ns lifetime due to pick-off annihilation, where the positron annihilates with a bulk electron with the appropriate spin. Depending on the implantation depth, some of the *o*–Ps will be thermalized.

The Setup

Our setup is greatly inspired by a method by Gidley *et al.* [GZMR76, GZ78]. Here, $E_+ \simeq 400$ eV positrons were guided into a confinement can of volume V_c through a small aperture of area A_a. The inside of the can was coated with MgO powder which almost completely reflects Ps. At the end of the can, a Channel Electron Multiplier (CEM) detector was located, cf. Figure 9.3a. The MgO coated opening of the CEM served two purposes. When struck by a positron, the avalanche of secondary electrons would give a timing reference of the arrival of a positron. Also, it served as a decent $e^+e^- \to$ Ps converter with an efficiency of $\simeq 15\%$. The lifetime of the Ps was studied by, basically, letting the CEM start a Time-to-Amplitude Converter (TAC) which was later stopped by three scintillators surrounding the region of interaction and detecting the annihilation photons. The measured decay spectrum was fitted with an exponential, describing a single lifetime component, above a uniform background. The lower edge of the fitting interval was chosen well away from the prompt annihilation (caused by singlet Ps and unbound positrons). Using this technique, the

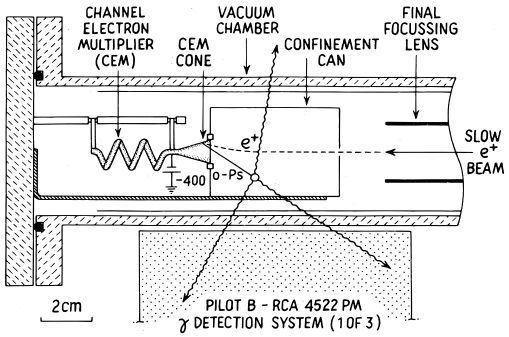

(a) The setup used in [GZMR76, GZ78]. The positrons enter the MgO-lined confinement can from right to left and strike a CEM detector. The detector pulse starts a TAC which is stopped by the scintillators or a TAC overflow. From [GZ78].

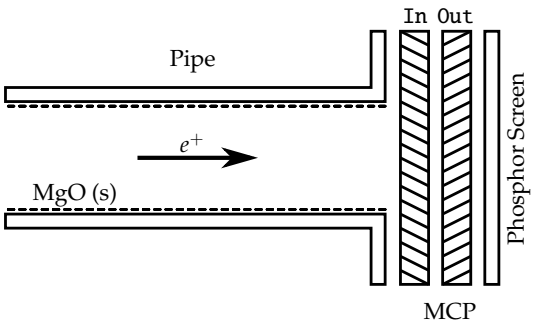

(b) Our Ps production region. A MgO coated Al pipe is mounted on the MCP detector (Chevron design). The figure is generally not to scale—especially the width of the channels (shown in white) are greatly exaggerated. The assembly is situated in a variable, guiding magnetic field.

Figure 9.3: Two similar methods of using a detector as the Ps production target.

lifetime of *o*–Ps was found to be $\tau_T = 141.8(3)$ ns by extrapolating to infinite can volume relative to aperture area $A_a/V_c \to 0$. This extrapolation treats Ps loss through the can aperture and interactions at the walls—a correction of order $\simeq 1$ ns.

A sketch of our very similar setup is shown in Figure 9.3b. The positrons were magnetically steered onto a MicroChannel Plate (MCP) detector comprising two MCP stages, labelled `In` and `Out`, and a phosphor screen. The three plates can be biased with voltages labelled V_I, V_O and V_P. Each MCP plate surface is covered by numerous angled channels (chevron design) leading from one face to the opposite. A charged particle entering one of the closely-packed channels of about $\varnothing$ 10 μm will generate a large number of secondary electrons due to multiple wall collisions ensured by an acceleration bias $V_O - V_I$ and the angle. Each microchannel is thus similar to a PMT, only with a continuous channel serving as dynodes. Finally, visualization of the electron cascade on the phosphor screen can be obtained with the bias $V_P - V_O$. The LEPS MRT was operated in DC mode, and the positrons were guided through an extraction and test beam line which reduced the positron count rate registered at the MCP to $\lesssim 10^5$ Hz.

In front of the MCP, a lathed Al pipe with a collar was installed. The $\varnothing$ 25 mm $\times$ 150 mm pipe gave some containment of the produced Ps. Although installing a lid with a small e^+ entrance aperture was tried, one end of the pipe was usually wide open. This gives an entrance aperture to volume ratio of $A_a/V_c = 1/l_c$, where $l_c = 150$ mm is the length of our can. The ratio of aperture area to can inner surface is in our case $A_a/A_c = 4\%$. With $E_{\mathrm{Ps}} = 1$ eV, the length of the Al pipe would be traversed in $2.5\tau_T$, in case of beeline trajectory.

Following the procedure of [GZ78], a thin layer of MgO was deposited on the inner walls by burning magnesium shavings in the pipe. The electrically grounded pipe would also screen the bias contact pins of the MCP detector. The voltages of the latter were set to $V_I \lesssim -200$ V—to slightly accelerate the incoming 20 eV positrons and deflect any electrons in the vacuum chamber—$V_O \simeq +1.8$ kV and $V_P \simeq +3$ kV. The MCP signal was readout from the `Out` electrode through a capacitor, cf. Fig-

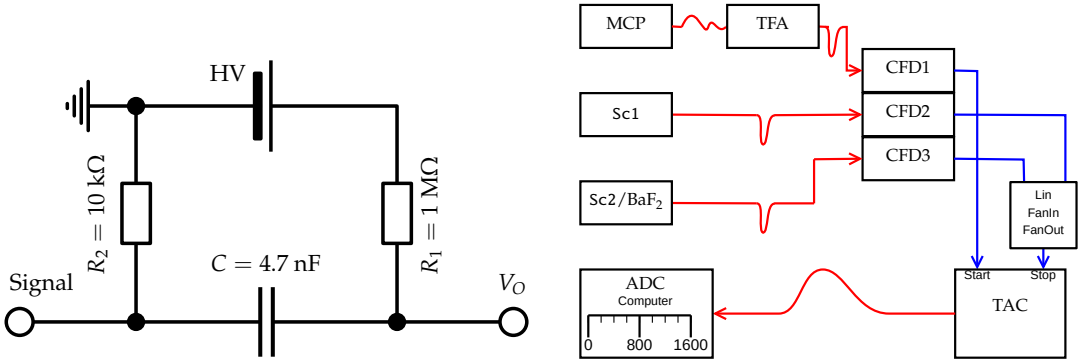

(a) A HV is applied to the `Out` plate while measuring the signal through a high-pass frequency filter constituted by $R_2C = 47$ µs.

(b) A sketch of the electronics applied for measuring the Ps lifetime. The blue lines carry logic signals, while the red carry analog signals. In the latter case, the pulse shapes are sketched.

Figure 9.4: Electronics setup for the Ps lifetime experiment.

ure 9.4a. In this way, an amplification could be maintained independently of the positron acceleration voltage (V_I).

The pipe and MCP were mounted centrally in the bore of a former EBIS magnet of length $l_m = 63.5$ cm. With an accurate, high-current power supply, a maximum field of $B \simeq 1120$ G was measured at $\simeq 130$ A. The current drift was monitored and found negligible. Also, the measured magnetic field was found to be very linear in the current source setpoint. Since $l_c \ll l_m$, fringe field effects are negligible.

The annihilation photons were registered with a pair of $20 \times 20 \times 5$ cm^3 plastic scintillators or, tentatively, a $\varnothing$ 35 mm $\times$ 50 mm BaF_2, where the latter is mounted on a fast PMT (Photonis XP2020Q) sensitive to the crystal's fast, ultraviolet component. On a rare occasion, the latter "stop" detector gave very large pulses not correlated with incoming particles. This could be due to a defect in the PMT or the crystal–PMT assembly. Because of this, the stop detectors were typically the two large organic scintillators. The scintillators were placed axially centered on the confinement can and radially adjacent to the magnet surface, about $r = 11$ cm from the interaction site. The two scintillators thus covered 30% of the full 4π solid angle.

A sketch of the used signal modules is seen in Figure 9.4b. MCPs are known to give "ringing" signals for $\simeq 1$ µs, after it is hit by the initial particle. To keep this from being registered as a double-hit, the MCP Constant Fraction Discriminator (CFD) was set to a blocking time of 1 µs. Also, the MCP signal was reshaped and inverted by a Timing Filter Amplifier (TFA). The timing signals from the stop detectors' CFDs were effectively `ORed` using a Linear FanIn/FanOut, thus increasing the detection efficiency. The stop detectors could also be run in coincidence mode (`AND`), which of course reduced the count rate considerably. The Ortec 437A TAC was operated with full range of 1 µs, corresponding to more than $7\tau_T$.

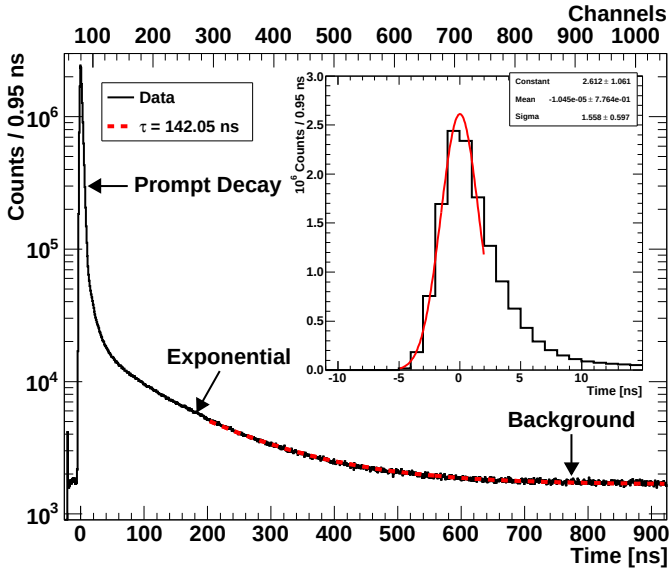

Figure 9.5: A typical decay spectrum with the prompt peak and a slower exponential decay on top of a flat background. In this case, the magnetic field is low, $B \simeq 40$ G. An exponential decay with $\tau = 142.05$ ns above our background level is shown for reference. The inset shows a Gaussian distribution fitted to the prompt peak. Especially the width of the latter is of interest.

9.3 Analysis

Single Component Fitting

A typical decay spectrum is seen in Figure 9.5. The so-called prompt peak (arising from annihilation of unbound positrons and p–Ps) gives a distinct timing reference. At larger times, a slower decaying lifetime component is seen before the spectrum reaches an almost flat background. In the inset of Figure 9.5, the FWHM of the prompt peak is found to be 3.67 ns, resembling the temporal noise of our detection system.

We estimate the lifetime using a simplified version of Eq. (9.12) with $\beta = 1$ (*i.e.* not describing the p–Ps decay) and a uniform background. At low magnetic field, only one lifetime component is assumed, $\lambda_T' = \lambda_T$. All parameter estimations (fits) were performed using the maximum likelihood estimator. In the field of precise parameter estimation from binned data, one should use a Poisson-based maximum likelihood estimator, since this class of estimators are less prone to be biased or inconsistent. A delightful review on the topic of statistics and estimators is given in [Jam06].

In between the prompt peak and the slower exponential, the pick-off decay of Ps in the bulk gives rise to lifetimes of order $\lesssim 30$ ns. Since we used a model including a finite number of lifetimes, one must steer clear of this region. To avoid the influence of the faster annihilation, the lower edge of the fitting region (f_{low}) was varied while keeping $f_{\text{Hi}} = 1024$. At each lower edge of the fitting region (f_{low}), a fit was performed yielding the parameter λ_T' with error and the reduced χ^2 per k degrees of freedom in the fit, $\chi_r^2 = \chi^2/k$. With a perfect model, the latter statistic should have a mean of 1. In Figure 9.6a, χ_r^2 is shown as a function of f_{low}. By including the low-

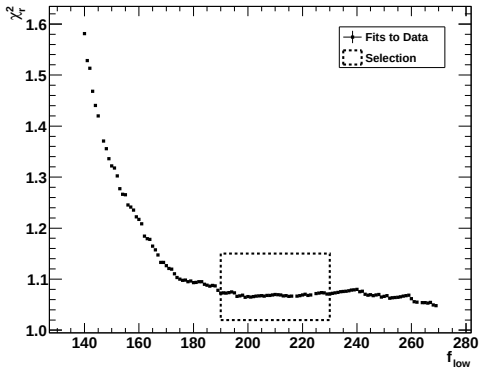

(a) As the lower edge of the fitting region (f_{low}) is increased, χ^2_r drops heavily, resembling a better match between data and model. The first few datapoints in the almost constant level are used to select the value of λ'_T.

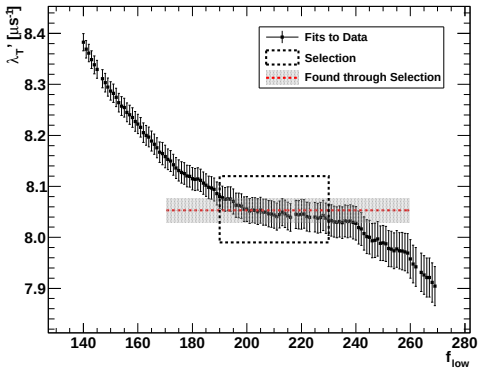

(b) The many fits yield different values of λ'_T but within the selection shown in (a), a plateau establishes. The decay rate found through a weighted fit is shown along with the 68% confidence interval.

Figure 9.6: The procedure of the Single Component Fitting.

est bins ($f_{\text{low}} \lesssim 170$), our single lifetime component fit is clearly not a good model of the data. However, at larger values of f_{low}, an almost constant value $\chi^2_r \simeq 1$ is reached. Within the first part of this constancy, the found decay rates also establish a plateau, cf. Figure 9.6b. In the channel range established from Figure 9.6a, an fit was performed to extract the value of λ'_T. It is important to stress that the parameters and errors shown here are correlated, since they correspond to various sections of the same data. Because of this, the variation of λ'_T in the selected region does not reflect the actual uncertainty. Instead, the smallest error found through parameter estimation in the selection was adapted. This scheme of determining the lifetime from a plateau is not novel but has been applied in other experimental studies of the *o*–Ps lifetime [HHKW87, ARG94, VZG03].

As also seen in Figure 9.6b, the low field spectra all indicated a single lifetime component lower than expected. At magnetic fields to yield $Q \simeq 1$, the average value was found to be $\lambda^0_T = (8.080 \pm 0.026)\ \mu\text{s}^{-1}$, corresponding to $\tau^0_T = (123.8 \pm 0.4)$ ns. The cause of this persistently lower value was not found until recently and will be discussed later.

Distribution of Lifetimes—MELT

As mentioned above, the method of parameter estimation will be limited to a finite number of lifetime components, and the fitting problem quickly complicates, if only a few extra degrees of freedom, *i.e.* lifetime components, are added to the parameter space. Because the distribution of positron lifetimes in solids can provide information on defects and porosity of a material, the problem of considering a distribution of lifetimes is well-investigated. Shukla *et al.* considered this problem and implemented a combination of a linear filter (removing noise in lifetime spectra) and the Bayesian method of quantified maximum entropy, altogether called the Maximum Entropy of LifeTime (MELT) program [SPH93]. The procedure allows for reconstruc-

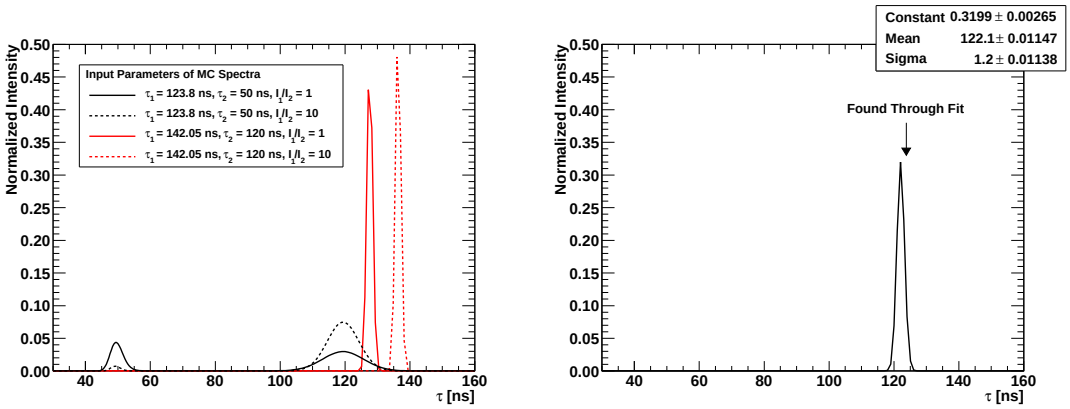

(a) Two-component MC toy data is analyzed with MELT. The program can clearly discern between the components as long as the lifetimes are very different.

(b) MELT analysis of the date shown in Figure 9.5. The lifetime found through the single component analysis is marked with the arrow. The parameters of a Gaussian fit to the distribution are shown.

Figure 9.7: MELT Study. By using the Bayesian approach of quantified maximum entropy, MELT is able to find the intensity distribution of lifetime components from a decay spectrum. In all cases, the entropy weight is 3×10^{-8}.

tion of the intensity distribution of lifetimes with no prior knowledge of the inherent distribution. The intensity of the lifetimes can be calculated on a logarithmically spaced lifetime grid taking a detector resolution into account. The quality of the technique in relation to positron lifetimes is discussed and well-tested through MC studies in [DE98]. The original MATLAB implementation by Shukla *et al.* from 1993 only needed slight implementation changes to be able to run on a modern computer.

9.4 Results & Discussion

In Figure 9.7a, the result of a MELT study of two-component toy MC data is shown. As seen here, MELT can discern two lifetime components when the difference between them is relatively large ($\tau_1/\tau_2 \simeq 2.5$ is examined)—even when one component is dominating ($I_1/I_2 = 10$). However, if the two lifetimes are similar ($\tau_1/\tau_2 \simeq 1.2$), MELT cannot distinguish the two exponential components and a single component is found with lifetime between τ_1 and τ_2. MELT initially seemed intriguing as it was thought to be able to discriminate between the quenched and un-quenched lifetimes of o–Ps. However, the method is not sensitive to the small difference at our maximum field of $B \simeq 1.1$ kG.

The low-field lifetime of $\tau_T^0 = (123.8 \pm 0.4)$ ns obtained through the single-component fit was suspected to be too low as a result of a contamination by some Ps of shorter lifetimes. Using the MELT implementation, the data shown in Figure 9.5 was analyzed from $f_{\text{low}} = 120$, leading to a very similar single lifetime component with $\langle\tau\rangle = (122.1 \pm 1.2)$ ns, cf. Figure 9.7b. Judging from this and the MELT MC study, the causes of the seemingly lower lifetime are restricted to a) a large systematic error in the setup (*e.g.* electronics, detectors, *etc.*) or b) influence of positronium with lifetimes only slightly below the vacuum value.

Epithermal *o*–Ps Contamination

In [GMZ95], Gidley *et al.* found that when positrons are implanted only shallowly in the Ps production target due to low energies E_+, a relatively large fraction of the positrons will return to the surface without having undergone a considerable amount of thermalizing collisions. These epithermal—or simply backscattered—positrons will at the surface form epithermal *o*–Ps with energies $\simeq$ 2–100 eV, depending on E_+. The fastest moving *o*–Ps component decays quickly due to heavy collisional quench at the walls of the confinement can, giving rise to lifetimes $\tau \lesssim 20$ ns. This component is easily separable from the vacuum lifetime due to its limited range in a decay spectrum. However, the slower epithermal *o*–Ps would have lifetimes in a band ($\simeq$ 70–140 ns) only slightly below the vacuum value [VZG03][3]. As demonstrated in Figure 9.7a, a contamination by the latter in the lifetime spectrum cannot be discarded by our analysis methods, but will give rise to a single, seemingly lower lifetime. During the experiment, we were unaware of this problem, but the experiment could be repeated following some of the guidelines provided in [GMZ95]

1. Increase the primary positron energy E_+. Gidley *et al.* found that the ratio of thermal to epithermal *o*–Ps formed scales approximately as E_+. By increasing the implantation energy, almost all *o*–Ps reaching the vacuum will be thermalized. In [VZG03], the effect of epithermal *o*–Ps was heavily reduced at $E_+ \simeq 5$ kV.

2. Use a confinement can of dimensions small enough to ensure a large number of wall collisions by the fastest moving *o*–Ps within τ_T. In this way, the fast *o*–Ps can effectively be quenched on a timescale (*e.g.* $\lesssim$ 20 ns) not affecting the determination of the longer vacuum lifetime. This scheme was demonstrated in [GMZ95] and employed in [VZG03].

3. Do not coat the confinement can with MgO. Although this method was originally devised by Gidley *et al.* [GZMR76, GZ78], they found that clean metal surfaces (*e.g.* Al) distinctively reduce the fast *o*–Ps yield by a factor $\simeq 3$ relative to MgO-lined surfaces.

In our data, $E_+ \simeq eV_I \lesssim 200$ eV and a MgO coating was used, whence fast *o*–Ps is at least relevant but also very likely to be the cause of the low lifetime of $\tau_T^0 = (123.8 \pm 0.4)$ ns. This could easily be solved by increasing the HV on the `In` plate of the MCP detector, thus raising E_+ and the implantation depth. However, the cause of the problem was not realized until the setup had been partly disassembled and moved, so the solutions were not feasibly tested.

Magnetic Quenching

Although we could not find convergence to $\tau_T = 142.05$ ns at low magnetic fields, we decided to proceed and also take data at the higher magnetic fields. Decay spectra were recorded at magnetic fields up to $B \simeq 1120$ G. At this maximum field, $Q = 0.787$ should be feasible.

[3] It was Søren L. Andersen who turned our attention to the effect of the epithermal *o*–Ps.

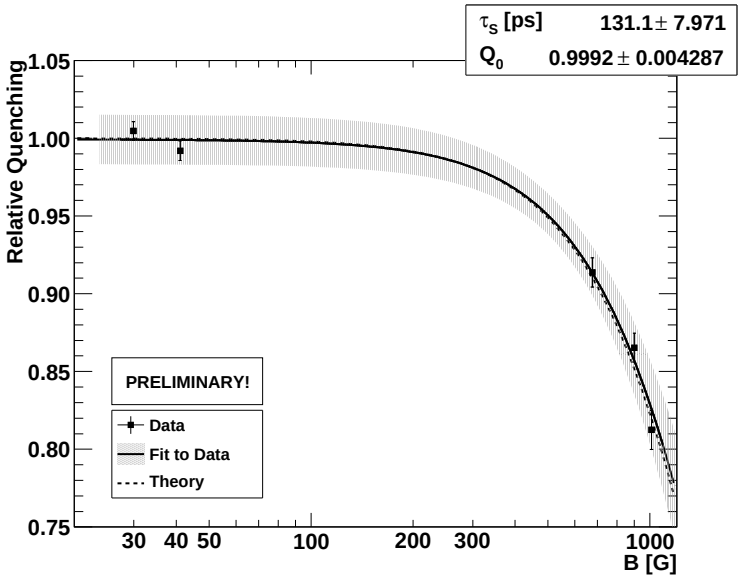

Figure 9.8: The relative quench curve—similar to Figure 9.2. As discussed, the ordinate has been scaled to the lifetime found at low field, 123.8 ns, not the expected $\tau_T = 142.05$ ns. A fit with Eq. (9.10) with the 95% confidence interval is shown along with the curve based on the theoretical value of τ_S.

Using the method of varying the lower edge of the fitting region, Eq. (9.12) with $\beta = 1$ was repeatedly fitted to each decay spectrum. In all fits, τ_T was fixed to the corresponding value found at low field, τ_T^0, representing the $|1, \pm 1\rangle$ component unaffected by magnetic quenching. At first surprisingly, the data *did* exhibit a clear tendency of lower extracted lifetimes τ_T' with larger magnetic fields. In fact, the ratio τ_T'/τ_T^0 was reasonably described by Eq. (9.10), if $\tau_T = \tau_T^0$ was set in the expression. In Figure 9.8, a part of our quench data is presented. The parameter Q_0 corresponds to Q at $B = 0$ G, *i.e.* it determines the quality of the scaling from all data points. Assuming $\Delta_1 = 0.841$ meV, $\tau_S = 131(8)$ ps is extracted from the shape of the fitted quench curve. Although this result is consistent with the result of [ARG94] ($\lambda_S = 125.14(3)$ ps), it is nowhere near their level of precision and each datapoint bears relatively large systematic errors, as already implied. Nevertheless, this tendency—being one of the *o*–Ps hallmarks—was warmly welcomed after numerous checks of the experimental setup—clearly, something was right.

The magnetic quenching should affect the lifetimes of the $|S, 0\rangle$ states regardless of the Ps speed. At our B fields, the slightly larger decay rate of the epithermal *o*–Ps gives rise to almost the same relative quenching Q. For example, using Eq. (9.10) with $\tau_S = 0.125$ ns, $\tau_T = 142.05$ ns results in $Q = 0.823$ at $B = 1$ kG, while $\tau_T = 100$ ns gives $Q = 0.868$. Such a small difference in relative quench is well within our statistical and systematic errors. If the observed low-field *o*–Ps lifetime is due to our analysis methods' limited ability to discriminate between the only slightly different lifetimes of the thermal and epithermal *o*–Ps, the magnetic quench phenomenon should persist, and τ_S can be extracted, albeit with a reduced accuracy.

9.5 Improvements

Besides the suggestions of improvements already discussed regarding the likely contamination by epithermal *o*–Ps, there are a number of issues to be dealt with, if τ_S is to be measured to a competitive precision with our setup.

As is visible in Figure 9.5, our data suffered from a large uniform background. One should heed a poor signal-to-background ratio as it can severely bias the lifetime estimation, however typically most pronounced at low statistics [BR02]. Testing the estimator on toy MC data with similar backgrounds would be sensible. The uniform background originates from a signal from the start detector followed by a stop signal at a random time interval later, *e.g.* due to noise in either detector. The background is heavily reduced if the two scintillators are run in coincidence mode (`AND`). In [GZMR76], the signal to background ratio improved by a factor $\simeq 6$, when requiring 2γ detection.

To avoid a large number of TAC overflows (starts not followed by stops within the TAC range), the less-frequent detector (e^+/γ) should be used as TAC start. In our case, the count rate of the γ-detecting scintillators is lower than that of the MCP due to the lower efficiency and solid angle coverage. When using the MCP as start detector, the unnecessarily large number of TAC starts can be harmful if the positron intensity is large compared to the TAC range. When more than one positron is involved in each readout, the e^+ hitting the MCP is not necessarily the one leading to the detected annihilation γ's. This pile-up phenomenon should not be relevant with our TAC range of 1 μs and MCP count rate $\lesssim 10^5$, but could be if, for example, a 50 mCi ^{22}Na source is installed in RGM-1, thus increasing the e^+ intensity by one order of magnitude[4]. To avoid this, an inverted decay spectrum—with scintillators as start and the delayed MCP as stop—should be used instead.

In our experiment, only one confinement can was lathed. Following Gidley *et al.*'s idea, one could benefit from comparing results obtained using cans of different dimensions. In this way, interactions at the can's wall can be corrected for. Containment of the *o*–Ps could also be improved by using a double can solution as in [VZG03], where the double aperture greatly reduces the effusion of Ps to regions of nonuniform γ detection efficiency.

◇ ◇ ◇

An experimental setup has been designed to measure the changing *o*–Ps lifetimes at different magnetic field strengths. Although the lifetime observed at $B \simeq 0$ G is only $\tau_T^0 = (123.8 \pm 0.4)$ ns, the magnetic quenching phenomenon is clearly observed. With some feasible improvements and an e^+ intensity upgrade, the quality of the observed *p*–Ps lifetime could be improved. This indirect measurement of τ_S has not been carried out in vacuum before. Although our *p*–Ps decay rate of $\tau_S = (131 \pm 8)$ ps is far from competitive with the value referenced from [ARG94], our experiment is certainly at the level of proof-of-principle.

[4] At the time of the Ps lifetime study, the ^{22}Na source had decayed to $\simeq 5$ mCi.

CHAPTER 10

OVERALL CONCLUSION

Part I

Since the bremsstrahlung formation length scales as $E_0{}^2(1-y)/\hbar\omega$, the formation length related effects must in a terrestrial accelerator experiment be sought at the lowest accessible relative photon energies $y \gtrsim 10^{-3}$, due to the limited primary energies available. To reach this goal, a new BGO calorimeter was utilized. When tested and calibrated with an electron beam of energies $E_0 \simeq$ 100–580 MeV, the detector exhibited linearity and acceptably low resolutions, despite the low HV of 405 V. When the first Background Compensated Power Spectra (BCPS) were systematically $\simeq$ 20–40% lower than expected levels, mainly a PMT overload was believed to be the cause, as stated in [II], since the PMT is not built for operation in an ultra-high-energy environment.

Later, the established method of background compensation was studied on toy MC data. Firstly, the MC study clearly showed that multi-photon effects are far from negligible even at the thinnest targets considered, $\Delta t/X_0 = 2.5\%$, whence heed should be payed when comparing such data to single-photon theoretical models. Intriguingly, the exaggerated pile-up effect was also found through these studies. This systematic effect was previously assumed to be negligible. However, the simulations showed that this effect would cause the BCPS to be *e.g.* $\simeq$ 40% lower than a pure spectrum at $\hbar\omega = 0.100$ GeV in the presence of a background of $\Delta t/X_0 = 2.5\%$. The effect was demonstrated analytically by introducing a simple BH power spectrum model including two-photon emission to describe pile-up. Through the model, the linear behaviour of the relative deviation of the BCPS with the background radiator thickness was explained. A paper discussing the phenomena is in preparation and will appear as [III]. The SR kink seen at low photon energies was also simulated. It is caused by subtraction of two spectra of targets with dissimilar bremsstrahlung photon yields, *i.e.* different relative SR contamination. For example, the kink is present in the difference between a raw spectrum and a background spectrum, due to their different thicknesses. The exaggerated pile-up will always influence the BCPS from the

H4 beam line, as the minimum material backgrounds (vacuum windows, scintillators, air, *etc*.) easily amounts to $\Delta t/X_0 \simeq 1.5\%$. The study has, however, *not* sunk the NA63 battleship but has proved the importance of always including a well-trusted reference target measurement. With the correction, essentially relative spectra can be procured. The BCPS corrected by the BGO efficiency will suffer from systematic errors vastly lower than the uncorrected BCPS.

Regarding the bremsstrahlung power spectrum's target thickness dependence, the region between the BH and LPM regime was poorly studied before the work presented here. With a number of targets of effectively different thicknesses, the TSF regime was mapped within $0.3 \lesssim \hbar\omega \lesssim 2$ GeV at $E_0 = 149$ GeV. The effect is important when considering kinematics and targets where MCS is strong, but the target cannot be considered semi-infinite. Since the dependencies on $\hbar\omega$ in the LPM and TSF regime, respectively, are very different, it is important to stress that the latter will replace the prior at $\hbar\omega \lesssim \hbar\omega_{\mathrm{TSF}}$.

A combined BGO efficiency—including the exaggerated pile-up, detector inefficiency and small beam impurities—was found and employed to correct all data of the TSF, low-Z LPM pilot study, and the latest sandwich data. The efficiency corrects both BH and LPM data convincingly at all photon energies above the SR kink, $\hbar\omega \gtrsim 0.3$ GeV, whence we assume the systematic error of the manipulation to be small over the full thickness range. The full thickness dependence of the bremsstrahlung process has thus been explored in this thesis.

A number of theoretical models were implemented for comparison with the data. Also, a semi-empirical logarithmic expression was devised and used to quantify the shape of the thickness dependence through the parameter b. The expression was shown to be a major component of [Bla97b] with $b_{\mathrm{B}} = 1/6\ell_\gamma \simeq 287/X_0$, in fair agreement with our data and the value found from [SF98b], $b_{\mathrm{SF}} = 319/X_0$. The logarithmic expression is ideal for back-of-the-envelope calculations, but when the situation calls for accuracy, one must resort to sophisticated models like [SF98b, Bla97b]. Although the formalism of [Bla97a] is supposed to be a refined version of [Bla97b], the prior was found to be considerably less compatible with our data.

Our searches for the so-called sandwich effect were presented. The results of different approaches show no significant deviation from the TSF effect of each foil in the target assembly. Regarding the existence of the effect, our searches are somewhat inconclusive, as we cannot completely rule out a very fluctuating foil spacing relative to the mean value. With the simplified and improved two-foil setup, the single gap can be controlled to a far greater extent, and many systematics can be ruled out, as the gap can be varied *in situ*. Different ways of mounting the foils have been explored, and surface measurements of the foils have shown RMS variations of the order $\lesssim 2.5$ μm, well-within our need. Using a number of BD calculations, the difference between a raw sandwich spectrum ($2 \times \mathrm{Ta}\delta t\mathrm{Air}120$) and its corresponding TSF spectrum ($2 \times \mathrm{Ta}\delta t\mathrm{Air}\infty$) was studied as a function of δt. Through simple considerations, a background's impact on the statistical errors and the needed statistics were examined. With the typical backgrounds in H4, $\delta t \simeq 30$ μm Ta appears optimal with respect to statistical errors.

In the SLAC E-146 experiment, the Migdal LPM theory fell short of describing the carbon data. This has incited our study of the LPM effect in low-Z materials. A feasibility study with aluminum and carbon at $E_0 = 207$ GeV was successfully concluded, whereas the data of our full-scale study at $E_0 = 178$ GeV still needs some

data analysis. To reach the attractive, lowest photon energies, a careful method of purging the effect of SR contamination in the BCPS is still under development.

Part II

After having surmounted the shipping damages, assembled the parts of the system, prepared pressurized air, sufficient cooling water and electrical power, the commissioning of LEPS could finally commence. Luckily, the actual commissioning phase went smoothly, and the high quality and versatility of the system shone through. Changes were made to the supplied LabVIEW control software, including software interlocks and complex procedures that our successors will surely benefit from. The system was found to comply well with supplier's specifications.

For now, LEPS has already been used in one experiment and others are intended over the next couple of years. In the first experiment, a lifetime study of positronium—the darling of bound-state non-relativistic QED—was performed. At the lowest magnetic fields, a lower lifetime component was observed. As discussed, this could very well be due to unthermalized *o*–Ps with slightly lower lifetimes. Our analysis methods were found to be unable to discriminate between two components of similar lifetimes, *e.g.* lifetimes of 142.05 ns and 120 ns, in the same decay spectrum. Under such circumstances, a single, averaged lifetime will be acquired.

Although the *o*–Ps lifetime measurement seems to have been influenced by a contamination of unthermalized *o*–Ps, the magnetic quench phenomenon was clearly observed, and a value of the *p*–Ps lifetime was found to be $\tau_S = 131(8)$ ps, consistent with [ARG94], however less accurate. Although the setup is not competitive at the present state, it could very well give rise to the first magnetic quench study of *p*–Ps lifetime in vacuum after some feasible improvements.

Appendices

APPENDIX A

GREEN'S FUNCTION FOR THE WAVE EQUATIONS

If the reader is generally interested in the method of Green's functions, I can highly recommend [MF53, Chap. 7], which is dedicated to this topic.

A.1 The Green's Function

We shall use the method of Green's functions to solve a set of inhomogeneous differential equations of the type

$$\underbrace{\left(\nabla^2 - \frac{1}{c^2}\frac{\partial^2}{\partial t^2}\right)}_{\mathcal{L}} \Psi(\boldsymbol{r}, t) = -4\pi f(\boldsymbol{r}, t) \,, \tag{A.1}$$

where the RHS function is the source of the general field $\Psi(\boldsymbol{r}, t)$ and $\mathcal{L}$ is a linear operator. In this case, the operator is the negative d'Alembertian $\mathcal{L} = -\Box$. The Green's function is generally defined through

$$\mathcal{L}\mathcal{G}(\boldsymbol{r}, t; \boldsymbol{r}_0, t_0) = -4\pi\delta(\boldsymbol{r} - \boldsymbol{r}_0)\delta(t - t_0) \tag{A.2a}$$

$$\iint \mathcal{L}\mathcal{G}(\boldsymbol{r}, t; \boldsymbol{r}_0, t_0) f(\boldsymbol{r}_0, t_0) d^3 r_0 dt_0 = -4\pi \iint \delta(\boldsymbol{r} - \boldsymbol{r}_0)\delta(t - t_0) f(\boldsymbol{r}_0, t_0) d^3 r_0 dt_0 \tag{A.2b}$$

$$= -4\pi f(\boldsymbol{r}, t) = \mathcal{L}\Psi(\boldsymbol{r}, t) \,. \tag{A.2c}$$

Since the linear operator $\mathcal{L}$ acts on the observer coordinates $(\boldsymbol{r}, t)$ and not the integration variables, the operator $\mathcal{L}$ can be taken outside of LHS integrals of Eq. (A.2c)

$$\mathcal{L} \iint \mathcal{G}(\boldsymbol{r}, t; \boldsymbol{r}_0, t_0) f(\boldsymbol{r}_0, t_0) d^3 \boldsymbol{r}_0 dt_0 = \mathcal{L}\Psi(\boldsymbol{r}, t)$$

$$\iint \mathcal{G}(\boldsymbol{r}, t; \boldsymbol{r}_0, t_0) f(\boldsymbol{r}_0, t_0) d^3 \boldsymbol{r}_0 dt_0 = \Psi(\boldsymbol{r}, t) \,. \tag{A.3}$$

By defining the Green's function through Eq. (A.2a), the differential problem considered in Eq. (A.1) is converted into an integral problem. The Green's function's

components are by definition the operators which progress the effect of $f(\boldsymbol{r}_0, t_0)$ (the source) into the solution (the effect) $\Psi(\boldsymbol{r}, t)$. We can benefit from using the Fourier transform from t-space to ω-space of both sides of Eq. (A.2a) with $\mathcal{L}$ as defined in Eq. (A.1)

$$\left(\nabla^2 - \frac{1}{c^2}\frac{\partial^2}{\partial t^2}\right) \overbrace{\int_{-\infty}^{\infty} \mathcal{G}(\boldsymbol{r}, t; \boldsymbol{r}_0, t_0) e^{i\omega t} dt}^{\mathcal{G}(\boldsymbol{r},\omega;\boldsymbol{r}_0,t_0)} = -4\pi \int_{-\infty}^{\infty} \delta(\boldsymbol{r} - \boldsymbol{r}_0)\delta(t - t_0) e^{i\omega t} dt$$

$$\left(\nabla^2 + \frac{\omega^2}{c^2}\right) \mathcal{G}(\boldsymbol{r}, \omega; \boldsymbol{r}_0, t_0) = -4\pi\delta(\underbrace{\boldsymbol{r} - \boldsymbol{r}_0}_{\boldsymbol{\mathcal{R}}}) e^{i\omega t_0} , \tag{A.4}$$

where the last equation is similar to Eq. (A.2a). The equation above thus defines the Fourier transformed Green's function $\mathcal{G}(\boldsymbol{r}, \omega; \boldsymbol{r}_0, t_0)$ which can be used to solve the inhomogeneous Helmholtz equation. If we consider a system with spherical symmetry around $\mathcal{R} = |\boldsymbol{\mathcal{R}}| = |\boldsymbol{r} - \boldsymbol{r}_0| = 0$ and no boundary surfaces, only the radial component of the Laplacian ∇^2 is non-vanishing [Jac98]

$$\frac{1}{\mathcal{R}}\frac{d^2}{d\mathcal{R}^2}[\mathcal{R}\mathcal{G}(\boldsymbol{r}, \omega; \boldsymbol{r}_0, t_0)] + k^2\mathcal{G}(\boldsymbol{r}, \omega; \boldsymbol{r}_0, t_0) = -4\pi\delta(\mathcal{R}) e^{i\omega t_0} , \tag{A.5}$$

where $k = \omega/c$. If we consider $\mathcal{R} \neq 0$, the equation is homogeneous and has the solution

$$\mathcal{G}(\boldsymbol{r}, \omega; \boldsymbol{r}_0, t_0) = \left[A\mathcal{G}_k^+(\mathcal{R}) + (1 - A)\mathcal{G}_k^-(\mathcal{R})\right] e^{i\omega t_0} , \qquad \mathcal{G}_k^{\pm}(\mathcal{R}) = \frac{e^{\pm ik\mathcal{R}}}{\mathcal{R}} , \tag{A.6}$$

where $0 \leq A \leq 1$. The solution is a linear combination of two terms representing a spherical wave originating from or converging to $\mathcal{R} = 0$ at $t = t_0$, respectively. We will consider the solution with $A = 1$, which can be inversely Fourier transformed back to

$$\begin{aligned}
\mathcal{G}(\boldsymbol{r}, t; \boldsymbol{r}_0, t_0) &= \frac{1}{2\pi}\int \mathcal{G}(\boldsymbol{r}, \omega; \boldsymbol{r}_0, t_0) e^{-i\omega t} d\omega \\
&= \frac{1}{2\pi}\int \frac{e^{ik\mathcal{R}}}{\mathcal{R}} e^{-i\omega(t - t_0)} d\omega && \text{(A.7a)} \\
&= \frac{1}{\mathcal{R}}\delta\big[t_0 - (t - \mathcal{R}/c)\big] , \qquad \mathcal{R}, t - t_0 > 0 . && \text{(A.7b)}
\end{aligned}$$

The result above is the retarded infinite space Green's function, where the δ-function includes causality, such that it describes the effect at $(\boldsymbol{r}, t)$ from a cause at $(\boldsymbol{r}_0, t_0 = t - \mathcal{R}/c)$.

A.2 The Wave Equations

In electrodynamics, the magnetic vector potential $\boldsymbol{A}$ is not uniquely defined since the magnetic field $\boldsymbol{B} = \boldsymbol{\nabla} \times \boldsymbol{A}$ is unchanged by adding a curl-free field (*i.e.* the gradient of a scalar field Λ) to $\boldsymbol{A}$. More precisely, if Λ is a solution to the homogeneous version of Eq. (A.1), the $\boldsymbol{E}$ and $\boldsymbol{B}$ fields are both unchanged under the combination of the operations

$$\left.\begin{array}{l} \boldsymbol{A} \to \boldsymbol{A} + \boldsymbol{\nabla}\Lambda \\ \Phi \to \Phi - \frac{\partial \Lambda}{\partial t} \end{array}\right\} \nabla^2\Lambda = \frac{1}{c}\frac{\partial^2\Lambda}{\partial t^2} , \tag{A.8}$$

where Φ is the electric scalar potential. In the Lorenz gauge, the Maxwell equations treat the electromagnetic potential and scalar fields on an equal footing

$$\nabla^2 \boldsymbol{A} - \frac{1}{c^2}\frac{\partial^2 \boldsymbol{A}}{\partial t^2} = -\Box \boldsymbol{A} = -\mu_0 \boldsymbol{J} \tag{A.9a}$$

$$\nabla^2 \Phi - \frac{1}{c^2}\frac{\partial^2 \Phi}{\partial t^2} = -\Box \Phi = -\rho/\epsilon_0 \,. \tag{A.9b}$$

The wave equations are of the type presented in Eq. (A.1)—a problem for which we have already found the Green's function (cf. Eq. (A.7a)–(A.7b)). In the case of Eq. (A.9a)–(A.9b), the sources of the fields are the current density $\boldsymbol{J}$ and the charge density ρ, respectively. The full solutions are

$$\boldsymbol{A}(\boldsymbol{r},t) = \boldsymbol{A}^{\text{in}}(\boldsymbol{r},t) + \frac{\mu_0}{4\pi}\iint \mathcal{G}(\boldsymbol{r},t;\boldsymbol{r}_0,t_0)\boldsymbol{J}(\boldsymbol{r}_0,t_0)dr_0^3 dt_0 \tag{A.10a}$$

$$\Phi(\boldsymbol{r},t) = \Phi^{\text{in}}(\boldsymbol{r},t) + \frac{1}{4\pi\epsilon_0}\iint \mathcal{G}(\boldsymbol{r},t;\boldsymbol{r}_0,t_0)\rho(\boldsymbol{r}_0,t_0)dr_0^3 dt_0 \,. \tag{A.10b}$$

In both cases, we consider an isolated source of fields, hence the incoming contributions (which were present before the source is 'turned on' at $t = t_0$) are zero.

Potentials of a Moving Charge

Because of the similarity of the equations for the vector potential and the scalar potential, we will only consider the expression for the prior. In the case of a moving particle with charge q, the current density is $\boldsymbol{J}(\boldsymbol{r},t) = q\boldsymbol{v}(t)\delta(\boldsymbol{r} - \boldsymbol{v}(t)t)$, where $\boldsymbol{v}(t)$ is the particle's velocity at time t. Then, the field can be written as

$$\begin{aligned}\boldsymbol{A}(\boldsymbol{r},t) &= \frac{\mu_0 q}{4\pi}\int_0^{t^+} dt_0 \int dr_0^3 \frac{\boldsymbol{v}(t_0)\delta(\boldsymbol{r}_0 - \boldsymbol{v}(t)t_0)}{\mathcal{R}}\delta\big[t_0 - (t - \mathcal{R}/c)\big] \\ &= \frac{\mu_0 q}{4\pi}\int_0^{t^+} dt_0 \frac{\boldsymbol{v}(t_0)\delta\big[(1/c)|\boldsymbol{r} - \boldsymbol{v}(t_0)t_0| - (t - t_0)\big]}{|\boldsymbol{r} - \boldsymbol{v}(t_0)t_0|}\,,\end{aligned} \tag{A.11}$$

where the upper integration limit is set to an arbitrarily small time interval beyond t, $t^+ = t + \epsilon$, to avoid dealing with the ambiguity of the value of $\delta(x)|_{x=0}$. In the case of uniform motion, $|\boldsymbol{v}(t)| = v$, the integral can be solved using the substitution [MF53, Sec. 7.3]

$$p(t_0) \equiv (1/c)|\boldsymbol{r} - \boldsymbol{v}t_0| + t_0 \Rightarrow \tag{A.12a}$$

$$\frac{dt_0}{|\boldsymbol{r} - \boldsymbol{v}t_0|} = \frac{dp}{|\boldsymbol{r} - \boldsymbol{v}t_0| - (\boldsymbol{v}\cdot\boldsymbol{r} - v^2 t_0)/c}\,. \tag{A.12b}$$

Utilizing this, the integral of Eq. (A.11) can be rewritten

$$\begin{aligned}\boldsymbol{A}(\boldsymbol{r},t) &= \frac{\mu_0 q}{4\pi}\int_{r/c}^{p(t^+)} \frac{\boldsymbol{v}\delta(p-t)dp}{|\boldsymbol{r} - \boldsymbol{v}t_0| - (\boldsymbol{v}\cdot\boldsymbol{r} - v^2 t_0)/c} \\ \boldsymbol{A}(\boldsymbol{r},t) &= \frac{\mu_0 q}{4\pi}\frac{\boldsymbol{v}}{\mathcal{R} - \boldsymbol{v}\cdot\boldsymbol{\mathcal{R}}/c} = \frac{\mu_0 q}{4\pi\mathcal{R}}\frac{\boldsymbol{v}}{1 - \boldsymbol{n}\cdot\boldsymbol{v}/c}\,,\end{aligned} \tag{A.13}$$

where $\boldsymbol{\mathcal{R}} = \boldsymbol{r} - \boldsymbol{v}t_0$ in the case of uniform motion, cf. Figure 1.1a. This is the Lièнard-Wiechert magnetic vector potential, and a similar result can be found for the scalar

potential

$$\Phi(\boldsymbol{r},t) = \frac{q}{4\pi\epsilon_0\mathcal{R}}\frac{1}{1-\boldsymbol{n}\cdot\boldsymbol{v}/c}\,. \tag{A.14}$$

In some problems, one can benefit from using the Fourier integral representation of $1/\mathcal{R}$

$$\begin{aligned}\frac{1}{\mathcal{R}} &= \frac{1}{2\pi^2}\int d^3k\frac{e^{i\boldsymbol{k}\cdot\boldsymbol{\mathcal{R}}}}{k^2}\\ \boldsymbol{A}(\boldsymbol{r},t) &= \frac{\mu_0 q}{8\pi^2}\int\frac{d^3k}{k}\frac{\boldsymbol{v}e^{i\boldsymbol{k}\cdot\boldsymbol{\mathcal{R}}}}{k-\boldsymbol{k}\cdot\boldsymbol{v}/c}\,.\end{aligned} \tag{A.15}$$

The electromagnetic fields can then be found using

$$\boldsymbol{E} = -\boldsymbol{\nabla}\Phi - \frac{\partial\boldsymbol{A}}{\partial t} \tag{A.16a}$$

$$\boldsymbol{B} = \boldsymbol{\nabla}\times\boldsymbol{A}\,. \tag{A.16b}$$

APPENDIX B

THEORY OF BLANKENBECLER AND DRELL

The theory of BD [BD96, Bla97b, Bla97a] has been used extensively in the work presented in Part I, whence a short introduction is given here. Their approach to bremsstrahlung is spun off their full quantum treatment of beamstrahlung [BD87]—a phenomenon which is very similar to bremsstrahlung—using the eikonal approximation.

B.1 Eikonal approximation

We consider a scattering potential which is of limited range a and varying smoothly. If the reduced de Broglie wavelength $\lambda\!\!\!^{-}_{\mathrm{B}} = \hbar/p_0$ of an incident particle of energy E_0, momentum p_0 and mass m is short compared to the range of the potential, *i.e.* $a/\lambda\!\!\!^{-}_{\mathrm{B}} = ka \gg 1$, a semi-classical approach can suffice. $|V_0|$ is a typical strength of the potential, and we restrict our analysis to the high energy regime $|V_0|/E_0 = |U_0|/k^2 \ll 1$, where $|U_0|$ is a typical strength of the reduced potential $U = 2mV/\hbar^2$.

To give an example, we inspect scattering of a spin-less, non-relativistic particle by a purely real and time-independent scattering potential, *i.e.* seek solutions to the time-independent Schrödinger equation

$$(\nabla^2 + k^2)\Psi_k(\boldsymbol{r}) = U(\boldsymbol{r})\Psi_k(\boldsymbol{r}) \,. \tag{B.1}$$

Because the scattering potential is considered weak and slowly varying, the solution can be recast as the product of the incident plane wave and a function of $\boldsymbol{r}$, $\Psi_k(\boldsymbol{r}) = e^{i\boldsymbol{k}\cdot\boldsymbol{r}}\phi(\boldsymbol{r})$. When inserted into the integral equation of Eq. (B.1), the Lippmann-Schwinger equation, we get an equation for the function $\phi(\boldsymbol{r})$, and an approximated solution is [BJ03]

$$\widetilde{\phi}(\boldsymbol{r}) = \exp\left[-\frac{i}{2k}\int_{-\infty}^{z} U(\boldsymbol{b}_\perp, z)dz\right] \,. \tag{B.2}$$

An approximation to the scattering wave function is thus in the eikonal approximation determined by an accumulation of a phase function, and the entire function can

be written as

$$\Psi_k(\boldsymbol{r}) \simeq \exp\left[i\boldsymbol{k}\cdot\boldsymbol{r} - \frac{i}{2k}\int_{-\infty}^{z} U(\boldsymbol{b}_\perp, z)dz\right] , \tag{B.3}$$

which is an example of an eikonal wave function.

B.2 Bremsstrahlung

Blankenbecler and Drell treats the problem of bremsstrahlung utilizing the eikonal approximation to find solutions to the Klein-Gordon equation for a relativistic but spinless particle in a static, external field $V \ll E_0$. In this section, we shall employ the units used in [BD96] (*i.e.* $\hbar = c = 1$) in which the Klein-Gordon equation can be written as

$$\left[(E_0 - V)^2 + \boldsymbol{\nabla}^2 - m^2)\right]\phi(\boldsymbol{r}) = 0 , \tag{B.4}$$

and the solutions are written in the typical eikonal form $\phi(k, \boldsymbol{r}) = \exp\left[i\Phi(\boldsymbol{r})\right]$. Inserting this into Eq. (B.4), an equation for the phase occurs

$$(E_0 - V)^2 - m^2 = \left[\boldsymbol{\nabla}\Phi(\boldsymbol{r})\right]^2 - i\boldsymbol{\nabla}^2\Phi(\boldsymbol{r}) . \tag{B.5}$$

The scattering potential can advantageously be written in cylindrical coordinates with the z axis along the incident particle's original trajectory $\boldsymbol{r} = \boldsymbol{b}_\perp + z\hat{\boldsymbol{v}}$, where $\hat{\boldsymbol{v}} = \boldsymbol{v}/v$ is a unit vector in the direction of the particle's velocity. In the amorphous medium, the sum of transverse fields along a segment of the particle's trajectory is considered independent of $b_\perp$, *i.e. where* at the surface the incident particle enters—assuming that the segment is several atomic spacings thick. These assumptions result in the potential

$$V(\boldsymbol{b}_\perp, z) = -\boldsymbol{b}_\perp \cdot \boldsymbol{E}_\perp(z) . \tag{B.6}$$

BD consider the total phase of bremsstrahlung given by [Bla97b]

$$\Phi^{\text{tot}} = \Phi - \Phi' - \boldsymbol{k}\cdot\boldsymbol{r} = -\boldsymbol{q}\cdot\boldsymbol{r} - \chi_0^{\text{tot}}(\boldsymbol{b}_\perp) - \frac{1}{p}\chi_1^{\text{tot}}(\boldsymbol{b}_\perp, z) ,$$

where Φ, Φ' and $\boldsymbol{k}\cdot\boldsymbol{r}$ are the phases of the electron, before and after scattering, and the photon, respectively. The latter phase does not deal with the medium's index of refraction. $\boldsymbol{q} = \boldsymbol{p}' + \boldsymbol{k} - \boldsymbol{p}$ is the usual momentum-transfer to the medium, where $\boldsymbol{p}$ and $\boldsymbol{p}'$ are the particle's momenta before and after collision, respectively. The function $\chi_0^{\text{tot}}(\boldsymbol{b}_\perp)$ is the typical, zeroth-order eikonal phase-shift function, which is independent of the value of z

$$\chi_0^{\text{tot}}(\boldsymbol{b}_\perp) = \int_{-\infty}^{\infty} dz' V(\boldsymbol{b}_\perp, z') . \tag{B.7}$$

while the expression for the z-dependent term $\chi_1^{\text{tot}}(\boldsymbol{b}_\perp, z)$ can be found in [BD96]. BD find the solutions to the incoming and scattered wave to order $1/p$ and $1/p'$, the initial and final momentum of the electron, respectively, and including terms of this

order is indispensable to describe the multiple scattering, thus also the LPM effect. The MCS angles are assumed to follow a Gaussian distribution.

BD treat the incoming electron as a wave packet that is scattered at the randomly distributed scattering centres. The purely transverse electrical fields along the particle's path are found by random for each path and considered independent from one longitudinal slice to another

$$\langle \boldsymbol{E}_\perp(z_2) \cdot \boldsymbol{E}_\perp(z_1) \rangle = \frac{\langle p_\perp^2 \rangle}{X_0(z_2)} \delta(z_2 - z_1) \,, \qquad \langle \theta_\mathrm{e}^2 \rangle(z) = \frac{\langle p_\perp^2 \rangle}{p^2} \frac{z}{X_0} \tag{B.8}$$

where $\delta(z)$ is the Dirac delta function and $\langle p_\perp^2 \rangle$ is the RMS transverse momentum due to multiple Coulomb scattering while traversing one radiation length. For the latter quantity, BD uses half of the expression found by Rossi [Ros52, Eq. (2.16.9)]. The resulting single photon radiation emission probability—which is statistically averaged from all possible electron paths—can be written as a double integral, where the two integration variables are $b_1 = z_1/\ell_{\mathrm{f}0}$ and $b_2 = z_2/\ell_{\mathrm{f}0}$—two points, in units of $\ell_{\mathrm{f}0}$, along the incident electron's original trajectory

$$I = \int_{-\infty}^{\infty} db_2 \int_{-\infty}^{b_2} db_1 I(b_2, b_1, b_t) \,,$$

where $b_t = \Delta t/\ell_{\mathrm{f}0}$. If the target is a single slab, located from $z = 0$ to $z = \Delta t$, the integral can be separated into terms covering different areas of the two-dimensional integration area [BD96]

$$\begin{aligned} \int_{-\infty}^{\infty} db_2 \int_{-\infty}^{b_2} db_1 = &\int_{-\infty}^{0} db_2 \int_{-\infty}^{b_2} db_1 + \int_{0}^{b_t} db_2 \int_{-\infty}^{0} db_1 \\ &+ \int_{0}^{b_t} db_2 \int_{0}^{b_2} db_1 + \int_{b_t}^{\infty} db_2 \int_{-\infty}^{0} db_1 \\ &+ \int_{b_t}^{\infty} db_2 \int_{0}^{b_t} db_1 + \int_{b_t}^{\infty} db_2 \int_{b_t}^{b_2} db_1 \,. \end{aligned}$$

The six terms on the right are refered to as $(--)$, $(0-)$, (00), $(+-)$, $(+0)$ and $(++)$, respectively. They can be negative individually, but the sum is always positive. Notice that (00) is the only of the six integrals where both coordinates are inside the target at all times. This bulk term is dominant when $\ell_{\mathrm{f}0} < \Delta t$, *i.e.* surface effects are negligible. Although $(+-)$ does not integrate over a region containing the target—only vacuum—it still contributes. The reason for this is that it contains non-vanishing cross terms from the squared sum of amplitudes corresponding to the respective vacuum regions—characteristic of an interference term. The terms from mixed regions $(0-)$, $(+0)$ and $(+-)$ contribute primarily when $\ell_{\mathrm{f}0} \gtrsim \Delta t$ [BD96].

Using the model's units, the BH intensity is simply $I_{\mathrm{BH}} = \frac{4\pi\Delta t}{3\alpha X_0}$ in the soft-photon limit. We can thus define a form factor $F(\hbar\omega, \Delta t, E_0)$ which contains all deviation from the BH result [BD96, Bla97b]

$$\frac{d\sigma_{\mathrm{tot}}}{d\hbar\omega} = F(\hbar\omega, \Delta t, E_0) \times \frac{d\sigma_{\mathrm{BH}}}{d\hbar\omega} \,,$$

where

$$F(\hbar\omega, \Delta t, E_0) = \int_{-\infty}^{\infty} db \int_{-\infty}^{\infty} db_2 F(b_2, b, b_t) \,, \tag{B.9}$$

and

$$F(b_2, b, b_t) = \frac{C(b)}{2Tb} \left\{ \left[1 + 3r(x) T \bar{\lambda}(b_2, b_2 - b, b_t) \right] \sin(c) - \sin(b) \right\} \tag{B.10}$$
$$c = b[1 + 6T\bar{\eta}(b_2, b_2 - b, b_t)] \,,$$

where $b = b_2 - b_1$, $T = \frac{\pi}{3} \frac{\Delta t}{\alpha X_0}$ is a scaled thickness parameter and $C(b)$ is a cutoff function (typically exponential) which kills any possible divergencies of the integral in the asymptotic regions very far from the target. This can safely be set to unity when using finite limits of the integral. The parameter $x = 1 - \hbar\omega / E_0$ describes the "softness" of the emitted photon. The x-dependence is exclusively through $r(x) = (1 + x^2)/2x$. Daniel V. Schroeder's PhD thesis [Sch90] regarding beamstrahlung contains expressions very similar to ones found in [BD96, Bla97b, Bla97a]. Schroeder generalizes the solutions to the Klein-Gordon equation to also describe Dirac spinors. When summing over the final helicity states, helicity changing and conserving terms occur, where the latter involves the function $r(x)$ and the prior involves $1 - r(x)$, cf. [Sch90, Eq. (4.84)]. The electron is thus properly treated as a Dirac particle by including both helicity conserving and helicity flipping terms in the integrand. In the limit of soft photons ($x \to 1$), the spin-flipping term vanishes and $r(x) \to 1$. Further two functions are defined and used in the expression above

$$\bar{\lambda}(b_2, b_1, b_t) = \frac{\int_{b_1}^{b_2} \frac{db'}{X_0(b')}}{\int_0^{b_t} \frac{db'}{X_0(b')}} = \frac{X_0}{b_t} \int_{b_1}^{b_2} \frac{db'}{X_0(b')} \tag{B.11a}$$

$$\bar{\eta}(b_2, b_1, b_t) = \frac{\int_{b_1}^{b_2} \frac{db'}{X_0(b')} \frac{(b_2 - b')(b' - b_1)}{b^2}}{\int_0^{b_t} \frac{db'}{X_0(b')}} \,. \tag{B.11b}$$

The BD formalism can thus be applied to a general longitudinal target geometry of varying radiation length $X_0(b)$.

APPENDIX C

POSITRONIUM IN INTENSE LASER FIELDS

C.1 MPI and ATI in Intense Laser-Field

Recent theoretical investigations of hydrogen-like atoms and ions [ML99] anticipate major differences in the probability of Multi-Photon Ionization (MPI) and Above Threshold Ionization (ATI) of hydrogen and Ps—two nonlinear processes. The differences are due to the very different reduced mass $\mu_r = m/2$ of Ps. By scaling the variables of the Schrödinger-equation, the generalized cross sections [BG66] for N-photon ionization of H and Ps are found to be of very different orders for large values of N

$$\underbrace{\hat{\sigma}_N(\mu_r = m/2, \omega)}_{\text{Ps}} = 2^{3N-1} \underbrace{\hat{\sigma}_N(\mu_r \approx m, 2\omega)}_{\text{H}} , \tag{C.1}$$

hence the cross section of six-photon ionization is $2^{17} \gtrsim 10^5$ times larger for Ps than for hydrogen. Experiments confirming the large differences have not yet been performed. We have prepared a crossed beam (Ps and laser) experiment that renders measurement of cross sections of two-, three- and six-photon ionization of Ps possible (at least relative to the values for hydrogen) with acceptable statistics using laser wavelengths of 355, 532 and 1064 nm, respectively. The latter is readily available from a Nd:YAG laser, while 532 and 355 nm are available through second and third harmonic generation of the 1064 nm laser using non-linear crystals [ME88].

The processes require the simultaneous absorption of a number of photons, so the photon flux obviously needs to be considerably large. We plan to focus the laser elliptically with a 2 mm major axis perpendicular to the direction of Ps-beam and a minor axis of 20 μm. The laser is capable of producing a 1.2 J pulse of duration 10 ns. These specifications correspond to a mean intensity of $1.2\,\text{J}/(10\,\text{ns} \times \pi/4 \times 2\,\text{mm} \times 20\,\mu\text{m}) = 3.8 \times 10^{11}\text{W/cm}^2$ and a lower limit of photon flux of $F \sim 6.8 \times 10^{29}/\text{cm}^2\text{s}$ (for 355 nm)—only a factor of 3 below the estimated saturation flux [ML99]. Such a laser can thus be further defocused to cover the majority of the Ps-containing volume and retain adequate photon-flux. Upon ionization of Ps, the leptons are born

in a laser field of considerable strength, which compels them to perform a quivering motion, requiring a minimum amount of kinetic energy—the ponderomotive potential—depending on the frequency ω and intensity I of the applied laser

$$U_p = 2\pi \frac{e^2 I}{mc\omega^2} \,. \tag{C.2}$$

This results in a raise of the effective ionization threshold, which can lead to channel closing when the total absorbed energy E_λ is less than the required $B_{\mathrm{Ps}} + U_p$. The probability of absorbing N photons to reach the threshold and further absorbing S photons is approximated by [ML99, Raa99]

$$\begin{aligned} P_{N+S}(t \sim \infty) &= 1 - \exp\left[- \int_{-\infty}^{\infty} \hat{\sigma}_{N+S} F(t)^{N+S} \mathrm{d}t \right] \\ &\approx 1 - \exp\left[-\hat{\sigma}_{N+S} F_0^{N+S} \tau_l \right] , \end{aligned} \tag{C.3}$$

where the generalized cross sections $\hat{\sigma}_{N+S}$ are calculated in [Mad04], F_0 is the peak value of the photon flux and τ_l is the effective pulse duration.

C.2 Experimental Setup

Using the positrons from LEPS, we expect $\simeq$ 30 ns pulses containing 5.43×10^5 positrons, if scaling our result in Eq. (8.10) to a 50 mCi ^{22}Na source and assuming an activity of 7 mCi at the time of measurement.

The positronium formation target could be a porous silica (SiO_2) film. Such a film gives markedly high $e^+ \to$ Ps conversion probabilities of $\simeq$ 30% [VZG03]. The local chemistry lab—led by Jacques Chevallier and Folmer Lyckegaard—has already put some research into growing porous SiO_2 films to fit our purpose.

The Magnetic Bottle

After ionization, the positrons are guided by a 2π magnetic field parallelizer into a Time-Of-Flight (TOF) spectrometer [KR83]. The instrument comprises an interaction chamber (where the Ps production and photo-ionization takes place) with a 1 T homogeneous magnetic field, and a 0.5 m flight tube with a 10^{-3} T homogeneous magnetic field, cf. Figure C.1a. The magnetic bottle renders it possible to measure the energies of half the positrons ($P_{\mathrm{spektro}} = 50\%$) by TOF-technique with energy resolutions as low as 15 meV [KR83]. This device has been tested in Aarhus using a pulsed beam of electrons where the resolution was found to be $\simeq$ 20 meV [B$^+$04].

In the $B = 1$ T field, the lifetimes of Ps are changed to $\tau_T' = 1/\lambda_T' = 6.6$ ns and $\tau_S' = 1/\lambda_S' = 127$ ps, cf. Eq. (9.9). Although the lifetime of the triplet is changed dramatically, it does not affect our experiment, as it takes only 0.2 ns to pass through the laser focus, assuming a Ps speed of 10^5 m/s. This time is used as the effective interaction time τ_l in the crossed beam. We presume that the efficiency of the Ps-production in the SiO_2 foil is unaffected by the magnetic field in the interaction chamber.

Also, the magnetic field introduces a Zeeman shift, which has not been taken into account in the calculations of the generalized cross sections. Since the expectation value of the total orbital magnetic moment of ground state Ps is zero, a linear

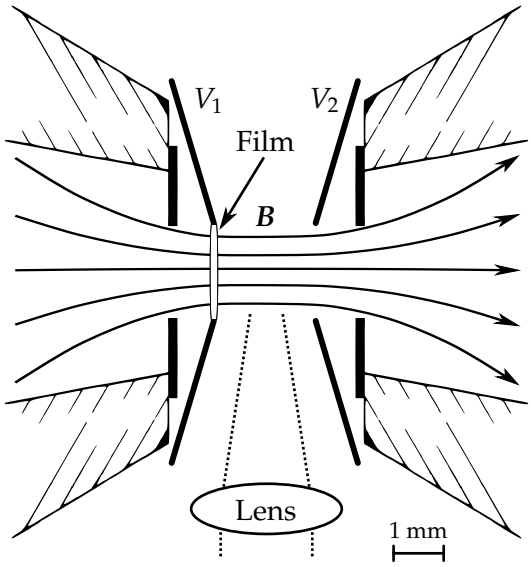

(a) Magnetic bottle and the interaction chamber. The focused laser beam will ionize Ps in the center of the chamber, thus liberating an electron. The electron is magnetically guided by the changing magnetic fields, cf. (b). The SiO_2 film is mounted on one of the electrodes, which can be bias with the voltages V_1 and V_2. The positrons traverse the film from left to right, thus forming Ps in the chamber where a laser beam is focused.

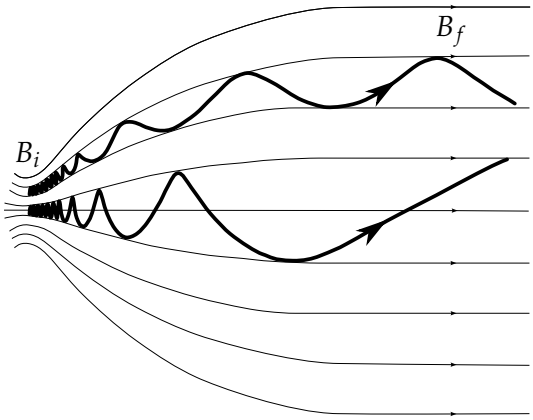

(b) Magnetic bottle: two electrons' trajectories are changed due to cyclotron motion in a slowly changing magnetic field between two homogeneous magnetic fields $B_i \gg B_f$. The electrons emitted in a 2π solid angle are thus all guided in the direction of a stop detector for the TOF measurement. From [Lun09], courtesy of M.D. Lund.

Figure C.1: The experimental setups for the MPI of Ps. Both figures are adapted from [KR83].

Zeeman effect cannot exist. Nevertheless, the shift appears as a result of the second-order interaction between the particles' spin magnetic moment and the magnetic field [FRS90, BP80, BLP82], rendering the Zeeman effect in Ps somewhat atypical. The energy levels of the three triplet states and the singlet are given in Eq. (9.8). In a $B = 1$ T field, the Zeeman shift of the energy levels is only 1.9% of the hyperfine splitting, Δ_1, hence the effect is considered negligible.

Anticipated Event Rate

I now estimate the event rate (ER) for the different MPI- and ATI-channels, given the conditions of the proposed experiment (cf. Table C.1). This quantity should be computed using the formula

$$\mathrm{ER} = \frac{N_{\mathrm{pulse}}}{\mathrm{s}} \times \frac{N_{e^+}}{\mathrm{pulse}} \times P_{\mathrm{SiO_2}}(e^+ \to \mathrm{Ps}) \times \underbrace{\hat{\sigma}_{N+S} \times F_0^{(N+S)} \times \tau_l}_{P_{N+S}} \times P_{\mathrm{spektro}}\,, \qquad \text{(C.4)}$$

and the results are shown in Table C.2. As can be seen there, the proposed experimental conditions leaves many MPI- and ATI-channels open. At this intensity, the ponderomotive shift is less than $E_\gamma - B_{\mathrm{Ps}}$ at all wavelengths. Nevertheless, the used intensity is a modest one, and $U_p = E_\lambda - B_{\mathrm{Ps}}$ occurs at $I_0 = 1.83 \times 10^{12}$ W/cm^2 for

$N_{\text{pulse}}/\text{s}$ (Hz)	N_{e^+}/pulse —	$P_{\text{SiO}_2}(e^+ \to \text{Ps})$ —	I_0 (W/cm^2)	τ_l (ns)	P_{spektro} —
2	5.43×10^5	0.3	3.8×10^{11}	0.2	0.50

Table C.1: Conditions in the proposed experiment.

λ (nm)	U_p (meV)	N —	S —	$E_\lambda - B_{\text{Ps}}$ (eV)	$\hat{\sigma}_{N+S}$ ($\text{cm}^{2(N+S)}\text{s}^{N+S-1}$)	ER (Hz)
355	4.50	2	0	0.19	4×10^{-49}	$1.6 \times 10^{+5}$
			1	3.68	8×10^{-82}	$8.3 \times 10^{+3}$
			2	7.17	2×10^{-114}	$1.4 \times 10^{+1}$
			3	10.66	3×10^{-147}	1.4×10^{-2}
532	10.1	3	0	0.19	1×10^{-80}	$1.6 \times 10^{+5}$
			1	2.52	2×10^{-112}	$7.1 \times 10^{+3}$
			2	4.85	1×10^{-144}	$3.6 \times 10^{+1}$
			3	7.18	1×10^{-176}	3.7×10^{-1}
1064	40.4	6	0	0.19	5×10^{-175}	$6.0 \times 10^{+2}$
			1	1.36	3×10^{-206}	$7.3 \times 10^{+1}$
			2	2.52	1×10^{-237}	$5.0 \times 10^{+0}$
			3	3.69	3×10^{-269}	3.1×10^{-1}
			4	4.85	8×10^{-301}	1.7×10^{-2}

Table C.2: Anticipated events per second for the different MPI- and ATI-channels given the proposed experiment conditions, Table C.1.

$(N, S) = (6, 0)$, hence channel closing should be detectable by better focusing. At a given wavelength, the pair's free energy after ionization $(E_\lambda - B_{\text{Ps}} - U_p)$ in the different channels are discrete by at least $\simeq 1$ eV—well separable by the spectrometer. The event rates in Table C.2 are judged from an optimistic point of view, but even if, say, four of the factors from Table C.1 should turn out to be half of the expected, this would only reduce the ER by a factor of 2^4, as Eq. (C.4) is linear in these factors. At least the ER of the MPI channels $(S = 0)$ remain considerable in such a more pessimistic point of view.

APPENDIX D

OUTLOOK

In the near future, NA63 intends to perform a couple of experiments revolving around the topics dealt with in the first part of this thesis. I will in the following give only a brief introduction to the general ideas of these experiments, as I have not contributed to the planning of them. My only aim of describing them here is completeness and to spur interest of the future experiments.

D.1 Magnetic Bremsstrahlung Suppression

Assuming a homogeneous magnetic field of strength B perpendicular to the particle trajectory, the small deflection angle acquired after travelling a distance x is

$$\theta_B(x) = \frac{eBx}{E_0} \tag{D.1}$$

We will consider the situation where the magnetic field deflects the electron outside the formation zone within $\ell_{\mathrm{f0}}/2$

$$\gamma_{\mathrm{L}}^{-1} \lesssim \theta_B(\ell_{\mathrm{f0}}/2) \Leftrightarrow 1 \lesssim \frac{eB\ell_{\mathrm{f0}}\gamma_{\mathrm{L}}}{2E_0} = \frac{eB\gamma_{\mathrm{L}}^3\hbar c}{E_0\hbar\omega}(1-y) = \frac{\gamma_{\mathrm{L}}eB\hbar}{m^2c^3}\frac{1-y}{y} = \frac{\gamma_{\mathrm{L}}B}{B_0}\frac{1-y}{y}$$
$$y \lesssim (1 + B_0/\gamma_{\mathrm{L}}B)^{-1} \simeq \gamma_{\mathrm{L}}B/B_0 \tag{D.2}$$

where $B_0 = m^2c^3/e\hbar = 4.4 \times 10^9$ T is the critical magnetic field. Through this crude estimation of the effect, Klein finds the an expression describing the relative suppression in case of strong suppression

$$S = \left(\frac{yB_0}{\gamma_{\mathrm{L}}B(1-y)}\right)^{2/3}, \tag{D.3}$$

A proper theoretical treatment of the effect is given in [BKS88]. At $E_0 = 207$ GeV and $B = 2$ T (saturated iron), the simple threshold in Eq. (D.2) is $y \lesssim 1.8 \times 10^{-4}$, corresponding to $\hbar\omega \lesssim 0.038$ GeV. Even though the effect is also detectable at larger

photon energies, this experiment will be especially sensitive to Synchrotron Radiation contamination. However, U. I. Uggerhøj has found conditions at which the experiment should be feasible. This requires quite an increase of the experimental setup's length, thus lowering the necessary field in the purging magnet. Under the mentioned circumstances, the power spectrum is lowered by 15% relative to $B = 0\,\mathrm{T}$. As discussed in Sec. 5.4, the statistical errors can increase heavily when combining two spectra, whence one should be very careful with acquiring sufficient statistics for significantly detecting the small suppression.

D.2 Bremsstrahlung from Lead Ions

In many renowned bremsstrahlung references, the bremsstrahlung from projectiles of spatial extent, *e.g.* an ion, is simply found by replacing m with the ion mass. However, as shown in [Sø05, Sø09], high energy bremsstrahlung photons can have wavelengths small enough to probe the constituents of the projectile nucleus. Above the corresponding photon energy, the power spectrum is heavily suppressed.

Within a few years, the SPS will inject Pb^{82+} ions in the CERN LHC, allowing for extracted bursts of $\gamma_\mathrm{L} = 170$ lead ions in the H4 beam area. The NA63 collaboration will then measure the effect of the ion's spatial extent on the bremsstrahlung power spectrum.

APPENDIX E

SYNOPSIS

Synopsis

When entering a medium, an electron travelling close to light speed will lose kinetic energy due to a large number of collisions with the material. At the highest energies, the dominant energy loss mechanism is bremsstrahlung. Although the basic bremsstrahlung mechanism is well-investigated, a number of deviations from this can take place under particular circumstances. This thesis has especially dealt with the behaviours in thin but dense targets. The phenomena are particularly pronounced at large particle energies, *i.e.* relevant to *e.g.* astrophysics. The principles of the phenomena are also transferable to other fields of physics.

On the route towards creating anti-hydrogen ($\overline{\mathrm{H}}$), one of the obstacles is attaining slow anti-electrons. A apparatus rendering this possible has been extensively tested in Aarhus. The apparatus will play a crucial role in our group's future $\overline{\mathrm{H}}$ production at CERN. In Aarhus, the apparatus has been used to study the atom-like state of an electron and a anti-electron, positronium (Ps). Having no nucleus, Ps can be considered as the link between hydrogen and anti-hydrogen, *i.e.* atom number zero.

Resumé

En elektron, der rejser tæt på lysets hastighed, vil i et materiale miste kinetisk energi på grund af et stort antal kollisioner med materialets atomer. Ved de højeste energier er den dominerende energitabsmekanisme bremsestråling. Hvis materialet besidder høj kerneladning og massefylde, sker der en række afvigelser fra den ellers velkendte mekanisme. Denne afhandling har især behandlet afvigelserne i tynde metalfolier. Fænomenerne er særligt udtalte ved høje energier, hvorfor studiet kun har været muligt ved CERN's acceleratorer. Afvigelserne har stor betydning for forståelsen af bremsestrålingen fra de mange kosmiske partikler, der konstant bombarderer jorden.

Desuden har studiet omhandlet et apparat, der kan nedbremse anti-elektroner. Inden for et par år vil apparatet spille en vigtig rolle i produktionen af anti-hydrogen $\overline{\mathrm{H}}$ på CERN. I Århus har apparatet har været brugt til at studere den atom-lignende tilstand af en elektron og en anti-elektron, positronium (Ps). Da Ps "mangler" en atomkerne, kan det betragtes som bindeleddet mellem hydrogen og anti-hydrogen, dvs. atom nummer nul.

BIBLIOGRAPHY

[A+90] B. Adeva *et al*. The construction of the L3 experiment. *Nucl. Instr. Meth. A* **289**, 35–102 (1990). doi:10.1016/0168-9002(90)90250-A.

[A+95] P. L. Anthony *et al*. An Accurate Measurement of the LPM Effect. *Phys. Rev. Lett.* **75**, 1949–1952 (1995). doi:10.1103/PhysRevLett.75.1949.

[A+96a] P. L. Anthony *et al*. Measurement of Dielectric Suppression of Bremsstrahlung. *Phys. Rev. Lett.* **76**, 3550–3553 (1996). doi:10.1103/PhysRevLett.76.3550.

[A+96b] H. Avakian *et al*. Performance of F101 radiation resistant lead glass shower counters. *Nucl. Instr. Meth. A* **378**, 155–161 (1996). doi:10.1016/0168-9002(96)00443-3.

[A+97] P. L. Anthony *et al*. Bremsstrahlung suppression due to the LPM and dielectric effects in a variety of materials. *Phys. Rev. D* **56**, 1373 (1997). doi:10.1103/PhysRevD.56.1373.

[AFS00] G. S. Adkins, R. N. Fell, and J. Sapirstein. Order α^2 Corrections to the Decay Rate of Orthopositronium. *Phys. Rev. Lett.* **84**, 5086–5089 (2000). doi:10.1103/PhysRevLett.84.5086.

[AFS02] G. S. Adkins, R. N. Fell, and J. Sapirstein. Two-Loop Correction to the Orthopositronium Decay Rate. *Annals of Physics* **295**, 136–193 (2002). doi:10.1006/aphy.2001.6219.

[AHD98] F. Anderegg, E. M. Hollmann, and C. F. Driscoll. Rotating Field Confinement of Pure Electron Plasmas Using Trivelpiece-Gould Modes. *Phys. Rev. Lett.* **81**, 4875–4878 (1998). doi:10.1103/PhysRevLett.81.4875.

[AJK04] S. Asai, O. Jinnouchi, and T. Kobayashi. Solution of orthopositronium lifetime puzzle. *Int. J. Mod. Phys.* **A19**, 3927–3938 (2004). doi:10.1142/S0217751X0402018X.

[ARG94] A. H. Al-Ramadhan and D. W. Gidley. New precision measurement of the decay rate of singlet positronium. *Phys. Rev. Lett.* **72**, 1632–1635 (1994). doi:10.1103/PhysRevLett.72.1632.

[AS64] Milton Abramowitz and Irene A. Stegun. *Handbook of Mathematical Functions with Formulas, Graphs, and Mathematical Tables*. Dover 10th edition (1964).

[AS96] A. I. Akhiezer and N. F. Shul'ga. *High Energy Electrodynamics in Matter*. Gordon and Breach (1996).

[B+89] J.A. Bakken *et al*. Study of the energy calibration of a high resolution electromagnetic calorimeter. *Nucl. Instr. Meth. A* **280**, 25–35 (1989). doi:10.1016/0168-9002(89)91269-2.

[B+04] P. Balling *et al*. Perspectives for pulsed positrons. *Nucl. Instr. Meth. B* **221**, 200–205 (2004). doi:10.1016/j.nimb.2004.03.055.

[BD87] Richard Blankenbecler and Sidney D. Drell. Quantum treatment of beamstrahlung. *Phys. Rev. D* **36**, 277–288 (1987). doi:10.1103/PhysRevD.36.277.

[BD96] Richard Blankenbecler and Sidney D. Drell. LPM effect for finite targets. *Phys. Rev. D* **53**, 6265–6281 (1996). doi:10.1103/PhysRevD.53.6265.

[BDSS77] G. Battistuzzi, B. Dainese, C. Signorini, and A.M. Stefanini. A plunger device for in-beam measurements of nuclear lifetimes. *Nucl. Instr. Meth.* **146**, 481–486 (1977). doi:10.1016/0029-554X(77)90197-5.

[Bet53] H. A. Bethe. Molière's Theory of Multiple Scattering. *Phys. Rev.* **89**, 1256–1266 (1953). doi:10.1103/PhysRev.89.1256.

[BG66] H. Barry Bebb and Albert Gold. Multiphoton Ionization of Hydrogen and Rare-Gas Atoms. *Phys. Rev.* **143**, 1–24 (1966). doi:10.1103/PhysRev.143.1.

[BG82] Lowell S. Brown and Gerald Gabrielse. Precision spectroscopy of a charged particle in an imperfect Penning trap. *Phys. Rev. A* **25**, 2423–2425 (1982). doi:10.1103/PhysRevA.25.2423.

[BG86] Lowell S. Brown and Gerald Gabrielse. Geonium theory: Physics of a single electron or ion in a Penning trap. *Rev. Mod. Phys.* **58**, 233–311 (1986). doi:10.1103/RevModPhys.58.233.

[BH34] H. Bethe and W. Heitler. On the Stopping of Fast Particles and on the Creation of Positive Electrons. *Proc. Roy. Soc. A* **146**, 83 (1934). doi:10.1098/rspa.1934.0140.

[BJ03] B. H. Bransden and C. J. Joachain. *Physics of Atoms and Molecules*. Prentice Hall 2nd edition (2003).

[BK98] V. N. Baier and V. M. Katkov. The Theory of the LPM Effect. *Phys. Rev. D* **57**, 3146 (1998). doi:10.1103/PhysRevD.57.3146.

[BK99a] V. N. Baier and V. M. Katkov. LPM effect and transition radiation in structured targets. *Phys. Rev. D* **60**, 076001 (1999). doi:10.1103/PhysRevD.60.076001.

[BK99b] V. N. Baier and V. M. Katkov. Multiphoton Effects in Energy Loss Spectra. *Phys. Rev. D* **59**, 056003 (1999). doi:10.1103/PhysRevD.59.056003.

[BK10] V. N. Baier and V. M. Katkov. The LPM effect in structured Ta target. Private communications (2010).

[BKR99] Robert Bluhm, V. Alan Kostelecký, and Neil Russell. *CPT* and Lorentz Tests in Hydrogen and Antihydrogen. *Phys. Rev. Lett.* **82**, 2254–2257 (1999). doi:10.1103/PhysRevLett.82.2254.

[BKS88] V. N. Baier, V. M. Katkov, and V. M. Strakhovenko. Radiation from relativistic particles colliding in a medium in the presense of an external field. *Sov. Phys. JETP* **67**, 70–77 (1988).

[Bla97a] Richard Blankenbecler. Multiple scattering and functional integrals. *Phys. Rev. D* **55**, 2441–2448 (1997). doi:10.1103/PhysRevD.55.2441.

[Bla97b] Richard Blankenbecler. Structured targets and the LPM effect. *Phys. Rev. D* **55**, 190–195 (1997). doi:10.1103/PhysRevD.55.190.

[Bla06] Richard Blankenbecler. Private communications (2006).

[BLP82] V. B. Berestetskii, E. M. Lifshitz, and L. P. Pitaevskii. *Quantum Electrodynamics* volume 4 of *Course of Theoretical Physics*. Elsevier Butterworth-Heinemann 2nd edition (1982).

[BM54] H. A. Bethe and L. C. Maximon. Theory of Bremsstrahlung and Pair Production. I. Differential Cross Section. *Phys. Rev.* **93**, 768–784 (1954). doi:10.1103/PhysRev.93.768.

[BP80] S Berko and H. N. Pendleton. Positronium. *Annual Review of Nuclear and Particle Science* **30**, 543–581 (1980). doi:10.1146/annurev.ns.30.120180.002551.

[BR02] U. C. Bergmann and K. Riisager. A systematic error in maximum likelihood fitting. *Nucl. Instr. Meth. A* **489**, 444–447 (2002). doi:10.1016/S0168-9002(02)00864-1.

[BS97] B. M. Bolotovskii and A. V. Serov. On the force line representation of radiation fields. *Phys. Usp.* **40**, 1055–1059 (1997). doi:10.1070/PU1997v040n10ABEH000293.

[CDG+05] D. B. Cassidy, S. H. M. Deng, R. G. Greaves, T. Maruo, N. Nishiyama, J. B. Snyder, H. K. M. Tanaka, and A. P. Mills Jr. Experiments with a High-Density Positronium Gas. *Phys. Rev. Lett.* **95**, 195006 (2005). doi:10.1103/PhysRevLett.95.195006.

[CER91] CERN Accelerators and Beams. Secondary Beams and Areas | Magnets [online]. (1991). Available from: http://ab-div-atb-ea.web.cern.ch/ab-div-atb-ea/pmwiki/pmwiki.php?n=Magnets.Magnets [cited 2010.03.01].

[CMJ07] D. B. Cassidy and A. P. Mills Jr. The Production of Molecular Positronium. *Nature* **449**, 195–197 (2007). doi:10.1038/nature06094.

[CMJB74] K. F. Canter, A. P. Mills Jr., and S. Berko. Efficient Positronium Formation by Slow Positrons Incident on Solid Targets. *Phys. Rev. Lett.* **33**, 7 (1974). doi:10.1103/PhysRevLett.33.7.

[CMJM81] S Chu, A. P. Mills Jr., and C. A. Murray. Thermodynamics of positronium thermal desorption from surfaces. *Phys. Rev. B* **23**, 2060–2064 (1981). doi:10.1103/PhysRevB.23.2060.

[Dav90] Ronald C. Davidson. *Physics of Nonneutral Plasma*. Addison-Wesley, Redwood City, CA (1990).

[DB52] Martin Deutsch and Sanborn C. Brown. Zeeman Effect and Hyperfine Splitting of Positronium. *Phys. Rev.* **85**, 1047–1048 (1952). doi:10.1103/PhysRev.85.1047.

[DBM54] Handel Davies, H. A. Bethe, and L. C. Maximon. Theory of Bremsstrahlung and Pair Production. II. Integral Cross Section for Pair Production. *Phys. Rev.* **93**, 788–795 (1954). doi:10.1103/PhysRev.93.788.

[DD51] Martin Deutsch and Everett Dulit. Short Range Interaction of Electrons and Fine Structure of Positronium. *Phys. Rev.* **84**, 601–602 (1951). doi:10.1103/PhysRev.84.601.

[DE98] G. Dlubek and S. Eichler. Do MELT or CONTIN Programs Accurately Reveal the o-Ps Lifetime Distribution in Polymers? Analysis of Simulated Lifetime Spectra. *Physica Status Solidi (a)* **168**, 333–350 (1998).

[DO99] Daniel H. E. Dubin and T. M. O'Neil. Trapped nonneutral plasmas, liquids, and crystals (the thermal equilibrium states). *Rev. Mod. Phys.* **71**, 87 (1999). doi:10.1103/RevModPhys.71.87.

[DSSS03] J. R. Danielson, P. Schmidt, J. P. Sullivan, and C. M. Surko. A Cryogenic, High-field Trap for Large Positron Plasmas and Cold Beams. In *NON-NEUTRAL PLASMA PHYSICS V: Workshop on Non-Neutral Plasmas* volume 692 pages 149–161. AIP (2003). doi:10.1063/1.1635170.

[Dun04] Richard A. Dunlap. *An Introduction to the Physics of Nuclei and Particles*. Thomson - Brooks/Cole 1st edition (2004).

[Fei66] E. L. Feinberg. High Energy Successive Interactions. *Sov. Phys. JETP* **23**, 132 (1966).

[FRS90] G. Feinberg, A. Rich, and J. Sucher. Quadratic Zeeman effect in positronium. *Phys. Rev. A* **41**, 3478–3480 (1990). doi:10.1103/PhysRevA.41.3478.

[FS86] S. P. Fomin and N. F. Shul'ga. On the space-time evolution of the process of ultrarelativistic electron radiation in a thin layer of substance. *Phys. Lett. A* **114**, 148 (1986). doi:10.1016/0375-9601(86)90544-X.

[Fur34] W. H. Furry. Approximate Wave Functions for High Energy Electrons in Coulomb Fields. *Phys. Rev.* **46**, 391–396 (1934). doi:10.1103/PhysRev.46.391.

[Gal] M. Galan. Table de Radionucléide [online]. Available from: `http://www.nucleide.org/DDEP_WG/Nuclides/Na-22_tables.pdf` [cited 2010.06.11].

[Gea03] Geant4 Collaboration. Geant4. *Nucl. Instr. Meth. A* **506**, 250–303 (2003). `doi:10.1016/S0168-9002(03)01368-8`.

[GM03] R. G. Greaves and J. Moxom. Design and Performance of a Trap-Based Positron Beam Source. *AIP Conference Proceedings* **692**, 140–148 (2003).

[GM08] R. G. Greaves and J. M. Moxom. Compression of trapped positrons in a single particle regime by a rotating electric field. *Physics of Plasmas* **15**, 072304 (2008). `doi:10.1063/1.2956335`.

[GMJ86] E. M. Gullikson and A. P. Mills Jr. Positron Dynamics in Rare-Gas Solids. *Phys. Rev. Lett.* **57**, 376–379 (1986). `doi:10.1103/PhysRevLett.57.376`.

[GMZ95] D. W. Gidley, D. N. McKinsey, and P. W. Zitzewitz. Fast positronium formation and dissociation at surfaces. *Journal of Applied Physics* **78**, 1406–1410 (1995). `doi:10.1063/1.360296`.

[Gre07] R. G. Greaves. Private communications (2007).

[GS00] R. G. Greaves and C. M. Surko. Inward Transport and Compression of a Positron Plasma by a Rotating Electric Field. *Phys. Rev. Lett.* **85**, 1883–1886 (2000). `doi:10.1103/PhysRevLett.85.1883`.

[GS02] R. G. Greaves and C. M. Surko. Positron trapping and the creation of high-quality trap-based positron beams. *Nucl. Instr. Meth. B* **192**, 90–96 (2002). `doi:10.1016/S0168-583X(02)00717-6`.

[GZ78] D. W. Gidley and P. W. Zitzewitz. Measurement of the vacuum decay rate of orthopositronium formed in an MgO-lined cavity. *Phys. Lett. A* **69**, 97–99 (1978). `doi:10.1016/0375-9601(78)90368-7`.

[GZMR76] D. W. Gidley, P. W. Zitzewitz, K. A. Marko, and A. Rich. Measurement of the Vacuum Decay Rate of Orthopositronium. *Phys. Rev. Lett.* **37**, 729–732 (1976). `doi:10.1103/PhysRevLett.37.729`.

[H$^+$03] H. D. Hansen *et al*. Is the Electron Radiation Length Constant at High Energies? *Phys. Rev. Lett.* **91**, 014801 (2003). `doi:10.1103/PhysRevLett.91.014801`.

[H$^+$04] H. D. Hansen *et al*. LPM effect for multihundred GeV electrons. *Phys. Rev. D* **69**, 032001 (2004). `doi:10.1103/PhysRevD.69.032001`.

[Hal54] Otto Halpern. Magnetic Quenching of the Positronium Decay. *Phys. Rev.* **94**, 904–907 (1954). `doi:10.1103/PhysRev.94.904`.

[HC05] T. Harko and K. S Cheng. Photon Emissivity of The Electrosphere of Bare Strange Stars. *Astrophys. J.* **622**, 1033 (2005). `doi:10.1086/428036`.

[Hei54] W. Heitler. *The Quantum Theory of Radiation*. Dover Publications 3rd edition (1954).

[HFG08] D. Hanneke, S. Fogwell, and G. Gabrielse. New Measurement of the Electron Magnetic Moment and the Fine Structure Constant. *Phys. Rev. Lett.* **100**, 120801 (2008). doi:10.1103/PhysRevLett.100.120801.

[HHKW87] P. Hasbach, G. Hilkert, E. Klempt, and G. Werth. Experimental determination of the ortho-positronium lifetime in vacuum. *Il Nuovo Cimento A* **97**, 419–425 (1987). doi:10.1007/BF02734466.

[J+04] P. Jaikumar *et al*. Bremsstrahlung photons from the bare surface of a strange quark star. *Phys. Rev. D* **70**, 023004 (2004). doi:10.1103/PhysRevD.70.023004.

[Jac98] John David Jackson. *Classical Electrodynamics*. John Wiley & Sons 3 edition (1998).

[Jam06] Frederick E. James. *Statistical Methods in Experimental Physics*. World Scientific Singapore 2nd edition (2006).

[KAK09] Y. Kataoka, S. Asai, and T. Kobayashi. First test of $\mathcal{O}(\alpha^2)$ correction of the orthopositronium decay rate. *Phys. Lett. B* **671**, 219–223 (2009). doi:10.1016/j.physletb.2008.12.008.

[Kar03] Savely G. Karshenboim. Precision Study of Positronium: Testing Bound State QED Theory. *Intl. Jour. of Mod. Phys. A* **19**, 3879–3896 (2003). arXiv:hep-ph/0310099v1.

[KKV08] Bernd A. Kniehl, Anatoly V. Kotikov, and Oleg L. Veretin. Orthopositronium Lifetime: Analytic Results in $\mathcal{O}(\alpha)$ and $\mathcal{O}(\alpha^3 \ln \alpha)$. *Phys. Rev. Lett.* **101**, 193401 (2008). doi:10.1103/PhysRevLett.101.193401.

[Kle99] Spencer Klein. Suppression of bremsstrahlung and pair production due to environmental factors. *Rev. Mod. Phys.* **71**, 1501–1538 (1999). doi:10.1103/RevModPhys.71.1501.

[KP00] B. Kämpfer and O. P. Pavlenko. The Ter-Mikaelian and Landau-Pomeranchuk effects for induced soft gluon radiation in a QCD medium. *Phys. Lett. B* **477**, 171–177 (2000). doi:10.1016/S0370-2693(00)00200-8.

[KR83] P. Kruit and F. H. Read. Magnetic field paralleliser for 2π electron-spectrometer and electron-image magnifier. *Journal of Physics E: Scientific Instruments* **16**, 313–324 (1983). Available from: http://stacks.iop.org/0022-3735/16/313.

[KST99] Boris Z. Kopeliovich, Andreas Schäfer, and Alexander V. Tarasov. Bremsstrahlung of a Quark Propagating Through a Nucleus. *Phys. Rev. C* **59**, 1609–1619 (1999). doi:10.1103/PhysRevC.59.1609.

[LD91] Gerald R. Lynch and Orin I. Dahl. Approximations to multiple Coulomb scattering. *Nucl. Instr. Meth. B* **58**, 6–10 (1991). doi:10.1016/0168-583X(91)95671-Y.

[LP53] L. D. Landau and I. J. Pomeranchuk. Electron-cascade Processes at Ultra-High Energies. *Dokl. Akad Nauk SSSR* **92**, 735 (1953).

[Lun09] Mikkel D. Lund. Commisioning of the ASACUSA Positron Beam Line. Master's thesis Department of Physics and Astronomy, Aarhus University (2009).

[Mad04] Lars Bojer Madsen. Positronium in laser fields. *Nucl. Instr. Meth. B* **221**, 174–181 (2004).

[MBSU08] A. Mangiarotti, S. Ballestrero, P. Sona, and U. I. Uggerhøj. Implementation of the LPM effect in the discrete-bremsstrahlung simulation of GEANT3 and Geant4. *Nucl. Instr. Meth. B* **266**, 5013–5019 (2008). doi:10.1016/j.nimb.2008.09.009.

[ME88] Peter W. Milonni and Joseph H. Eberly. *Lasers*. John Wiley and Sons. 1st edition (1988).

[MF53] Philip M. Morse and Herman Feshbach. *Methods of Theoretical Physics*. International Series in Pure and Applied Physics. McGraw-Hill New-York (1953).

[Mig56] A. B. Migdal. Bremsstrahlung and Pair Production in Condensed Media at High Energies. *Phys. Rev.* **103**, 1811–1820 (1956). doi:10.1103/PhysRev.103.1811.

[Mik97] U. I. Mikkelsen. *Experimental Investigations of the Interaction of Multi-GeV Particles with Strong Crystalline Fields*. PhD thesis, Institute for Storage Ring Facilities and SL-EA (CERN) (1997).

[MJ83] A. P. Mills Jr. Experimentation with Low Energy Positron Beams. In *Positron Solid-State Physics: Proceedings of the Int. School of Physics, Enrico Fermi* volume 83 page 455 (1983).

[MJG86] A. P. Mills Jr. and E. M. Gullikson. Solid neon moderator for producing slow positrons. *Applied Physics Letters* **49**, 1121–1123 (1986).

[ML99] L. B. Madsen and P. Lambropoulos. Scaling of hydrogenic atoms and ions interacting with laser fields: Positronium in a laser field. *Phys. Rev. A* **59**, 4574–4579 (1999). doi:10.1103/PhysRevA.59.4574.

[NGRZ90] J. S. Nico, D. W. Gidley, A. Rich, and P. W. Zitzewitz. Precision measurement of the orthopositronium decay rate using the vacuum technique. *Phys. Rev. Lett.* **65**, 1344–1347 (1990). doi:10.1103/PhysRevLett.65.1344.

[Oha80] H. C. Ohanian. Electromagnetic radiation fields: A simple approach via field lines. *Am. J. Phys.* **48**, 170 (1980).

[OL76] A. O'Hagan and Tom Leonard. Bayes estimation subject to uncertainty about parameter constraints. *Biometrika* **63**, 201–203 (1976). doi:10.1093/biomet/63.1.201.

[P+10] Randolf Pohl *et al*. The size of the proton. *Nature* **466**, 213–216 (2010). doi:10.1038/nature09250.

[Pal68] G. D. Palazzi. High-Energy Bremsstrahlung and Electron Pair Production in Thin Crystals. *Rev. Mod. Phys.* **40**, 611 (1968). doi:10.1103/RevModPhys.40.611.

[PCC+91] M. R. Poulsen, M. Charlton, J. Chevallier, B. I. Deutch, L. V. Jørgensen, and G Laricchia. Thermal activation of positronium from thin Ag(100) films in backscattering and transmission geometries. *Journal of Physics: Condensed Matter* **3**, 2849–2858 (1991). doi:10.1088/0953-8984/3/17/002.

[Per00] Donald H. Perkins. *Introduction to High Energy Physics*. Cambridge University Press (2000).

[Pho10] Photonis. XP2262 Characteristics [online]. (2010). Available from: http://www.electrontubes.com/pdf/XP2262.pdf.

[Raa99] Mette K. Raarup,. *Studies of Strong Field Phenomena and Negative Ions at the Storage Ring ASTRID,*. PhD thesis, Institute of Physics and Astonomi, University of Aarhus (1999).

[Ric81] Arthur Rich. Recent experimental advances in positronium research. *Rev. Mod. Phys.* **53**, 127–165 (1981). doi:10.1103/RevModPhys.53.127.

[Ros52] Bruno Benedetto Rossi. *High-Energy Particles*. Prentice-Hall, New York (1952).

[Rub04] A. Rubbia. Positronium as a probe for new physics beyond the standard model. *Int. J. Mod. Phys.* **A19**, 3961–3985 (2004). doi:10.1142/S0217751X0402021X.

[S+82] Todor Stanev *et al*. Development of ultrahigh-energy electromagnetic cascades in water and lead including the LPM effect. *Phys. Rev. D* **25**, 1291–1304 (1982). doi:10.1103/PhysRevD.25.1291.

[Sch90] Daniel V. Schroeder. *Beamstrahlung and QED Backgrounds at Future Linear Colliders*. PhD thesis, SLAC Report No. 371 (1990). Available from: http://www.slac.stanford.edu/cgi-wrap/getdoc/slac-r-371.pdf.

[Sco63] William T. Scott. The Theory of Small-Angle Multiple Scattering of Fast Charged Particles. *Rev. Mod. Phys.* **35**, 231–313 (1963). doi:10.1103/RevModPhys.35.231.

[SF78] N. F. Shul'ga and S. P. Fomin. Suppression of radiation in an amorphous medium and in a crystal. *JETP Letters* **27**, 117 (1978).

[SF98a] N. F. Shul'ga and S. P. Fomin. Bremsstrahlung of ultrarelativistic electrons in a thin layer of substance. *Nucl. Instr. Meth. B* **145**, 73–79 (1998). doi:10.1016/S0168-583X(98)00372-3.

[SF98b] N. F. Shul'ga and S. P. Fomin. Effect of Multiple Scattering on the Emission of Ultrarelativistic Electrons in a Thin Layer of Matter. *Sov. Phys. JETP* **86**, 32 (1998).

[SG04] C. M. Surko and R. G. Greaves. Emerging science and technology of antimatter plasmas and trap-based beams. *Physics of Plasmas* **11**, 2333 (2004). doi:10.1063/1.1651487.

[SL88] Peter J. Schultz and K. G. Lynn. Interaction of positron beams with surfaces, thin films, and interfaces. *Rev. Mod. Phys.* **60**, 701–779 (1988). doi:10.1103/RevModPhys.60.701.

[SLP89] C. M. Surko, M. Leventhal, and A. Passner. Positron Plasma in the Laboratory. *Phys. Rev. Lett.* **62**, 901–904 (1989). doi:10.1103/PhysRevLett.62.901.

[Sø92] Allan H. Sørensen. On the suppression of the gluon radiation for quark jets penetrating a dense quark gas. *Z. Phys. C* **53**, 595–600 (1992). doi:10.1007/BF01559735.

[Sø96] Allan H. Sørensen. Channeling, Bremsstrahlung and Pair Creation in Single Crystals. *Nucl. Instr. Meth. B* **119**, 1–29 (1996). doi:10.1016/S0168-583X(96)90267-0.

[Sø05] Allan H. Sørensen. Pair production and bremsstrahlung contributions to the stopping of relativistic heavy ions. *Nucl. Instr. Meth. B* **230**, 12–16 (2005). doi:10.1016/j.nimb.2004.12.009.

[Sø09] Allan H. Sørensen. Bremsstrahlung from relativistic heavy ions in matter. *Phys. Rev. A* **81**, 022901 (2009). doi:10.1103/PhysRevA.81.022901.

[SPH93] A. Shukla, M. Peter, and L. Hoffmann. Analysis of positron lifetime spectra using quantified maximum entropy and a general linear filter. *Nucl. Instr. Meth. A* **335**, 310–317 (1993). doi:10.1016/0168-9002(93)90286-Q.

[Ter61] F. F. Ternovskiĭ. On The Theory of Radiative Processes in Piecewise Homegeneous Media. *Sov. Phys. JETP* **12**, 123 (1961).

[TM53] M. L. Ter-Mikaelian. High Energy Electromagnetic Processes in Condensed Matter. *JETP* **25**, 296 (1953).

[TM72] M. L. Ter-Mikaelian. *High Energy Electromagnetic Processes in Condensed Matter*. John Wiley & Sons (1972).

[Tsa74] Yung-Su Tsai. Pair production and bremsstrahlung of charged leptons. *Rev. Mod. Phys.* **46**, 815–851 (1974). doi:10.1103/RevModPhys.46.815.

[Tsi72] R. Y. Tsien. Pictures of Dynamic Electric Fields. *Am. J. Phys.* **40**, 46 (1972). doi:10.1119/1.1986445.

[Ugg05] U. I. Uggerhøj. The Interaction of Relativistic Particles with Strong Crystalline Fields. *Rev. Mod. Phys.* **77**, 1131 (2005). doi:10.1103/RevModPhys.77.1131.

[Ugg06] U. I. Uggerhøj. Penetration Phenomena at Relativistic Energies. *Mat. Fys. Medd. Dan. Vid. Selsk.* **52**, 699–729 (2006).

[VZG03] R. S. Vallery, P. W. Zitzewitz, and D. W. Gidley. Resolution of the Orthopositronium-Lifetime Puzzle. *Phys. Rev. Lett.* **90**, 203402 (2003). doi:10.1103/PhysRevLett.90.203402.

[WGP95] Xin-Nian Wang, Miklos Gyulassy, and Michael Plümer. LPM Effect in QCD and Radiative Energy Loss in a Quark-Gluon Plasma. *Phys. Rev. D* **51**, 3436–3446 (1995). doi:10.1103/PhysRevD.51.3436.

[Wie10] Wiener. NemBOX [online]. (2010). Available from: http://www.wiener-d.com/products/16/92.html.

[Wik10] Wikipedia. Skew Normal Distribution [online]. (2010). Available from: http://en.wikipedia.org/wiki/Skew_normal_distribution.

[Y+06] W.-M. Yao *et al*. (Particle Data Group). *Journal of Physics G* **33**, 1–1232 (2006). doi:10.1088/0954-3899/33/1/001.

[Zak96] B. G. Zakharov. LPM Effect for Finite-size Targets. *JETP Lett.* **64**, 781 (1996). doi:10.1134/1.567126.